



**HAL**  
open science

## Charge and Entropy Transport in Dilute Metals

Alexandre Jaoui

► **To cite this version:**

Alexandre Jaoui. Charge and Entropy Transport in Dilute Metals. Strongly Correlated Electrons [cond-mat.str-el]. Sorbonne Université, 2019. English. NNT : 2019SORUS151 . tel-02950527

**HAL Id: tel-02950527**

**<https://theses.hal.science/tel-02950527>**

Submitted on 28 Sep 2020

**HAL** is a multi-disciplinary open access archive for the deposit and dissemination of scientific research documents, whether they are published or not. The documents may come from teaching and research institutions in France or abroad, or from public or private research centers.

L'archive ouverte pluridisciplinaire **HAL**, est destinée au dépôt et à la diffusion de documents scientifiques de niveau recherche, publiés ou non, émanant des établissements d'enseignement et de recherche français ou étrangers, des laboratoires publics ou privés.



COLLÈGE  
DE FRANCE  
—1530—

ESPCI  PARIS | PSL 

**THÈSE DE DOCTORAT DE  
L'UNIVERSITÉ PIERRE ET MARIE CURIE**

Spécialité **Physique**

Ecole doctorale Physique en Ile-de-France (ED654)  
Réalisée au : LPEM ESPCI Paris & JEIP Collège de France  
Présentée par

**Alexandre Jaoui**

Pour obtenir le grade de

**DOCTEUR de l'UNIVERSITÉ PIERRE ET MARIE  
CURIE**

Sujet de la thèse :

**Transport de Charge et d'Entropie dans les  
Métaux Dilués**

Soutenue le 08 Octobre 2019 au Collège de France à Paris

Devant le jury composé de :

Mme. Elena HASSINGER	Rapporteur
M. David CARPENTIER	Rapporteur
M. Abhay SHUKLA	Examineur
M. Mike SUTHERLAND	Examineur
M. Benoît FAUQUÉ	Directeur
M. Kamran BEHNIA	co-Directeur



## Abstract

---

This manuscript focuses on the electronic heat/charge transport dichotomy and the beyond-quantum-limit transport properties of dilute metals.

In the first part, we report on a study of two semi-metals,  $WP_2$  and Sb. In both cases, we found that the Wiedemann-Franz (WF) law is recovered at sufficiently low temperature ( $T \approx 2K$ ), but not at  $T \approx 15K$ . A careful examination shows that the finite-temperature deviation from the WF law is due to a mismatch between the prefactors of the  $T^2$ -resistivities, which arises because of electron-electron scattering. In the Boltzmann picture of transport such a difference is expected if there were abundant small-angle scattering among electrons. However, if we remember that momentum-conserving fermion-fermion collisions in normal-state liquid  $^3He$  also produce a  $T^2$ -resistivity, this opens the door for an alternative interpretation : the possible existence of a hydrodynamic regime for electrons in these semi-metals at the crossover between ballistic and diffusive regimes. In this scenario, the larger  $T$ -square thermal resistivity is caused by momentum-conserving collisions which decay the energy current and not the charge current. In the case of elemental Sb, we found that both charge and heat conductivities become ballistic at low temperature in millimetric samples and the ratio of the two  $T$ -square prefactors evolves with sample size. This observation supports the hydrodynamic scenario. Finally, we find that the phononic thermal conductivity also displays a large hydrodynamic correction in a narrow temperature window.

The second part of this thesis deals with the fate of the Fermi sea in the quantum limit. In the doped semi-conductor InAs we observe the existence of a field-induced insulating state for all geometries of transport. The comparison with the succession of field-induced states in graphite up to  $B = 90T$ , where in-plane metallicity coexists with a  $c$ -axis insulating behavior, reveals that the ground state of a 3D electron gas beyond the quantum limit is system-dependent. The observation of a saturating resistivity accompanied by vanishing thermoelectric coefficients for  $T < 1K$  and  $B > 14T$  in InAs points to the existence of a conductive surface state.

---

## Remerciements

---

Avant toutes choses je souhaite remercier les nombreuses personnes qui ont participé, directement ou indirectement, au travail réalisé durant ces trois dernières années.

Je tiens à remercier tout particulièrement les membres du jury pour l'intérêt qu'ils ont porté à mes recherches et leur travail d'évaluation. Je remercie Abhay Shukla d'avoir accepté d'endosser le rôle de président du jury ainsi que David Carpentier et Elena Hassinger pour leurs rôles de rapporteurs. Je remercie tout particulièrement Elena Hassinger pour les nombreuses corrections apportées à mon manuscrit.

Ma thèse s'est déroulée sous la direction de Benoît Fauqué et Kamran Behnia. Plus que de simples remerciements sont de rigueur; j'ai eu la chance d'apprendre à leur côtés tant sur le plan expérimental, fondamental que humain. Enfin, merci de m'avoir montré qu'il est possible de ramener au premier plan des sujets négligés depuis des décennies.

Je tiens évidemment à remercier l'ensemble des membres et des gestionnaires des deux laboratoires où j'ai passé ces trois ans : le LPEM à l'ESPCI et les JEIP du Collège de France. Je remercie évidemment aussi mes collègues à Nijmegen, Grenoble et Toulouse pour m'avoir permis de réaliser des expériences à fort champ magnétique et pour leur dur labeur en tant que contact local.

Évidemment, je remercie à chaque instant mes proches, à commencer par mes parents pour m'avoir permis d'être où j'en suis, ma soeur, mon frère, ma famille et mes amis pour le soutien et la joie qu'ils m'apportent. Enfin, Éva, je te remercie pour tout.

# Table of contents

<b>1</b>	<b>Introduction</b>	<b>1</b>
<b>2</b>	<b>Introduction to Heat &amp; Charge Transport</b>	<b>7</b>
2.1	The free electron gas . . . . .	8
2.1.1	The Drude model : a first glimpse at the Wiedemann-Franz law . . . . .	8
2.1.2	Sommerfeld's addition : exact Wiedemann-Franz law for non-interacting electrons . . . . .	10
2.2	Evolution of the Wiedemann-Franz law at finite temperature . . . . .	12
2.2.1	Small-angle & large-angle scattering . . . . .	12
2.2.2	Fermi liquid theory : electron - electron scattering . . . . .	14
2.2.3	'Ideal' resistance of metals . . . . .	15
2.2.4	Normal & Umklapp scattering processes . . . . .	15
2.3	Bosonic thermal conductivity : Phonons . . . . .	16
2.4	Heat & charge interplay : the thermoelectric tensor . . . . .	18
2.4.1	Thermopower . . . . .	18
2.4.2	Nernst effect . . . . .	20
2.5	Magnetoresistance . . . . .	21
<b>3</b>	<b>Experimental aspects</b>	<b>25</b>
3.1	Cryogenics & Magnets . . . . .	26
3.1.1	Physical Property Measurement System : PPMS . . . . .	26
3.1.2	Dilution Fridge . . . . .	27
3.1.3	High-field facilities . . . . .	28
3.2	4-point measurement setup . . . . .	28
3.3	Electrical resistivity measurement . . . . .	29
3.3.1	In-field geometries . . . . .	29
3.3.2	Sample holder . . . . .	30
3.3.3	Experimental banana skin : electrical transport . . . . .	30

3.4	Thermal conductivity and thermo-electrical measurements . . . . .	31
3.4.1	Setups . . . . .	31
3.4.2	Excluding thermal leaks . . . . .	32
3.4.3	Recovering the Wiedemann-Franz law in Silver . . . . .	33
<b>4</b>	<b>Fate of the Fermi sea in the quantum limit : InAs Vs Graphite</b>	<b>35</b>
4.1	Introduction & motivation . . . . .	36
4.1.1	Fermiology of graphite . . . . .	37
4.1.2	Field-induced states of graphite . . . . .	38
4.1.3	Presentation of Indium Arsenide . . . . .	43
4.2	Indium arsenide in the deep quantum limit . . . . .	48
4.2.1	Resistivity in the field-induced state . . . . .	50
4.2.2	Vanishing thermoelectric coefficients . . . . .	53
4.3	Discussion on the in-field transport properties of dilute metals . . . . .	56
4.3.1	Study of the activated behavior . . . . .	56
4.3.2	Electronic ground state of dilute metals in the deep quantum limit . . . . .	59
4.3.3	Towards a second conduction channel in InAs ? . . . . .	60
4.4	First Conclusion . . . . .	62
<b>5</b>	<b>Charge and Entropy transport in WP<sub>2</sub></b>	<b>63</b>
5.1	Presentation of WP <sub>2</sub> . . . . .	64
5.1.1	Fermiology of WP <sub>2</sub> . . . . .	65
5.1.2	Transport properties of WP <sub>2</sub> . . . . .	66
5.1.3	Samples presentation . . . . .	67
5.2	Experimental results - WP <sub>2</sub> . . . . .	68
5.2.1	Temperature dependence of the electrical resistivity . . . . .	68
5.2.2	Temperature dependence of the thermal conductivity . . . . .	69
5.3	Discussion on the strong heat/charge transport dichotomy . . . . .	71
5.3.1	Phononic thermal conductivity . . . . .	71
5.3.2	Temperature dependence of the Lorenz number . . . . .	73
5.3.3	Abundant small-angle resistive electron-electron scattering . . . . .	75
5.4	Conclusion on the heat/charge transport dichotomy of WP <sub>2</sub> . . . . .	77
<b>6</b>	<b>Charge and Entropy transport in Antimony</b>	<b>79</b>
6.1	Presentation of Antimony . . . . .	81
6.1.1	Fermiology of Sb . . . . .	81
6.1.2	Samples presentation . . . . .	84

6.2	Study of the electrical resistivity of Sb . . . . .	85
6.2.1	Temperature dependence of the resistivity . . . . .	85
6.2.2	Study of the magnetoresistance . . . . .	87
6.3	Study of the thermal conductivity of Sb . . . . .	90
6.3.1	The recovery of the Wiedemann-Franz law at low temperature . . . . .	90
6.3.2	In-field Temperature dependence of the thermal conductivity . . . . .	91
6.3.3	High field dependence of the thermal conductivity . . . . .	92
6.3.4	Study of the specific heat . . . . .	94
6.3.5	Study of the thermoelectric effects in Sb . . . . .	95
6.4	Discussion on the thermal transport properties of Sb . . . . .	98
6.4.1	Separation of the electronic and phononic thermal conductivities . . . . .	99
6.4.2	Origin of the $1/B$ -periodic oscillations . . . . .	104
6.5	Conclusion on the electronic and phononic transport properties of Sb . . . . .	110
<b>7</b>	<b>Hydrodynamic Flow of Quasiparticles</b>	<b>111</b>
7.1	Introduction to hydrodynamic transport . . . . .	113
7.1.1	Gurzhi's hierarchy of scattering times . . . . .	113
7.1.2	An experimental challenge . . . . .	115
7.1.3	The case of $^3\text{He}$ . . . . .	116
7.2	Quantifying normal and resistive mean-free-paths of electrons . . . . .	118
7.2.1	Determination of a hydrodynamic temperature window . . . . .	118
7.3	Discussion on the emergence of a hydrodynamic electronic transport properties in $\text{WP}_2$ and Sb . . . . .	120
7.3.1	Study of possible hydrodynamic signatures in $\text{WP}_2$ . . . . .	120
7.3.2	Size-dependence of the resistivity $T^2$ -prefactor in Sb . . . . .	123
7.3.3	Discussion on the thermal conductivity of phonons in Sb . . . . .	125
<b>8</b>	<b>Conclusion</b>	<b>133</b>
	<b>References</b>	<b>137</b>
	<b>List of figures</b>	<b>151</b>
	<b>Appendix Supplementary Data</b>	<b>163</b>
.1	Supplementary Data : Graphite . . . . .	163
.2	Supplementary Data : $\text{WP}_2$ . . . . .	164
.3	Supplementary Data : Sb . . . . .	166



# Chapter 1

## Introduction

The definition of metallicity has been intensely debated for more than a century now. While P. Drude and A. H. Lorentz were the first to associate the phenomenon of electrical conductivity with the free electron gas, it was A. Sommerfeld and F. Bloch who introduced the Fermi-Dirac statistics in the model to acknowledge the quantum nature of the electron. For the first time, it became possible to reconcile theory and experimental reports on the specific heat of alkali metals [1]. However, this semi-classical description fails to describe non-alkali metals. The victory of the modern electron theory was to link the electronic transport properties of a metal to its individual Fermi surface. As an example, the FS of the alkali Na is a sphere (shown in figure 1.1.a) whereas elemental lead displays a hard-to-describe but certainly non-spherical FS (featured in figure 1.1.b). Both materials exhibit disparate transport properties [2, 3]. Just like the wildlife at the summit of a mountain differs from the one down in the valley, the transport properties of a metal evolve with the shape of its Fermi surface. At this point, a new definition of a metal emerges, it is 'a solid with a Fermi surface' [4] associated with a first energy scale : the Fermi energy  $E_F$ .

The electrons responsible for the finite conductivity at  $T = 0$  are located in the vicinity of the Fermi surface. Since they belong to a partially filled electronic band (see figure 1.1.c) they can be easily scattered to previously unoccupied states under the effect of an electric field. In other words, they contribute to electrical conductivity.

Quite the contrary, if electrons in the highest occupied states have no continuum of unoccupied states to be scattered to, the system does not respond when subjected to an electric field : it is now an insulator. Its Fermi level is buried deep in a forbidden energy gap, as illustrated in figure 1.1.c. The gap is material dependent and extends over several eV in most insulators or undoped semi-conductors.

One of them is silicon. In undoped samples  $\sigma \xrightarrow{T \rightarrow 0} 0$  was verified : the system is an insulator. When dopants are added to a semi-conductor, such as phosphorus to Si, more and

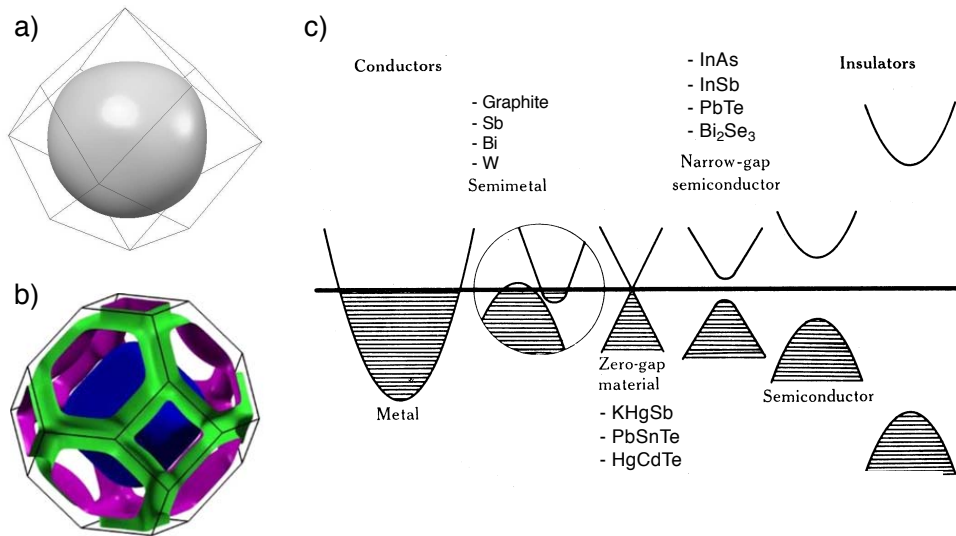


Fig. 1.1 **a)** Fermi surface of Sodium in the first Brillouin zone of the body centered cubic lattice from Lee [5]. **b)** Fermi surface of lead in the first Brillouin zone of a cubic face centered Bravais lattice. Figure from Hermann *et al.* [6]. **c)** Schematic representation of the typical band structure of metals, semi-conductors, semi-metals, zero-gap systems and insulators. Examples of materials corresponding to each class are indicated. Figure from J.P. Issi [7]

more impurity energy levels emerge in the gap. As they begin to aggregate, an impurity band is formed (figure 1.2.a). With further increase of the doping, the density of impurities becomes high enough to permit the overlapping of the electronic wavefunctions; the electrons start to delocalize and the conductivity becomes finite at  $T = 0$ . Here, the Fermi energy is pinned in the impurity band (figure 1.2.b). It was to account for this charge delocalization without a Fermi surface, reported in Si:P as an example [8], that Mott described metals in the broadest sense as 'systems which conduct electricity at  $T = 0$ ' [9].

Finally, once the doping exceeds a critical value, the highest occupied band of the semiconductor and the impurity band begin to overlap marking the emergence of a Fermi surface with bulk carrier concentrations as low as  $10^{15} \text{ cm}^{-3}$  in systems with large Bohr radius [10]. This carrier density is to be compared to  $n \approx 10^{22} \text{ cm}^{-3}$  in usual metals. The study of doped semi-conductors leads to fundamental results as well as multiple applications amongst which we find one of the building blocks of modern electronics : the transistor. Recently, it was shown that narrow-gap semi-conductors can display a 3D-like Dirac dispersion. Those systems, sketched as zero-gap materials in figure 1.1.c, have been actively investigated in the context of topological materials.

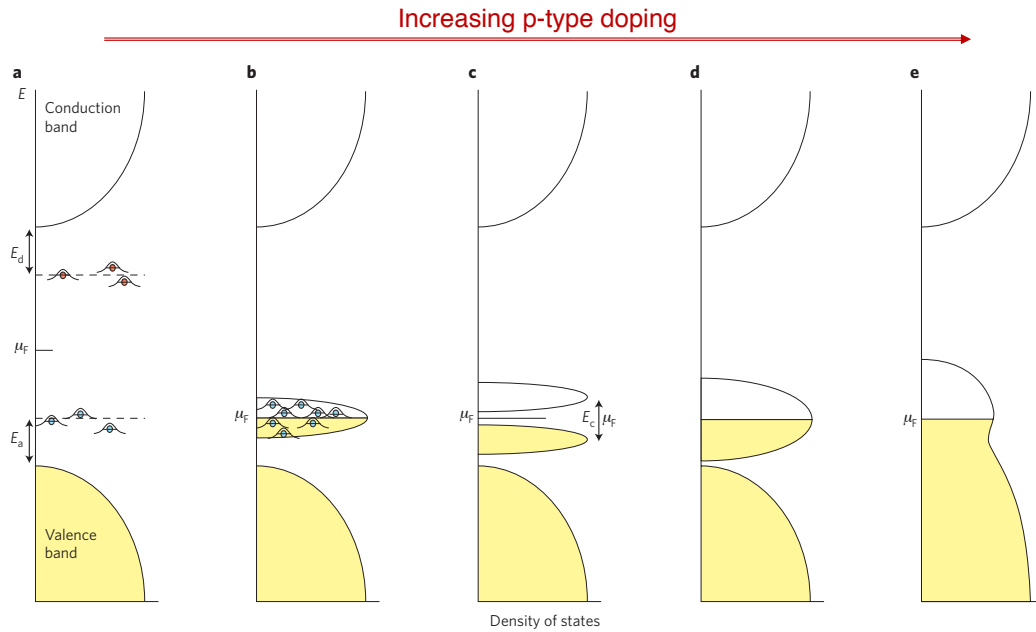


Fig. 1.2 Evolution of the electronic density of states and band structure with increasing doping in a semi-conductor. Doping increases from a to e. Coloured area represents filled states. Sketch from Blase *et al.* [11]

Low electronic concentration metallicity is also found in another class of solids : the semi-metals. The electronic band structure of these solids reveals the existence of a small band overlap (sketched in figure 1.1.c), far from what is observed in conventional metals. This band structure leads to a small Fermi surface composed of hole and electron pockets. Amongst the semi-metals we find graphite, which has a carrier concentration of  $n_e = n_h = 3 \times 10^{18} \text{cm}^{-3}$  and the non-insulating pentavalent elements such as Sb with  $n = 5 \times 10^{19} \text{cm}^{-3}$  (determined from the study of quantum oscillations). While these carrier concentrations are similar to those of doped semi-conductors, the absence of ionized impurities in semi-metals allows for a strong suppression of the rate of resistive scattering events affecting charge carriers. As a consequence, the mean-free-path of charge carriers in bulk semi-metals can be larger than in metals or doped semi-conductors, to the point where ballistic conduction can be attained at low temperatures. This regime of transport was reported in bulk Sb [12].

This observation makes bulk semi-metals great candidates to study the crossover from ballistic to diffusive transport, a region where the highly anticipated hydrodynamic regime of electrons is expected. This viscous flow of charge carriers was predicted by Gurzhi more than 50 years ago [13] and has been a subject of great attention in the last couple of years, both from a theoretical and experimental perspective [14, 15]. The hydrodynamic regime is

expected to emerge as a deviation from the conventional Boltzmannian picture of transport caused by an abundance of momentum-conserving collisions in comparison with boundary and momentum-relaxing scattering events affecting quasiparticles. Experimental signatures were discussed in potassium in 1984 [16] but the first experimental observation came ten years later, in a 2D system, with the work of M.J.M. de Jong and L.W. Molenkamp [17]. No other reports were found until very recently, when hydrodynamic electrons were spotted in graphene [18, 19] and in the 3D metal PdCoO<sub>2</sub> [20]. This observation, in a context where a possible link between hydrodynamic transport and Wiedemann-Franz law breakdown was suggested [21–24], lead us to compare the charge and heat transport properties of two bulk semi-metals : WP<sub>2</sub> and Sb.

The study of dilute metals allowed us to tackle another problematic : the existence of a universal electronic ground state of a 3D metal beyond its quantum limit. This limit corresponds to the confinement of all electrons in the lowest Landau level under the effect of a sufficiently high magnetic field. For conventional metals, such as Cu, the cyclotron energy remains much smaller than the Fermi energy unless several thousands of Teslas are applied. This makes the quantum limit experimentally unattainable. But in the case of dilute metals, only a few Tesla are sufficient to have comparable cyclotron and Fermi energy, granting physicists an easy access to the study of bulk metals beyond the quantum limit. The physics of a 3D electron gas in the quantum limit has been particularly studied in the case of graphite and lead to the discovery of a succession of field-induced phases associated with density-wave instabilities [25, 26] or in the topological insulator KHgSb [27]. To test the hypothesis of a ubiquitous ground state, we decided to study another dilute metal with an entirely different Fermi surface than graphite : Indium arsenide (InAs). This material is a III-V semi-conductor with a quantum limit standing at only  $B = 4\text{T}$  [8] which remains largely unexplored to this day.

In this thesis we will present electrical and thermal transport as well as thermoelectricity measurements to address the two aforementioned thematics. Dilute metals, whether it is because of their easily accessible quantum limit or because they offer millimetric electronic mean-free-path, constitute a perfect playground for these studies.

The next chapter will serve as a reminder of the theoretical elements at the cornerstone of heat and charge transport in metals. Then, an overview of the experimental setup and protocols applied throughout this work will be detailed in chapter 3. The core of the experimental results acquired throughout the three years of this PhD begins in chapter 4 with a study of the electrical transport and thermoelectric coefficients of the III-V semi-conductor InAs in the quantum limit. We confirm the existence of a field-induced insulating state followed, to our surprise, by a saturation of the resistivity and vanishing thermoelectric

coefficients at higher field. This observation yields fundamental differences between the ground states of graphite and InAs beyond the quantum limit. Then, chapter 5 will be dedicated to the comparison of the thermal and electrical transport properties of another dilute metal,  $WP_2$ . We confirm the observation of a quasi-unprecedentedly high heat/charge transport dichotomy, indicated by a previous report, which we explain without invoking the initially proposed hydrodynamic regime of electrons. In light of this study of  $WP_2$ , we proceeded to probe the departure from the Wiedemann-Franz law in another semi-metal with an even lower electronic density while retaining comparable purity. We will show in chapter 6 that millimetric samples of antimony fits this role perfectly. In this system, however, the phonons have a non-negligible contribution to the thermal conductivity. In a context of clear separation of the electronic and phononic terms, we reveal the emergence of  $1/B$ -periodic oscillations in the high field phonon thermal conductivity, which we associate with electron-phonon scattering and a size-dependent Lorenz ratio (which describes the heat/charge dichotomy). While we fail to unfold the origin of this last observation in a semi-classical framework, the hydrodynamic picture developed in chapter 7 gives a coherent explanation. This alternate description accounts for the deviation from the conventional transport that we observe both for electrons and phonons in Sb.



# Chapter 2

## Introduction to Heat & Charge Transport

---

### Résumé du chapitre

*Ce chapitre vise à introduire les éléments théoriques nécessaires à notre étude du transport de charge et d'entropie dans les métaux dilués. Tout d'abord, l'étude du modèle de Drude-Sommerfeld permettra d'établir la loi de Wiedemann-Franz dans le cadre d'un gaz d'électrons libres. Ensuite, nous montrerons comment les différents processus de diffusion qui dominent le transport électronique à température finie imposent une déviation à cette loi. Nous étudierons ensuite l'autre canal de conduction de la chaleur présent dans les solides : les phonons. Enfin, nous présenterons l'évolution d'un gaz d'électrons 3D dans un champ magnétique.*

---

### Summary of the chapter

In this chapter we will present the different theoretical results at the cornerstone of the following discussions on the charge and entropy transport properties of dilute metals. Through the study of the Drude-Sommerfeld model, we will establish the Wiedemann-Franz law (WFL) for a free electron gas. Then, we will present how the emergence of inelastic scattering at finite temperature drives a downward deviation from the WFL. On the contrary, an upward deviation from the WFL can also emerge at finite temperature : we will discuss

phonons as a second heat conduction channel in metals. Finally, we will focus on the evolution of a 3D electron gas in a magnetic field to define the notion of quantum limit.

## 2.1 The free electron gas

Let us first approach the electrical and thermal transport properties of electrons within the Drude model. This oversimplified classical model of the electron gas will still give a good introduction to a fundamental law which is extensively discussed in this thesis : the Wiedemann-Franz law. This result will then be specified by considering the quantum nature of the electron with Sommerfeld model.

### 2.1.1 The Drude model : a first glimpse at the Wiedemann-Franz law

**Basic premises** Only three years after J.J. Thomson's discovery of the electron (1897), Paul Drude had the great idea to picture metals as gases of free electrons. He then derived a classical theory of electrical and thermal conduction through the kinetic theory of gases. To do so, he assumed the following hypothesis :

- (1) The collisions are treated as instantaneous and uncorrelated events that abruptly alter the velocity of an electron.
- (2) *Independent electron approximation* Between collisions, a given electron does not interact with other electrons.
- (3) *Free electron approximation* Between collisions, a given electron does not interact with the ions. Combined with the independent electron approximation, this implies that electrons travel in a straight line between collisions if there is no external field applied to the system.
- (4) The probability of an electron undergoing a collision in a time interval  $dt$  is  $dt/\tau$ . The time  $\tau$ , known as the relaxation time, does not depend on the position nor momentum of the electron.
- (5) Only collisions thermalize electrons. After a collisions, an electron is at the temperature of its local environment.

**DC-conductivity of a metal** The great success of Drude model was to recover Ohm's law and to give an estimate of the resistivity at play. The conductivity  $\sigma$  is defined by  $\mathbf{j} = \sigma \mathbf{E}$

where  $\mathbf{j}$  is the current density and  $\mathbf{E}$  the electrical field. It can be further derived by the equation of the drift acceleration of an electron in the stationary regime to reach the famous Drude conductivity (eq.2.1).

$$\sigma = \frac{ne^2\tau}{m} \quad (2.1)$$

Let us look at the implications of formula 2.1 for a usual metal with a room temperature resistivity  $\rho \approx 1\mu\Omega\text{.cm}$ . If we assume an electronic mass  $m = m_0$ , the mass of the free electron, and the usual  $n \approx 10^{22}$  electrons per  $\text{cm}^3$ , we can evaluate the relaxation time at  $\tau \approx 10^{-14}\text{s}$ . It is easier to discuss this number in terms of mean-free-path between collisions :  $l = v_0\tau$  where we evaluated  $v_0 \approx 10^7 \text{ m.s}^{-1}$  from the classical equipartition of energy. We determine that  $l \approx 0.1$  to  $1 \text{ nm}$  in usual metals, close to the inter-atomic distance. While this value is a classical and only a first order approximation, comparing it with experimental reports such as the effective millimetric mean-free-path found at low temperature in Sb [12] suggests that Drude's hypothesis of electrons 'bumping' off ions is wrong.

**Thermal conductivity & first derivation of the Wiedemann-Franz law** In spite of the aforementioned issue, which is one of several, the Drude model still had a second great success : a close-to-quantitative explanation of the empirical law of Wiedemann and Franz (1853). They reported that the ratio  $\kappa/\sigma T$  at room temperature, where  $\kappa$  is the thermal conductivity, is very similar amongst all metals. To verify this hypothesis, let us compute the thermal conductivity of a metal in the Drude model. Before doing so, we need to make another bold assumption : all the heat flowing in a metal is carried by charge carriers. While this hypothesis is often verified in high-conductivity metals, we will see in a next section that the existence of a phonon contribution to thermal conductivity may complicate the study of  $\kappa$ . Finally, we mention that  $\kappa$  is a tensor.

Just like in the case of electrical conductivity, we start off from a phenomenological model : the Fourier's law  $j_Q = -\kappa\nabla T$  where  $j_Q$  is the thermal current density.  $j_Q$  is also determined simply from a kinetic model :  $j_Q = \frac{1}{3}v^2c_v(-\nabla T)$  where  $c_v = (dE/dT)/V$  where  $E$  is the thermal energy of the electron gas and  $c_v$  is named the electronic specific heat. We thus reach equation 2.2. We also indicate that equation 2.2 is true for any type of quasiparticle with associated specific heat, speed and mean-free-path.

$$\kappa = \frac{1}{3}l \times v \times c_v. \quad (2.2)$$

If we now form the ratio between thermal and electrical conductivities, we see that  $\frac{\kappa}{\sigma} = \frac{\frac{1}{3}c_v m v^2}{n e^2}$ . Thanks to energy equipartition, we find  $c_v = \frac{3}{2}k_B n$  and  $\frac{1}{2}m v^2 = \frac{3}{2}k_B T$ , where  $k_B$  is Boltzmann constant.

We finally reach  $\frac{\kappa}{\sigma T} = \frac{3}{2}\left(\frac{k_B}{e}\right)^2$ , i.e  $\kappa/\sigma T$  is a constant. Numerically, this value is close to half what was reported experimentally at the time, but an error in Drude's calculation introduced an extra factor 2 which caused an unexpected good agreement of his model with experimental reports. Yet, there's more. When Drude evaluated the electronic contribution to specific heat at room temperature, he overestimated it by a factor 100 while he also underestimated the mean square electronic speed by close to 100.

Thank to this fortuitous cancellation of mistakes, Drude reached a result only 20% off the Wiedemann-Franz law as we know it today. But in spite of his mistakes, the qualitative agreement with the experiment was an impressive success at the cornerstone of the modern electron theory.

### 2.1.2 Sommerfeld's addition : exact Wiedemann-Franz law for non-interacting electrons

**The Fermi surface** The aforementioned mismatch between the experimental specific heat reported in metals and the value predicted by Drude cast a shadow over his theory. In his model, he made the assumption that the electronic velocity distribution was that of an ordinary classical gas of density  $n$  described by the Maxwell-Boltzmann distribution. The number of electrons per unit volume with velocity  $v$  in a range  $dv$  around  $\mathbf{v}$  is given by equation 2.3.

$$f_B(\mathbf{v}) = n \left(\frac{m}{2\pi k_B T}\right)^{3/2} e^{-mv^2/2k_B T} \quad (2.3)$$

Sommerfeld managed to describe the specific heat of metals with a single modification of the Drude model : the electronic velocity distribution had to be replaced by the quantum Fermi-Dirac distribution to account for the quantum nature of the electron (equation 2.4). In this equation the constant  $T_0$  is determined by the normalization condition  $n = \int f(\mathbf{v})d\mathbf{v}$  and typically reaches several  $10^4\text{K}$ .

$$f(\mathbf{v}) = \frac{(m/\hbar)^3}{4\pi^3} \frac{1}{\exp(\frac{1}{2}mv^2 - k_B T_0)/k_B T + 1} \quad (2.4)$$

Because of the Fermi-Dirac distribution, the study of the ground state properties of the electron gas in the Sommerfeld model yields a good approximate of its room temperature properties : the characteristic temperatures at play are usually too large to cause a difference

between the  $T = 0\text{K}$  and  $T = 300\text{K}$  properties of the free electron gas. Computation of the ground state, starting from Schrödinger equation are detailed in the famous book by Ashcroft & Mermin [1].

The solution defines a vast region of  $k$ -space which is allowed for the  $N$  non-interacting electrons. The ground state correspond to the one by one filling, according to Pauli exclusion principle, of the allowed one-electron levels in  $k$ -space. The resulting ground state is a sphere and its surface separates the occupied states from the unoccupied states : this is the Fermi surface which is defined by its radius  $k_F$ . The electronic density,  $n = N/V$ , can now be defined by equation 2.5 :

$$n = \frac{k_F^3}{3\pi^2} \quad (2.5)$$

The Fermi temperature  $T_F$ , Fermi energy  $E_F$  and Fermi velocity  $v_F$  are also deduced from  $k_F$ . We now wish to compute the thermal conductivity of the free electron gas in the Sommerfeld model.

**The Wiedemann-Franz law** Passing from Drude to Sommerfeld model the electrons went from a gas of free particles to a free fermion gas. As a consequence, the specific heat can no longer be wrongfully described by the classical equipartition of energy as it was in Drude model, rather it should include the Fermi-Dirac statistic.

The calculation yields a T-linear specific heat, featured in equation 2.6 [1]. This prediction is in good agreement with experimental reports in alkali metals.

$$c_v = \frac{\pi^2}{3} \left( \frac{k_B T}{E_F} \right) n k_B \quad (2.6)$$

The mean square velocity is also modified : we switch from the classical thermal definition of the electron velocity to the Fermi velocity  $v_F$  which describes the quantum nature of the electron.

On the contrary, the Drude expression for the conductivity remains unchanged : as long as the relaxation time  $\tau$  is independent of energy and momentum and the electron trajectory remain semi-classical, i.e. a quantum object following a classical trajectory, there is no reason to observe a modification of the conductivity.  $\sigma$  is still defined by equation 2.1.

Finally, we can construct the ratio  $\kappa/\sigma$  in equation 2.7 which accounts for the quantum nature of the electron.

$$\frac{\kappa}{\sigma} = \frac{\pi^2}{3} \left( \frac{k_b}{e} \right)^2 \times T = L_0 \times T = 2.44 \times 10^{-8} \text{ W} \cdot \Omega \cdot \text{K}^{-2} \quad (2.7)$$

We recover here the Wiedemann-Franz law in the case of a free electron gas. The value of the universal Lorenz number  $L_0$ , now computed with Sommerfeld theory and consequently named Sommerfeld value, is in very good agreement with the experimental observation realised at room temperature in metals.

For further simplicity, we define the thermal resistivity in equation 2.8. The WFL is satisfied when  $\rho = (WT)$ .

$$(WT) = \frac{L_0 T}{\kappa} \quad (2.8)$$

Overall, this approximation gives a good description of the quantum behavior of conduction electrons, and allows to give a first accurate demonstration of the Wiedemann-Franz law for non-interacting electrons. More general computation of the Wiedemann-Franz law, from Boltzmann transport equation can be found in Ziman's book [28]. We do not wish to develop these calculations but emphasize the criterion of validity of the Wiedemann-Franz law : the electrons must form a degenerate Fermi-Dirac assembly and only undergo elastic scattering events.

## 2.2 Evolution of the Wiedemann-Franz law at finite temperature

So far, we have ignored the existence of scattering events amongst charge carriers and between charge carriers and phonons in the electronic transport properties. Yet, these scattering events dictate the finite temperature electronic transport properties of metals. To remedy this lack of attention, we will first present the distinction between small and large angle scattering events before discussing the different scattering mechanisms which affect charge carriers. This will lead us to the evolution of the Wiedemann-Franz law at finite temperature.

### 2.2.1 Small-angle & large-angle scattering

For any type of collisions between an excited electron and another quasiparticle, the electron can be scattered right around the Fermi sphere. This process reverses its direction. We will refer to this type of collision as horizontal (or large-angle) processes. Such scattering events degrades both the momentum and the energy of the quasiparticle, and as a consequence do not necessarily alter the validity of the Wiedemann-Franz law. Horizontal scattering is illustrated in figure 2.1.

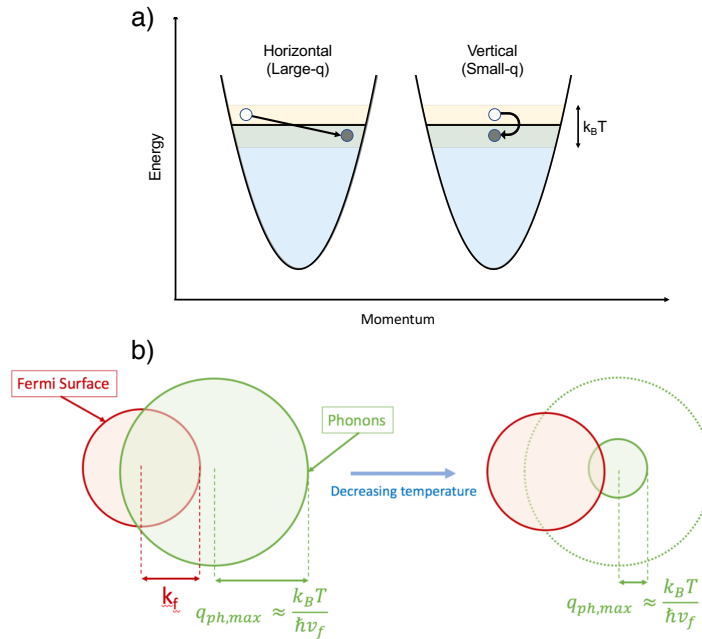


Fig. 2.1 **a)** Sketch of the evolution of the maximum phonon wave-vector with temperature. **b)** A schematic representation highlighting the difference between horizontal and vertical inelastic scattering. Both kinds of processes degrade heat transport. Their effect on momentum transport is however very different. Arrows indicate scattering from one state to another.

Yet there are also vertical transitions, in which an excited electron loses all its extra energy and falls below the Fermi level with no momentum relaxation. Such a process has little effect on electrical conductivity but affects thermal conductivity as much as horizontal scattering does. As a consequence, vertical transitions are by definition inelastic processes and they induce a deviation from the Wiedemann-Franz law. They are represented in figure 2.1.

We understand that horizontal and vertical scattering events will not contribute equally to heat and charge transport : when calculating a 'relaxation time' linked to one of these scattering events, in the case of electrical transport, the presence of a  $(1 - \cos \theta)$  pondering factor will disfavor small-angle scattering. No such term exists for thermal conductivity. This unequal importance of vertical events for electrical and thermal conductivities, pulls down the  $L(T)/L_0$  ratio at finite temperature and generates a finite-temperature breakdown of the Wiedemann-Franz law both for electron - electron scattering and electron-phonon scattering [28], which as we will see dominate at finite temperature.

### 2.2.2 Fermi liquid theory : electron - electron scattering

Let us first take into consideration the effect of electron - electron scattering on the transport properties of a metal. To do so, we turn to Landau's theory of Fermi liquids [29, 30]. It describes the properties of fermionic systems at temperatures  $T \ll T_F$ . While the most cited example is normal-state liquid  $^3\text{He}$ , which will be discussed in Chapter 6, the Fermi liquid theory can also be used to describe the low temperature electronic properties of metals. As we know from the Drude-Sommerfeld theory, the  $N$  electrons present in a metal fill the Fermi sea up to the Fermi surface and define the Fermi wavelength  $k_F$ . Yet, this model does not take into consideration how the presence of an electron affects the distribution of the other electrons in its vicinity. The Fermi liquid theory accounts for this interaction, as long as no phase transition is induced and that the screening of the Coulomb interaction is sufficient to destroy long-range interaction. In this framework, a particle is associated with an effective mass  $m^*$  and a lifetime  $\tau_{qp} \propto 1/(E - E_F)^2$  to account for the interactions with other particles. We refer to this renormalized particle as a quasiparticle.

The deeper the electron is in the Fermi sea, the shorter it lives; this feature illustrates how the Pauli exclusion principle restrict the scattering events between electrons to particles within a layer of thickness  $k_B T$  around the Fermi surface. As a consequence, at  $T = 0$ , there are no possible inelastic collisions between electrons. At finite temperature however, the relaxation rate of the quasiparticles presents a  $T^2$  dependence, which is the most characteristic property of a Landau Fermi liquid.

In light of equation 2.1, the resistivity of a Fermi liquid can thus be written as  $\rho = \rho_0 + A_2 \times T^2$  and as we have seen, all electronic collisions also contribute to the thermal resistivity ( $WT$ ) (eq.2.8), we also expect a thermal resistivity ( $WT$ ) =  $(W_0 T) + B_2 \times T^2$  to emerge.

At  $T = 0$ , electrons only undergo scattering events with impurities and boundaries of the system : these collisions are elastic by definition and thus the Wiedemann-Franz law is satisfied, i.e.  $\rho_0 = (W_0 T)$ .

Let us now turn to the effect of the aforementioned pondering  $(1 - \cos(\theta))$  factor present in the  $T^2$ -dependent electrical resistivity. After integration, it leads to a mismatch between the prefactors in the form of  $B_2 > A_2$ . As a consequence, in the presence of electron - electron scattering :  $(WT) \neq \rho$ .

As a conclusion, electron - electron scattering implies the existence of a finite temperature downward deviation from the WFL. This phenomenon has been observed in the heavy fermion systems  $\text{CeRhIn}_5$  [31] and  $\text{UPt}_3$  [32].

### 2.2.3 'Ideal' resistance of metals

In most metals, finite temperature transport is dominated by the scattering events involving charge carriers and the lattice vibrations. The calculation of the so-called 'ideal' resistance of metals, due to electron - phonon collisions, can be realized in the Bloch-Grüneisen picture [28]. The resulting electrical resistivity is presented in equation 2.9 whereas the thermal resistivity associated with electron - phonon scattering is shown in equation 2.10.

$$\rho_{e-ph} \propto T \times \int_0^{\frac{k_B T}{\hbar v_s}} (1 - \cos(\theta)) \sin(\theta) d\theta \propto T^5 \quad (2.9)$$

$$(WT)_{e-ph} \propto T \times \int_0^{\frac{k_B T}{\hbar v_s}} \sin(\theta) d\theta \propto T^3 \quad (2.10)$$

The electron-phonon collisions yield a  $T^5$  electric resistivity and a  $T^3$  thermal resistivity [28]. The higher exponent for charge transport is due to the variation of the maximal wave-vector of the thermally-excited phonons with temperature :  $q_{ph} = \frac{k_B T}{\hbar v_s}$  : small-angle phonon-scattering becomes more frequent with cooling. This is illustrated in the sketch of figure 2.1.a. Therefore, the capacity of phonons to degrade a momentum current declines faster than their ability to impede energy transport. This power-law difference leads to  $L(T)/L_0 < 1$  in the intermediate temperature window (below the Debye temperature), when phonon scattering dominates over  $e^-$ - $e^-$  impurity scattering, but all phonons are not thermally excited. This phenomenon is, for example, typically observed in elemental metals [33, 34].

According to Matthiessen's rule, the contribution due to each type of scattering event add up to form the total resistivity of the metal.

### 2.2.4 Normal & Umklapp scattering processes

In the case of electron - electron scattering, a purely electronic collision has been proposed to relax the total momentum of the electron gas and to lead to a  $T^2$  contribution to resistivity. At first glance, such phenomenon can appear as surprising : the total momentum before and after a collision involving two electrons should be conserved. In order to relax momentum, the electron - electron scattering event must be accompanied by losing part of the total momentum to the lattice. Two known ways for such a momentum transfer are often invoked [35]. The first is Baber mechanism, in which electrons exchanging momentum belong to two distinct reservoirs and have different masses. The second is an Umklapp process, where the change in the momentum of the colliding electrons is accompanied by the loss of one reciprocal lattice wave-vector

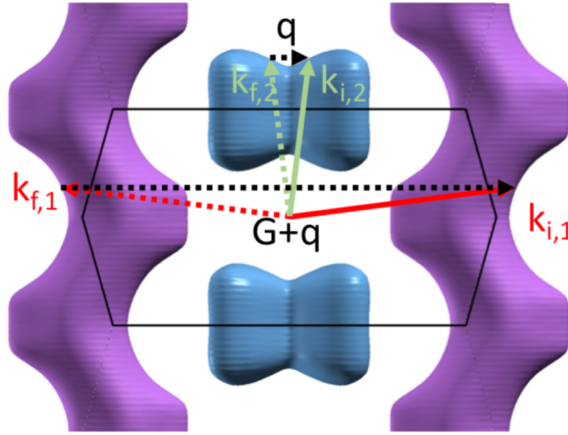


Fig. 2.2 Illustration of an Umklapp inter-electronic collisions on a top view of the Fermi surface of  $WP_2$ . The arrows illustrate wave-vectors during an inter-band Umklapp and small-angle scattering event.  $k_{i,n}$  and  $k_{f,n}$  are carrier momenta,  $k_{f,2} - k_{i,2} = \vec{q}$  and  $k_{f,1} - k_{i,1} = \vec{G} + \vec{q}$ .

A sketch of an Umklapp scattering event, in the context of electron - electron scattering illustrated on a cut of FS of the semi-metal  $WP_2$  (presented in Chapter 5), is featured in figure 2.2. We notice that the definition of the BZ plays a role in the defining a collision as umklapp [36].

Of course, Umklapp events are not limited to electronic collisions, they also describe resistive phonon - phonon scattering events. In that case, they are defined in opposition to 'normal' scattering which conserve the total momentum of phonons. We will see in the next section that if it was not for the existence of umklapp phonon-phonon scattering, the thermal conductivity of solids would diverge with temperature.

## 2.3 Bosonic thermal conductivity : Phonons

So far, we have focused on the heat carried by charge carriers in a metal. We now turn to the second heat conduction channel present in a solid : phonons. Because they are bosons, it is easy to think of phonons as if they were a gas of particle. In elementary kinetic theory, it is shown that the thermal conductivity can be written as equation 2.2 where  $c_V$  is the phononic specific heat ,  $v_S$  is the sound velocity and  $l$  the mean-free-path associated with phonons.

**Phonon specific heat** Considering each boson as a harmonic oscillator which satisfies the Bose-Einstein statistic, we can define the specific heat from the internal energy  $U$  of the system by equation 2.11 :

$$c_V = \frac{\partial}{\partial T} \left( \int_{BZ} \left( \frac{\hbar\omega(\mathbf{q})}{\exp(\frac{\hbar\omega(\mathbf{q})}{k_B T}) - 1} \right) \frac{d\mathbf{q}^3}{(2\pi)^3} \right) \quad (2.11)$$

In the case where  $T \ll \theta_D$ , where  $\theta_D$  is the Debye temperature, we can assume that optical modes are not excited : the thermal energy is too small. We are left with acoustic modes only. This is the Debye approximation where  $\omega = v_S q$ . The specific heat can thus be re-written as eq.2.12 :

$$c_V = \frac{6}{\pi^2} \int_0^\infty \frac{\partial}{\partial T} \left( \frac{\hbar v_S q^3 dq}{\exp(\frac{\hbar v_S q}{k_B T}) - 1} \right) \quad (2.12)$$

Which can be written as equation 2.13 in the  $T \ll \theta_D$  limit :

$$c_V = \frac{2\pi^2}{5} \left( \frac{k_B^4}{\hbar^3 v_S^3} T^3 \right) \quad (2.13)$$

As a conclusion the low temperature specific heat of phonon behaves as  $T^3$  in the low temperature regime. As the temperature increases and  $T > \theta_D$ , the Debye approximation fails and the Dulong-Petit law is recovered : the specific heat saturates in temperature.

**Phonon thermal conductivity** In practice, the other key parameter for the phononic thermal conductivity, the mean-free-path of the phonons becomes comparable to the sample size at low temperature (proximity to the ballistic regime). As a consequence, the thermal conductivity due to phonons behaves as  $\kappa_{phonons} \propto T^3$  in the low temperature regime (region A in figure 2.3).

As temperatures increases, if we have only phonon-phonon normal scattering, which conserves momentum, any heat current carried by phonons would not be dissipated and the thermal conductivity would become infinite. We mention that at the difference with the heat conduction of a gas, this is made possible by the absence of net conservation of 'particles' in a phonon gas.

The finite conductivity of the crystal emerges because of the existence of phonon-phonon umklapp scattering. At high temperature, when U-scattering dominates entirely the phonon flow, the thermal conductivity is found to scale as  $\kappa \propto T^{-1}$  [28]. This is the diffusive regime of transport illustrated by region D in figure 2.3. But interesting features can emerge at the crossover between the ballistic and the diffusive regime of phonons.

First, when umklapp scattering events emerge but remain rare, the thermal conductivity is expected to evolve as  $\kappa \propto \exp \theta_D / \alpha T$ . This is the Ziman regime (region C in figure 2.3).

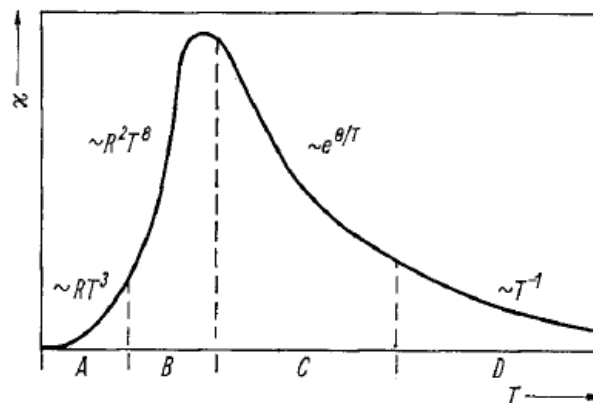


Fig. 2.3 Predicted phononic thermal conductivity as a function of temperature. Regions A,B,C and D correspond respectively to the ballistic, hydrodynamic, Ziman and diffusive regimes phonons. Figure from Beck *et al.* [37]

Second, at the border with the ballistic regime, the emergence of a hydrodynamic flow of phonons was predicted by R.N Gurzhi [13]. It is represented as region B in figure 2.3. It was later observed in a handful of solids [38–42]. This hydrodynamic correction, with a temperature dependence of the phonon thermal conductivity up to  $T^8$ , is central to this thesis and will be extensively discussed in Chapter 7.

As a conclusion, the thermal conductivity of a metal can emerge from two channels : charge carriers and phonons. While we expect the electronic component to be much larger than the phononic one in metals, the example of Sb presented in Chapter 6 will show us otherwise.

## 2.4 Heat & charge interplay : the thermoelectric tensor

So far we have considered the electrical and thermal conductivities. We will now consider the interplay between heat and charge transport. In the broad lines, thermoelectricity refers to the conversion of a temperature gradient to a voltage and vice-versa. We will focus on the thermopower and Nernst coefficient.

### 2.4.1 Thermopower

Upon the application of a temperature gradient across a homogeneous metallic system, the electrons at the colder end of the sample have less thermal energy than those at the hotter end. This induces a net particle flow of electrons from the hot side to the cold side. As a consequence, electrons accumulate at the cold end and voltage settles across the conductor.

The Seebeck coefficient  $S_{xx}$  is determined through equation 2.14 where  $\Delta_{xx}T$  is the applied temperature difference along the x-axis and  $\Delta V_{xx}$  is the voltage measured along the x-axis.

$$S_{xx} = \frac{\Delta V_{xx}}{\Delta T_{xx}} \quad (2.14)$$

More fundamentally, we can think of the thermopower as a measure of the net entropy carried per charge carrier. There are two contribution to the thermopower of metallic systems : the diffusive one ( $S_d$ ) and the phonon drag effect ( $S_p$ ).

**Diffusive thermopower** Let us first give a qualitative overview of the diffusive thermopower by considering a 3D free electron gas. The only electrons which contribute are located in a layer of  $k_B T$  near the Fermi surface. As a consequence, there are  $k_B T / E_F$  electrons at play. The entropy carried by a charge carrier can be approximated to  $k_B T / T$  per  $e$ . As a consequence we expect the diffusion thermopower of a 3D electron gas to scale as  $k_B^2 T / e E_F$ .

This result is confirmed by a more detailed computation realised by Mott *et al.* [10] by using the linearized Boltzmann transport equation for a degenerate metal in the relaxation time approximation. It leads to the following expression 2.15 ( $\sigma$  is the electrical :

$$S_d = \frac{\pi^2 k_B^2 T}{3e} \left( \frac{\partial(\sigma(E))}{\partial E} \right)_{E=E_F} \quad (2.15)$$

$$\frac{S_{xx}}{T} = \frac{\pi^2}{3} \left( \frac{k_B}{e} \right) \frac{1}{T_F} \quad (2.16)$$

The diffusive thermopower falls to zero at  $T = 0$  according to the 2<sup>nd</sup> principle of thermodynamics. With increasing temperature, it is expected to increase linearly with temperature [43]. Its amplitude is determined by the derivative of the conductivity, i.e. in the Drude picture, by the derivative of the density of state, Fermi velocity and relaxation time of the QP.

**Phonon drag thermopower** The second component of the thermopower is related to the phonon drag effect : if the electron - phonon interaction is sufficiently strong, the ballistic phonons 'drag' the carriers along the temperature gradient. This results in an increased thermopower. The magnitude of this phonon drag thermopower is directly linked to the strength of the interaction between the charge carriers and the phonons [44]. Also, the relaxation time associated with electron - phonon interaction must be shorter than the phonon

- phonon characteristic scattering time, so that the phonon drag effect takes place rather than an inter-phonon scattering event. This is why at high temperature the phonon drag effect is exceeded by phonon-phonon Umklapp scattering. At low enough temperature, the phonon drag also becomes negligible : there are not enough populated phonon modes to significantly contribute to the thermopower. As a consequence, the thermopower due to phonon drag peaks at finite temperature.

### 2.4.2 Nernst effect

The Nernst effect is a second thermoelectric effect which we will study in this thesis. It was reported for the first time in bismuth by Nernst and Ettingshausen in 1886. The Nernst, or Nernst-Ettingshausen effect corresponds to the appearance of a transverse voltage (along the y-axis) upon the application of a thermal gradient (along the x-axis) of a sample in presence of a magnetic field (along the z-axis).

It is written as (see equation 2.17) where  $\beta = L_x/L_y$  is a geometric factor,  $\Delta_{xx}T$  is still the applied temperature difference along the x-axis and  $\Delta V_{xy}$  is the voltage along the y-axis.

$$S_{xy} = \frac{\Delta V_{xy}}{|\Delta T_{xx}| \times \beta} \quad (2.17)$$

Just like in the case of the thermopower, quasiparticles contribute to the Nernst coefficient. We also mention that, in the case of a compensated system such as Sb (Chapter 6) or WP<sub>2</sub> (Chapter 5), an ambipolar Nernst effect can arise. It was, for example, observed in the metal NbSe<sub>2</sub> [45]. Another contribution to the Nernst effect, due to vortexes, is relevant in the context of superconductors but will not be discuss in this thesis.

**Quasiparticle contribution** Let us first focus on the case of a single type of carriers and a single energy band. The linearized Boltzmann transport equation applied to a degenerate metal in the relaxation time approximation provides a simple formula for the Nernst coefficient [46]. It is featured in equation 2.18.

$$S_{xy,qp} = \frac{\pi^2 k_B^2 T}{3e} \left( \frac{\partial(\sigma_{xy}(E))}{\partial E} \right)_{E=E_F} \quad (2.18)$$

In order to estimate the order of magnitude of equation 2.18, we can approximate the quasiparticle contribution to the Nernst coefficient by the expression 2.19 where  $v = S_{xy}/B$ . This approximate value indicates that high carrier mobility  $\mu$  (low effective mass, high relaxation time) and low Fermi temperature  $T_F$  lead to high Nernst coefficients. This explains why the Nernst coefficient of Bi is high : all conditions are fulfilled.

$$\frac{v}{T} = \frac{\pi^2 k_B \mu}{3 e T_F} \quad (2.19)$$

While it is obvious that the Nernst coefficient evolves with magnetic field, we have not discussed the evolution of the thermopower with applied magnetic field. We will see that the thermopower is also greatly affected. We will discuss these effects in the specific context of the different systems studied in this thesis : u-InAs (Chapter 4) and Sb (Chapter 6).

Let us now pursue with the effect of an external magnetic field on a 3D gas of electrons and in particular on its electrical resistivity.

## 2.5 Magnetoresistance

The term magnetoresistance describes the evolution of the resistivity tensor of a material when confronted to an external magnetic field. Let us discuss the origin of the general magnetoresistance in metals as well as the Shubnikov-de Haas effect.

**Magnetoresistance in the Drude model** The classical equation of motion in an external electromagnetic ( $\mathbf{E}, \mathbf{B}$ ) field is written as eq.2.20.

$$m^* \frac{d\vec{v}}{dt} = -e(\vec{E} + \vec{v} \times \vec{B}) - \frac{m^*}{\tau} \vec{v} \quad (2.20)$$

If we define  $\hat{\mu}$  as the mobility tensor of the electrons, their velocity in the stationary state is written as equation 2.21.

$$\vec{v} = \hat{\mu} \cdot (\vec{E} + \vec{v} \times \vec{B}) \quad (2.21)$$

Let us continue with the simplest Fermi surface : a spherical FS. The magnetic field is applied along the z-axis :  $\vec{B} = (0, 0, B)$ . We deduce the conductivity tensor and its inverse the resistivity tensor  $\hat{\rho}$  featured in equation 2.22 from the relation  $\vec{j} = -ne\vec{v} = \hat{\sigma}\vec{E}$  [47].

$$\hat{\sigma}(B) = \frac{ne}{1 + \mu_x \mu_y B^2} \begin{pmatrix} \mu_x & -\mu_x \mu_y B \\ \mu_x \mu_y B & \mu_y \end{pmatrix} \quad (2.22)$$

$$\hat{\rho}(B) = \frac{1}{ne \mu_x \mu_y} \begin{pmatrix} \mu_y & \mu_x \mu_y B \\ -\mu_x \mu_y B & \mu_x \end{pmatrix}$$

Since the velocity along the magnetic field is not affected by the Lorenz force, there is no longitudinal magnetoresistance. More surprisingly, the transverse magnetoresistance  $\rho_{xx}$

and  $\rho_{yy}$  for a single spherical FS with mobility anisotropy is also null (see equation 2.22). This result contradicts our intuitive understanding of magnetoresistance. Yet, a finite Hall resistivity  $\rho_{xy} = -\rho_{yx} = -B/ne$  emerges. In this model, the Hall resistivity is proportional to the carrier density.

**Magnetoresistance in semi-metals** We now turn to semi-metals where electrons and holes coexist. We define the mobility tensor for holes as  $\hat{v}$  and the hole density  $p$ . The total conductivity is now written as  $\hat{\sigma}(B) = \hat{\sigma}_e(B) + \hat{\sigma}_h(B)$ . This leads to equation 2.23 where  $\sigma_{i,j}$  are given by equation 2.24.

$$\begin{pmatrix} \sigma_{e1} + \sigma_{h1} & -\sigma_{e2} + \sigma_{h2} \\ \sigma_{e2} - \sigma_{h2} & \sigma_{e1} + \sigma_{h1} \end{pmatrix} \quad (2.23)$$

$$\begin{aligned} \sigma_{e1} &= \frac{ne\mu_x}{1 + \mu_x\mu_y B^2} & \sigma_{e2} &= \frac{ne\mu_x\mu_y B}{1 + \mu_x\mu_y B^2} \\ \sigma_{h1} &= \frac{pev_x}{1 + v_xv_y B^2} & \sigma_{h2} &= \frac{pev_xv_y B}{1 + v_xv_y B^2} \end{aligned} \quad (2.24)$$

We finally reach the expression 2.25 for the transverse magnetoresistance of a semi-metal. In the high field limit,  $\mu_x\mu_y B^2 \gg 1$  and  $v_xv_y B^2 \gg 1$ , this expression becomes equation 2.26. In the uncompensated case,  $n \neq p$ , the magnetoresistance saturates at high field. On the contrary, in the compensated case  $n = p$ , the magnetoresistance never saturates and exhibits a  $B^2$  dependence at high field. With simultaneous holes and electrons, the Hall resistivity at high field is now given by equation 2.27 [1]. An illustration of the magnetoresistance of three semi-metals, Bi, Sb and WTe<sub>2</sub>, is shown in figure 6.2.a. Finally, we mention that multi-valley systems (only one type of carrier, but with more than one valley) also exhibit magnetoresistance effects [47].

$$\rho_{xx} = \frac{\sigma_{e1} + \sigma_{h1}}{(\sigma_{e1} + \sigma_{h1})^2 + (\sigma_{e2} - \sigma_{h2})^2} \quad (2.25)$$

$$\rho_{xx}^{hf} \simeq \frac{1}{e} \frac{(\frac{n}{\mu_y} + \frac{p}{v_y})B^2}{(\frac{n}{\mu_y} + \frac{p}{v_y})^2 + (n-p)^2 B^2} \quad (2.26)$$

$$\rho_{yx}^{hf} \simeq \frac{-B}{e} \frac{(n-p)^2 B^2}{(\frac{n}{\mu_y} + \frac{p}{v_y})^2 + (n-p)^2 B^2} \quad (2.27)$$

Let us now discuss another a magnetoresistance effect which can be used to probe the Fermi surface of a metal : the Shubnikov de Haas effect.

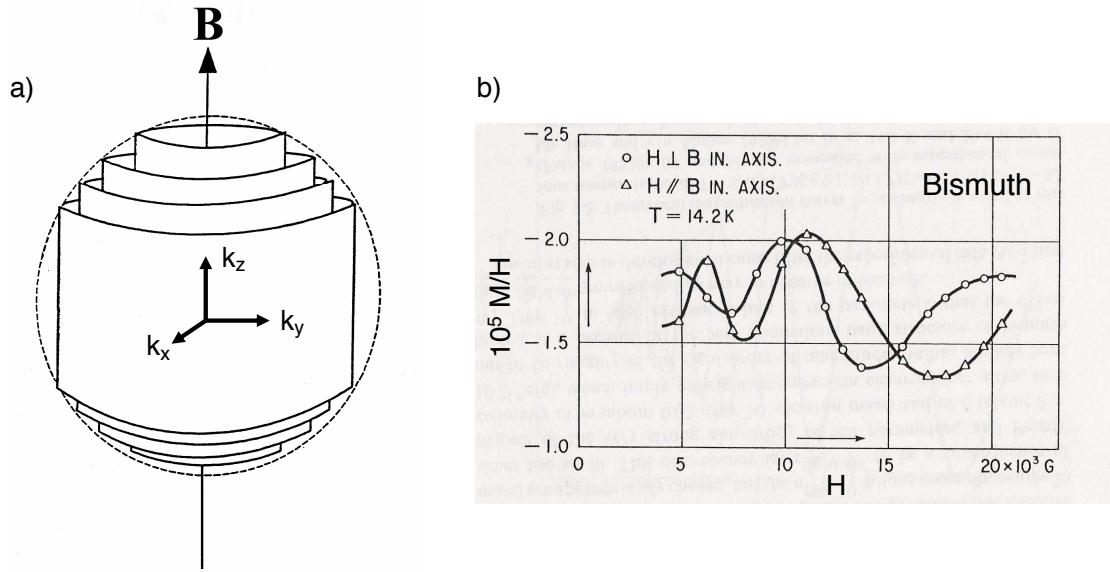


Fig. 2.4 a) Quantized energy levels of a 3D electron gas in a magnetic field. The electrons are confined in Landau cylinders for  $B \neq 0$ . Only states within the Fermi sphere,  $|\mathbf{k}| < k_F$  are occupied. b) First observation of QO in magnetization measurement (dHvA effect) of Bismuth at  $T = 14.2$  K.

**Quantum oscillations** In 1930, Shubnikov and de Haas observed the existence of oscillations in the magnetoresistance of Bi at low temperature. This first observation, at  $T = 14.2$  K, is reported in figure 2.4.b. Soon after this discovery, de Haas and van Alphen also reported the observation of similar oscillations in the magnetization of bismuth. Over the years, similar observations have been made in other metals.

It was Landau who gave the first explanation of these quantum oscillations. When an external magnetic field is applied to a 3D electron gas along the  $z$ -axis, the energy dispersion is quantified in the perpendicular plane, i.e. the  $(x,y)$  plane. Each level, named Landau level, corresponds to a quantum number  $n$  and is degenerate so that the kinetic energy along the magnetic field remains unchanged. The energy of the  $n^{\text{th}}$  spin-split Landau level is given by equation 2.28 where  $g$  is the Landé factor and  $\mu_B$  the Bohr magneton. A sketch of the resulting LL is presented in figure 2.4.a. The levels are separated by a constant energy which depends linearly on the magnetic field  $\hbar\omega_c = \frac{\hbar e}{m^*} B$ . As the field increases, the Landau levels are more and more distant and less and less LL satisfy  $E < E_F$ , i.e. less and less Landau levels are populated.

$$E_n = \left(n + \frac{1}{2}\right)\hbar\omega_c + \frac{1}{2} \frac{\hbar^2 k_z^2}{m^*} \pm \frac{1}{2} g \mu_B B^2 \quad (2.28)$$

When the field becomes large enough so that the thermal energy is smaller than the LL spacing,  $\hbar\omega_c > k_B T$ , and that  $\omega_c \tau \gg 1$ , the density of state at the Fermi level varies brutally when a LL crosses the Fermi level : oscillations emerge in the thermodynamic and transport properties with a frequency  $1/B$ .

Consequently, the QO yield a direct access to the electronic structure of metals. The period of the oscillations is linked to the cross-sectional area of the Fermi surface perpendicular to the applied magnetic field. It is given by the Onsager relation (equation 2.29) where  $\mathcal{A}_{\mathcal{F}}$  is the aforementioned cross-section. To this day, the study of QO remains largely used to probe the FS of metals.

$$\Delta\left(\frac{1}{B}\right) = \frac{e\hbar}{E_F m^*} = \frac{2\pi e}{\hbar \mathcal{A}_{\mathcal{F}}} \quad (2.29)$$

The amplitude of the magnetization oscillations was explained by the original theory of Lifshitz and Kosevich [48]. This result was computed in the case of 3D metals with an arbitrary dispersion  $E(k)$  when the LL spacing is smaller than the characteristic dispersion along the direction of the field. This formula, written in equation 2.30, describes the smearing out of the Fermi Dirac distribution at finite temperature. In uncorrelated metals, the LK theory is also often used to describe the amplitude of the SdH oscillations. Only the temperature dependence is detailed in equation 2.31 as we will discuss it later in this thesis where  $u(B) = \frac{2\pi^2 k_B m^*}{e\hbar B}$ . All other details of the LK theory can be found in Shoenberg's book [49].

$$A(B) = R_T(B, T) \times R_D(B) \times R_{MB}(B) \sin\left(2\pi \frac{f_0}{B} + \Phi\right) \quad (2.30)$$

$$R_T(B, T) = \frac{u(B)T}{\sinh[u(B)T]} \quad (2.31)$$

# Chapter 3

## Experimental aspects

---

### Résumé du chapitre

*Ce chapitre décrit les différents instruments de mesure et la fabrication des porte-échantillons utilisés pour mesurer les propriétés de transport électrique et thermique et de thermoélectricité présentées dans cette thèse. En particulier, nous présentons l'insert construit au sein notre groupe afin de pouvoir mesurer  $\kappa$ ,  $\rho$  et  $S$  dans une configuration 4-point dans un PPMS. A travers la vérification expérimentale de la loi de Wiedemann-Franz dans un échantillon d'argent à  $B = 0T$  et  $B = 10T$ , nous assurons le bon fonctionnement de cet insert sous champ.*

---

### Summary of the chapter

This chapter describes the material and the experimental protocols which have been used to measure the electrical and thermal conductivities as well as the thermoelectric coefficients reported in this thesis. In particular, we present the home-built insert designed to measure  $\kappa$ ,  $\rho$  and  $S$  in a 4-terminal configuration in a PPMS. The proper functioning of this stick is ensured by the experimental recovery of the WFL in silver at  $B = 0T$  and  $B = 10T$ .

## 3.1 Cryogenics & Magnets

We start with a presentation of the cryogenic systems and their associated magnets available in our group and in high-field facilities where some experimental part of this work has been carried out.

### 3.1.1 Physical Property Measurement System : PPMS

The Physical Property Measurement System (PPMS), constructed by Quantum Design, is our go-to system for measuring transport properties between  $T = 1.9\text{K}$  and  $T = 400\text{K}$  while applying a magnetic field up to  $B = 13.8\text{T}$ . The cryostat is cooled by a circulation of  $^4\text{He}$  gas while the magnetic field is generated by a superconducting  $\text{Nb}_3\text{Sn}$ -based magnet. A residual field up to  $B = 120\text{Oe}$  can be found in the magnet.

The PPMS is equipped with 12 wires, each able to carry up to  $I = 2\text{A}$ , which directly connects the bottom connector inside the sample chamber to an output. The bottom connector can only be connected to a compatible sample holder, named a 'puck'. This puck is at the foundation of all of the PPMS measurement inserts. We also underline the presence of a low-frequency lock-in amplifier for 4-point resistivity measurements. This built-in option is however limited to a maximal current  $I = 5\text{mA}$  injected in the sample. If a higher current is required, we rather use a Keithley 2100 as the current source.

Besides these basic features of the PPMS, one can add accessories and options. In our case, the PPMS was equipped with the horizontal rotator accessory. This system, composed of a rotation stick and a motor, plugs in the PPMS and allows resistivity measurements with variation of the relative angle between the magnetic field and the sample holder. The rotation is restricted to a plane. More options can also be bought to tune one's PPMS to advanced experimental capacities.

But one may also develop his plug-in accessories for specific measurements. The main criteria is, as mentioned before, the compatibility with the 12 pins at the bottom of the sample chamber. With that in mind, we built a thermal transport and thermoelectricity measurement stick where the 12 pins are connected to 2 thermometers and one heater ( $3 \times 4$  contacts) in order to locally probe/heat the temperature of a sample, fixed on a cold finger. An additional line of 12 copper wires emerges from the top of the stick. These additional copper wires allow resistivity and thermoelectricity measurements of the sample.

One of the main concern when building this stick was to ensure that the temperature of the sample chamber was not affected by the presence of the stick. To do so, the stick was equipped with screens to damp thermal leak. The thermometry of the stick as well as a test experiment on a silver sample is featured bellow.

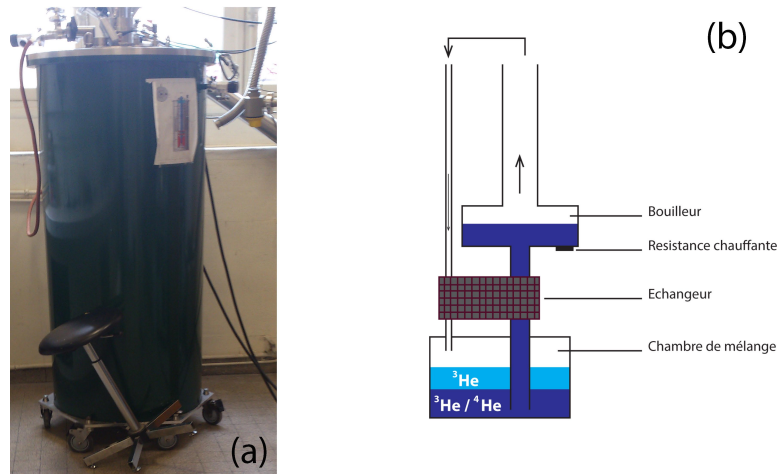


Fig. 3.1 **a)** The cryostat is equipped with a superconducting magnet (reaching up to  $B = 17\text{T}$ ) at ESPCI Paris. One may notice the metallic stool left by an unnamed student during a field sweep up to  $B = 17\text{T}$ . **b)** Schematic representation of a dilution fridge. The cooling power emerges from the dilution of the light phase ( ${}^3\text{He}$ ) to the mixed, and heavier, phase (deep blue). The sample holder is in thermal contact with the mixing chamber. Figure from C. Collignon [50].

### 3.1.2 Dilution Fridge

While the PPMS covers vast ranges of temperature and magnetic fields, the study of certain phenomenon requires sub-Kelvin temperatures and even higher magnetic fields than  $B = 13.8\text{T}$ . In that case, we turn to a dilution fridge equipped with a  $17\text{T}$ -magnet (figure 3.1.a). One should also keep in mind that a residual field, from the superconducting magnet, can be applied to the sample.

The working principle of a dilution fridge is described in figure 3.1.b. Its cooling process is based on the phase equilibrium of a  ${}^3\text{He}/{}^4\text{He}$  mixture and is already extensively described in the literature. The base temperature of this fridge is  $T \approx 30\text{mK}$ .

The insert which was mostly used during this thesis has 26 phosphor bronze wires which directly connect the bottom pins, to which the wires of the sample holder are soldered, to the output connector at the top of the stick. Naked sample holders (SH) are bulk pieces of copper with a bottom M8-screw, which are crafted to fit on the stick and equipped in function of the experiment and the ranges of temperature/magnetic fields we wish to focus on. Further details on thermometry, crucial for thermal transport and thermoelectricity experiments, are detail in the next sections.

### 3.1.3 High-field facilities

Our study of dilute metals beyond the quantum limit, presented in chapter 4, lead us to measure the resistivity and thermoelectric properties of some samples up to very high fields.

**Static fields** We were able to conduce electrical transport experiments in static field up to  $B = 33\text{T}$  down to  $T = 0.4\text{K}$  in the HFML in Nijmegen, Netherland and electrical, thermal and thermo-electrical transport up to  $B = 35\text{T}$ , also static, down to  $T = 0.3\text{K}$  at the LNCMI Grenoble, France. The low temperatures were attained with  $^3\text{He}$  refrigerators.

The high static fields, amongst the highest in the world, are generated by resistive magnets. The constituting solenoids are made out of resistive metal (copper), as opposed to superconducting magnets, which permit a very high current flow in the magnet and thus generates high magnetic field as well as large Joule heating. In order to dissipate the heat, the magnet is cooled down by a high-debit water cooling system (thankfully, a river flows next to both facilities). Another limitation of the coil is its mechanical resistance to the large stress caused by the Lorentz force at high-field.

**Pulsed fields** To probe the quantum limit even deeper, we measured graphite and InAs samples in pulsed field up to  $B = 56\text{T}$  for InAs and  $B = 88\text{T}$  for graphite down to  $T = 1.5\text{K}$ . The cooling is ensured by a  $^4\text{He}$  system while the field is generated by the synchronized discharge of a bank of capacitor in a triple nested coil [51]. Synchronisation, determination of the field, heat dissipation and Lorenz force are only part of the issues emerging when working with pulsed fields of this amplitude.

Finally, let us look at the energy scales of these experiments. The energy required to generate a pulsed magnetic field of  $B = 90\text{T}$  is  $P \approx 12\text{MJ}$ , sensibly the same energy to maintain a static field of  $B = 30\text{T}$  during 1 sec. We can look at these numbers from a very french energetic perspective with the following elements of comparison : one person travelling from Paris to Marseille in a high-speed train consumes around  $200\text{kJ}$  (1/60 of a  $B = 90\text{T}$  pulsed field) whereas a cyclist over the entire Tour de France burns around  $100\text{MJ}$  ( $\approx 8$  seconds in a static field of  $B = 30\text{T}$ ).

## 3.2 4-point measurement setup

Let us first remind the fundamental difference between a 4-point measurement in comparison to a 2-point one. In the case of a 4-point setup, the current is injected via 2 electrodes while the tension is measured through 2 other electrodes. A 2-point setup, on the contrary, uses the same two electrodes to inject the current and to probe the voltage difference.

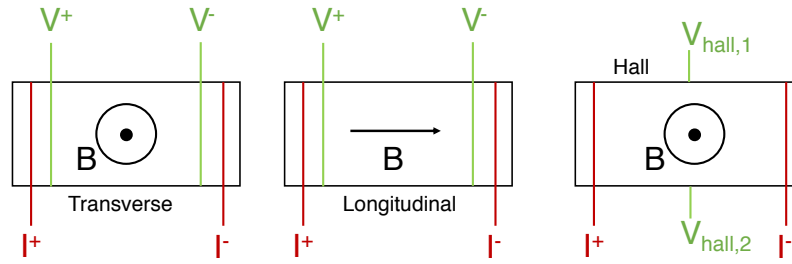


Fig. 3.2 **a)** Transverse magnetoresistivity measurement geometry **b)** Longitudinal magnetoresistivity measurement geometry **c)** Hall resistivity measurement geometry

When a resistance is measured in a 2-point configuration, the measured resistance is the sum of the resistances of the sample and the contact resistance. While this may not be a problem for large resistances, it might induce a large discrepancy when measuring small resistances (high conductivities).

A 4-point configuration, on the other hand, excludes the contact resistances. Even in the case of poor contact quality, leaving aside heating and other problems associated with high contact resistances, the measured resistance is reliable. The calculation for the 2 scenarios is straightforward and can be found easily in the literature.

### 3.3 Electrical resistivity measurement

Let us now turn to the protocol and common considerations for electrical transport. We first introduce the features of the typical sample holder used for these experiments and discuss experimental considerations one should bear in mind when measuring  $\rho$ . The various geometries of transport in presence of a magnetic field will be presented first.

#### 3.3.1 In-field geometries

Throughout this thesis we will discuss magnetoresistivity measurements in different geometries. These geometries are introduced here. The transverse and longitudinal geometries are determined by the relative orientation of the injected current and the magnetic field while the Hall geometry is specific to probe the Hall effect. A supporting sketch is shown in figure 3.2.

The transverse geometry (Fig 3.2.a) correspond to an applied electrical current  $j_Q$  orthogonal to the applied magnetic field  $B$ . The voltage is probed in the direction of  $j_Q$ .

The longitudinal (Fig 3.2.b) geometry corresponds to colinear applied electrical current  $j_Q$ , magnetic field  $B$  and voltage probes.

Finally, in order to measure the Hall resistivity  $B$  and  $j_Q$  are set orthogonal to maximize the signal and the voltage is probed perpendicularly to the direction of  $j_Q$  (Fig 3.2.c).

### 3.3.2 Sample holder

To build a sample holder (SH) for an electrical transport measurement for the dilution fridge is a straightforward task : starting with the bare sample holder, which has to ensure good thermal connection with the mixing chamber in a dilution fridge, we had electrical pins on the top surface, a  $\text{RuO}_2$  resistor to serve as a SH heater and a pre-calibrated thermometer glued to the SH with high thermal conductivity varnish or paste (Lakeshore GE Varnish or Dupont silver paste as examples). The sample is then glued on the SH with GE Varnish and Ag or Pt wires ( $25\mu\text{m}$  diameter) are fixed on its surface with silver paste. For all samples contacted with silver paste presented in the study the contact resistance remained sub-ohmic down to mK temperatures. The contact wires fixed on the sample are finally connected to the pins and copper wires are soldered to connect the pins of the SH to the insert.

### 3.3.3 Experimental banana skin : electrical transport

Here are presented some common considerations one should keep in mind when measuring the electrical resistivity of a material down to very low temperatures. The first regards the temperature : one should always ensure that good thermal contact between the sample holder and the sample is achieved. The second, closely linked to the first, is to always check for self-heating due to a large current entering the sample and heating it by Joule effect. A simple check is to verify reproducibility of the result with different currents. This has to be emphasized when measuring systems with a very large magnetoresistance.

Speaking of large magnetoresistance, the presence of a residual field applied to the sample by a superconducting magnet, as small as  $B = 100\text{Oe}$ , can radically transform the outcome of an experiment. As an example, we will present in the following thesis the resistivity of a large slab of Sb, which, at  $T = 2\text{K}$  is off by a factor of 4 in presence of a field of  $B = 100\text{Oe}$ .

Finally, when measuring the magnetoresistance one should check for misalignment. In the longitudinal configuration this can be done by rotating the sample in order to minimize the Hall effect. For the transverse geometry however, this is linked to experimental material and setup.

While this section can seem a little sanctimonious, it is not the intent. It should rather serve as a reminder for future student working on electrical transport of high MR compounds.

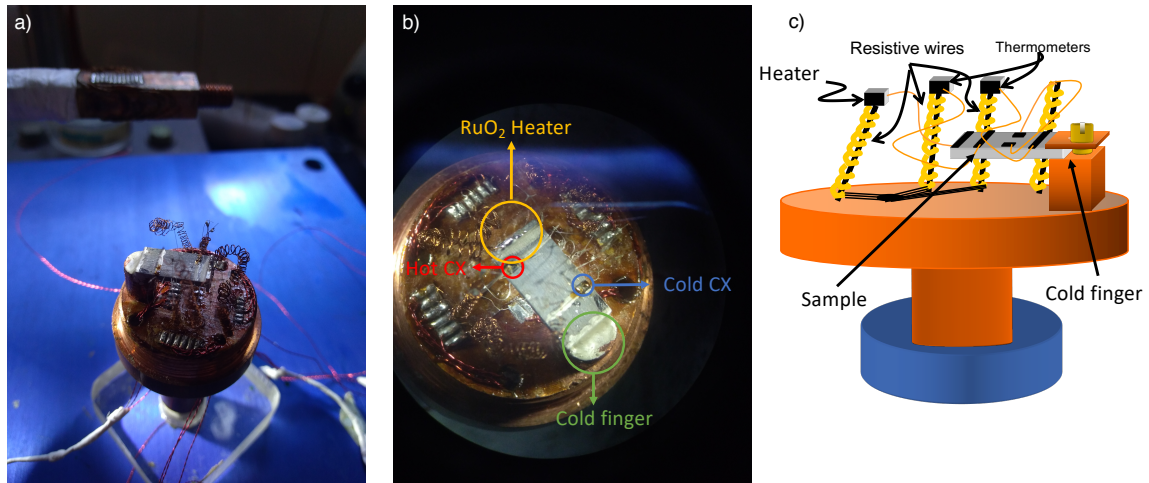


Fig. 3.3 **a)** Photography of the sample holder used to measure, amongst other, the thermal conductivity, thermopower and Nernst coefficient in the  $(1 \times 5 \times 10) \text{ mm}^3$  Sb sample fixed on the cold finger. **b)** Zoom on the sample. The cold finger, hot and cold thermometer and sample heater are indicated by arrows. **c)** Schematic representation of the sample holder [43].

## 3.4 Thermal conductivity and thermo-electrical measurements

Let us now turn to the experimental setup and protocol behind our reports on thermal conductivity and thermoelectric coefficient.

### 3.4.1 Setups

A thermal conductivity and thermoelectricity setup is only slightly more complex to imagine than an electrical transport one. However, it is much more cumbersome to fabricate. As an example, a photo of a thermal transport sample holder with a large Sb sample installed is featured in figure 3.3.a and explained by the sketch in figure 3.3.c.

The thermometers used to probe locally the temperature of the samples are either Cernox chips CX-1010/CX-1030/CX-1050 (chosen upon the temperature range of interest) or RuO<sub>2</sub>-base thermometers (which display a small magnetoresistance). The temperature of the thermometer is determined by the evaluation of the 4-point resistivity of the thermometer. To do so, 2 pairs of twisted manganin wires (to increase length) are soldered to the thermometers on one side and soldered to contact pads, glued at the bottom of the SH on the other side. The use of twisted manganin wires ensures electrical conduction without thermal loss. To probe the temperature of the sample, the thermometers are then connected either directly

on the sample (with silver paste or GE varnish) or, if the size of the sample forbids a direct connection, via Ag or Pt wires of small diameter. A heater, most usually a RuO<sub>2</sub>-based resistor, is then connected to one extremity of the sample and its resistance is measured in 4-terminal configuration. The other extremity of the sample is connected to the cold finger, i.e. the sample holder, with a high thermal conductivity paste (GE varnish or silver paste again). Finally, a shield set to protect the thermometry from radiation and the sample chamber is thoroughly carefully pumped at  $T = 300\text{K}$  to avoid thermal leaks.

The measurement is realised by sending a current in the sample-heater while probing its voltage difference in order to determine the heating power and after the sample-thermometers reach a steady regime, by measuring the temperature at two difference points of the sample to construct the temperature difference. The ratio of these two quantities divided by the geometric factor yields the thermal conductivity of the sample.

However, one needs to ensure that no thermal leak or contamination happens in the system and poisons the measurements. This is the subject of the next section.

### 3.4.2 Excluding thermal leaks

We wish to prove that the manganin wires are resistive enough to isolate thermally the thermometers and the heater from the sample holder, and as a consequence, yield a reliable measure of the local temperature of the sample

In the following chapters we will report on thermal conductivities up to  $T = 30\text{K}$ . At these temperatures, the thermal conductivity of manganin is  $\kappa = 4.97\text{W.K}^{-1}.\text{m}^{-1}$  [52]. The manganin wires have a diameter of  $50\mu\text{m}$  and typical length of  $l = 20\text{cm}$ . The geometric factor is  $\alpha = 3.93 \times 10^{-7}\text{m}$ . The thermal conductance of the wires is thus  $\kappa_{\text{Manganin}} = 2.0 \times 10^{-6} \text{W.K}^{-1}$ .

This value is more than 3 orders of magnitude below the thermal conductance of the Ag or Pt wires connecting the thermometers and heater to the sample (in the situation where they are directly glued to the sample) [52]. It is also negligible in comparison to the thermal conductance of the samples presented below.

As a consequence, the heat loss through the manganin wires is negligible : all the heat from the sample-heater is transferred to the sample while the sample-thermometers probe the local temperature of the sample without contamination from the SH.

We mention another potential source of contamination : radiations. While they are expected at high temperature, they can alter high precision measurements on high thermal conductivity materials as early as  $T = 30\text{K}$ . A shield is present to damp this phenomenon but the most efficient way to avoid it is to glue the thermometers directly on the sample.

Finally, one last source of experimental error is improper pumping of the sample chamber at  $T = 300\text{K}$  leading to traces of gas, especially He.

These potential source of experimental failure are to be kept in mind during thermal conductivity and thermoelectricity measurements.

### 3.4.3 Recovering the Wiedemann-Franz law in Silver

In order to confirm our experimental protocol both at  $B = 0\text{T}$  and under an applied magnetic field, we measured the thermal conductivity and electrical resistivity of a silver sample. We measured a simple polycrystalline Ag wire with a  $25\mu\text{m}$  diameter and  $10\text{mm}$  length from Goodfellow with a purity of  $99.997\%$ .

For metallic samples of such small limiting dimensions, the phonon contribution to thermal conductivity is expected to be negligible in comparison with the large electronic component. Considering that Ag is a common metal with a small magnetoresistance, in which the Wiedemann-Franz law has been verified below helium temperatures, we expect to recover the WFL both at zero field and in presence of a magnetic field at low temperature.

The resistivity, plotted as  $L_0/\rho$  with  $L_0$  the aforementioned Sommerfeld value is shown as a function of temperature both at  $B < 10\text{Oe}$  and  $B = 10\text{T}$  in figure 3.4.a alongside the thermal conductivity, represented as  $\kappa/T$  also for both fields. Both quantities increase with decreasing values and saturate at the same value, within less than  $5\%$  error. This result is confirmed both at  $B < 10\text{Oe}$  and  $B = 10\text{T}$ .

Following the definition of  $L(T)$  given in the first chapter, We plotted the Lorenz ratio,  $L(T)/L_0$  as a function of temperatures for both fields in figure 3.4.b. We do observe that the WFL is experimentally recovered around  $T = 5\text{K}$  whether or not an external magnetic field is applied and that upon increasing the temperature, the Lorenz ratio diverges from the Sommerfeld value. This divergence, as discussed in Chapter 1, is associated with the emergence of electron - phonon scattering at finite temperature.

As a conclusion, we have proven that our 4-point experimental setup and protocol is well fitted to probe the electrical and thermal conductivities of metals down to  $T = 2\text{K}$ , even in presence of an applied field as high as  $B = 10\text{T}$ .

**Conclusion** Most sample holder must be tailored to match the range of temperature/field required for an experiment, leading to cumbersome fabrication steps. We also reminded the reader of the most common experimental imprecisions to avoid in these measurements.

Now that we have reminded the theoretical minimum and the experimental elements needed to discuss the work detailed below, we will get into the core of this thesis. The first subject we will tackle is the study of undoped InAs and graphite in the deep quantum limit.

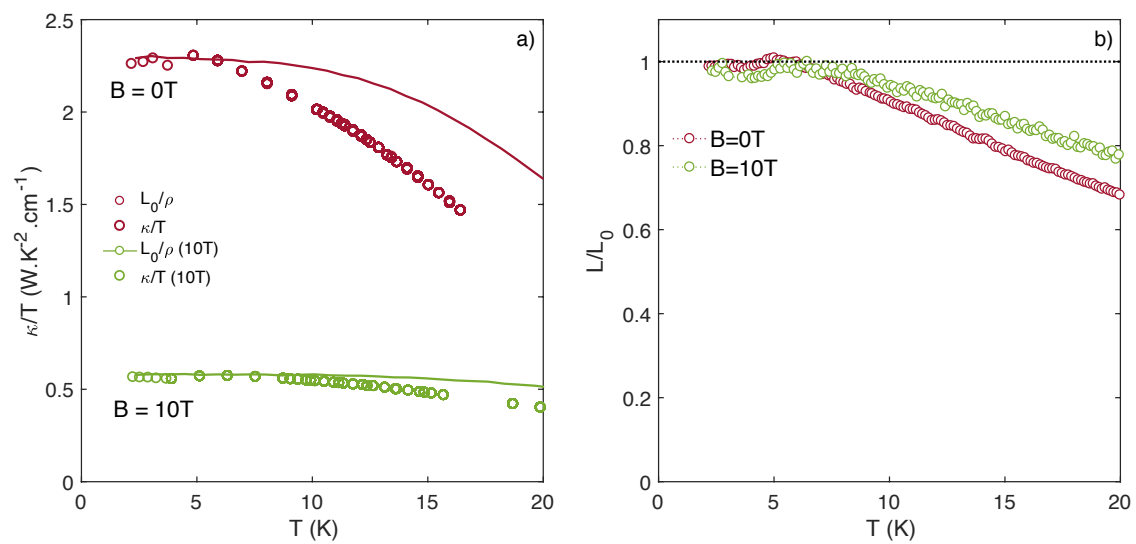


Fig. 3.4 **a)**  $\kappa/T$  and  $L_0/\rho$  plotted for the Ag sample at  $B = 0\text{T}$  (red) and  $B = 10\text{T}$  (green). The WFL is recovered when the two graphs, at equal field, meet. **b)** Lorenz number of the Ag sample as a function of temperature plotted for  $B = 0\text{T}$  and  $B = 10\text{T}$ .

# Chapter 4

## Fate of the Fermi sea in the quantum limit : InAs Vs Graphite

---

### Résumé du chapitre

*Le spectre électronique d'un gaz tridimensionnel d'électrons évolue vers un ensemble de niveaux quantifiés sous l'effet d'un champ magnétique externe. À mesure que ce champ augmente, le nombre de niveaux d'énergie peuplés diminue jusqu'au point où seul le dernier niveau de Landau est occupé : le système a alors atteint sa limite quantique. Le spectre électronique devient alors analogue à un système 1D pour lequel de nombreuses instabilités électroniques sont attendues telles que des ondes de densité de charge (CDW) ou des ondes de densité de spin (SDW) [53]. L'étude des propriétés électriques et thermoélectriques de graphite jusqu'à  $B = 90.5T$ , bien au-delà de la limite quantique, révèle l'existence d'une succession de trois phases induites par le champ magnétique qui ont été associées à la formation d'ondes de densité. Afin de tester l'universalité de cette phase, nous présentons une étude du transport électrique et de la thermo-électricité dans un autre métal dilué : InAs. Nous rapportons l'existence d'un état isolant induit par le champ magnétique associé à l'ouverture d'un gap énergétique dans les conductivités électriques transverse, longitudinale et Hall, sans signe de fermeture jusqu'à  $B = 56T$ . Ce résultat contraste avec l'observation d'une résistivité hors-plan isolante qui coexiste avec des plans de graphène métalliques dans graphite. À la lumière de cette comparaison nous concluons que l'état fondamental d'un métal 3D au-delà de la limite quantique n'est pas universel mais propre à chaque système. Enfin, nos mesures révèlent une saturation vers un régime linéaire en champ et indépendant de la température dans la résistivité haut-champ de InAs accompagné d'un thermoélectricité*

*inattendue. Nous associons cette observation à l'existence d'un état de surface conducteur dans InAs.*

---

## Summary of the chapter

The electronic spectrum of a 3D electron gas evolves to a set of quantized levels under the effect of an external magnetic field. As the field increases, fewer energy levels are populated up to the point where only the lowest Landau level (LL) is occupied : the system has reached the quantum limit (QL). The electronic spectrum becomes analogous to a 1D system which is highly sensitive to electronic instabilities such as charge density waves (CDW) or spin density waves (SDW) [53]. In graphite, the study of low temperature electrical and thermo-electrical properties up to  $B = 90.5\text{T}$ , far beyond the quantum limit, revealed the existence of a succession of three field-induced phases associated with density wave (DW) transitions. This observation raises the question of the existence of a ubiquitous ground state of 3D metals beyond the QL. To answer this question, we report on the electrical and thermo-electrical transport properties of another dilute metal beyond its QL : InAs. We observe in this compounds a field-induced insulating state with gapped transverse, longitudinal and Hall conductivities. This result contrasts with the observation of coexistent insulating out-of-plane resistivity and in-plane metallicity in graphite. In light of this comparison, we conclude that, despite some similarities, there is no universal ground state for a 3D metal but rather an individual ground state associated with each system. Finally, our measurements in InAs show a saturation into a B-linear temperature-independent resistivity accompanied by vanishing thermoelectric coefficients at high field. The existence of a conductive surface states is coherent with this observation.

---

## 4.1 Introduction & motivation

The observation of a succession of thermodynamic electronic phase transitions in graphite ignited our interest for the study of another dilute metal in the deep quantum limit : u-InAs. To set the stage for this study we will first introduce the fermiology of both compounds and review the reports on the field-induced states observed in graphite.

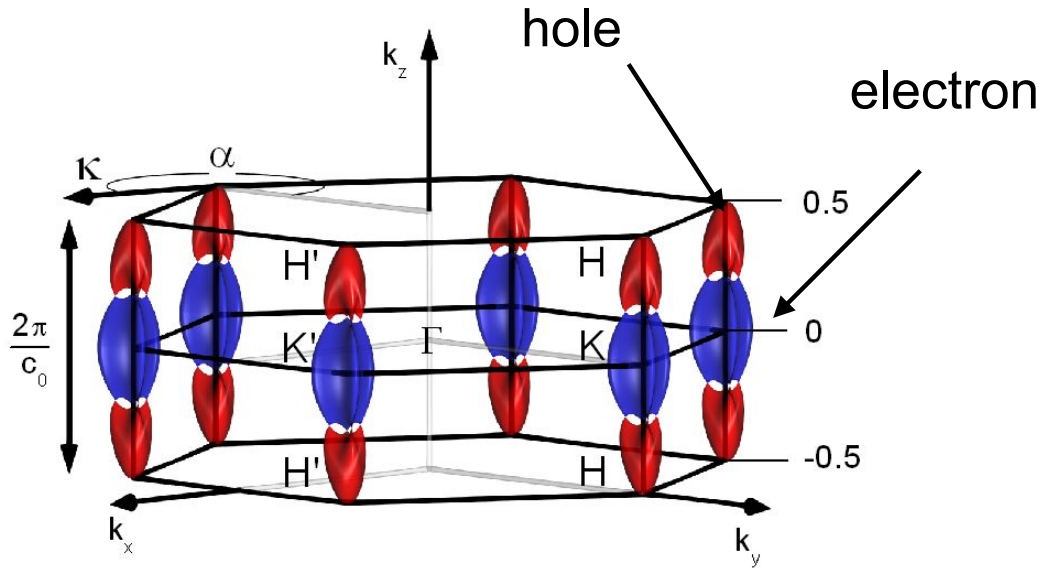


Fig. 4.1 Schematic representation of the Fermi surface of graphite in the Brillouin zone by S.B. Hubbard *et al.* [54]. The electron and hole pockets are located along the H-K-H and H-K'-H direction of the BZ.

#### 4.1.1 Fermiology of graphite

Graphite is one of the allotropic variety of crystalline carbon. It is made of a stacking of hexagonal planar lattices of carbon, the graphene layers, along the  $c$ -axis [55].

Its electronic structure was first computed in the 50s. First, P.R. Wallace proved that only the  $\pi$  bands close to the vertical edges of the BZ are relevant to the band structure [56]. Then, Slonczewski, Weiss and McClure showed that the electronic band structure can be mapped out by a tight binding model in the graphene planes which interact through a hopping term [57, 58]. This model was labelled the SWM-model. It revealed the compensated semi-metallic nature of graphite with a small 3D Fermi surface composed of electron and hole pockets with maximal cross sections respectively at  $k_z = 0.00\text{m}^{-1}$  and  $k_z = 0.35\text{m}^{-1}$ . The in-plane dispersion is parabolic for holes and electrons except at the H point of the BZ where the linear dispersion is reminiscent of graphene. This Fermi surface, represented in the Brillouin zone (BZ) for the hexagonal lattice, is shown in figure 4.1.

The electronic concentration of graphite was deduced from quantum oscillations :  $n \approx p \approx 3 \times 10^{18}\text{cm}^{-3}$ . As indicated in the first chapter, a consequence of this low electronic concentration is that the quantum limit is encountered as low as  $B_{QL} = 7.5\text{T}$ . With further increase of the magnetic field, a succession of field-induced states is observed.

### 4.1.2 Field-induced states of graphite

**In-plane resistivity up to  $B = 75\text{T}$**  The first evidence of field-induced state of graphite was reported by Tanuma *et al.* [59] and was later confirmed by a variety of experimental studies which have been reviewed recently [60, 25]. The signature of this phase is illustrated in figure 4.2.a with in-plane resistivity measurement up to  $B = 70\text{T}$  (along the  $c$ -axis) by Fauqué *et al.* [61], at temperatures ranging from  $T = 1.5\text{K}$  to  $T = 10\text{K}$ .

The in-plane resistivity increases by several orders of magnitude upon the application of a magnetic field before reaching saturating at  $B \approx 20\text{T}$  and a sharp increase of the in-plane magnetoresistance is reported at  $B \approx 28\text{T}$ . This feature is suppressed for  $T > 10\text{K}$ . With further increase of the field,  $R_a$  slowly decreases up to  $B = 70\text{T}$ . Besides this background evolution,  $R_a$  also presents sharp features at high field. The first of these anomalies, labelled  $\alpha$ , corresponds to a sudden increase at a temperature dependent field. It is indicated by an arrow in figure 4.2.a. This feature was linked to a change in the electronic ground state of graphite [25]. The onset of the  $\alpha$ -transition is shifted to higher magnetic fields as the temperature increases and is suppressed above  $T = 10\text{K}$ . At higher field we observe another structure in the in-plane resistance : a plateau near  $B = 35\text{T}$  emerges. This plateau is favored by low temperatures and has been attributed to a second transition, labelled  $\beta$  on figure 4.2.a. Upon further increase of the magnetic field, at  $B = 53\text{T}$ , we observe a drop of  $R_a$  back to the low fields (a few Teslas) resistance values. For  $53\text{T} < B < 70\text{T}$ , the resistivity decreases with increasing field.

The evolution of the in-plane resistivity with temperature is illustrated at  $B = 64\text{T}$  in figure 4.2.c.  $R_a$  present a  $B$ -linear magnetoresistance. While the temperature dependence of the magnetoresistance is only plotted at  $B = 64\text{T}$ , we can easily transpose this result to other fields from figure 4.2.a. The in-plane resistivity of graphite is metallic up to  $B = 70\text{T}$ .

**Out-of-plane resistivity up to  $B = 75\text{T}$**  We will now focus on the evolution of the out-of-plane resistivity  $R_c$  of graphite as a function of magnetic field.

This quantity has been less studied for experimental reasons : the two varieties of graphite with low stacking defect, natural graphite and Kish, are flakes with millimetric in-plane length and a  $c$ -axis extension of the order of  $\approx 10\mu\text{m}$ . It is thus extremely difficult to measure the  $c$ -axis resistivity without any in-plane contamination. In addition, the anisotropy ratio varies significantly between the different types of graphite.

Despite these difficulties, the study of the  $c$ -axis transport in the field-induced state has been very fruitful [63] and revealed a remarkable sensitivity of  $R_c$  to the first field induced states.

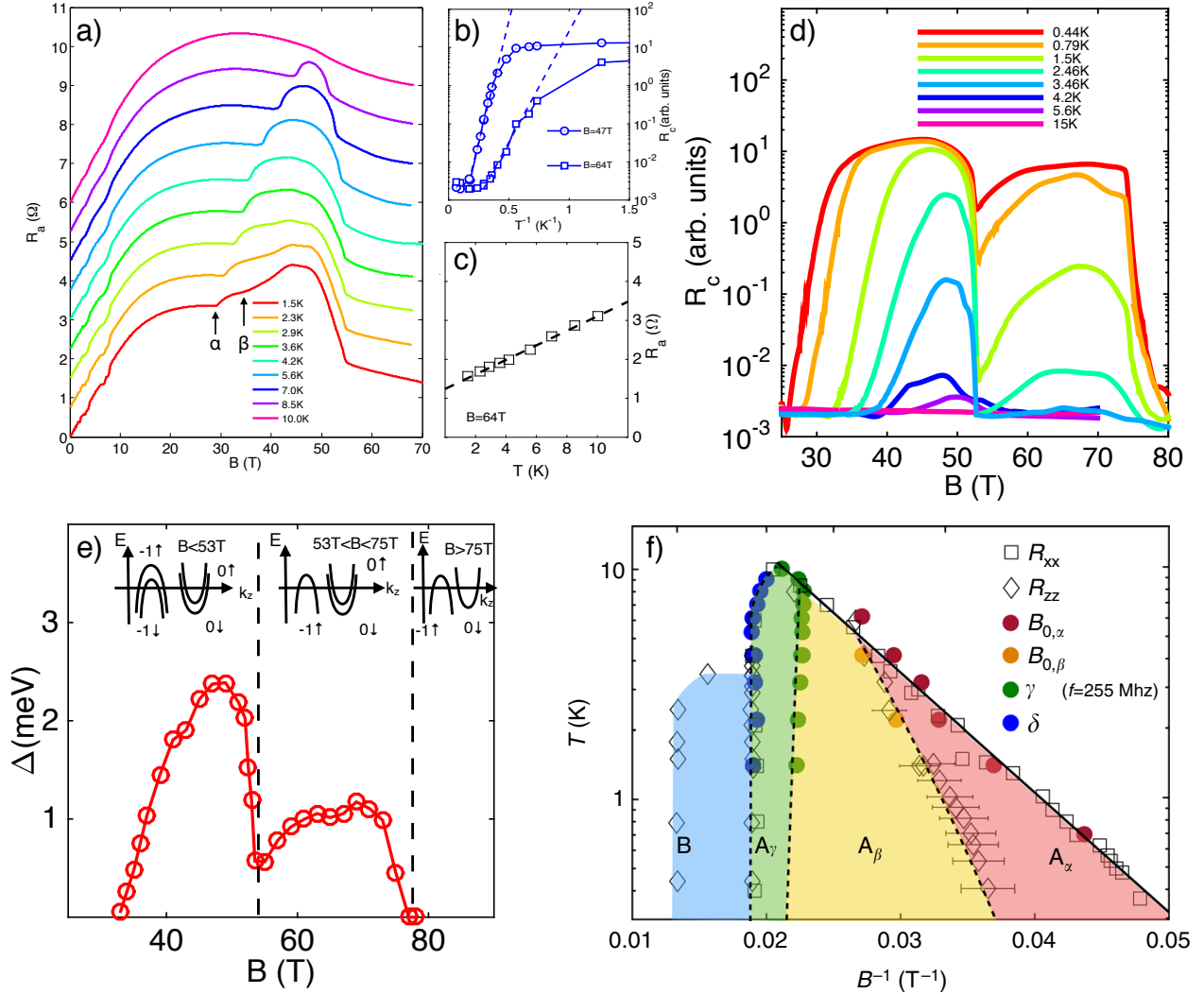


Fig. 4.2 **a)** In-plane magnetoresistance ( $R_a$ ) of Kish graphite up to  $B = 70T$  for temperatures between  $T = 1.5K$  and  $T = 10K$ . The magnetic field is applied along the  $c$ -axis. The curves are shifted for clarity. **b)**  $R_c$  (shown in **d)** as a function of  $T^{-1}$  for  $B = 47T$  (circles) and  $B = 64T$  (squares) in a log scale. Dashed lines are Arrhenius fits to  $R_c$ . **c)**  $R_a$  as a function of temperature for  $B = 64T$ . **d)** Out-of-plane magnetoresistance  $R_c$  in semi-logarithmic scale of Kish graphite up to  $B = 80T$  and down to  $T = 0.44K$ . **e)** Field dependence of the gap deduced from the activating behavior of  $R_c$ . Inset is a sketch of the occupied Landau sub-levels with increasing magnetic field. **f)**  $(B^{-1}, \log(T))$  phase diagram of graphite. Graph from Le Boeuf *et al.* [62].

The out-of-plane resistance of a Kish sample, also from Fauqué *et al.* [61], is plotted as a function of the magnetic field up to  $B = 80\text{T}$  at various temperatures from  $T = 0.44\text{K}$  to  $T = 15\text{K}$  in figure 4.2.d. We observe an increase by more than 3 orders of magnitude of the out-of-plane resistivity at the  $\beta$ -transition. Surprisingly, in contrast with the in-plane magnetoresistance, the c-axis magnetoresistance displays an insulating behavior.

In both regions of fields [30T,53T] and [53T,75T],  $R_c$  has a strong temperature dependence which is illustrated at  $B = 47\text{T}$  and  $B = 64\text{T}$  is plotted in a semi-log scale as a function of  $T^{-1}$  in figure 4.2.b.

$\log(R_c)$  evolves linearly with  $T^{-1}$ , i.e presents an activated behavior, over several orders of magnitude before saturating both at low and high temperatures. The energy gap in this interval,  $\delta$ , is determined from an Arrhenius law and is plotted in figure 4.2.e as a function of the magnetic field. Its amplitude increases to reach a first maximum at  $B = 47\text{T}$  where  $\delta = 2.4\text{meV}$  and then sharply decreases down to  $\delta = 0.5\text{meV}$  at the (first) re-entrance field  $B = 53\text{T}$ . With further increase of the field, the gap increases again and saturates between  $B = 60\text{T}$  to  $B = 75\text{T}$  at a value close to  $\delta = 1\text{meV}$ . The gap finally decreases suddenly and closes at  $B = 75\text{T}$ . This is the second re-entrance field.

Contrary to the in-plane resistivity which remained metallic up to  $B = 75\text{T}$ ,  $R_c$  shows an insulating behavior in both field-induced states.

**(B,T) phase diagram** So far, the in-plane and out-of-plane resistivity reports established the existence of two successive field-induced states in graphite. The resulting phase diagram as a function of field and temperature is plotted in figure 4.2.f. Both the A-phase and the B-phase present simultaneous in-plane metallicity with c-axis field-induced insulating behavior.

Let us now turn to a recent study which explores the resistivity of graphite up to  $B = 90.5\text{T}$ . Zhu *et al.* reported on the in-plane and out-of-plane resistivities of natural graphite samples up to  $B = 90.5\text{T}$  from  $T = 1.4\text{K}$  to  $T = 9\text{K}$  [26]. Their measurements, shown in figure 4.3, reveal a sharp increase of  $R_a$  for  $B > 75\text{T}$  at sufficiently low temperature while the out-of-plane resistivity remains quasi-constant for  $75\text{T} < B < 90\text{T}$ . They associate this feature with a third field-induced state, labelled the C-phase, which was absent of the  $(B, T)$  phase diagram presented (Figure 4.2.e). The updated phase diagram is presented in 4.3.c.

This observation of the C-phase was reported in a natural sample. We confirm this observation through the study of the in-plane resistivity of a natural graphite sample of exceptional quality up to  $B = 88\text{T}$ .

$R_a$  of this sample is plotted as a function of temperature for  $B < 100\text{e}$  in figure 4.4.a. His residual resistivity ratio  $RRR_{NG-1} = 200$  is, to the best of our knowledge, the highest

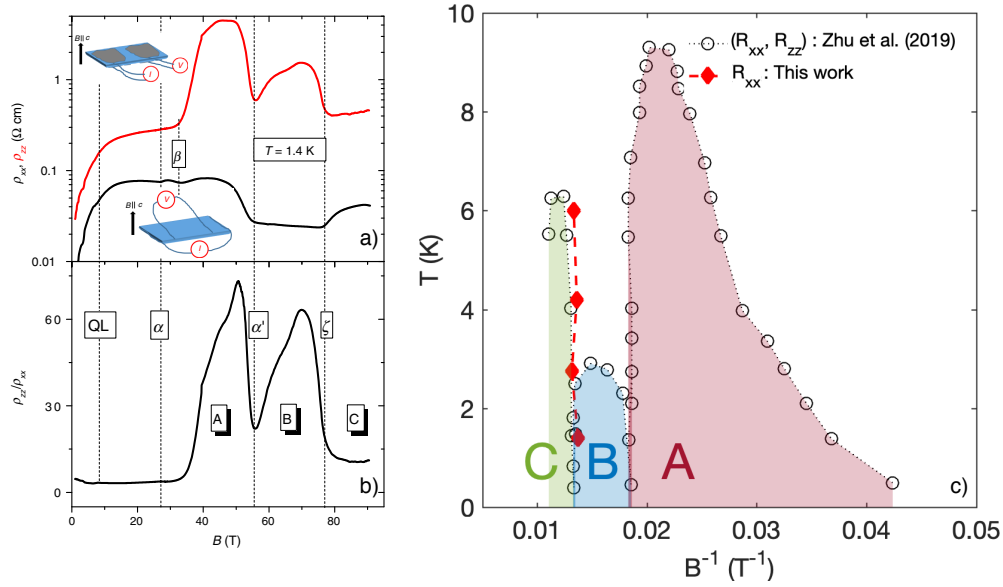


Fig. 4.3 **a)** Field dependence of the in-plane resistivity  $\rho_{xx}$  and the out-of-plane resistivity  $\rho_{zz}$  of a kish graphite sample up to  $B = 90.5\text{ T}$  at  $T = 1.4\text{ K}$  from Zhu *et al.* [26]. Sketches show the measurement geometries. **b)** Field dependence of  $\rho_{zz}/\rho_{xx}$ . The QL as well as the three phases are indicated by dotted lines. The zero-field anisotropy reaches 500. **c)**  $(B^{-1}, T)$  phase diagram of graphite with inputs from Zhu *et al.* (black) and this work (red).

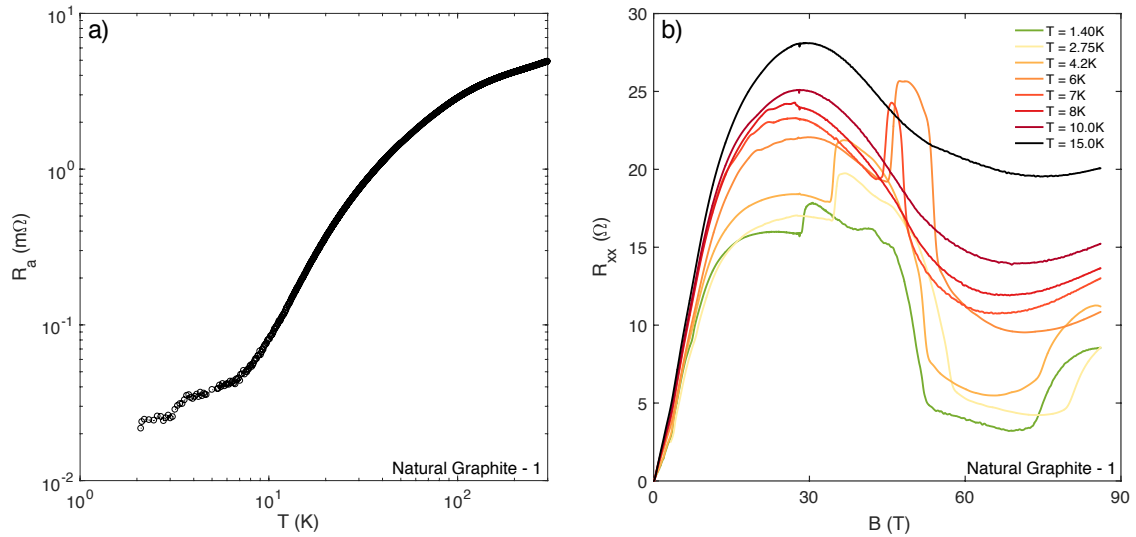


Fig. 4.4 **a)** In-plane resistivity  $R_a$  plotted as a function of temperature for a sample of natural graphite (labelled NG-1) of high quality. **b)** In-plane magnetoresistivity  $R_{xx}$  plotted as a function of  $B$  up to  $B = 86\text{ T}$  at various temperature for sample NG-1.

ever reported in graphite. It guarantees high crystalline quality and low contamination of the c-axis in the in-plane resistivity. This lack of contamination makes this sample particularly fit to explore the  $B > 75\text{T}$  C-phase : this phase was discovered through a sharp increase in the in-plane resistivity with evolution of the c-axis resistivity (figure 4.3.b), yet at these magnetic fields,  $R_c$  is an order of magnitude higher than  $R_a$  and would hide the in-plane signal in case of large c-axis contamination.

The evolution of  $R_a$  for NG-1 is presented as a function of magnetic field in figure 4.4.b. Our results are in good agreement with the report by Zhu *et al.* : At  $B = 75\text{T}$ , we observe a sharp increase of the in-field resistivity for  $T = 1.4\text{K}$  to  $T = 6\text{K}$ . This increase saturates at the highest recorded field  $B \approx 88\text{T}$  and appears to start decreasing for the  $T = 4.2\text{K}$  data over the last Tesla.

Our experimental results on a high quality natural graphite confirm the existence of the C-phase and allow us to contribute to the updated  $(B, T)$  phase diagram of graphite in the QL (Fig 4.3.c).

**Origin of the field-induced states : density-wave transitions** Let us now turn to the origin of the field-induced states of graphite. Shortly after their discovery, these successive field-induced states were attributed to the formation of charge density waves along the magnetic field in the  $(n = 0,+)$  LL [64]. However, other DW instabilities have been proposed such as spin density waves [65] and more recently excitons [66]. There is yet no consensus on the nature of the DW. Nevertheless, a consensus on the essential ingredients in favor of an electronic instability in the quantum limit emerged. Both a change in the effective dimensionality of the charge carriers from 3D to 1D because of the magnetic field and an enhancement of the electron-electron interaction, in particular when the magnetic field is near a field for which a low LL empties, are required. For both reasons, these instabilities are thought to be driven by the electron - electron interaction.

In the case of graphite, the compensated nature of the FS and the valley degree of freedom have to be considered. For  $B > 7.5\text{T}$ , as represented in the sketch of fig 4.2.e four Landau levels are occupied (respectively  $(0,\pm)$  for the hole pocket and  $(-1,\pm)$  for the electron pocket), and therefore several instabilities involving either a CDW or a SDW have been proposed. First, Yoshokia and Fukuyama [64] suggested the formation of two charge-density-waves along the c-axis, with opposite phases in order to minimize Coulomb interaction, in the two valleys along the H-K-H and H-K'-H directions of the Brillouin zone. However, this scenario was later challenged by Takahashi al. [65], who argued that the electrons along the H-K-H and H-K'-H directions do not belong to the same layers. In other words, the cancellation of the Coulomb interaction cannot be at work in each layer. Instead, he suggested that a

transverse SDW forms in the ( $n = 0, \pm$ ) LLs. Finally, Akiba *et al.* recently proposed that the observed gapped out-of-plane conduction above  $B = 53\text{T}$  is associated with an excitonic BCS-like state [66]. This excitonic scenario has been a subject of further attention recently [67] and Zhu *et al.* submitted evidence that the insulating state destroyed at  $B = 75\text{T}$  is an excitonic condensate of electron-hole pairs [26].

Moreover, the observation by Fauqué *et al.* of an activated conductivity along the  $c$ -axis which coexists with metallic conductivity in the graphene planes contrasts with what has been reported in other 1D density-wave systems. Rather, the coexistence of these two features for a bulk system with a fully gaped electronic spectrum points to the existence of a second channel of conduction in the system [61]. From a theoretical standpoint, this observation qualifies graphite as a possible host of the 3D quantum Hall effect.

Finally, we indicate that the emergence of a density-wave transition is not limited to semi-metals. Nesting vectors can also exist in the case of a doped semi-conductor with a single Fermi surface and lead to a DW-transition. More generally it is predicted to happen in any system, brought deep enough in its quantum limit and at sufficiently low enough temperature [53]. In order to test the universality of such instability we have studied the case of u-InAs. In this system, the QL is reached at only  $B = 4\text{T}$ , making it an ideal subject of investigation which has been, so far, poorly studied.

### 4.1.3 Presentation of Indium Arsenide

Indium arsenide is an intermetallic compound formed between the group IIIb element In and the group Vb element As. It is a narrow gap semi-conductor,  $E_g = 0.35\text{eV}$  at  $T = 300\text{K}$ , which crystallizes in the zinc-blende (ZnS) structure (cubic space group F43m). The carrier concentration  $n = 2.0 - 2.2 \times 10^{16}\text{cm}^{-3}$  [68, 69] and the high electronic mobility  $\mu = 40000\text{cm}^2.\text{V}^{-1}.\text{s}^{-1}$  [70] were established from Hall resistivity measurements. The effective mass of the electrons,  $m^* = 0.023 \times m_0$  was determined by magneto-optical measurements [71].

Let us confirm the shape of the Fermi surface, the electronic concentration and more generally the transport properties of u-InAs through our electrical transport measurements. Our work was done on undoped InAs (u-InAs) samples cut from a  $t = 500\mu\text{m}$  thick wafer grown by the Liquid Encapsulated Czochralski (LEC) method. The different samples were cleaved into bar-like geometries of width  $w \approx 500\mu\text{m}$  with millimetric lengths.

**Temperature dependence** In the absence of magnetic field, the resistivity  $\rho$  of u-InAs as a function of temperature is represented in figure 4.5. From  $T = 300\text{K}$  to  $T = 95\text{K}$ ,  $\rho$  decreases linearly with decreasing temperature. The resistivity reaches a minimum at  $T_{min} = 95\text{K}$  and

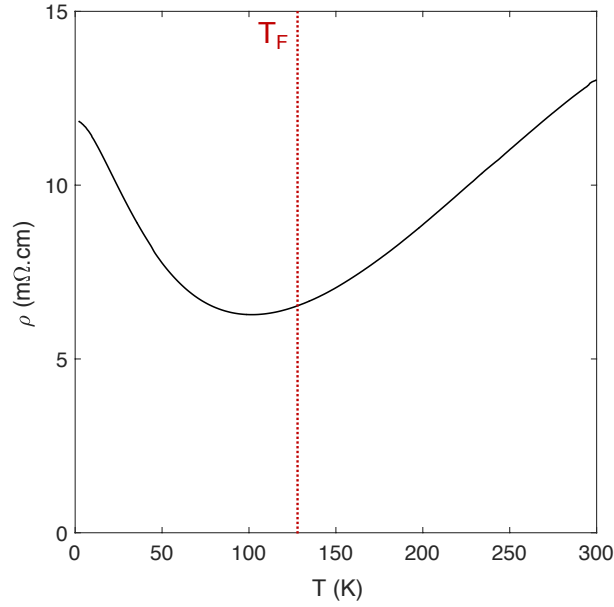


Fig. 4.5 Resistivity of undoped n-type InAs as a function of temperature. Sample is a slab of dimension  $(0.75 \times 0.5 \times 6)$  mm<sup>3</sup>. The dotted vertical line indicates the value of u-InAs Fermi temperature  $T_F = 130$ K.

increases with further decreasing temperature down to dilution temperatures. The resistivity at  $T = 300$ K and  $T = 2.0$ K are very similar.

Let us first evaluate the Fermi temperature  $T_F$  from the aforementioned carrier concentration and effective mass reported in the literature. We find  $T_F = 130$ K. When  $T < T_F$ , the resistivity is dominated by the scattering with the ionized impurities, it decreases with increasing temperature. Above  $T_F$  however,  $\rho$  is dominated by the electron - phonon scattering process and thus becomes  $T$ -linear. The resistivity of u-InAs is characteristic of a semi-conductor with ionized impurities. We now turn to its magnetoresistance to establish the fermiology of u-InAs.

**Angular dependence of the magnetoresistance** Let us first discuss the evolution of the resistivity when an external magnetic field is applied. We report on the transverse magnetoresistance  $\rho_{xx}$  in figure 4.6.a and the longitudinal magnetoresistance  $\rho_{zz}$  in figure 4.6.b. Both quantities are plotted as functions of the magnetic field up to  $B = 13.8$ T for temperatures ranging from  $T = 2.15$ K to  $T = 100$ K. In the transverse configuration,  $\theta = 0^\circ$ , the magnetic field is oriented along the  $[1\ 0\ 0]$  direction whereas in the longitudinal geometry,  $\theta = 90^\circ$ , it is oriented along the  $[1\ 1\ 0]$  direction.

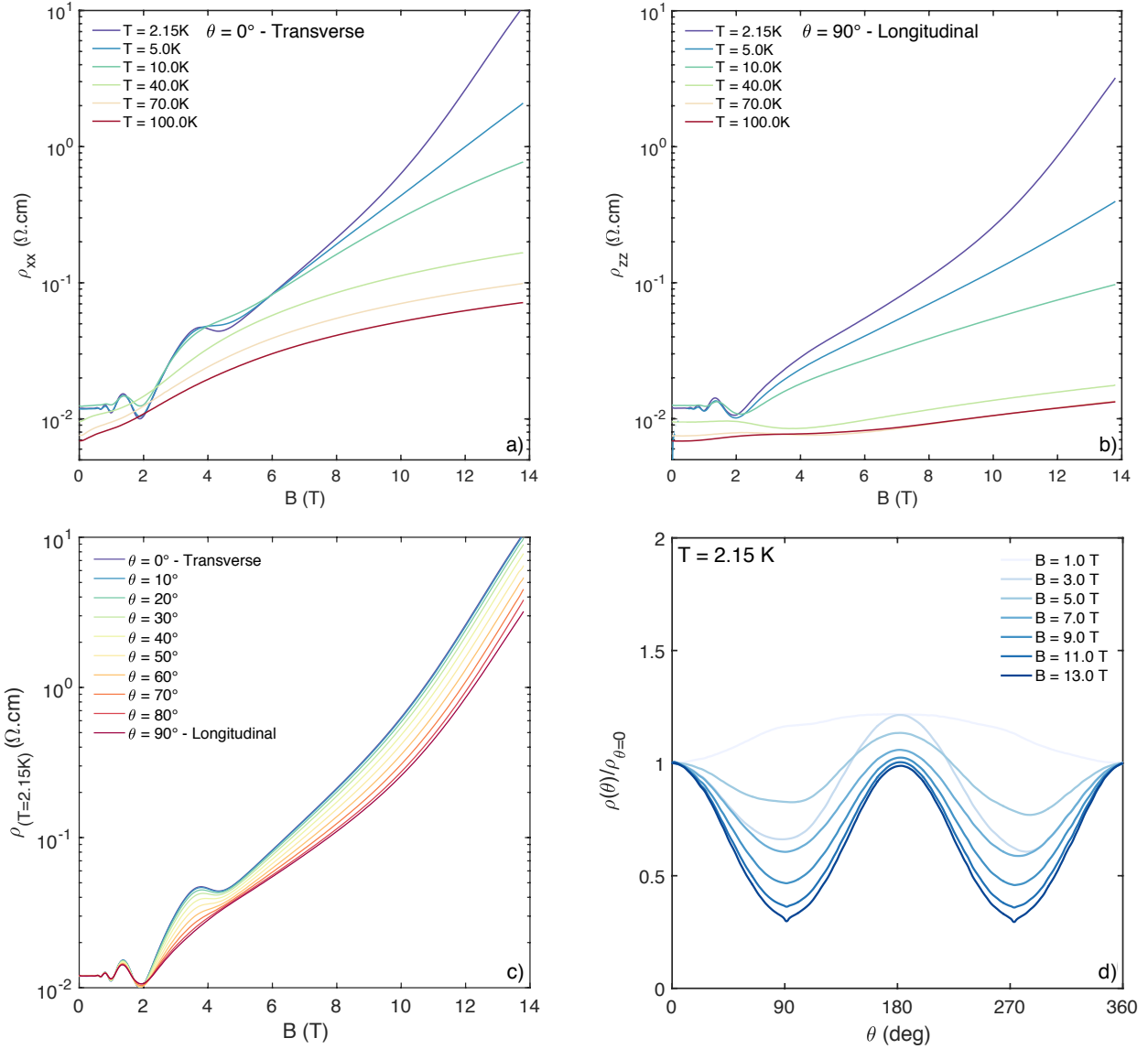


Fig. 4.6 **a**) Transverse magnetoresistance ( $j_Q \perp B$ )  $\rho_{xx}$  as a function of magnetic field up to  $B = 14\text{T}$  for different temperatures. **b**) Longitudinal ( $j_Q \parallel B$ ) magnetoresistance  $\rho_{zz}$  as a function of magnetic field up to  $B = 14\text{T}$  for the same array of temperatures. Both datasets were acquired during the same experimental run. **c**) Magnetoresistance  $\rho$  as a function of the magnetic field for various angle  $\theta = (\vec{j}_Q, \vec{B})$  from transverse ( $\theta = 0^\circ$ ) to longitudinal ( $\theta = 90^\circ$ ) geometries. Temperature was set to at  $T = 2.15\text{K}$ . **d**) Magnetoresistance  $\rho_\theta$  plotted as  $\rho_\theta/\rho_{\theta=0}$  as a function of the angle  $\theta = (\vec{j}_Q, \vec{B})$  for static magnetic fields at  $T = 2.15\text{K}$ . All sets of data were acquired during the same experimental run.

For  $B < 3.85\text{T}$ , we do not observe any MR in  $\rho_{xx}$  and  $\rho_{zz}$ , only quantum oscillations for  $T < 5\text{K}$ . While all the peaks up to  $B = 2\text{T}$  are identical in  $\rho_{xx}$  and  $\rho_{zz}$ , the peak at  $B = 3.85\text{T}$  is absent in  $\rho_{zz}$  even though it is observed in  $\rho_{xx}$ . This absence is emphasized in figure 4.6.c which shows the magnetoresistivity as a function of the magnetic field for various angles ranging from transverse,  $\theta = 0^\circ$ , to longitudinal  $\theta = 90^\circ$  geometry. Figure 4.6.c also reveals a small evolution of the resistivity, up to factor of 3, caused by the relative orientation of the current and field.

**Fermiology of u-InAs** We now turn to the analysis of the observed quantum oscillations. First we wish to determine the electronic concentration and the effective mass of the electrons in this wafer of u-InAs.

**1 - Carrier concentration** One way to evaluate the charge carrier concentration is to study the frequency of the quantum oscillations  $f$  through the Onsager relation. This relation has been detailed in chapter 1. We measure  $f = 1.85\text{T}$ , which yields an electronic concentration :  $n = 1.6 \times 10^{16} \text{ cm}^{-3}$ . This value is around 30% lower than the aforementioned reports from Hall measurements [69, 68].

**2 - Effective mass** Next, the temperature dependence of the amplitude of the QO peaks allows us to determine the effective mass  $m^* = 0.023 \times m_0$  of the carriers in light of the Lifschitz-Kosevich model. The method is illustrated in figure 4.7.b and was also presented in the first chapter of the present thesis. We notice that this value does not evolve with magnetic field (as seen on the inset). The effective mass of carriers in u-InAs matches the aforementioned literature [71].

**3 - Entrance in the quantum limit** Now that we have confirmed the electronic concentration and effective mass of the carriers, we wish to confirm that the  $B = 3.85\text{T}$  peak marks the entrance in the quantum limit [68, 72]. To do so, we compute the evolution of the Fermi energy as a function of the magnetic field. The position of the lowest Landau level is set by the Landé factor  $g = -14.6$  [73] and the Fermi energy  $E_F$  calculated from the previously determined Fermi temperature. to the experimental oscillations of  $\rho_{xx}$  in figure 4.7.a. We observe that the population/depopulation of the successive Landau levels matches the extrema of the resistivity and for  $B > 3.85\text{T}$ , all electrons are predicted to lay in the lowest Landau level. For  $B > 3.85\text{T}$  the quantum limit is reached in u-InAs.

Finally, we can track the evolution of the amplitude and frequency of the QO upon variation of the angle between the electrical current and the magnetic field in figure 4.7.c. We observe no variation of the position of the peaks (the  $B = 3.85\text{T}$  peak is not discussed here) nor of their amplitude with  $\theta$ . As a consequence, the frequency of the QO does not evolve with  $\theta$  and we can conclude that the cross-section of the Fermi surface shows no angular

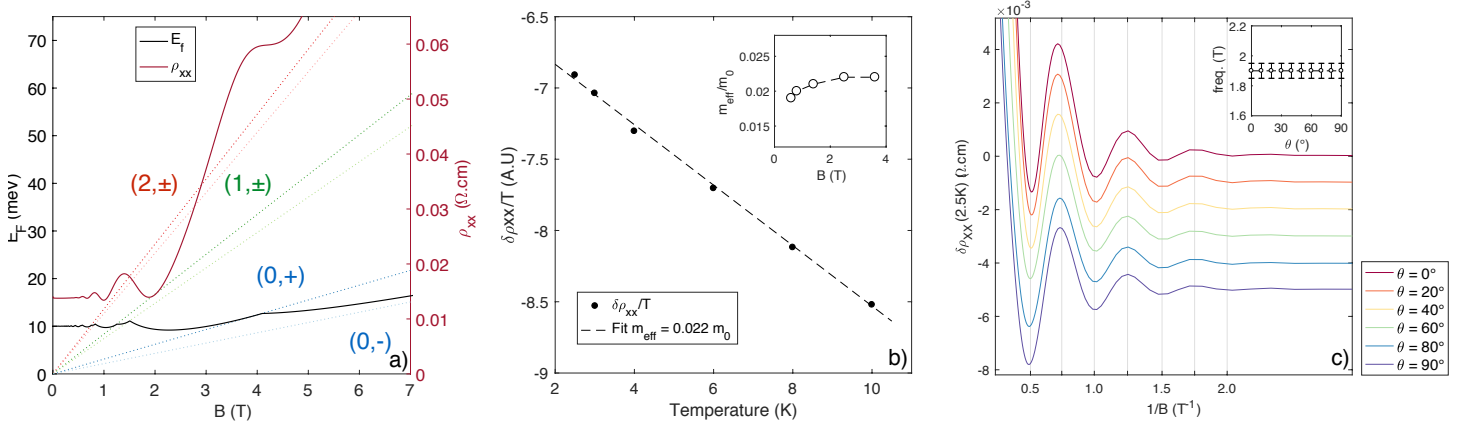


Fig. 4.7 **a)** Left-axis : computed Fermi energy  $E_F$  plotted as a function of magnetic field for u-InAs. Right axis :  $\rho_{xx}$  plotted as a function of magnetic field at  $T = 2.0\text{K}$  **b)** Logarithm of the amplitude of the QO ( $\delta\rho_{xx}$  determined by removing a polynomial background to the magnetoresistance) plotted as  $\log \delta\rho_{xx}/T$  as a function of temperature. The straight line fit corresponds to an effective mass  $m^* = 0.023 \times m_0$  determined at  $B = 3.85\text{T}$ . The inset shows the evolution of  $m^*$  with field. **c)** Evolution of the QO plotted as a function of  $B^{-1}$  for different angles  $\theta$ . The inset shows the extracted frequency of QO as a function of the angle.

dependence. While the in-plane rotation is not studied here, we can safely conclude that the FS of u-InAs is highly isotropic, i.e. close to a sphere. This result is in agreement with previous report of a spherical FS located at the  $\Gamma$ -point of the BZ [72].

**Field-induced state in u-InAs** We have shown that u-InAs enters the quantum limit at a field of only  $B = 3.85\text{T}$ . Upon further increase of the magnetic field, we observe a large increase of the resistivity both in the transverse geometry, figure 4.6.a, and the longitudinal one, figure 4.6.b. Both resistivities increase by several orders of magnitude for  $B > 5\text{T}$  and display large temperature dependence : a field-induced insulating state emerges.

This result confirms by prior experimental observations [72, 74]. This phenomenon was associated with the 'magnetic freeze-out' regime [75] : the intense magnetic field shrinks the electronic wave-function to a volume lower than the average volume of impurity ions, which results in a electron-impurity bound state with an increasing binding energy as the field is increased. This phenomenon is schematically represented in figure 4.1.a. The electrons are 'frozen-out' of the lowest Landau level and the carrier concentration drops. This leads to a sharp increase of the transverse and Hall resistivity.

The onset of this magnetic field assisted Mott-Anderson transition is defined by equation 4.1. It involves the spatial extension of the electronic wave-function along the applied

magnetic field  $a_{\parallel,B}$ , its extension perpendicular to the field  $a_{\perp,B}$  and the average distance between ionized impurities  $n^{1/3}$ . From a theoretical standpoint, three factors are going to affect these quantities : the thermal excitation, the screening of the impurities and the effective Bohr radius [76].

$$\begin{aligned} a_B \times n^{1/3} &\approx 0.25 \\ a_B &= (a_{\perp,B}^2/a_{\parallel,B}) \end{aligned} \quad (4.1)$$

This transition has been particularly studied in semiconductors with low electronic carrier concentration : undoped-InSb with nominal  $n = 2 - 5 \times 10^{15} \text{ cm}^{-3}$  [77–79],  $\text{Hg}_{1-x}\text{Cd}_x\text{Te}$  with  $n = 1 - 10 \times 10^{14} \text{ cm}^{-3}$  [78, 80] and u-InAs [72]. As an example, the increase in  $\rho_{xx}$  and  $\rho_{Hall}$  due to the magnetic freeze-out in n-type InSb ( $n = 2.5 \times 10^{15} \text{ cm}^{-3}$ ) is presented to the reader in figure 4.8.a. It has to be noticed that the driving force of the field-induced transition observed in doped semi-conductors is fundamentally different than in graphite in which it is associated with  $e^-e^-$  interaction. In addition to this interaction, in a doped semi-conductor one has to consider the interaction between electrons and ionized impurities. This last interaction can be the strongest and pin down the ground state.

We emphasize again that this compound has not been studied to sub-kelvin temperatures and high magnetic fields deep in the magnetic freeze-out regime (besides an observation of a small negative longitudinal magnetoresistance [81] up to  $B = 20\text{T}$ ). Also, its thermoelectric properties have been ignored as we could only find a low field study of the Nernst-Ettingshausen effect which dates back to half a century ago [68]. The lack of interest for the fate of bulk u-InAs in field is surprising in regard of the attention it recently received in the context of device and hetero-structures [82].

u-InAs thus appears as a very interesting playground to study the ground state of a 3D electron gas in the deep quantum limit, especially in light of all the work done on graphite.

## 4.2 Indium arsenide in the deep quantum limit

In order to deepen our understanding of the field-induced state observed in u-InAs, we will now investigate the resistivity to unexplored low temperatures and high magnetic fields.

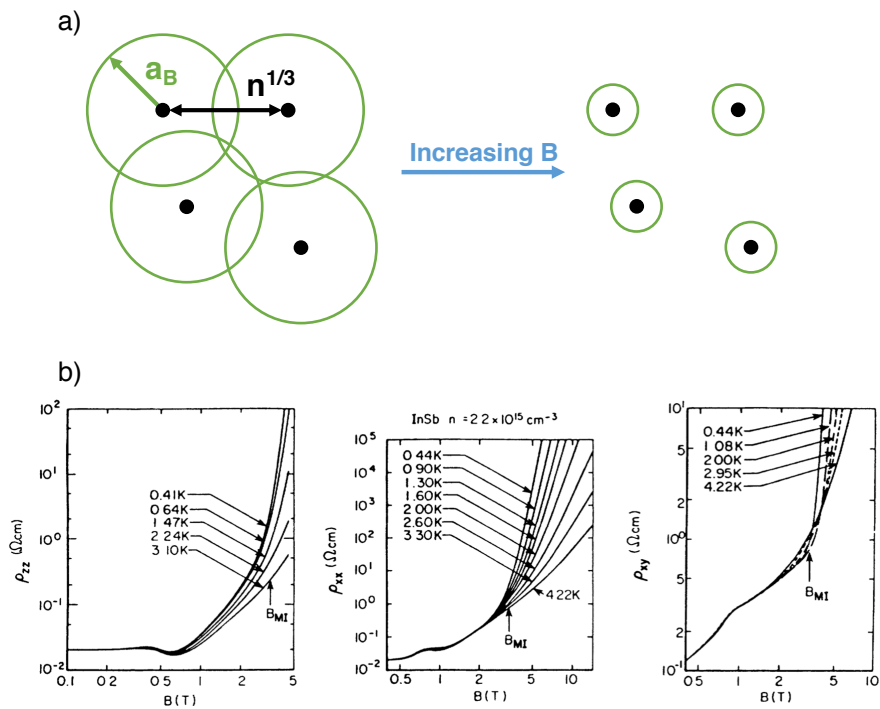


Fig. 4.8 **a)** Schematic representation of the emergence of the magnetic freeze-out regime in regard of the relative spatial extension of the electronic wave-function  $a_B$  and the average distance between impurities  $n^{1/3}$ . **b)** Evolution of  $\rho_{xx}$ ,  $\rho_{zz}$  and  $\rho_{xy}$  in undoped n-InSb in the magnetic freeze-out regime in the quantum limit. The carrier concentration is 10 times lower than u-InAs.

### 4.2.1 Resistivity in the field-induced state

**Transverse, longitudinal & Hall resistivities** We measured the transverse, longitudinal and Hall resistivities as functions of magnetic field at different fixed temperatures. They are respectively shown in figures 4.9.a and c, 4.9.b and 4.9.d.

Before discussing the result, we wish to introduce the different samples studied here in different geometries. All samples were cut from the same homogeneous wafer and their size will be presented as (width  $\times$  thickness  $\times$  length). The contacts were pasted on the [1,0,0] surface with silver paste.

The transverse resistivity featured in figure 4.9.a was measured on sample #1 of dimension  $(0.8 \times 0.5 \times 2.4)\text{mm}^3$  in pulsed magnetic fields at LNCMI in Toulouse, France while the sample #3 presented in figure 4.9.c has been measured on a  $(0.45 \times 0.5 \times 3.3)$  in static fields up to  $B = 34\text{T}$  at LNCMI Grenoble, France. The longitudinal resistivity, figure 4.9.a, was measured on sample #2 of similar dimensions :  $(0.8 \times 0.5 \times 4.2)\text{mm}^3$ . Finally, the Hall resistivity (figure 4.9.c) was measured on sample #3 simultaneously as the transverse resistivity feature in figure 4.9.c.

The resistivity shows a similar field-dependence in all three different geometries of measurement over the whole interval of field studied. As a consequence, we will use the generic term resistivity in the discussion to refer interchangeably to  $\rho_{xx}$ ,  $\rho_{xy}$  and  $\rho_{zz}$  unless otherwise specified. We will now discuss three different regions of field.

We define  $B_{M-I}$  as the field at which the magnetoresistance increases sharply in the  $T \rightarrow 0$  limit. We find  $B_{M-I} \approx 8\text{T}$ . This field increases temperature.

The first region,  $0 < B < B_{M-I}$ , has already been discussed. For  $B > B_{M-I}$ , the resistivity becomes presents a strong temperature dependence : while  $\rho$  increases by 3 to 4 orders of magnitude at  $T \approx 1\text{K}$ , it only increases by a factor 20 at  $T = 20\text{K}$ .  $B_{M-I}$  corresponds to the entrance in the magnetic freeze-out regime [72].

However, at higher field we report the emergence of a second characteristic field, labelled  $B_{lin}$ , corresponding to the entrance in a saturation regime for the resistivity. For  $B > B_{lin}$ , the resistivity increases linearly with the magnetic field and becomes independent of the temperature.  $B_{lin}$  is shifted to higher fields with higher temperatures, as an example for  $T = 6\text{K}$  we observe no saturation at  $B = 56\text{T}$  whereas for  $T = 0.33\text{K}$  it is attained at  $B = 12\text{T}$ . This observation constitutes the first novel result of this study : the emergence of a third regime of magnetoresistance in u-InAs.

We now turn to the comparison of the saturation regime in  $\rho_{xx}$  for two different samples cut from the same wafer with very similar geometries. The values of the saturation observed in #1 (Fig 4.9.a) and #3 (Fig 4.9.c) differ by a factor of 10. Even though we only show data of saturation in  $\rho_{xx}$  for two samples here, the sample dependent saturation regime is ubiquitous

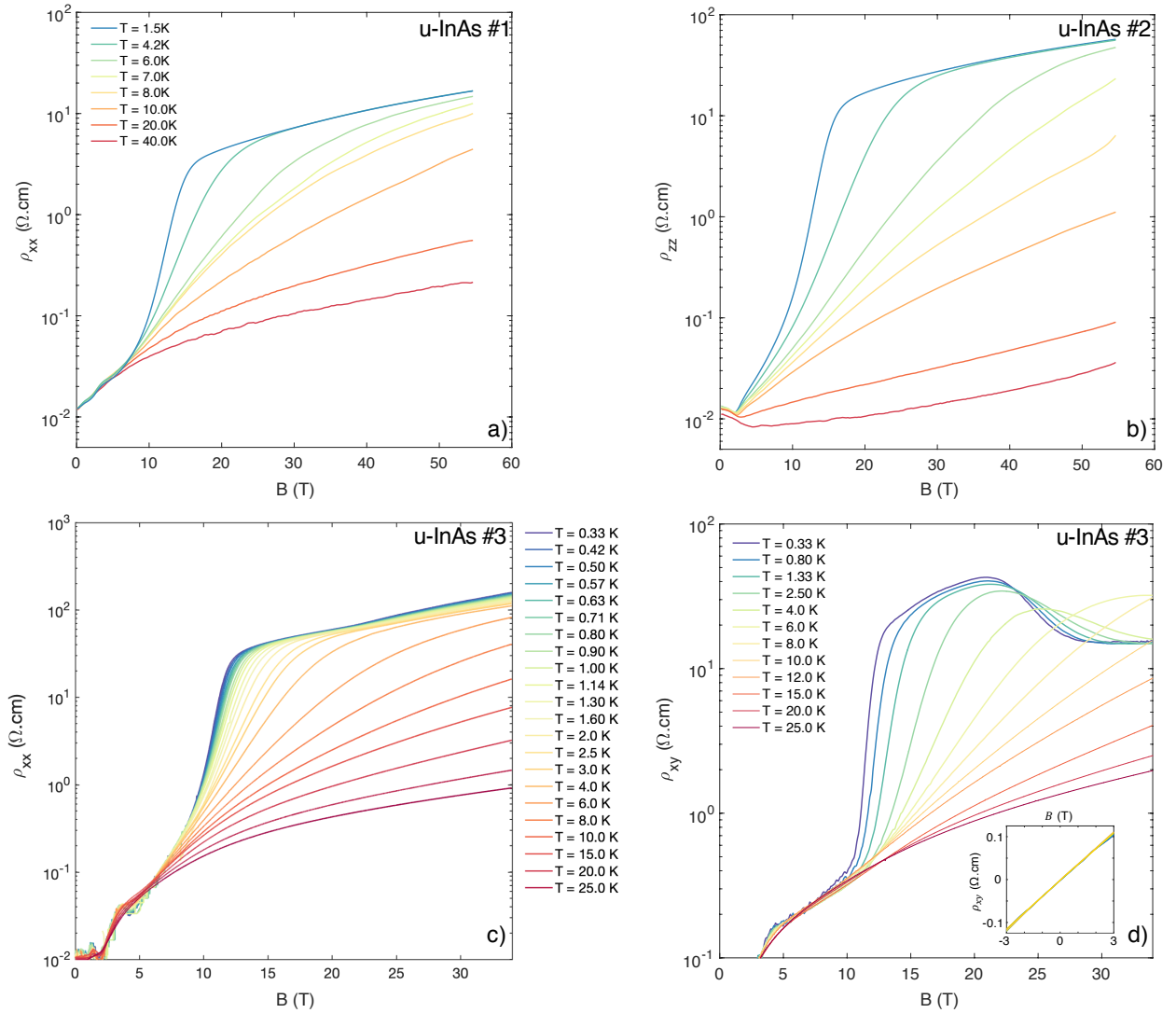


Fig. 4.9 **a)** Transverse magnetoresistance  $R_{xx}$  as a function of the magnetic field up to  $B = 56\text{T}$  at various temperatures from  $T = 1.5\text{K}$  to  $T = 40\text{K}$ . Measurement in pulsed field realised in LNCMI Toulouse on u-InAs sample #1. Signal is not symmetrized which explains the low field difference with c.. **b)** Longitudinal magnetoresistance  $R_{zz}$  as a function of the magnetic field up to  $B = 56\text{T}$  at various temperatures from  $T = 1.5\text{K}$  to  $T = 40\text{K}$ . Measurement in pulsed field realised in LNCMI Toulouse on u-InAs sample #2. **c)** Transverse magnetoresistivity  $\rho_{xx}$  as a function of the magnetic field up to  $B = 34\text{T}$  at various temperatures from  $T = 0.33\text{K}$  to  $T = 25\text{K}$ . Measurement in static field realised in LNCMI Grenoble on u-InAs sample #3. **d)** Hall resistivity  $\rho_{xy}$  as a function of the magnetic field up to  $B = 34\text{T}$  at various temperatures from  $T = 0.33\text{K}$  to  $T = 25\text{K}$ . Measurement in static field realised in LNCMI Grenoble on u-InAs sample #3. Inset shows the low field Hall resistivity.

to transverse/longitudinal/Hall resistivities and was confirmed by the study of 8 different samples with similar geometries, same experimental protocol and same origin.

**Study of the electronic concentration** We now turn to the analysis of the electronic concentration and charge carriers mobility deduced from the Hall resistivity.

The low field linear evolution of the Hall resistivity (inset of figure 4.9.d yields a temperature independent carrier concentration of  $n = 2.2 \times 10^{16} \text{cm}^{-3}$  (compared to  $n = 1.6 \times 10^{16} \text{cm}^{-3}$  from QO). At higher field, figure 4.10.a shows that the field-induced insulating state is accompanied by a drop of the carrier concentration followed by a saturation at  $n_H = 3.5 \times 10^{14} \text{cm}^{-3}$  for fields between  $B = 12\text{T}$  and  $B = 22\text{T}$  in the low temperature regime. For  $B > 22\text{T}$ ,  $n_H$  increases back and saturates at  $n_H = 1.5 \times 10^{15} \text{cm}^{-3}$ . As the temperature increases, the effect on the electronic concentration vanishes and, as an example,  $n_H$  at  $T = 25\text{K}$  is quasi-constant up to  $B = 34\text{T}$ . We can also extract the mobility ( $\mu = ne\sigma$ ) from the comparison of the transverse and Hall conductivities. The result is presented in figure 4.10.b. The mobility drops between  $B = 0\text{T}$  and  $B = 2\text{T}$  by a factor  $\approx 50$  and then slowly decreases further with increasing field. The mobility at  $B = 34\text{T}$  is more than 2 orders of magnitude lower than the 0-field mobility. The mobility shows a smaller temperature dependence than the carrier concentration : besides some small features (local minima), the mobility at  $T = 25.0\text{K}$  shows very little differences with the one determined at dilution temperatures.

The observation of a saturating  $n_H$  and mobility in the deep quantum limit is puzzling. Indeed, in the magnetic freeze-out picture, we expect  $n_H$  to monotonously go down as the field is increased [78]. Instead, we observe a residual carrier concentration close to  $n_H \approx 10^{14} - 10^{15}$  which is temperature independent for  $T < 5\text{K}$ .

In conclusion, we show that in the QL of u-InAs the resistivity, whatever the current direction, has insulating behavior above a critical field  $B_{M-I}$  concomitant with a drop in the carrier concentration  $n_H$ . At higher field, we discovered the emergence of saturation regime of transport. In this regime, the resistivity departs from the insulating behavior and adopts a close to  $B$ -linear behavior with no temperature dependence under low-temperature/high-field conditions accompanied by a saturation of  $n_H$ . Consequently, this saturation regime can be seen as the existence of a residual carrier contribution.

In order to further investigate the origin of this third regime of magnetoresistivity, we turn to the unexplored thermoelectric coefficients of u-InAs.

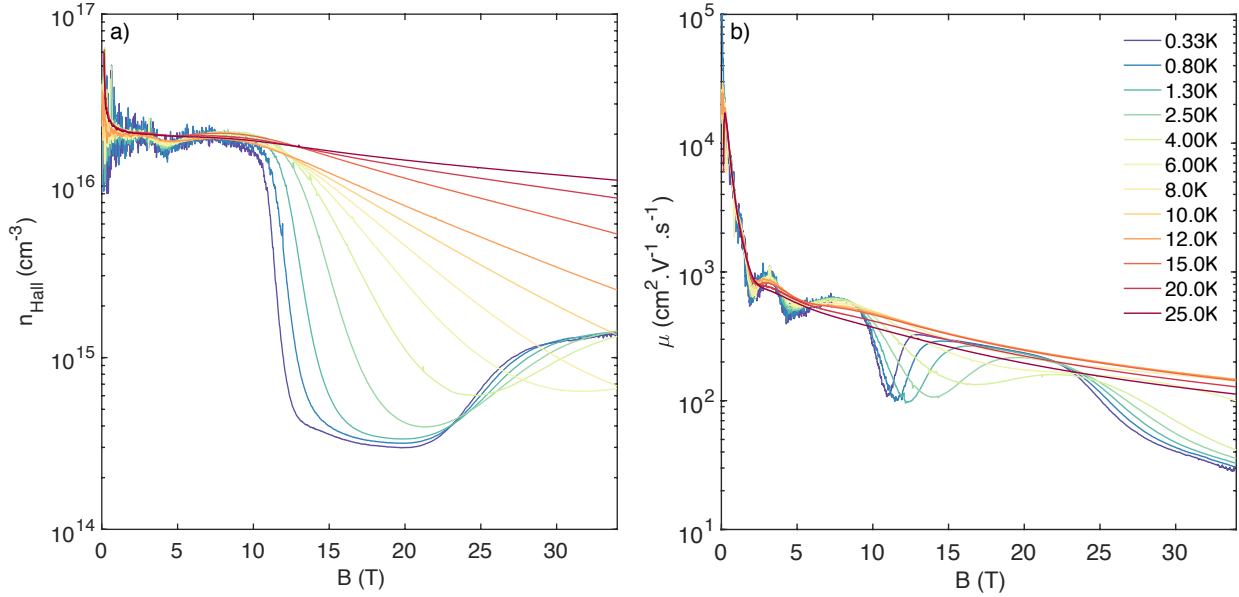


Fig. 4.10 **a)** Electronic concentration  $n_H$  as a function of magnetic field for various temperatures in u-InAs. **b)** Mobility of the charge carriers  $\mu_H$  determined from the Hall resistivity plotted as a function of magnetic field for various temperatures in u-InAs.

## 4.2.2 Vanishing thermoelectric coefficients

Thermoelectricity measurements are a powerful probe of electronic phase transition : it was successfully used to study the field-induced states of graphite [83] or in u-InSb where a giant Nernst effect has been observed in the magnetic freeze-out regime [84].

**Thermal conductivity** The first quantity we wish to report is the low temperature thermal conductivity.  $\kappa$  is plotted as a function of temperature up to  $T = 6.0\text{K}$  in figure 4.11.a. A previous report on a sample of u-InAs with similar size completes our data-set and indicates the existence of a peak in  $\kappa$  at  $T = 15\text{K}$  [85] with  $\kappa$  reaching up to  $\kappa \approx 5000\text{W.K}^{-1}.\text{m}^{-1}$  (millimetric sample). Over the whole range of study, since  $\rho \approx 10\text{m}\Omega.\text{cm}$ , the electronic contribution to  $\kappa$  is much smaller than the phononic contribution. As a consequence,  $\kappa$  is entirely due to phonons. This result is coherent with the  $T^3$ -dependence of  $\kappa$ .

**Zero-field value of  $S_{xx}$**  We report on  $S_{xx}$  plotted as  $S_{xx}/T$  as a function of temperature for  $B = 0\text{T}$  in figure 4.11.b. Below  $T < 3\text{K}$ , a constant  $S_{xx}/T = 8.5\mu\text{V.K}^{-2}$  is observed followed by a small peak at  $T = 6.5\text{K}$ . The thermopower drops with further increase of the temperature and reaches  $S_{xx}/T = 0.1\mu\text{V.K}^{-2}$  at  $T = 35\text{K}$ .

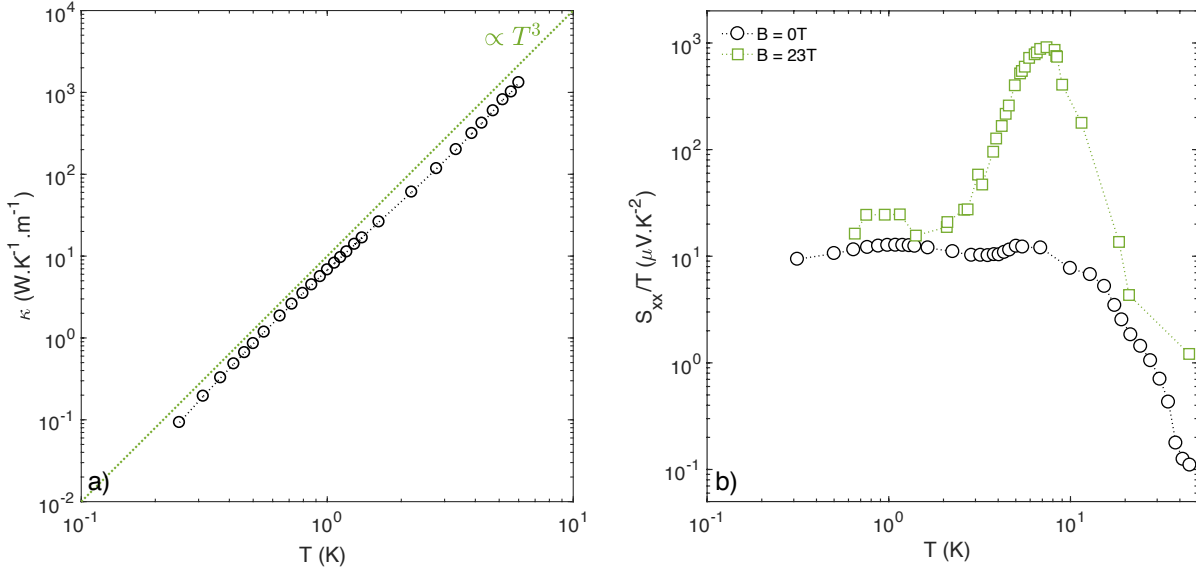


Fig. 4.11 **a)** Thermal conductivity  $\kappa$  plotted as a function of temperature in u-InAs. The green dotted line indicate a  $T^3$  dependence. **b)** Thermopower plotted as  $S_{xx}/T$  for applied magnetic fields  $B = 0\text{T}$  and  $B = 23\text{T}$ .

$$\frac{S_{xx}}{T} = \frac{\pi^2}{3} \left( \frac{k_B}{e} \right) \frac{1}{T_F} \quad (4.2)$$

The low temperature saturation of  $S_{xx}/T$  indicates that the diffusive contribution dominates the thermopower below  $T = 3\text{K}$ . We can compare the saturation value to the expected QP contribution in this regime, which is given by equation 4.2. With  $T_F = 130\text{K}$ , the diffusive contribution from equation 4.2 is expected to be  $S_{xx,th}/T = 3\mu\text{V.K}^{-2}$ , which is  $\approx 1/3$  of the measured value. This discrepancy can be associated the energy dependence of the scattering time associated with ionized impurity scattering.

**In-field** We turn to the evolution of the thermopower as a function of the magnetic field.  $S_{xx}/T$  is plotted as a function of  $B$  for various temperatures in figure 4.12.a. In the low magnetic field region,  $B < 4\text{T}$ , and at low enough temperature  $S_{xx}/T$  does not evolve with the magnetic field besides the presence of QO. These oscillations are damped with increasing temperatures. Once in the quantum limit,  $B > 4\text{T}$ , the thermopower starts increasing with magnetic field until it reaches a maximum, two orders of magnitude (at most) higher than the zero-field value. The position in field  $B_{max}$  and amplitude  $A_{max}$  of this maximum depend on the temperature. For temperatures  $T < 8\text{K}$ ,  $B_{max}$  and  $A_{max}$  both increase with increasing

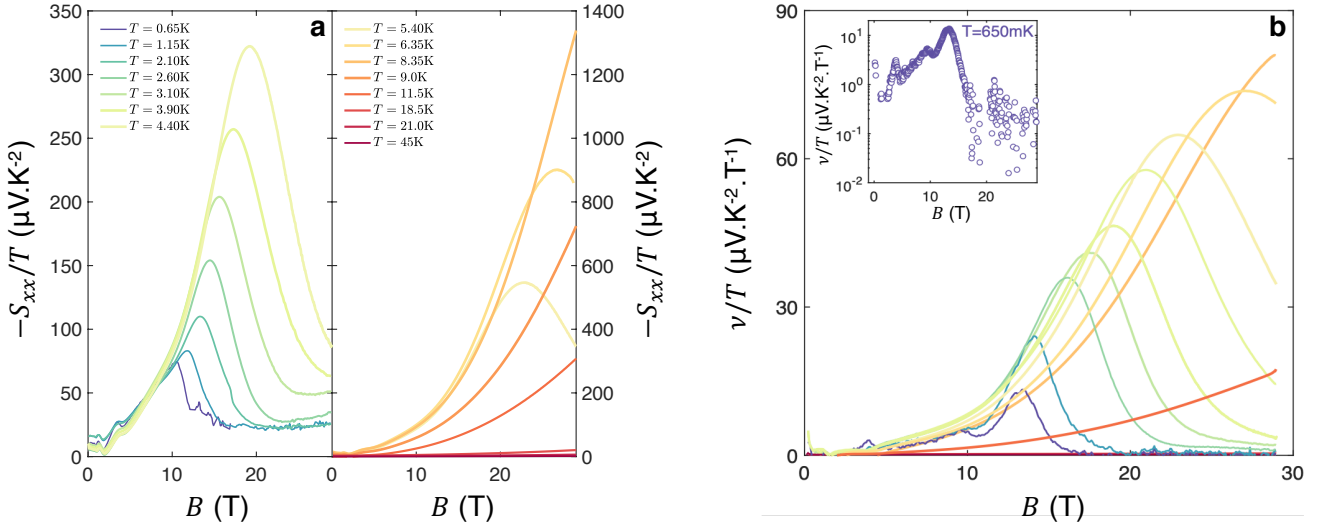


Fig. 4.12 **a**)  $S_{xx}/T$  plotted as a function of magnetic field for various temperatures. Temperatures are separated in two plots for clarity. **b**) Nernst coefficient, plotted as  $\nu/T$  as a function of magnetic field for various temperatures. The inset focuses the  $T = 650\text{mK}$  Nernst coefficient  $\nu/T$ . Both graphs share the same legend.

temperatures. On the contrary, for  $T > 8\text{K}$ ,  $B_{max}$  is not observed and  $A_{max}$  decreases with increasing temperature.

The main result of this section is the evolution of the thermopower upon further increase of the field. When  $B > B_{max}$ , the thermopower drops and reaches a quasi-constant and low saturation value. This is similar to the behavior of the resistivity presented in the previous section. The amplitude of the  $S_{xx}/T$  plateau is not temperature independent, contrary to our report on the saturation regime of  $\rho_{xx,zz}$ . The comparison of two samples from the same wafer with similar geometries shows that the  $S_{xx}/T$  plateau value is also sample dependent. In a second sample, the high-field thermopower changes sign and saturates at a negative value. This is highly reminiscent of the mismatch between the high-field saturation resistivities of different u-InAs samples.

The drop of the thermopower is surprising : for an insulator we expect  $S_{xx}/T \xrightarrow{B \rightarrow +\infty} +\infty$ . But instead, in the field-induced insulating state of u-InAs we observe  $S_{xx}/T \xrightarrow{B \rightarrow +\infty} 0$ . This result is another evidence that we are dealing with a 'non-trivial' insulator.

The increase in the thermopower caused by the magnetic field is emphasized in figure 4.11.b. Upon the application of a strong magnetic field,  $B = 23\text{T}$ , the temperature dependence of  $S_{xx}/T$  is transformed. At low temperatures,  $T < 2\text{K}$ ,  $S_{xx}^{B=23\text{T}}/T \approx 2S_{xx}^{B=0\text{T}}/T$ , i.e. a small increase of the thermopower. However, for  $T > 2\text{K}$ , the aforementioned peak in  $S_{xx}^{B=0\text{T}}/T$

is greatly enhanced and reaches  $S_{xx}^{B=23T}/T = 1000 \mu\text{V.K}^{-2}$  at  $T = 6.5\text{K}$ . This represents an increase by 2 orders of magnitude of the thermopower when  $B = 23\text{T}$  is applied. Upon further heating of the system, the thermopower falls and reaches a few  $\mu\text{V.K}^{-2}$  at  $T = 20\text{K}$ .

We now turn to the study of a second thermoelectric coefficient : the Nernst coefficient. This quantity was measured simultaneously as the thermopower. We define the Nernst coefficient  $v = S_{xy}/B$  and plot  $v$  as  $v/T$  in figure 4.12.b. We observe a behavior similar to the one of the thermopower. The Nernst signal presents a peak which amplitude and field of occurrence increase with increasing temperature up to  $T = 8.5\text{K}$ . At higher temperatures, the peak is suppressed and  $v/T$  decreases with increasing temperatures. After the peak, the signal vanishes.

To conclude, we report on low temperature vanishing thermopower and Nernst coefficient in u-InAs. This surprising behavior is a strong deviation from the expect thermoelectric tensor of a dilute metal in the deep quantum limit which can be illustrated by the case of  $\text{Bi}_2\text{Se}_3$  [86] or  $\text{PbSnTe}$  [87].

### 4.3 Discussion on the in-field transport properties of dilute metals

The reported dichotomy between in-plane metallic resistivity and out-of-plane insulating resistivity in graphite comes as a surprise. The energy spectrum of this semi-metal is entirely gaped, thus we do not expected the graphene planes to remain metallic after the DW-phase transition. The case of u-InAs serves as a good counter-example : the field-induced insulating behavior is observed in all geometries of transport. We will now discuss and compare the gap opening in these two systems pushed deep in their quantum limit.

#### 4.3.1 Study of the activated behavior

**u-InAs** We first focus on the evolution with temperature of the transverse and longitudinal resistivities of u-InAs in the field-induced state. To do so,  $\rho_{xx}$  and  $\rho_{zz}$  are plotted respectively in figure 4.13.a and b using a semi-logarithmic scale and as a function of  $T^{-1}$  for different applied magnetic fields.

We observe a linear dependence of both  $\log \rho_{xx}$  and  $\log \rho_{zz}$  as a function of  $T^{-1}$  at high temperatures. This behavior is found at all the magnetic fields showed here. Upon decreasing temperatures, we observe a saturation of  $\log \rho_{xx}$  and  $\log \rho_{zz}$ . This phenomenon corresponds to the previously indicated 'saturation' regime where a B-linear temperature-independent resistivity emerges in the deep quantum limit of u-InAs (discussed in Fig 4.9).

For temperatures high enough to avoid this saturation of the resistivity, the dotted line displayed in figure 4.13.a and b yields an adequate fit of the data to an Arrhenius law. This law describes the thermally activated conduction in the high temperatures range and is described in equation 4.3. The good quality of these fits, at each magnetic field, allow us to extract an activation gap from  $\rho_{xx}$  and  $\rho_{zz}$ .

$$\rho_{xx,zz} = \rho_{xx,zz}^0 \times e^{-\frac{\Delta}{k_B T}} \quad (4.3)$$

The evolution of this energy gap is plotted as a function of magnetic field in figure 4.13.c. We confronted the different data sets from different experiments we lead on different samples (PPMS, dilution fridge up to  $B = 17T$ ,  $B = 34T$  static in Grenoble and  $B = 56T$  pulsed in Toulouse) presented above. Good coherence was attained, leading to the reasonably small error-bars shown in figure 4.13.c.

We see that the activation gap opens up in both the transverse and longitudinal resistivities upon application of a magnetic field  $B > 4T$ . The gap then increases sub-linearly with increasing field up to  $B = 56T$  where it reaches  $\approx 4-5meV$ . We observe a slight mismatch between the two gaps : the gap determined from  $\rho_{xx}$  appears  $\approx 10$  to  $40\%$  smaller than the one determined from  $\rho_{zz}$ . The gap  $\Delta_{zz}$  also appears to open up at lower magnetic field,  $B \approx 4T$  while  $\Delta_{xx}$  starts increasing around  $B \approx 7T$ . This discrepancy should yet be considered small in light of the error-bars.

We can conclude that the field-induced state emerging in the deep quantum limit of u-InAs is accompanied by the smooth opening of an isotropic gap in the system. This gap grows larger as the field is increased and shows no clear sign of saturation up to  $B = 54T$  where it reaches close to  $\Delta = 5mev$  for both geometries.

**Graphite** We now turn to the temperature dependence of the in-plane and out-of-plane magnetoresistivity of graphite. We show  $R_a$  and  $\log R_c$  respectively as a function of  $T$  and  $T^{-1}$  for different magnetic fields in the first ordered state in figure 4.13.d and e. The out-of-plane data featured in 4.13.e were measured in pulsed field on a natural graphite sample (NG-3) up to  $B = 56T$  for different temperatures.  $R_c$  for sample NG-3 plotted as a function of magnetic field is featured in the annex.

We start with the in-plane resistance  $R_a$  in Fig 4.13.d. For  $B = 30T$  and  $B = 65T$ ,  $R_a$  increases linearly with increasing  $T$ . We can thus confirm that at both fields, the graphene planes do not show any insulating behavior : they present a metallic behavior with a T-linear magnetoresistance.

At the contrary, the c-axis resistance measured in another natural graphite sample, presented in 4.13.e shows a strong insulating behavior at high field. For all the fields considered,

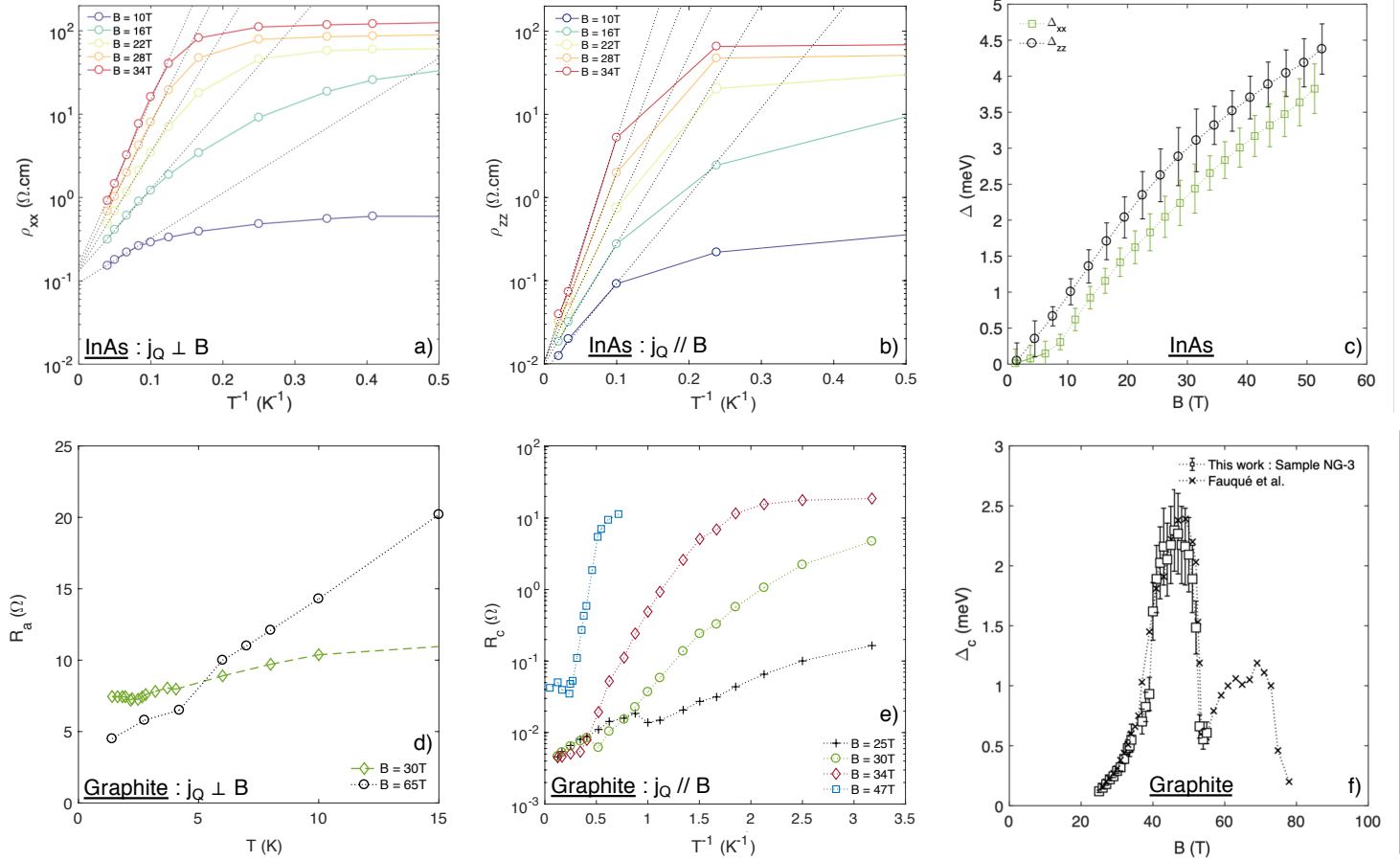


Fig. 4.13 **a)** **u-InAs**  $\rho_{zz}$  plotted as a function of  $T^{-1}$  in a semi-log scale for different magnetic fields. **b)** **u-InAs**  $\rho_{zz}$  plotted as a function of  $T^{-1}$  in a semi-log scale for different magnetic fields. In panels a and b the dotted lines correspond to a fit to an Arrhenius law. **c)** **u-InAs** Energy gap deduced from an Arrhenius law corresponding to the  $\rho_{xx}$  (a) and  $\rho_{zz}$  (b) data. **d)** **Graphite** In-plane resistance  $R_a$  of a natural graphite sample plotted as a function of  $T$  for different magnetic fields. Data plotted as function of magnetic field in the appendix. **e)** **Graphite** Out-of-plane resistance of natural graphite sample NG-3  $R_c$  plotted as a function of  $T^{-1}$  in a semi-log scale for different magnetic fields. **f)** Energy gap deduced from an Arrhenius law fit of the  $R_c$  data presented in panel (b) (sample NG-3) and data by Fauqué *et al.* [61]

we observe a linear in  $T^{-1}$  behavior of  $\log R_c$  over a finite temperature window in the ordered state. This linearity indicates an activated behavior of  $R_c$  which is then followed by deviations from the Arrhenius law at higher and lower temperatures.

On the low temperatures side, the deviation from the Arrhenius law implies the existence of a residual metallic conductance channel along the c-axis : Fauqué *et al.* proposed the existence of an edge state to account for this phenomenon. We will further discuss this result in a next section. On the other hand, at high temperatures, the out-of-plane resistance also saturates. This result can be associated to a residual contribution from the graphene planes : as the temperatures increases their conductivity increases and thus the decreasing c-axis resistance is buried by the in-plane pollution.

The two saturation regimes left aside, we can extract the activation gap from  $R_c$  and present it as a function of the magnetic field in figure 4.13.f. We also feature the data determined by Fauqué *et al.* [61]. We observe that the gap opens up around  $B = 25\text{T}$  and grows up to  $\Delta = 2.5\text{ meV}$  at  $B = 47\text{T}$  before closing down to  $\Delta = 0.5\text{ meV}$  at  $B = 56\text{T}$ . Our results on the out-of-plane resistivity of graphite confirm the previous reports [59, 88–90, 63, 83, 61, 26].

We can conclude that an activation gap of a few meV opens up in the field-induced state of both graphite and u-InAs in the deep quantum limit. This feature is also observed in u-InSb [77–79] and  $\text{Hg}_{1-x}\text{Cd}_x\text{Te}$  [78, 80] in the quantum limit (non-exhaustive list). However, in u-InAs, we observe an insulating behavior for all geometries of transport studied, with a common high field saturation regime. This observation only makes the coexistence of in-plane metallicity and c-axis insulating behavior in the ordered state of graphite only more mysterious.

### 4.3.2 Electronic ground state of dilute metals in the deep quantum limit

The study of u-InAs and graphite in the quantum limit reveals the existence of a field-induced insulating state in both systems. In first approach, the two field-induced states may appears as similar. We will discuss this assumption in the next few lines.

In the case of graphite we observe a thermodynamic transition at  $B = 25\text{T}$  with the opening of an activation gap in the c-axis electrical conductivity while the graphene planes remain metallic. This feature has been linked to the formation of a charge-density wave transition resulting from the  $2k_F$  nesting process [64]. This field-induced state is destroyed at  $B = 53\text{T}$ . But this first ordered state is followed by a similar one at higher field, also successively induced then destroyed by the increasing magnetic field [61]. The observation of an activated

behavior in  $R_c$  while  $R_a$  remains metallic in both field-induced states is enigmatic. The coexistence of these two features for a bulk system with a fully gaped electronic spectrum points to the existence of a second channel of conduction in the system [61].

Our study of u-InAs also reveals the emergence of a field-induced insulating state in the deep quantum limit. The temperature dependence of the resistivity, in various geometries of measurement, indicates an activated behavior of the resistivity with an isotropic gap of a few meV, comparable to the amplitude of the gap we determined in graphite. Other dilute metals InSb and  $\text{Hg}_{1-x}\text{Cd}_x\text{Te}$  [78] reveal a field-induced phase transition to an insulating state. This field-induced state has been associated with the magnetic freeze-out regime : a Mott-Anderson transition induced by the magnetic field. But this study of u-InAs also suggests the existence of a metallic conduction channel at high magnetic field and low temperatures with the saturation regime.

Evidences points to the existence of a variety of fundamental states of a 3D electron gas in the quantum limit. While a common feature is to be a field-induced insulator with a fully gaped electronic spectrum, the anisotropic effect observed in graphite, when compared to u-InAs, indicates strong discrepancies in the fundamental state of both systems far in the QL. Yet, result point to a similar feature in both systems : the existence of an edge conduction channel.

### 4.3.3 Towards a second conduction channel in InAs ?

We will now discuss the possibility of the observation of a surface state in u-InAs. The study of  $\rho_{xx,xy,zz}$  has revealed the emergence of a saturation of the resistivity at low enough temperature and far in the field-induced state. All component of the resistivity tensor adopt a temperature independent behavior. But this result is in direct contradiction with the observation of a field-induced insulating state of the bulk which yields  $\sigma_{bulk} \propto e^{\frac{-\Delta}{k_B T}} \xrightarrow{T \rightarrow 0K} 0$ . A finite conductivity, in the  $T \rightarrow 0K$  limit implies the existence of a second channel of conduction, i.e a total conductivity written as 4.4.

$$\sigma_{total} = \sigma_{bulk} + \sigma_S \quad (4.4)$$

The observation of a vanishing thermopower in the same context is also puzzling. According to Mott formula, we expect for the bulk  $S \propto \frac{\partial \ln(\sigma)}{\partial \epsilon} = \frac{\Delta}{k_B T} \frac{\partial \Delta}{\partial B} \frac{\partial B}{\partial \epsilon}$ . As a consequence, we expect the thermopower of bulk u-InAs to behave as  $S_{bulk} \propto \frac{-\Delta}{k_B T} \xrightarrow{T \rightarrow 0K} \infty$  in the field-induced state. This is, for example, what was observed in the deep quantum limit of u-InSb which enters the same magnetic freeze-out regime [84] or in the case of  $\text{PF}_6$  [91]. This is prediction is in contradiction with our observation in u-InAs. However, the assumption

that two types of carriers with conductivity and thermopower  $(\sigma_{bulk}, S_{bulk})$  and  $(\sigma_S, S_S)$  exist gives a satisfactory explanation to our result. We note the aforementioned total conductivity  $\sigma_{total}$  and the total thermopower  $S_{total}$  (which is detailed in 4.5).

$$S_{total} = \frac{(\sigma_{bulk} \times S_{bulk} + \sigma_S \times S_S)}{\sigma_{total}} \quad (4.5)$$

As a consequence, for a bulk insulating state, we expect both  $\sigma_{total} \xrightarrow{T \rightarrow 0K} \sigma_S$  and  $S_{total} \xrightarrow{T \rightarrow 0K} S_S$ .

We propose this metallic contribution to be associated with a surface state in u-InAs. This explanation is coherent with the variation of the saturation values of both  $\rho$  and  $S_{xx}$  at high field from one sample to another (cut of the same wafer). The size and quality of the surface can will play a role in the the value of  $\sigma_S$  and  $S_S$ . Also, an ARPES (angle resolved photo-emission spectroscopy) study of u-InAs have proven the existence of a charge accumulation layer (n-type) at the surface of u-InAs [92].

In order to confirm, or infirm, the surface nature of transport in the QL of u-InAs, we propose the following experiments.

**Size-effect** It is the first obvious choice to probe the existence of a surface state. Changing the volume to surface ratio of u-InAs should affect the saturation regime if due to a surface contribution.

**Ionic liquid gating** Because the wafer has a high roughness, a solid gate would not yield a high enough electronic accumulation on the surface to affect its resistivity. However, by applying a voltage between a drop of electrolyte and the surface of u-InAs on which the drop sits, a large electric field of the order of  $10 \text{ MV.cm}^{-2}$  is created at the interface drop/u-InAs thanks to the formation of an electric double layer [93]. One can reach charge density accumulations as high  $10^{15} \text{ cm}^{-2}$  through this technique far beyond the limitations of dielectric solid gating. In u-InAs nano-wires, this technique showed a clear change from semiconductor to quasi-metallic behavior [93].

**Corbino disk geometry** Finally, we propose to turn to non-local transport measurements to isolate the alleged surface contribution in u-InAs from the bulk contribution. The use of a 'Corbino disk' geometry has been successfully developped and used to separate bulk and surface contributions to the electrical resistivity in the case of  $\text{SmB}_6$  [94] and further developped for 3D topological insulators [95]. We point to the experimental protocol of Syers *et al.* for development [94].

We can conclude that the high-field behavior of u-InAs shows signatures of a second and metallic conduction channel. The existence of a charge accumulation layer at the surface of this compound points to the existence of a surface state. However, we have not reported on unambiguous observation of this surface state in u-InAs yet. This remain an open question for experimentalists.

## 4.4 First Conclusion

The magnetic field is expected to induce a many-body gap in a metal brought beyond its quantum limit. Our experimental study of the conductivity tensors of u-InAs and graphite in the deep quantum limit shows evidence of this prediction : we observe the opening of an activation gap in both systems. However, there are crucial differences between the ground states of these 3D metals beyond the QL. First, there is a succession of field-induced states, i.e. gap closing, in graphite whereas in the case of u-InAs only one phase transition is observed and the gap increases monotonously up to  $B = 56\text{T}$ . Second, a gap opens up in the transverse, longitudinal and Hall resistivity of u-InAs while we observe a field-induced c-axis insulating state with coexistent in-plane metallicity in graphite. We conclude that there is no ubiquitous ground state for a 3D metal in the QL, but rather there is a variety of ground states determined by the specific properties of each system. Yet, a common feature to 3D metals beyond the quantum limit was predicted : the existence of edge states [96, 97]. In the case of graphite, a conductive edge state was proposed to account for the in-plane metallicity [61]. In u-InAs, we report on the observation of a temperature independent B-linear magnetoresistance accompanied by vanishing thermoelectric coefficients at high field. This result is coherent with the presence of a charge accumulation layers on the surface and makes the existence of an edge channel in graphite even more unique.

To conclude, our work illustrates that the variety of fundamental ground states for a 3D electron gas beyond the quantum limit makes a great playground for condensed matter physicists which lead to discoveries such as the most expected 3D quantum Hall effect in  $\text{ZrTe}_5$  [98] or new states of matter in Weyl semimetals [99].

# Chapter 5

## Charge and Entropy transport in $WP_2$

---

### Résumé du chapitre

*Ce chapitre est dédié à l'étude du transport électrique et thermique dans le diphosphine de tungsten ( $WP_2$ ). A travers des mesures de résistivité électrique et thermique, nous observons que la loi de Wiedemann-Franz est satisfaite à basse température ( $T < 2K$ ) dans ce semimetal. Cependant, une augmentation de la température du système engendre une forte dichotomie entre transport de charge et de chaleur. Ce phénomène se manifeste par une déviation du nombre de Lorenz par rapport à la constante de Sommerfeld. Cette déviation est maximale à  $T = 13K$ . Cette inégalité entre transport de charge et de chaleur à température finie est universelle aux systèmes métalliques, elle résulte des processus de diffusion inélastiques qui affectent les électrons. Son amplitude dans  $WP_2$  est cependant largement plus grande que dans la plus part des autres métaux. Afin d'expliquer l'origine de cette forte déviation, nous avons étudié séparément les différentes composantes de la résistivité électrique et thermique, chacune étant associée à un processus de diffusion spécifique. Notre étude relève qu'il existe un facteur 5 entre le préfacteur du terme de diffusion interélectronique de la résistivité électrique et celui de la résistivité thermique. Cette différence est à l'origine du fort contraste entre transport de charge et de chaleur observé dans  $WP_2$ . Nous associons cet écart à une abondance particulière de processus de diffusion inter-electroniques à petit angle, particulièrement favorisés par la topologie de la surface de Fermi de  $WP_2$ . Motivés par notre étude, des résultats théoriques ont démontré qu'un fort écrantage des électrons dans un semimetal permet un ratio de Lorenz arbitrairement bas, c'est à dire une déviation de la loi de Wiedemann-Franz à température finie arbitrairement grande. Nous concluons*

*que le très grand écart à la loi de Wiedemann-Franz observé à température finie dans WP<sub>2</sub> s'explique dans un cadre semi-classique.*

---

## Summary of the chapter

This chapter is dedicated to the study of the electrical and thermal resistivities of bulk single crystals of WP<sub>2</sub>. The comparison between these two quantities yields two main results. First, we observe the recovery of the Wiedemann-Franz law at  $T < 2\text{K}$ . Second, we measure a large finite temperature departure, maximal at  $T = 13\text{K}$ , from the aforementioned law. While the existence of inelastic scattering affecting electrons at finite temperature makes this deviation ubiquitous in metals, the comparison with its recorded amplitude in other metallic systems indicates that WP<sub>2</sub> features one of the largest heat/charge transport dichotomy of all bulk metals. To unriddle the origin of this large deviation, we separated both the electrical and thermal resistivities into additive separate contributions which we associated with either boundary, electron - electron or electron - phonon scattering. We concluded that the existence of a five-fold mismatch between the  $T$ -square prefactors of the electrical and thermal resistivities is the driving factor of the departure from the WFL. We associate this mismatch with an abundance of inter-electronic small-angle collisions, particularly favored by the topology of the Fermi surface of this material. Motivated by this study, theoretical work showed that strong screening of the electrons in a semimetal can lead to an arbitrarily small Lorenz ratio, i.e. confirmed the possibility of an arbitrarily large finite temperature deviation from the Wiedemann-Franz law in a semi-metal. We conclude that the large charge/heat transport dichotomy in WP<sub>2</sub> can be explained in a semi-classical framework.

---

## 5.1 Presentation of WP<sub>2</sub>

Throughout the following section we will introduce the material under scrutiny in this chapter : WP<sub>2</sub>. First we will present its fermiology, i.e its band structure and Fermi surface, then we will present previous reports on the transport properties of this compounds. Finally, we will focus on the geometry and orientation of the samples presented in this work.

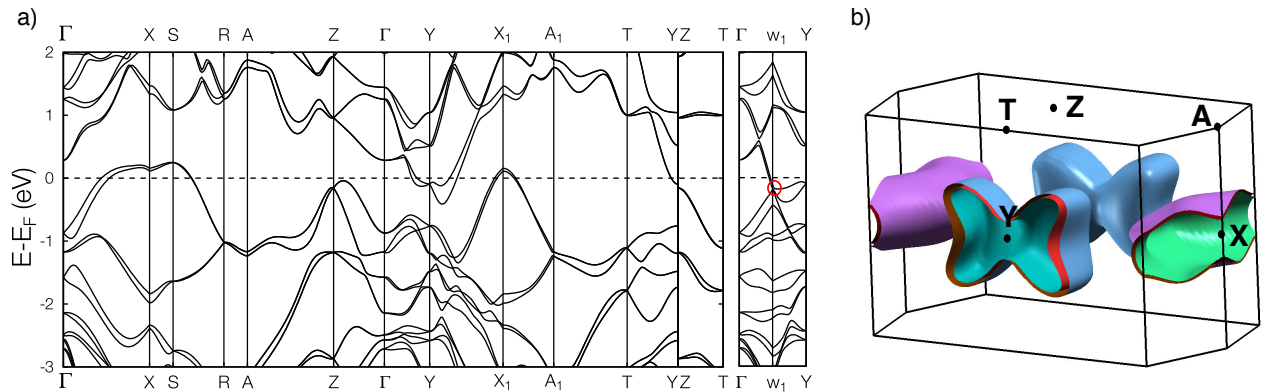


Fig. 5.1 **a)** DFT computed band structure of WP<sub>2</sub> along high symmetry direction of the Brillouin zone [100]. **b)** DFT-computed 3D Fermi Surface of WP<sub>2</sub> in the rectangular BZ.

### 5.1.1 Fermiology of WP<sub>2</sub>

Tungsten diphosphide WP<sub>2</sub> is a 3D material which crystallizes in an orthorhombic structure (namely the non-symmorphic Cmc2<sub>1</sub> space group). Each tungsten atom is surrounded by seven phosphorus atoms, six located at the corners of triangular prisms while the seventh stands outside one of the rectangular faces.

The electronic band structure of WP<sub>2</sub> was computed from first principles (DFT calculations lead by A. Subedi). The band structure is presented along the high symmetry directions of the Brillouin zone (BZ) in figure 5.1.a. It is in good agreement with previous calculations [100] and confirms the high compensation of WP<sub>2</sub> with a computed carrier concentration  $n = 2.5 \times 10^{21} \text{ cm}^{-3}$ . The Fermi surface (FS) associated with the electronic band structure is constituted of 2 hole and 2 electron pockets, all located at the Brillouin zone boundary. The FS in the first BZ is represented in figure 5.1.b. A close inspection of the band structure reveals the semimetallic nature of WP<sub>2</sub>, but also shows the presence of eight points in the  $k_z = 0$  plane where the valence and conduction bands touch. These points are located away from any high-symmetry line. The 8 points can be deduced from two non-equivalent points by mirror and time reversal symmetry. These two non-equivalent gap closing points are indicated in the electronic band structure by a red circle on figure 5.1.a : they are respectively found at 0.471eV and 0.340eV below the Fermi surface. As a consequence, WP<sub>2</sub> was predicted to be a Weyl semimetal [100]. This has lead WP<sub>2</sub> to gather a lot of experimental attention in the recent years. The prediction was eventually confirmed experimentally [101].

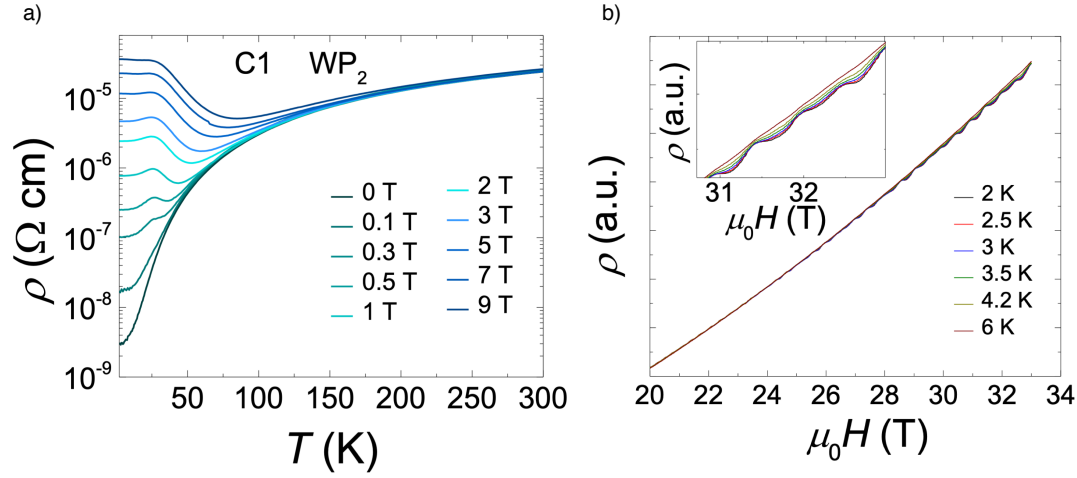


Fig. 5.2 **a)** Resistivity along the a-axis as a function of temperature for different applied magnetic fields. Sample is a needle-like single crystal of WP<sub>2</sub>. **b)** Magnetoresistance of WP<sub>2</sub> as a function of  $B$  in the high field region for different temperatures. Both datasets are from Kumar *et al.* [102]

### 5.1.2 Transport properties of WP<sub>2</sub>

Amongst these reports we find studies of the electrical resistivity. Needle-like single crystals of WP<sub>2</sub> were measured along the a-axis [102, 103]. The resistivity decrease from  $\rho(300\text{K}) = 40\mu\Omega\text{.cm}$  at room temperature to a residual term  $\rho(2\text{K}) = 1$  to  $10 \text{ n}\Omega\text{.cm}$ .  $\rho$  as a function of temperature is shown in figure 5.2.a. The WP<sub>2</sub> single crystals yield an impressively high room-temperature Residual Resistivity Ratio for a binary compound :  $(RRR) = \frac{\rho(300\text{K})}{\rho(2\text{K})} \approx 10000$ . This result indicates the high purity of the crystals. This allows the mean-free-path of the charge carriers, deduced from the residual resistivity,  $l_e = 0.5 \text{ mm}$ , to be comparable to the limiting dimension of the sample. WP<sub>2</sub> is thus a highly clean semi-metal in which charge carriers can reach a near-ballistic regime of transport at low temperature.

Another way to reveal a remarkable sample quality is to measure the magnetoresistance (MR) of this system. Reports on the MR of WP<sub>2</sub> samples are featured in figure 5.2.a [104, 102]. The MR follows a  $B^2$ -dependence up to  $B = 10\text{T}$  and reaches  $\text{MR} \approx 10^6\%$  at  $(T=2\text{K}, B=9\text{T})$ . This value is one order of magnitude higher than what has been recorded in WTe<sub>2</sub> [105] and comparable to reports on the magnetoresistance of small samples of Sb [106]. It implies a large electronic mobility in WP<sub>2</sub>. This result is confirmed by the observation of quantum oscillations in the high-field resistivity of this compound. We also

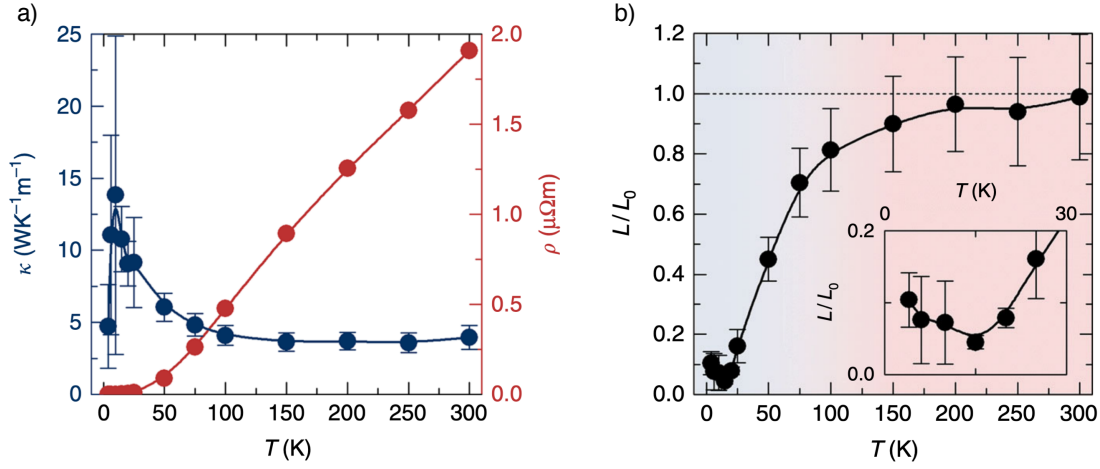


Fig. 5.3 **a)** Thermal conductivity (blue) and electrical resistivity (red) of a micro-ribbon of WP<sub>2</sub> measured by Gooth *et al.* [107]. **b)** Lorenz ratio  $L(T) = \kappa/T\sigma$  plotted as  $L(T)/L_0$  as a function of temperature.  $L_0$  is the Sommerfeld value of the Lorenz ratio. Inset shows a focus on the low temperature region.

indicate that there is a difference of 3 orders of magnitude between the transport and the Dingle mobility in this system [102].

The thermal transport properties of WP<sub>2</sub> have also been previously investigated [107]. Measurements were carried on a micro-ribbon ( $2.5\mu\text{m}$  wide) of WP<sub>2</sub> where the thermal conductivity, shown in figure 5.2.a, was measured with a 2-point setup (where the heaters also play the role of thermometers). The comparison with the electrical resistivity, shown in 5.2.a, reveals that the Lorenz ratio ( $L = \frac{\kappa}{\sigma T}$ ) holds an unprecedentedly large deviation from the Sommerfeld value at  $T = 11\text{K}$  with no sign of low temperature recovery of the Wiedemann-Franz law (WFL) down to  $T = 5\text{K}$  (Fig 5.2.b). This strong dichotomy between heat and charge transport in WP<sub>2</sub> was associated with the emergence of a hydrodynamic regime of electrons [107]. This result motivated us to study the thermal conductivity of bulk single crystals of WP<sub>2</sub> in a 4-point geometry.

### 5.1.3 Samples presentation

The samples measured in this study were 3 needle-like single-crystals grown along the  $a$ -axis. They presented very similar dimensions :  $(1-2 \times 0.1 \times 0.1) \text{mm}^3$ . The samples are similar to those detailed in [102] : they were grown by chemical vapor transport. Starting materials were red phosphorous (Alfa-Aesar, 99.999%) and tungsten trioxide (Alfa-Aesar, 99.998%) with iodine as a transport agent. The materials were taken in an evacuated fused silica

ampoule. The transport reaction was carried out in a two-zone-furnace with a temperature gradient of  $1000^\circ\text{C}$  ( $T_1$ ) to  $900^\circ\text{C}$  ( $T_2$ ) for several weeks. After reaction, the ampoule was removed from the furnace and quenched in water. The metallic needle-like crystals were later characterized by X-ray diffraction.

The samples were contacted with  $10\ \mu\text{m}$  diameter Pt wires fixed with silver paste. The contact resistance were sub-Ohmic. The sample was then setup to our home-made PPMS-compatible stick which has been presented in chapter 2. All measurements took place in a PPMS with  $j \parallel (a\text{-axis})$  for both heat and electrical currents. The electrical and thermal resistivities were measured with the same setup while the residual magnetic field present in the magnet was carefully suppressed during the measurements by a slow field sweep of a resistivity.

## 5.2 Experimental results - $\text{WP}_2$

We will now report on the experimental determination of both the electrical resistivity and thermal conductivity of a bulk single crystal of  $\text{WP}_2$  along the a-axis and down to  $T = 2.0\text{K}$ .

### 5.2.1 Temperature dependence of the electrical resistivity

**Zero-field** Figure 5.4.a shows the resistivity as a function of temperature in a  $\text{WP}_2$  single crystal. In the absence of an external magnetic field, we observe a decrease of the resistivity with decreasing temperature down to  $T = 2\text{K}$ .

The residual resistivity  $\rho_0$  of this sample is  $\rho_0 = 4.8\text{n}\Omega\cdot\text{cm}$  which yields a RRR of  $(RRR) = \rho(300\text{K})/\rho(2\text{K}) = 9600$ . The residual resistivities  $\rho_0$  of the 3 different samples were found to lie between 4 and 6  $\text{n}\Omega\cdot\text{cm}$ . Besides the variations of the residual term, no detectable difference in the temperature dependence of the resistivity was found between the different samples. For clarity reasons we will only feature the data from one of the three samples in the following study.

At  $T = 2.0\text{K}$  we can determine the electronic mean-free-path  $l_e$  and compare it to prior reports. With a carrier density of  $n = 2.5 \times 10^{21}\ \text{cm}^{-3}$  (from QO) and assuming in first approximation the effective mass of the charge carriers to be  $m_0$  (which is a reasonable approximation for all pockets [102]), we can compute  $l_e$  in the low temperature region from Drude model 5.1. We reach  $l_e \approx 80\ \mu\text{m}$ . This is to be compared to the sample limiting dimension  $\approx 100\ \mu\text{m}$ . We conclude that the charge carriers behave as ballistic quasiparticles at low temperatures in the sample under scrutiny.

$$l_e = \frac{\hbar k_F}{ne^2 \rho_0} \quad (5.1)$$

To further study the temperature dependence of the resistivity, we plot  $\rho$  as a function of  $T^2$  in figure 5.4.b. We observe that for  $T^2 < 100\text{K}^2$ , the resistivity varies linearly with  $T^2$  and can be fitted to a  $A_2 \times T^2$  term with  $A_2 = 16.6 \text{ p}\Omega\cdot\text{cm}\cdot\text{K}^{-2}$ . For  $T^2 > 100\text{K}^2$  we observe an upturn from the  $T^2$  behavior. We present  $\delta\rho_a = \rho - \rho_0 - A_2 \times T^2$  as a function of  $T^5$  in the inset of figure 5.4.b. We observe that the deviation from the  $T^2$  temperature dependence,  $\delta\rho_a$ , behaves as  $T^5$ .

**Field dependence** Upon application of a magnetic field of  $B = 10\text{T}$ , the resistivity increases by 4 orders of magnitude at  $T = 2\text{K}$  (Fig 5.4.a). The  $B = 10\text{T}$  resistivity then decreases with increasing temperature. Yet, it remains several orders of magnitude higher than the 0-field resistivity throughout the temperature range of this study.

We conclude that the electrical resistivity increases with increasing temperature, starting from the residual term  $\rho_0$ , following a  $T^2$  temperature dependence up to  $T = 10\text{K}$ . Above this temperature a  $T^5$  contribution emerges. Around  $T = 30\text{K}$  the resistivity becomes  $\rho \propto T^\gamma$  with  $\gamma < 5$  decreasing with increasing temperature up to  $T = 100\text{K}$  when finally  $\gamma = 1$ ; the resistivity of WP<sub>2</sub> becomes  $T$ -linear. We are thus able to separate the different contributions of the electrical resistivity of WP<sub>2</sub> between  $T = 2\text{K}$  and  $T = 30\text{K}$ . Also, we emphasize the large MR of this semi-metal. To pursue our study of the electronic transport properties of WP<sub>2</sub> we now turn to its thermal conductivity.

## 5.2.2 Temperature dependence of the thermal conductivity

In the following section we present data on the thermal conductivity  $\kappa$  of the aforementioned bulk single crystal of WP<sub>2</sub>. The results are presented in figure 5.5.a.

We observe that the 0-field thermal conductivity increases with decreasing temperature, peaks at  $T = 7\text{K}$ , and decreases with further cooling of the sample. The application of a magnetic field  $B = 10\text{T}$  decreases the thermal conductivity by at least one order of magnitude over the temperature range of study.

To compare simply the electrical and thermal transport we define the thermal resistivity  $WT = \frac{L_0 T}{\kappa}$  where  $L_0 = 2.44 \times 10^{-8} \text{ W}\cdot\Omega\cdot\text{K}^{-2}$  is the Sommerfeld number.  $WT$  is expressed in  $\Omega\cdot\text{cm}$  and plotted as a function of  $T^2$  in figure 5.5.b. We observe that for  $T < 7\text{K}$  the thermal resistivity follows  $B_2 \times T^2$  with  $B_2 = 75.6 \text{ p}\Omega\cdot\text{cm}\cdot\text{K}^{-2}$ . For  $T > 7\text{K}$ , we observe an upturn from the  $T^2$ -dependence. The inset of figure 5.5.b shows this deviation,  $\delta WT =$

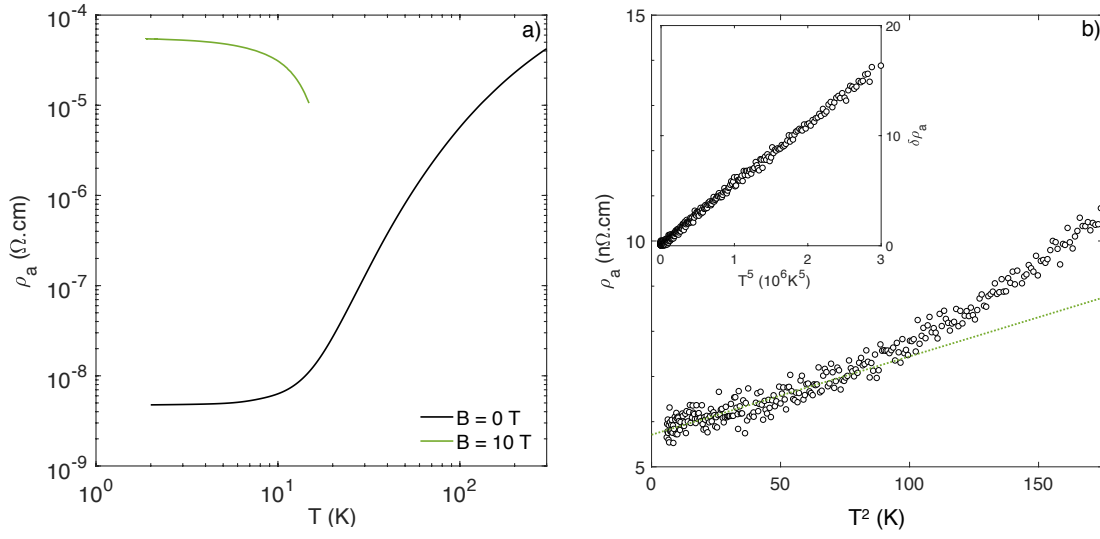


Fig. 5.4 **a)** Resistivity  $\rho_a$ , measured along the  $a$ -axis of a single crystal of WP<sub>2</sub> as a function of temperature for  $B = 0$  T and  $B = 10$  T. **b)** Resistivity  $\rho_a$  ( $\text{n}\Omega \cdot \text{cm}$ ) plotted as a function of  $T^2$ . Inset shows  $\delta\rho_a$  plotted as a function of  $T^5$  up to  $T = 20$  K.

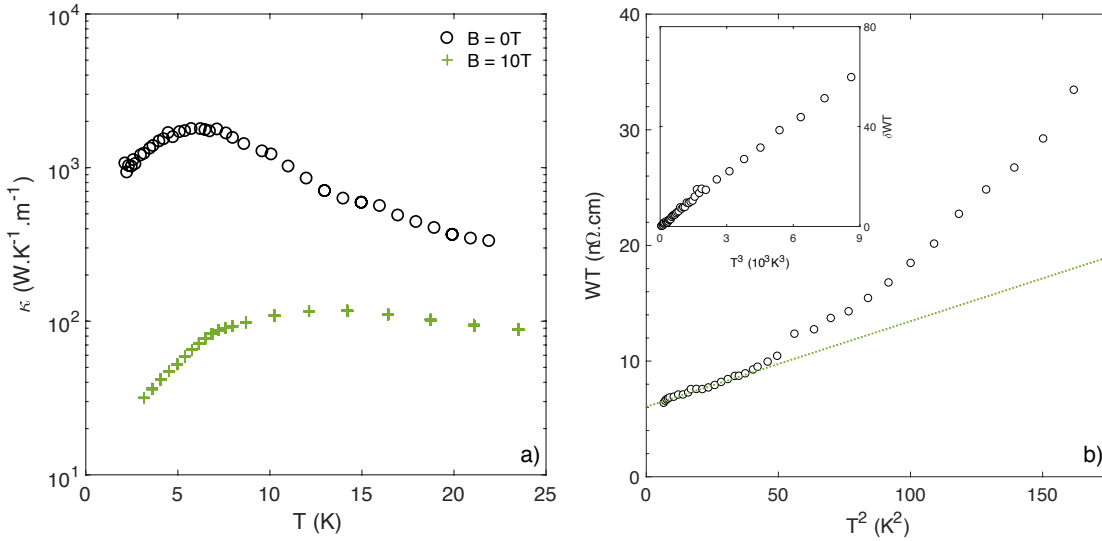


Fig. 5.5 **a)** Thermal conductivity  $\kappa$ , measured along the  $a$ -axis of a single crystal of WP<sub>2</sub> as a function of temperature for  $B = 0$  T and  $B = 10$  T. **b)** Thermal resistivity,  $WT = \frac{L_0 T}{\kappa}$ , as a function of  $T^2$ . The dotted line is a linear fit to the  $T < 8$  K data. The inset shows  $\delta WT = WT - W_0 T - B_2 T^2$  as a function of  $T^3$  expressed in  $\text{n}\Omega \cdot \text{cm}$ .

$WT - W_0T - B_2T^2$ , as a function of  $T^3$ . We can thus conclude that the upward deviation follows a  $T^3$  behavior.

We can summarize this section as the following : the thermal resistivity of bulk WP<sub>2</sub> shows a similar behavior than its electrical counterpart.  $WT$  can be broken down into a residual contribution  $W_0T$ , a  $T^2$ -dependent part which dominates up to  $T = 7\text{K}$  and a higher order term,  $B_3 \times T^3$  which controls the thermal resistivity at higher temperatures.

## 5.3 Discussion on the strong heat/charge transport dichotomy

In light of our measurements of the electrical and thermal resistivities of WP<sub>2</sub>, we will now discuss the experimental recovery of the Wiedemann-Franz law at  $T = 2\text{K}$  and the emergence of a strong finite temperature dichotomy between electronic charge and heat transport.

### 5.3.1 Phononic thermal conductivity

The thermal conductivity of a metallic systems results from various additive contributions : one from charge carriers, which we label  $\kappa_{electrons}$ , and another from phonons, named  $\kappa_{phonons}$ . Also, a third contribution due to ambipolar diffusion  $\kappa_{ambipolar}$  can be found. As we wish to compare the electronic heat and charge transport properties of WP<sub>2</sub>, we first need to separate  $\kappa_{electrons}$  from the other components of the total thermal conductivity. This section is dedicated to this process.

**Ambipolar term** Let us first show that an ambipolar contribution is negligible in WP<sub>2</sub>. It is instructive to recall the case of semimetallic bismuth, in which thermal transport is dominated by phonons. In such a compensated system, an ambipolar contribution to the thermal conductivity, arising from a counter-flow of heat-carrying electrons and holes was expected to be present [108, 109]. An ambipolar contribution would have led to an upward deviation of  $L/L_0$  from unity. However, Uher and Goldsmid [108] found (after subtracting the lattice contribution) that  $L/L_0 < 1$  in bismuth at finite temperature. This point to a negligible ambipolar contribution to the thermal conductivity of Bi at low temperatures. The reason is that the electron and hole gases are degenerate in Bi below room temperature, and thus the ambipolar contribution is small in proportion to  $T/E_F$  [7]. With strongly degenerate holes and electrons in WP<sub>2</sub> at low temperatures, we also expect no significant ambipolar heat transport in WP<sub>2</sub>. We conclude that in WP<sub>2</sub> :  $\kappa = \kappa_{phonons} + \kappa_{electrons}$ .

**Phononic thermal conductivity** We now turn to the thermal conductivity of lattice vibrations. We recall that WP<sub>2</sub> presents a large magnetoresistance. Precisely, the electrical resistivity at  $T = 2\text{K}$  increases by a factor  $10^4$  (Fig.5.4.b) when a magnetic field  $B = 10\text{T}$  is applied. According to the WFL, the electronic thermal conductivity  $\kappa_{electrons}$  decreases by the same order of magnitude. When  $B = 10\text{T}$  is applied to the sample, we observe in figure 5.5.a that the thermal conductivity is only reduced by 2 orders of magnitude. Since there are only two channels of heat conduction in the system, this result implies that  $\kappa(B = 10\text{T})$  is no other than  $\kappa_{phonons}(B = 10\text{T})$ . From the high-field thermal conductivity of WP<sub>2</sub> we are able to evaluate the thermal conductivity of phonons. We further assume that the thermal conductivity of phonons is, at the first order, independent of the field, i.e.  $\kappa_{phonons} \approx \kappa_{phonons}(B = 10\text{T})$

We can now compare  $\kappa_{phonons}$  and the total thermal conductivity at zero field. We observe that  $\kappa(B = 0\text{T}) \gg \kappa_{phonons}$ . As a consequence,  $\kappa_{electrons} \gg \kappa_{phonons}$  in the absence of an applied magnetic field. We can thus neglect the phonon contribution to the total thermal conductivity and assume that  $\kappa$  in this WP<sub>2</sub> sample is entirely electronic at zero field.

**Phonons mean-free-path** But we can also extract further information on the phonons in this system from the high field thermal conductivity. We know that  $\kappa_{phonons}$  is related to the specific heat of phonons by equation 2.2. The heat capacity was studied experimentally, as part of this work [110], by Kumar *et al.* from the Max-Planck Institute in Dresden, Germany. The result is presented in figure 5.6.a.

Just like the thermal conductivity, the specific heat has an electronic and a phononic contribution. In order to derive the specific heat due to phonons only, without the exact phonon dispersion curve, we have to make an approximation. We will consider that for  $T \ll \theta_D$  with  $\theta_D = 445\text{K}$ , the Debye approximation is valid. It yields a  $T^3$ -dependent phononic specific heat. On the other hand, the electronic contribution takes the form of a  $T$ -linear term. We define the specific heat from both contributions in equation 5.2 :

$$C_p = \gamma T + C_3 \cdot T^3 \quad (5.2)$$

Figure 5.6.a presents the specific heat  $C_p$  plotted as  $C_p/T$  as a function of  $T^2$  from measurements in WP<sub>2</sub>. Below  $T = 4\text{K}$ , we are able to estimate both contributions. First, from the intercept with the y-axis we determine the electronic contribution  $C_{el} = \gamma T$ . Then the slope gives us access to the phononic contribution. We find  $C_3 = 6.62 \times 10^{-2} \text{ mJ} \cdot \text{mol}^{-1} \cdot \text{K}^{-4}$ . Also, the inset of Fig.5.6.a shows that the  $T^3$  contribution to the specific heat is suppressed at  $T \approx 40\text{K}$  as we head toward a saturating regime of  $C_p$ . The Dulong-Petit law is then recovered.

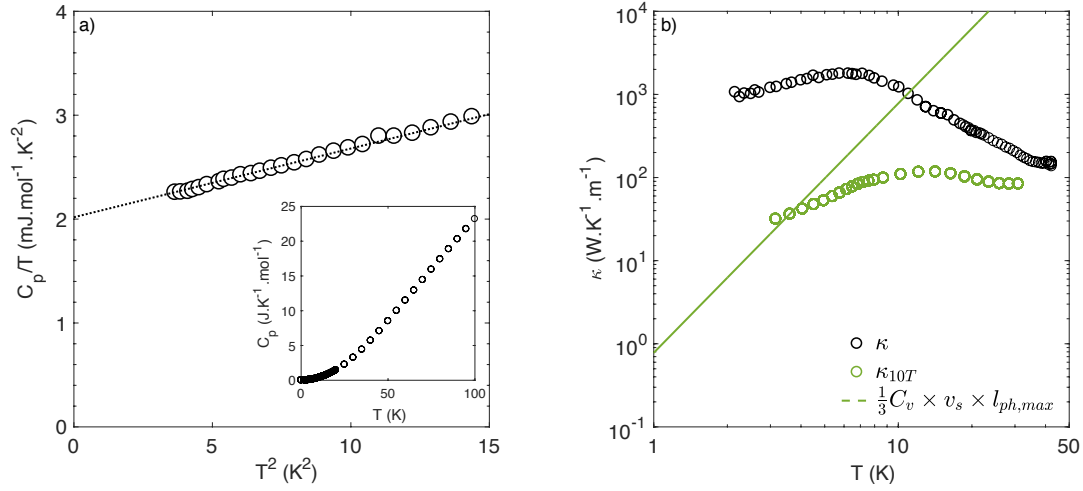


Fig. 5.6 a) Specific Heat plotted as  $C_p/T$  as a function of  $T^2$  for  $WP_2$ . The inset shows the specific heat plotted as  $C_p$  as a function of  $T$  up to  $T = 100K$ . b) Thermal conductivity,  $\kappa$ , as a function of temperature in  $WP_2$  for  $B = 0T$  (black dots) and  $B = 10T$  (green dots). The dotted line corresponds to the ballistic thermal conductivity of phonons in  $WP_2$ .

We have thus determined the specific heat of phonons in  $WP_2$ . Using equation 2.2, we can now determine the mean-free-path of phonons at low temperature in  $WP_2$ . To do so, we assume a speed of sound of  $v_s = 5000m.s^{-1}$  (similar to that of W). At  $T = 3K$ , we determine  $l_{ph} = 80\mu m$ . Since the limiting dimension of the sample is  $100\mu m$ , this result implies that phonons are close to the ballistic regime at  $T = 3K$ . The evolution of the thermal conductivity in the case of ballistic phonons is represented by the dotted line in figure 5.6.b. While a proximity to the ballistic regime of phonons is observed at  $T = 3K$ , upon increasing temperature a downward deviation from the ballistic regime emerges. This deviation is the result of Umklapp scattering of phonons, which eventually dominate transport at finite temperature and leads to the peak observed in  $\kappa_{phonons}$ , in figure 5.6.b, around  $T = 15K$ . The flow of phonons is then dominated by resistive collisions.

We come to the conclusion that for temperatures from  $T = 2K$  to  $T = 20K$ , the zero-field thermal conductivity of a  $(0.1 \times 0.1 \times 0.9) mm^3$  single crystal of  $WP_2$  due to charge carriers.

### 5.3.2 Temperature dependence of the Lorenz number

We have determined both the electrical resistivity and electronic thermal conductivity in  $WP_2$ . In order to compare both quantities, we define the Lorenz number  $L(T) = \frac{\kappa \rho}{T}$ .  $L(T)$  is plotted as  $L(T)/L_0$  as a function of temperature in figure 5.7. According to our data,  $L/L_0$  is close to 0.5 at  $T = 40K$  and decreases with decreasing temperature until it becomes as low as 0.25 at

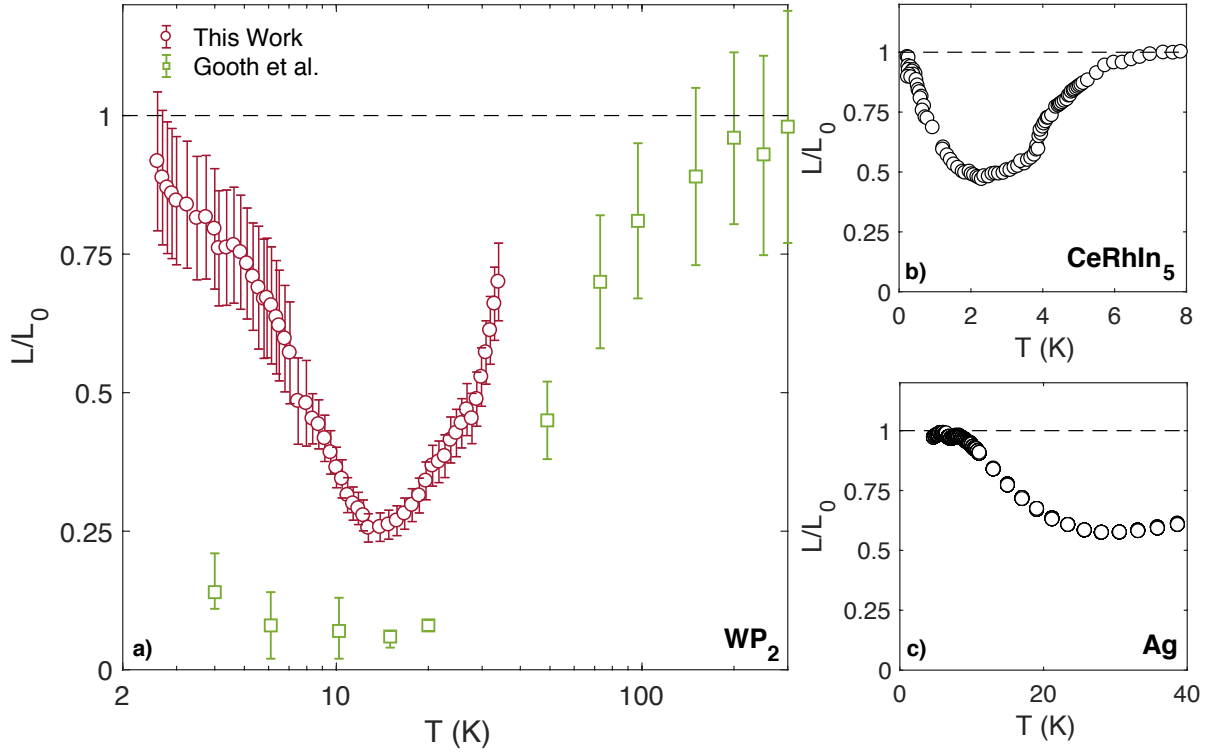


Fig. 5.7 **a)** Ratio of Lorenz,  $L(T) = \frac{\kappa}{T\sigma}$  to Sommerfeld  $L_0 = 2.44 \times 10^{-8} \text{ W}\cdot\Omega\cdot\text{K}^{-2}$ , numbers as a function of temperature (red). The data reported for a micro-ribbon of WP<sub>2</sub> [107] are shown in green. **b)**  $L(T)/L_0$  as a function of temperature in CeRhIn<sub>5</sub> [31]. **c)**  $L(T)/L_0$  as a function of temperature for an Ag wire with a  $50\mu\text{m}$  diameter and 99.99% purity. WP<sub>2</sub> and Ag were measured with the same experimental setup.

$T = 13\text{K}$ . This is in qualitative agreement with the observation originally reported by Gooth *et al.* [107], who first described the very low magnitude of the  $L/L_0$  ratio in WP<sub>2</sub>. However, the two sets of data diverge at low temperature and we recover the expected equality between  $L$  and  $L_0$ , i.e. an experimental verification of the Wiedemann-Franz law, at low temperature.

The comparison with two other metals, Ag and CeRhIn<sub>5</sub>, is instructive. Fig.5.7.b displays the temperature dependence of  $L/L_0$  in the heavy fermion antiferromagnet, CeRhIn<sub>5</sub> as reported by Paglione *et al.* [31]. The  $L/L_0$  ratio, close to unity at  $T = 8\text{K}$ , decreases with decreasing temperature and becomes as low as 0.5 at  $T = 2\text{K}$ , before shooting upwards and attaining unity around  $T = 100\text{mK}$ . In Ag, as seen in Fig.5.7.c which presents our data obtained on a silver wire, a similar downward deviation of the  $L/L_0$  ratio is detectable. Close to unity below  $T = 8\text{K}$ , it decreases with warming and attains a minimum of 0.6 at  $T = 30\text{K}$  before increasing again. Both Ag and CeRhIn<sub>5</sub> show smaller deviation than what we observe in WP<sub>2</sub>.

Similar behavior was also observed in high-purity Cu half a century ago [33], in other elements such as Al and Zn [34], in the heavy-fermion metals  $UPt_3$  [32],  $CeCoIn_5$  [111] as well as in magnetically-ordered elements like Ni [112] or Co [113]. Only W [114] showed a deviation with comparable amplitude to the one we report in  $WP_2$ .

As a conclusion for this section, while we recovered the Wiedemann-Franz law in bulk  $WP_2$  at low temperature, we measured a particularly large finite temperature deviation of the Lorenz number from the Sommerfeld value in  $WP_2$ :  $L/L_0 = 0.25$  at  $T = 13K$ . This deviation is larger than what was reported in any other metallic systems besides elemental tungsten (to the best of our knowledge).

### 5.3.3 Abundant small-angle resistive electron-electron scattering

To understand the amplitude of the deviation let's first discuss why we expect this downward departure in finite temperature metals in the first place. In the scattering-based Boltzmann picture, we have shown in chapter 2 that thermal and electrical transport are affected in different ways by inelastic collisions labeled as "horizontal" and "vertical" (see sketch in Fig.2.1.b).

But the deviation from the Wiedemann-Franz law observed in  $WP_2$  at finite temperature is larger than what has been reported in most of other metals. To explain this behavior we need to identify which small-angle scattering process affecting electrons is dominant.

On the microscopic level, we have shown that two distinct types of vertical scattering events can drive the Lorenz ratio down in a metal at finite temperature. The first is electron-phonon scattering [28] relevant in elemental metals whereas a second source of q-selectivity concerns momentum-relaxing electron-electron scattering [115]. This second route towards  $L(T)/L_0 < 1$ , is prominent in correlated metals [116, 117].

In order to determine what set of microscopic collisions causes the downward deviation from the WFL in  $WP_2$ , we identified and quantified the different contributions to the thermal and electrical resistivities of the system.

We have determined that both  $\rho$  and  $WT$  are  $T^2$ -dependent for  $T < 7K$  with distinct prefactors. An upward deviation from the low-temperature quadratic behavior occurs for both quantities, at different temperatures and in different fashions. The resistivities can be written as a sum of three distinct contributions that we identify as scattering of charge carriers by defects, electrons and phonons. We assume these scattering mechanisms to be additive. Note that since the data are limited to a temperature window in which  $T > \frac{\hbar}{k_B\tau}$ , no Altshuler-Aronov corrections are expected [117]. The expressions for  $\rho$  and  $WT$  become :

$$\rho = \rho_0 + A_2T^2 + A_5T^5 \quad (5.3)$$

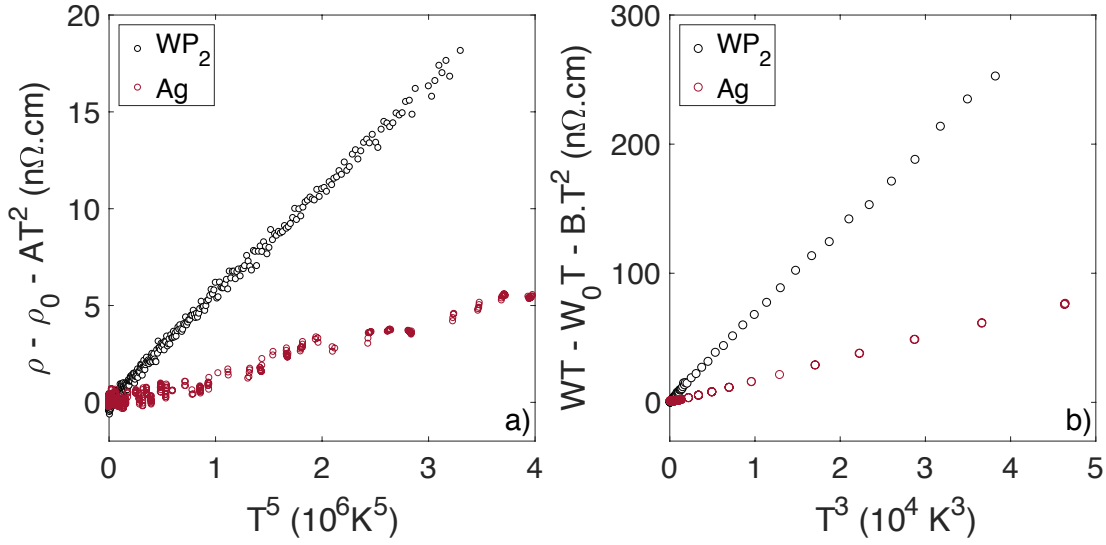


Fig. 5.8 a) Inelastic electrical resistivity  $\delta\rho$  caused by phonon scattering in WP<sub>2</sub> (Black) and Ag (Red) as a function of  $T^5$ . b) Inelastic thermal resistivity,  $\delta WT$ , in WP<sub>2</sub> (Black) and Ag (Red) as a function of  $T^3$ . The ratio of the two slopes is similar for heat and charge transport.

$$WT = W_0T + B_2T^2 + B_3T^3 \quad (5.4)$$

Our experimental results are in agreement with what is expected from equations 5.3 and 5.4, i.e. that  $\rho_0 = W_0T$  and  $A_2 \neq B_2$ .

It is now instructive to compare WP<sub>2</sub> and Ag to examine the possible role played by inelastic phonon scattering. Fig.5.8 compares the amplitude of the  $T^5$  terms in WP<sub>2</sub> and Ag. As seen in the Figure 5.8, the amplitude of both  $A_5$  and  $B_3$  is larger in WP<sub>2</sub>. More quantitatively,  $A_5(\text{WP}_2)/A_5(\text{Ag}) = 3.4$  and  $B_3(\text{WP}_2)/B_3(\text{Ag}) = 3.6$ . In other words, the  $B_3$  and  $A_5$  ratios of WP<sub>2</sub> and Ag are similar in magnitude, which implies that phonon scattering is not the origin of the unusually low magnitude of the Lorenz number in WP<sub>2</sub>.

Having ruled out a major role played by phonon scattering in setting the low magnitude of  $L/L_0$ , let us turn our attention to electron-electron scattering. As stated above, the prefactors of the T-square terms in  $\rho$  and  $WT$ , namely  $A_2$  and  $B_2$ , are unequal. The ratio  $A_2/B_2$  is as low as 0.22, well below what was observed in different metals, such as CeRhIn<sub>5</sub> ( $A_2/B_2 \simeq 0.4$ ) [31], UPt<sub>3</sub> ( $A_2/B_2 \simeq 0.65$ ) [32], or nickel ( $A_2/B_2 \simeq 0.4$ ) [112]. This feature pulls down the magnitude of the  $L/L_0$  ratio in WP<sub>2</sub>. It can be explained by unusually abundant vertical electronic events (involving a small change in the wave-vector of one of the colliding electrons). These could be either Umklapp or inter-band, involving collisions between hole-like and electron-like carriers belonging to different pockets.

The profusion of small-angle scattering is further confirmed, in the case of electron-impurity, by the observation of a strong discrepancy, up to 3 orders of magnitude, between

the transport and the Dingle mobility in this material [102]. This is presumably because of a very long screening length, weakening large-angle scattering and helping momentum conservation along long distances.

To have electron-electron collisions which are simultaneously small-angle, Umklapp and intra-band, one needs a Fermi surface component located at the zone boundary [118]. Interestingly, as seen in the 3D representation of the FS (Fig5.1.b) this is the case for WP<sub>2</sub>. Such a configuration allows abundant intra-band low-q Umklapp scattering. According to previous theoretical calculations [119, 103], the weight of small-angle scattering can pull down the  $A_2/B_2$  (and the  $L/L_0$ ) ratio. However, the lowest number found by these theories ( $\simeq 0.38$ ) is well above what was found here by our experiment on WP<sub>2</sub> ( $A_2/B_2 \simeq 0.22$ ), as well as what was reported long ago in the case of tungsten [114]. Nevertheless, following the present experimental observation, Li and Maslov showed [120] that in a compensated metal with a long-range Coulomb interaction amongst the charge carriers, the Lorenz ratio is given by equation 5.5, where  $\kappa$  is the (inverse) screening length and  $k_F$  is the (common) Fermi momentum of the electron and hole pockets. By assumption,  $\kappa \ll k_F$  and thus  $L/L_0$  can be arbitrarily small in this model.

$$L/L_0 = (\kappa/k_F)^2/2 \quad (5.5)$$

## 5.4 Conclusion on the heat/charge transport dichotomy of WP<sub>2</sub>

In summary, we found that WP<sub>2</sub> obeys the Wiedemann-Franz law at T = 2K but drastically deviates from it at finite temperature. The amplitude of the departure is higher than what is observed in most other metals. We recalled that this finite temperature dichotomy between charge and heat transport is universal in metallic systems because of small angle scattering. These collisions weaken heat conduction more intensely than they affect electrical conductivity. We found the exceptionally low magnitude of the  $L/L_0$  ratio to mirror the discrepancy between the amplitude of the T-square prefactors of the thermal and electrical resistivities. This observation yields that electron-electron scattering is at the origin of the exceptionally large downward deviation from the Wiedemann-Franz law in WP<sub>2</sub>. This can only happen if small-angle momentum-relaxing electronic scattering events are unusually frequent. These collisions are actually favored in WP<sub>2</sub> by the topology of the Fermi surface which is located at the boundary of the Brillouin zone. This semi-classical approach explains the large dichotomy between heat and charge transport that we measure in WP<sub>2</sub>. In the larger

picture, this study motivated theoretical work which concluded that, in a semi-metal, there is a priori no limit to the deviation from the Wiedemann-Franz law at finite temperature.

# Chapter 6

## Charge and Entropy transport in Antimony

---

### Résumé du chapitre

*Ce chapitre est dédié à l'étude du transport électrique et thermique dans différentes tailles d'échantillons d'antimoine (Sb). Malgré de précents rapports qui font état d'une des plus grandes magnétorésistances connue et de la possibilité pour les porteurs de charge d'entrer dans le régime ballistique à basse température, ce semi-métal n'a été que peu étudié.*

*Dans un premier temps, nous présentons l'évolution de la résistivité électrique en fonction de la température de  $T \approx 1K$  jusqu'à  $T = 30K$ . Nous observons que les collisions inter-électroniques dominent le transport électronique à  $T < 8K$ . La dépendance en taille des résistivité résiduelles et des préfacteur de la résistivité en  $T^2$  indiquent la proximité avec le régime ballistique à basse température.*

*Dans un second temps, nous nous sommes concentrés sur la conductivité thermique de Sb. Favorisée par la taille millimétrique des échantillons, la contribution phononique ne pouvait être ignorée dans Sb comme elle le fut dans WP<sub>2</sub>. Les deux composantes, électronique et phononique, ont été séparées quantitativement par une étude en champ. La partie électronique indique que la loi de Wiedemann-Franz est vérifiée dans Sb à  $T = 2K$  et subit une déviation due aux collisions électroniques à température finie d'une amplitude comparable aux autres métaux (sauf WP<sub>2</sub>). L'étude de différentes tailles d'échantillon révèle une dépendance en taille du ratio de Lorenz.*

*Enfin, nous avons isolé la composante phononique de la conductivité thermique. Nous rapportons l'émergence d'oscillations périodiques en  $1/B$  de  $\kappa_{ph}$  pour  $B > 5T$  entre  $T = 0.4K$*

*et  $T = 10\text{K}$ . Bien que ces oscillations rappellent les oscillations quantiques, il est impossible de leur associer une nature purement électronique sans induire une violation par plusieurs ordres de grandeur de la loi de WF. Leur origine se trouve plutôt dans l'absorption/emission de phonons par des porteurs de charges qui sont alors diffusés d'un niveau de Landau à un autre.*

---

## Summary of the chapter

This chapter is a report on the electrical and thermal conductivities of different sizes of elemental antimony samples. In spite of early work showing one of the strongest recorded magnetoresistance and an attainable ballistic regime of electrons at low temperatures, this semi-metal remains poorly investigated. We first report on the temperature dependence of the electrical resistivity between  $T \approx 1\text{K}$  and  $T = 30\text{K}$ . We observe that inter-electronic collisions dominate electrical transport for  $T < 8\text{K}$ . The prefactor of this  $T^2$ -resistivity evolves with sample size, as well as the residual resistivity, proving the proximity to the ballistic regime for low temperatures electrons. In a second time, we turn to the thermal conductivity of Sb. Favored by millimetric samples, the phononic contribution to the thermal conductivity could not be ignored in Sb as it was in  $\text{WP}_2$ . We separate the two contributions, electronic and phononic, by an in-field study of  $\kappa$ . The electronic fraction reveals that the WFL is satisfied in Sb below  $T = 2\text{K}$  and followed by a size-dependent finite temperature violation. The amplitude of this departure is comparable to most metals reported in the literature, i.e. half what we measured in  $\text{WP}_2$  (chapter 5). We show that this deviation is also associated with electronic collisions. Finally, we focus on the phonon component of the thermal conductivity. We report the existence of  $1/B$ -periodic oscillations of  $\kappa_{ph}$  for  $B > 5\text{T}$  between  $T = 0.4\text{K}$  and  $T = 10\text{K}$ . While these oscillations are reminiscent of quantum oscillations, a purely electronic origin would imply a violation of the WFL by several orders of magnitude. Rather, their origin is found on the absorption or emission of phonons by charge carriers which are scattered from one Landau level to another.

---

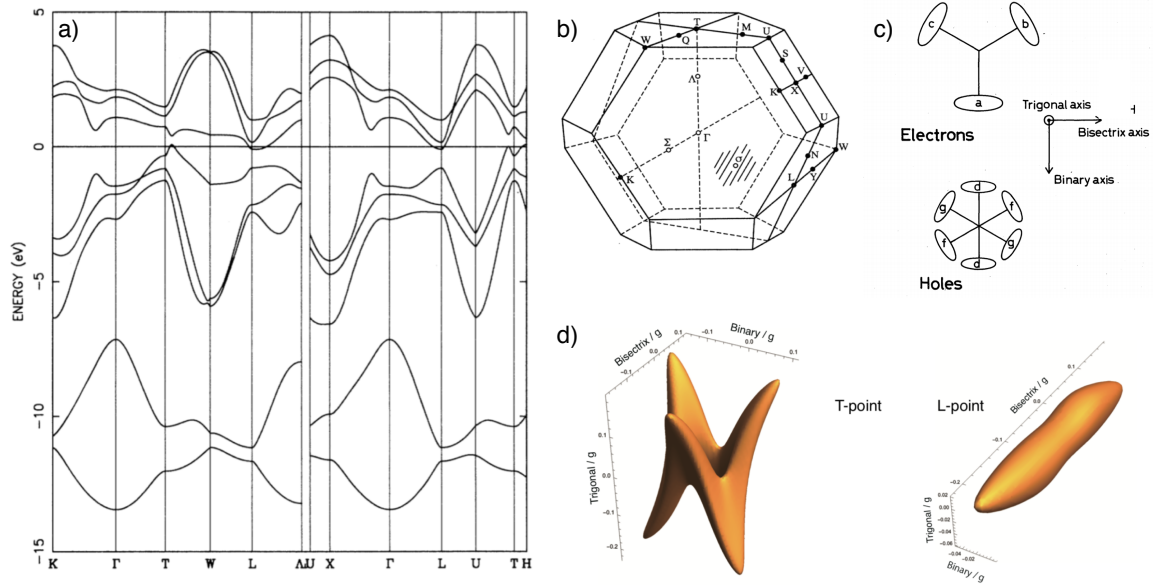


Fig. 6.1 **a)** Band structure of Sb along various symmetry lines from [121]. **b)** Brillouin zone for the rhombohedral structure. **c)** Representation of the Fermi surface of Sb from [122]. **d)** Fermi surface of the electron pockets (at the L-point) and hole pockets (at the T-point) according to the Liu and Allen [121] tight-binding model. Close to the T-point the 6 ellipsoids merge to form a unique object. Experimentally no evidence allows to conclude whether or not the ellipsoids merge.

## 6.1 Presentation of Antimony

We begin the corpus of this report by an introduction to the state-of-the-art electronic and transport properties of Sb. We will also present the different samples studied in the course of this project.

### 6.1.1 Fermiology of Sb

Antimony is a semimetal with a rhombohedral crystal structure. The band structure, determined from a third-neighbor tight-binding model [121] is represented in figure 6.1.a alongside the Brillouin zone for the rhombohedral structure (Fig.6.1.b). The ensuing Fermi surface (FS) of Sb is sketched in figure 6.1.c [122]. It is composed of three electron pockets centered at the L-point of the Brillouin zone and six hole pockets located in the (trigonal, bisectrix) plane in the vicinity of the T-point where they, following theoretical predictions, merge into a single object [123–125]. Yet, no experimental results allow to discriminate between 6 distinct ellipsoids and a single entity at the T-point.

Direction	$m_{electrons}$ ( $m_0$ )	$m_{holes}$ ( $m_0$ )
1'	0.093	0.068
2'	1.140	0.920
3'	0.088	0.050

Table 6.1 Mass tensor for the holes & electrons of Sb along the principal direction of the ellipsoids [106, 126]

Individually, the hole and electron pockets are anisotropic ellipsoids with one of the short axes oriented along the binary direction while the mean direction of the elongation is titled in the (trigonal, bisectrix) plane from the bisectrix direction.

The Fermi surface has also been intensively studied from an experimental standpoint through different probes. The high mobility of the carrier allows for the observation of quantum oscillations in the resistivity, thermoelectric tensor, magnetization and magneto-acoustic effect of Sb [124, 106, 125, 123]. The spectral analysis of the QO yields a Fermi surface in good agreement with the band calculations and a carrier concentration of  $n = 5.5 \times 10^{19} \text{ cm}^{-3}$  was deduced. As an example, QO measured in the Hall effect with ( $j \parallel$  bisectrix) and ( $B \parallel$  trigonal), which is the geometry on which we will focus on in this study, are shown in figure 6.2.c. The Fourier transform (FT) of these oscillations is also featured in figure 6.2.d. In this geometry, there are two main frequencies with comparable amplitudes which stand out :  $f_1 = 100\text{T}$  and  $f_2 = 380\text{T}$ . They are respectively associated with the hole pockets and the electron pockets [106].

Also, the study of the SdH effect [106] and the De Haas-van Alfen (dHvA) effect [124] in the trigonal-bisectrix plane revealed a planar anisotropy of the Fermi wavevector of 6.4 for electrons and 3.2 for holes. We can compare this anisotropy to the evolution of the effective masses of the carriers along the ellipsoid principal axis (1', 2', 3') from [126]. The results are featured in table 6.1. A mismatch between the anisotropy of the Fermi momentum and the anisotropy of the effective mass is observed. It was associated with a deviation from the ellipsoidal pocket for electrons and holes [106].

The high mobility of charge carriers in Sb results both of its semimetallic nature and its chemical simplicity [12, 127]. In millimetric samples, the mobility of charge carriers can attain  $\mu \approx 10000 \text{ m}^2 \cdot \text{V}^{-1} \cdot \text{s}^{-1}$  while smaller samples usually display a mobility of the order of  $\mu \approx 100 \text{ m}^2 \cdot \text{V}^{-1} \cdot \text{s}^{-1}$ . The latter is an order of magnitude higher than in graphite (discussed in chapter 3) and of the order of what we reported in  $\text{WP}_2$  (discussed in chapter 4). The combination of highly mobile charge carriers and a low electronic concentration in Sb leads to one of the largest recorded MR [106, 128, 129]. Contrary to other metallic

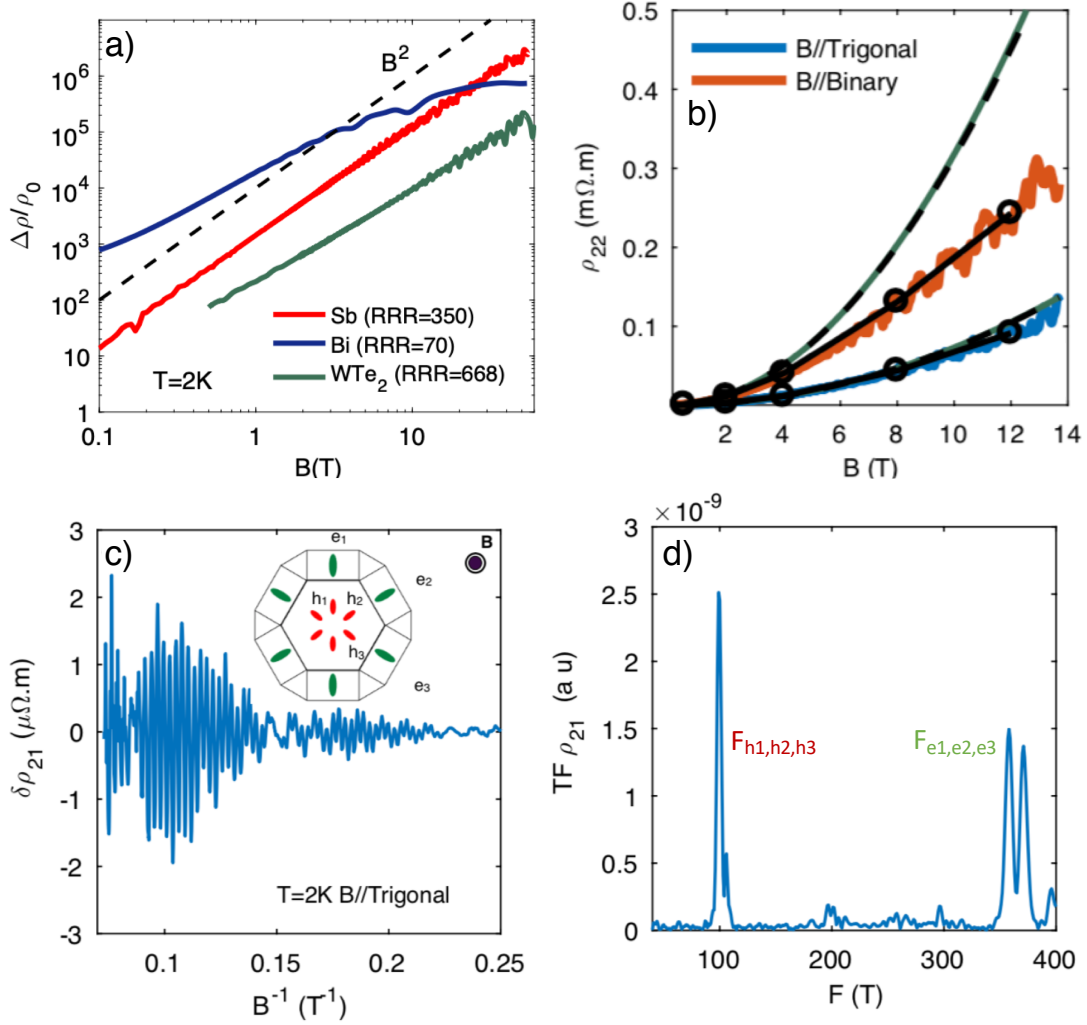


Fig. 6.2 **a)** Magnetoresistance of selected semimetals ( $(\rho(B) - \rho_0)/\rho_0$ ): Sb (red), Bi (blue) and  $\text{WTe}_2$  (green) as a function of magnetic field at  $T = 2\text{K}$  from [106]. The black line indicates a  $B^2$  behavior. **b)**  $\rho_{22}$  plotted here as a function of  $B$  in a linear scale [106]. Quantum oscillations appear for  $B > 3\text{T}$ . **c)** Oscillating part of the resistivity  $\delta\rho$  as a function of  $B^{-1}$  at  $T = 2\text{K}$ . The inset shows a sketch of the Fermi surface of Sb and the direction along which the field is applied. **d)** Fourier transform of the oscillations reported in (c).

systems, the magnetoresistance of Sb does not show signs of saturation up to  $B = 60\text{T}$ , as shown in figure 6.2.a. This observation can be explained by the almost perfect compensation of charge carriers. The deviation from perfect compensation was then evaluated from MR measurements and confirmed to be small :  $\Delta n/n$  ( $\Delta n/n \approx 10^{-3} - 10^{-4}$ ) [106]. Finally, the analysis of the QO allows us to determine the Dingle mobility  $\mu_D$  and compare it to the mobility  $\mu_\rho$  deduced from  $\rho_{22}$ . The ratio  $\mu_\rho/\mu_D$  reaching values up to 250 implies and indicates that small angle electron - impurity scattering is dominant in Sb [106].

Let's continue this presentation of the state-of-the-art transport properties of antimony with early reports on the thermal conductivity of millimetric Sb samples.  $\kappa$  was measured as a function of temperature and under the effect of an external magnetic field. An experimental determination of  $\kappa$  is featured in figure 6.3.a down to  $T = 4\text{K}$ . This experiment was conducted on a polycrystalline rod of diameter  $d = 5\text{mm}$  by White et al. [130]. The grain size was described by the authors as 'very much greater than 0.1mm'. The thermal conductivity was measured at  $B = 0\text{T}$  and upon application of an external magnetic field. These measurements lead to the separation of the electronic and phononic parts of the thermal conductivity of the rod. The electronic fraction showed that the Wiedemann-Franz law was roughly recovered at low temperature. The heat transported by the lattice waves was evaluated but poorly discussed in this first study.

Following reports nevertheless focused more on the phononic thermal transport properties of rods of Sb [131–133]. One result of particular interest is the observation by Long et al. of  $1/B$ -periodic oscillations of  $\kappa$ . Upon sweeping the magnetic field, after the initial drop of thermal conductivity at a few Teslas,  $\kappa$  starts to oscillate. This result is presented in 6.3 [132]. Because of their amplitude, the oscillations were not associated with oscillations of the electronic contribution to  $\kappa$  : a discrepancy of at least 3 orders of magnitude between the oscillations of  $\rho$  and  $\kappa$  emerges through the WFL. These oscillations were rather associated with the oscillation of the electronic density due to Landau quantization. Recent observations have showed the same oscillating behavior in wide variety of semimetals : Bi [134], Graphite [135], NbP [136] and TaAs [137]. These reports did not investigate these oscillations down to low temperature in a clear context of separation of the electronic and phononic thermal conductivities. So far, no agreement on the origin of this phenomenon has been reached.

### 6.1.2 Samples presentation

The Sb samples presented in this work are single crystals. The samples designated by #1 and #2 in table 6.2 were prepared in the same batch while sample #3 comes from a different provider. Sample #3 is a precisely cut slab however, samples #2 and #3 are bar-like with rough edges. These are the 3 samples we used to carry out the following study of the effect

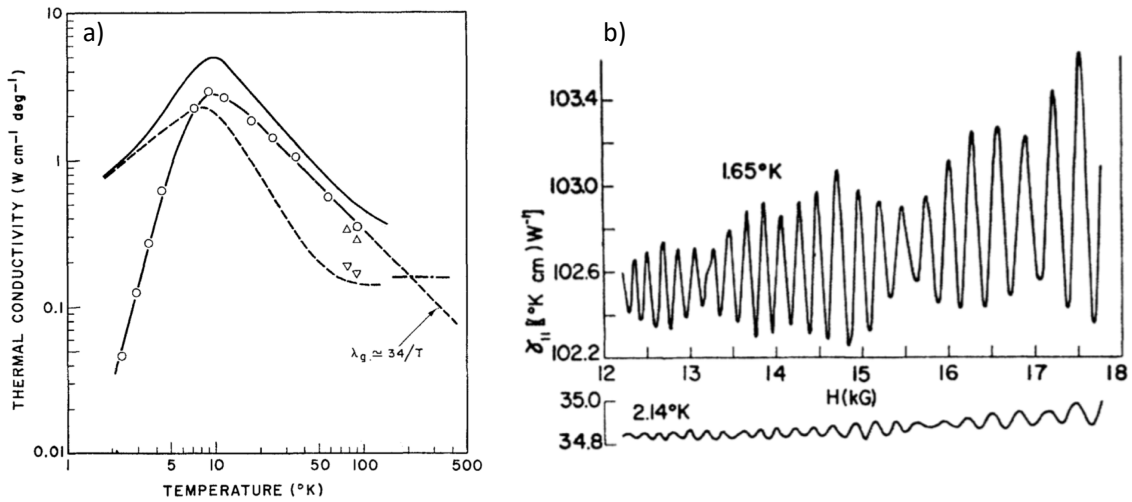


Fig. 6.3 **a)** Thermal conductivity as a function of temperature for a millimetric Sb sample. The full line corresponds to  $\kappa$ , the line with markers (circles) refers to  $\kappa_{ph}$  and the broken line is  $\kappa_e$ . The graph is from [130]. **b)** The high-field thermomagnetoconductivity  $\gamma_{11} = L_0 T / \kappa$  as a function of magnetic field. Graph taken from [132].

of size on the transport properties of Sb. The dimensions of the samples are presented in table 6.2. We define the cross section of the slabs by the following parameter :  $\bar{s} = \sqrt{w \times t}$  with width ( $w$ ) and thickness ( $t$ ). We will refer to the samples using the  $\bar{s}$  parameter.

## 6.2 Study of the electrical resistivity of Sb

In the following section we will present our results on the electrical resistivity of the different Sb samples. First, we will study the temperature dependence of the resistivity in absence of a magnetic field. In a second time we will report on the large magnetoresistance of the samples.

### 6.2.1 Temperature dependence of the resistivity

We report on the electrical resistivity as a function of temperature for the three previously presented Sb samples. Their resistivities along the bisectrix direction  $\rho_{22}$  are presented as a function of temperature in figure 6.4.a. The inset shows a sketch of the geometry and the orientation of the slabs. We emphasize that special attention was paid to suppress any residual magnetic field present in the superconducting magnet down to  $B = 10\text{Oe}$ .

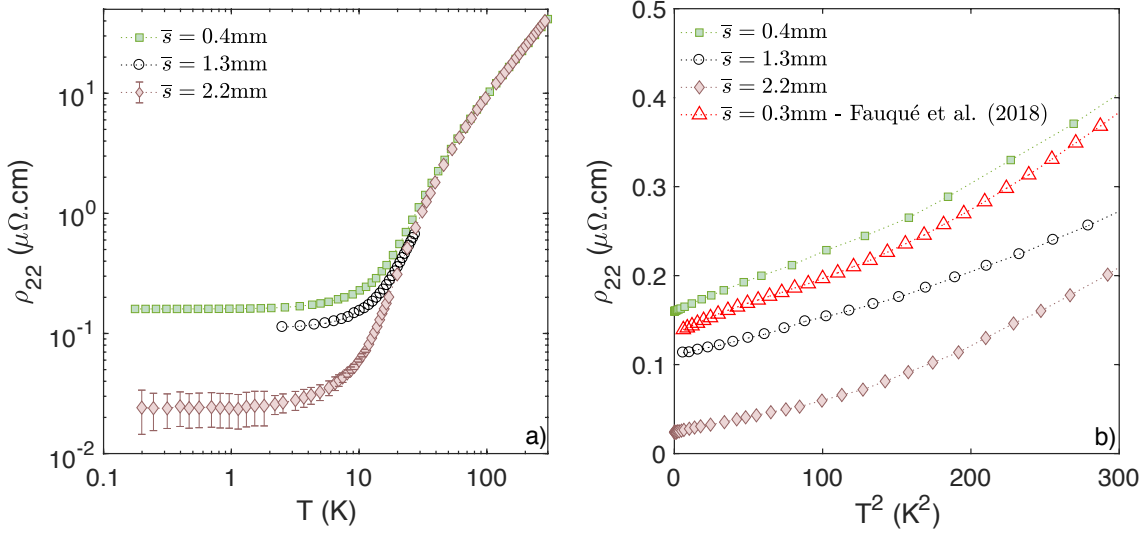


Fig. 6.4 **a)** Electrical resistivity along the bisectrix direction  $\rho_{22}$  as a function of temperature for three different geometries of Sb samples denoted by the  $\bar{s}$  parameter. The inset explicitly defines  $\bar{s}$  and the orientation of the crystals. Note that the  $\bar{s}=1.26$ mm sample displays irregular dimensions and poor orientation. **b)** The same  $\rho_{22}$  plotted here as a function  $T^2$ . The red markers refer to data from Fauqué et al. [106] with a sample geometry defined by  $\bar{s}=0.3$ mm.

Sample	Dimensions (mm <sup>3</sup> )	$\bar{s}$ (mm)	$\rho_0$ (nΩ.cm)	RRR	$l_e$ (mm)	$A_2$ (nΩ.cm.K <sup>-2</sup> )
S1	(0.3x0.5x4.1)	0.39	159	260	0.02	$0.70 \pm 0.03$
S2	(0.4x4x2.8)	1.26	110	370	0.04	$0.44 \pm 0.06$
S3	(1x5x10)	2.24	24.1	2000	0.11	$0.32 \pm 0.07$

Table 6.2 Electrical transport properties of the Sb samples.

All samples showed a room temperature resistivity  $\rho_{300K} = 41\mu\Omega.cm$ . From  $T = 300K$  to  $T = 25K$ ,  $\rho_{22}$  does not display any notable sample dependence. Upon further decrease of the temperature, the resistivity presents a size-dependent behavior. The residual resistivity ratio (RRR =  $\rho_{300K}/\rho_{2K}$ ) decreases as the size of the sample increases. The residual resistivities of the different samples, along with their RRRs, are presented in table 6.2.

We can now evaluate the low temperature electronic mean-free-path (mfp)  $l_e$ . It is determined through equation 5.1 with the following parameters :  $k_F$ ,  $\rho_0$  and  $n$ . To determine  $k_F$  and  $n$ , along the bisectrix, we rely on the known fermiology of the system. Using the carrier density determined from QO oscillations  $n = 5.5 \times 10^{19}cm^{-3}$  [106] we find an average Fermi wavevector  $k_F = 0.8nm^{-1}$  and  $E_F = 94meV$ . The values of  $l_e$  are presented in table 6.2.

As suggested by the size dependence of  $\rho_{22}$  below  $T = 25\text{K}$ , the value of the electronic mean-free-path reveals a proximity to the ballistic regime for low temperature charge carriers. This result is coherent with previous reports of ballistic transport in millimetric Sb samples with RRRs up to of the order of  $10^4$  [12].

We then pursued by investigating the inelastic contributions to  $\rho_{22}$  at finite temperature. The resistivity is plotted as a function of  $T^2$  in figure 6.4.b. For temperatures up to  $T \approx 10\text{K}$ , the resistivity shows a  $T^2$  behavior. It can be written as :  $\rho_{22} = \rho_0 + A_2 \times T^2$ . The value of  $A_2$  for the three different samples are listed in Table 6.2.  $A_2$  evolves with the sample size. This is the first main result of this chapter. The red line featured in Fig.6.4.b represents data from Fauqué et al. [106] for a sample of size  $\bar{s} = 0.3\text{mm}$  similar to our smallest sample of size  $\bar{s} = 0.4\text{mm}$ . We can observe that both samples, from different batches, show similar  $\rho_{22}$  temperature dependence. Above  $T = 10\text{K}$ , an upward deviation from the  $T^2$  behavior is observed in all different samples. This result is coherent with an increasing rate of inelastic electron - phonon scattering as the temperature is increased. The upturn, once removed from the residual and  $T^2$ -term, does not follow the  $T^5$  dependence which is expected in the Grüneisen model and remains an open question.

## 6.2.2 Study of the magnetoresistance

In the following section we report on the magnetoresistance of the three aforementioned Sb samples. We have measured the transverse magnetoresistance along the bisectrix direction for the small ( $\bar{s} = 0.4\text{mm}$ ) and large ( $\bar{s} = 2.2\text{mm}$ ) samples. Figure 6.5.a presents the magnetoresistance, defined as  $MR = \rho(B)/\rho_0$  at  $T = 100\text{mK}$ .

We first pinpoint the value of the magnetoresistance of the  $\bar{s} = 2.2\text{mm}$  sample :  $MR = 10^8\%$  at  $B = 9\text{T}$  and  $T = 2\text{K}$ . We can compare this value to previous reports on lower quality Sb samples ( $MR \approx 10^6\%$  at  $(2\text{K}, 9\text{T})$  in [106]), to other semimetals such as Bismuth [138],  $\text{WTe}_2$  [105, 139],  $\text{WP}_2$  [103, 102] and also to the III-V semiconductor InAs presented earlier in this thesis. To the best of our knowledge, we have recorded here the highest magnetoresistance of any bulk 3D system. The record breaking property of the  $\bar{s} = 2.2\text{mm}$  sample reflects its high purity and the high mobility of charge carriers.

The high electronic mobility of Sb is further underlined by the observation of quantum oscillations in the resistivity. Both  $\rho_{22}$  (current injected and voltage probed along the bisectrix direction) and  $\rho_{21}$  (current injected along the bisectrix direction and voltage probed along the binary direction) as a function of applied magnetic field are presented in figure 6.6.a and c. The  $1/B$ -periodic oscillations are a signature of the SdH effect. We were able to extract two QO frequencies,  $f_1 = 100 \pm 5\text{T}$  and  $f_2 = 380 \pm 20\text{T}$  through the Fourier transform of  $\rho_{22}$  (Fig 6.6.b) and  $\rho_{21}$  (Fig 6.6.d). While the two frequencies are visible in both geometries of

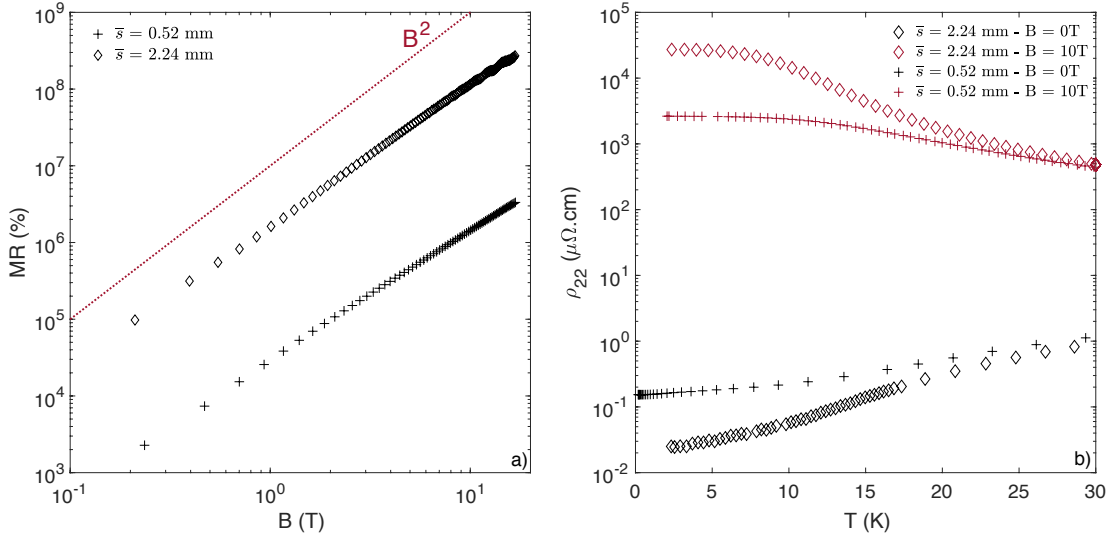


Fig. 6.5 **a)** Transverse magnetoresistance  $MR = (\rho(B) - \rho_0)/\rho_0$  as a function of magnetic field for two samples at  $T = 100\text{mK}$ . The red dotted line shows a  $T^2$  behavior. **b)**  $\rho_{22}$  plotted here as a function  $T$  for the small and large samples both at  $B = 0\text{T}$  and  $B = 10\text{T}$ .

measurement, the relative amplitudes of the high frequency and low frequency peaks differ. Both peaks show a comparable amplitude in the FFT of  $\rho_{21}$  whereas the  $f_1$  peak displays a larger amplitude than  $f_2$  in  $\rho_{22}$ . These results are coherent with previous observation by Fauqué et al. [106]. The low frequency,  $f_1$ , is associated with the hole pockets (for  $B$  applied along the trigonal axis) whereas the high frequency  $f_2$  corresponds to the electrons pockets (in the same configuration) [106, 126].

Finally we turn to the field dependence of the resistivity of sample  $\bar{s} = 2.2\text{mm}$ . It follows a  $B^{1.85}$  dependence, with no sign of saturation up to  $B = 17\text{T}$ .  $\rho_{22}$  of sample  $\bar{s} = 0.4\text{mm}$ , on the other hand, shows a  $B^{1.85}$  dependence up to  $B = 10\text{T}$ , which then starts to saturate upon further increase of the magnetic field. The field dependence goes down to  $B^{1.6}$  around  $B = 17\text{T}$ .

The temperature dependence of  $\rho_{22}$  for both samples in a static magnetic field of  $B = 10\text{T}$  was also studied. The results are featured in figure 6.5.b. The  $B = 0\text{T}$  data have been presented in Fig 6.4.a. We notice that upon application of a strong magnetic field,  $B = 10\text{T}$ , the temperature dependence of the resistivity  $\rho_{22}$  is modified : it decreases with increasing temperature. The magnetoresistance is also higher in sample  $\bar{s} = 2.2\text{mm}$  which is consistent with the data from Fig.6.5.a. Finally, we observe a saturation of  $\rho_{22}$  below  $T = 5\text{K}$  at  $B = 10\text{T}$ . We do not have magnetoresistance data on the  $\bar{s} = 1.3\text{mm}$  sample.

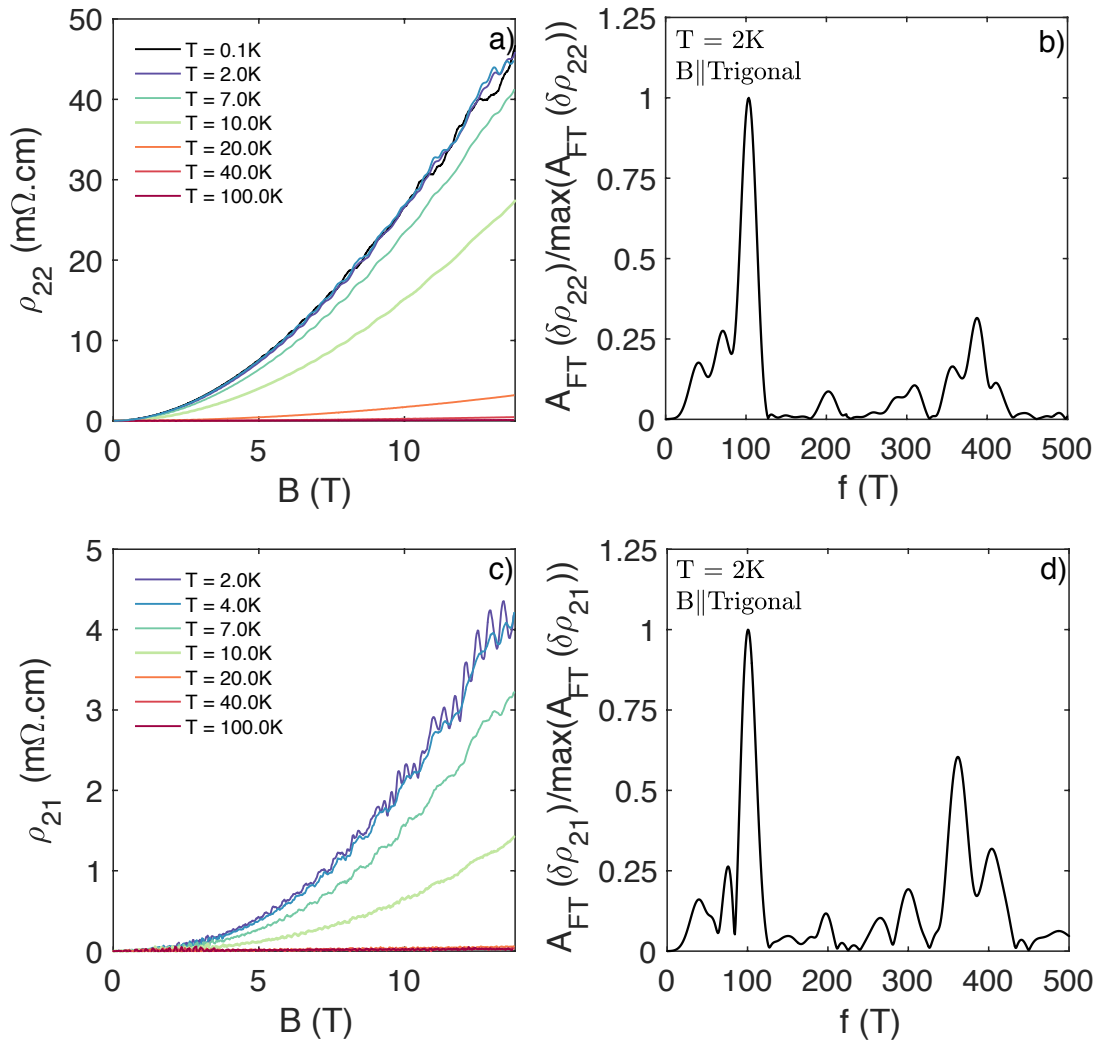


Fig. 6.6 **a)**  $\rho_{22}$  as a function of  $B$  for various temperatures in sample  $\bar{s} = 2.2\text{mm}$ . The magnetic field is applied along the trigonal direction. **b)** Fourier transform of  $\rho_{22}$  presented in a. **c)**  $\rho_{21}$  as a function of  $B$  for various temperatures in sample  $\bar{s} = 2.2\text{mm}$ . The magnetic field is applied along the trigonal direction. **d)** Fourier transform of  $\rho_{21}$  in c.

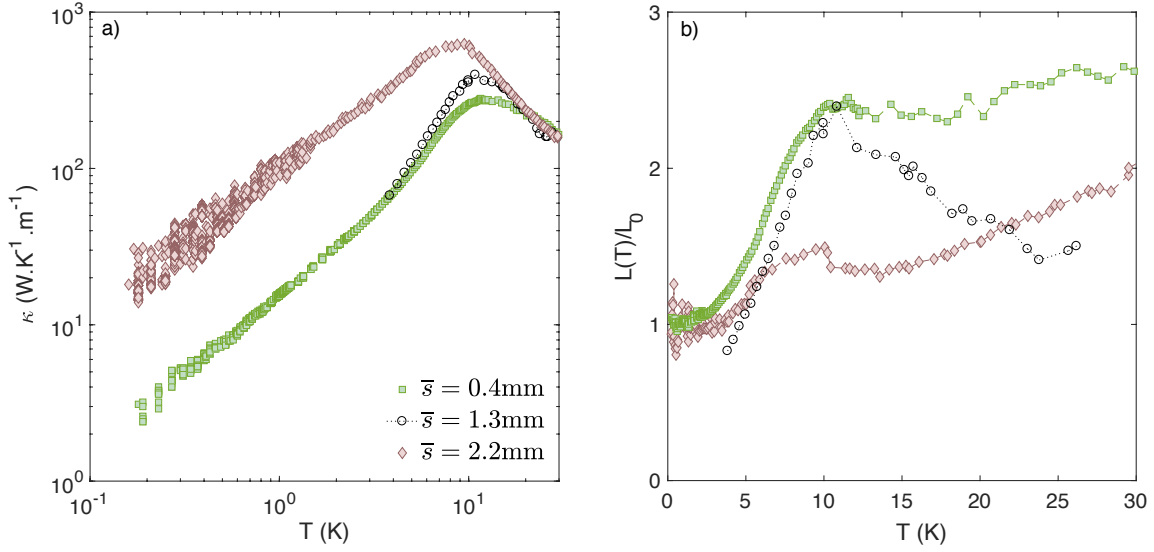


Fig. 6.7 **a)** Thermal conductivity  $\kappa$  plotted as a function of temperature for three different bulk Sb geometries. The measurements were done along the bisectrix direction of the samples. **b)** Lorenz ratio  $L(T) = \kappa\rho/(T.L_0)$  plotted as a function of temperature for the three samples. The same colormap is used in a and b.

### 6.3 Study of the thermal conductivity of Sb

This section is devoted to the main experimental result of this chapter, the experimental determination of the thermal conductivity of the three Sb samples along the bisectrix direction. We studied  $\kappa$  as a function of the temperature, the magnetic field and the sample size.

#### 6.3.1 The recovery of the Wiedemann-Franz law at low temperature

First of all let us compare the thermal conductivity and the electrical resistivity of these samples at low temperature to observe whether or not the Wiedemann-Franz law is recovered at low temperatures.

Figure 6.7 shows  $\kappa$  as a function of temperature for the three samples. The measurements were performed according to the experimental protocol presented in chapter 2, i.e. the standard one-heater-two-thermometers setup. Extra care was also given to suppress the residual magnetic field down to  $B = 5$  Oe. Measurements from  $T = 2$ K to  $T = 30$ K were performed on our home made PPMS-compatible stick while the temperature range  $T = 0.1$ K to  $T = 4$ K was done in a dilution fridge.

We observe that the three samples display similar thermal conductivities between  $T = 15$ K and  $T = 30$ K. However, upon decreasing temperature, the  $\bar{s} = 0.4$ mm sample deviates

and peaks around  $T = 11\text{K}$  before decreasing with further decrease of the temperature. The  $\bar{s} = 1.3\text{mm}$  sample reaches a maximal value at  $T = 9\text{K}$  whereas the largest sample,  $\bar{s} = 2.2\text{mm}$ , encounters a maximum in  $\kappa$  at  $T \approx 8\text{K}$ . For all three samples, the thermal conductivity decreases upon further cooling. The small and large samples show a  $T$ -linear behavior below  $T = 1\text{K}$ .

To simplify the comparison between electrical and thermal transport we introduce the thermal resistivity  $(WT) = L_0T/\kappa$ . From our measurements of both  $\rho_{22}$  and  $(WT)$  we can construct the Lorenz ratio  $L(T) = (\frac{\rho}{WT})L_0$  (as defined in chapter 1) and determine its evolution with temperature. The results are plotted in figure 6.7.b. We see that at high temperature  $L(T) > 1$  for all three samples. This indicates an upward deviation from the Wiedemann-Franz law. Upon decreasing temperature the Lorenz ratio decreases toward the validation of the Wiedemann-Franz law :  $L(T)/L_0 = 1$ . This condition is satisfied for the three samples below  $T = 1\text{K}$ . This result is given within experimental error represented by the cloud of points for each data sets. We are able to confirm from the raw thermal conductivity data that the Wiedemann-Franz law is recovered, within errorbars, below  $T = 2\text{K}$  in the different samples.

### 6.3.2 In-field Temperature dependence of the thermal conductivity

In the following section we show the evolution with temperature of the thermal conductivity when an external magnetic field is applied to the Sb samples.

Special care was taken to calibrate the thermometers at the specific magnetic field of the measurements (as detailed in chapter 2). Figure 6.8.a shows the thermal conductivity  $\kappa$  as a function of temperature for different magnetic fields applied to the  $\bar{s} = 0.4\text{mm}$  sample.

We observe a rapid decrease of  $\kappa$  upon application of an external magnetic field. This decrease is observed upon application of a magnetic field as small as  $B = 0.02\text{T}$  (see inset of Fig.6.8.a).  $\kappa$  then saturates for  $B > 0.6\text{T}$  in sample S1. We will refer to this floor value of the thermal conductivity as  $\kappa_{B\text{-saturated}}$ .

Figure 6.8.b presents  $\kappa_{B\text{-saturated}}$  for the three different samples of this study. Measurements were repeated for a variety (at least 5) of magnetic field for each sample until  $\kappa_{B\text{-saturated}}$  was determined unambiguously. We underline that  $\kappa_{B\text{-saturated}}$  is orders of magnitude smaller than  $\kappa$  in the sub-Kelvin region.

The three samples display similar behaviors when confronted to an external magnetic field. On figure 6.8.b we see that  $\kappa_{B\text{-saturated}}$  is size independent for temperatures  $T < 1\text{K}$  and  $T > 15\text{K}$ . Only when  $1 < T < 15\text{K}$  do we observe variations of  $\kappa_{B\text{-saturated}}$  between the three samples.  $\kappa$  displays a maximum at a sample-dependent temperature  $T \approx 8 - 15\text{K}$  before decreasing monotonously with further increase of the temperature. Below this maximum,

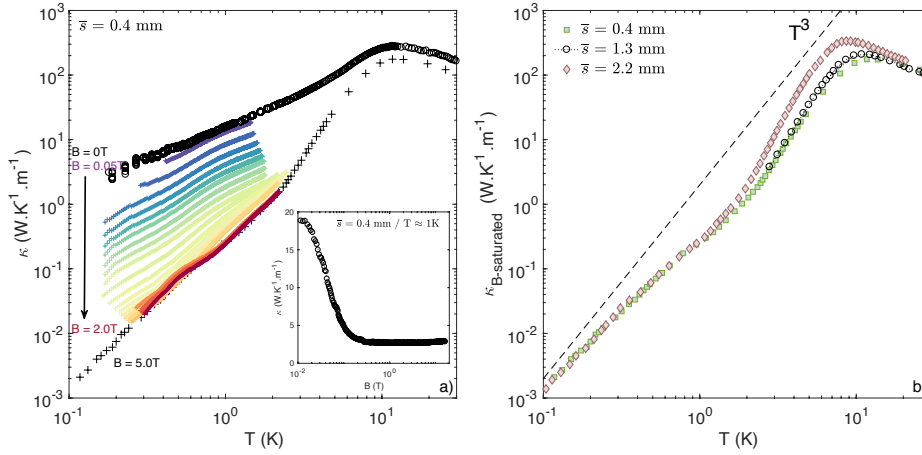


Fig. 6.8 **a)** Thermal conductivity  $\kappa$  plotted as a function of temperature for the small,  $\bar{s} = 0.4\text{mm}$  sample. Black circles represent  $B = 0\text{T}$  data whereas black crosses refer to  $B = 5\text{T}$  data. The color-map represents an increase of the magnetic field from  $B = 0\text{T}$  to  $B = 2\text{T}$  with a step of  $B = 0.05\text{T}$ . Above  $B = 1.4\text{T}$  there is no visible difference in the temperature dependence of  $\kappa$ . Inset shows  $\kappa$  as a function of  $B$  for the same sample at  $T \approx 2\text{K}$ . The temperature of the sample changes when sweeping the field upon a constant heat current. **b)** Non magnetic field dependent thermal conductivity  $\kappa_{B\text{-saturated}}$  as a function of temperature for the three Sb samples. The broken black line represents a  $T^3$  behavior.

$\kappa_{B\text{-saturated}}$  follows a power law  $\kappa_{B\text{-saturated}} \propto T^\gamma$  with  $\gamma > 3$ , respectively  $\gamma = (3.6, 3.8$  and  $4.3)$  for samples  $\bar{s} = 0.4\text{mm}$ ,  $\bar{s} = 1.3$  mm and  $\bar{s} = 2.2$  mm. For comparison, the dashed black line in Fig 6.8.b represents a  $T^3$  behavior.

The temperature dependence of  $\kappa_{B\text{-saturated}}$  and its evolution with the size of the sample form the second main result of this study. It will be further discussed in chapter 6.

### 6.3.3 High field dependence of the thermal conductivity

We also studied the counterpart of the previous result : the thermal conductivity as a function of magnetic field up to  $B = 17\text{T}$  at a constant temperature. As shown in the inset of figure 6.8.a, the thermal conductivity drops drastically when a small magnetic field is applied to the sample.  $\kappa$  then saturates around  $B \approx 1\text{T}$ .

In the low field region, the sudden drop of  $\kappa$  upon sweeping the field induces a change in the temperature of the sample when a constant heat current is applied. Maintaining a constant temperature would require immediate feedback and iteration between the heater and the thermometers, which is a very cumbersome procedure when dealing with finite response time between the sample and the thermometers. But we observe that the thermal conductivity

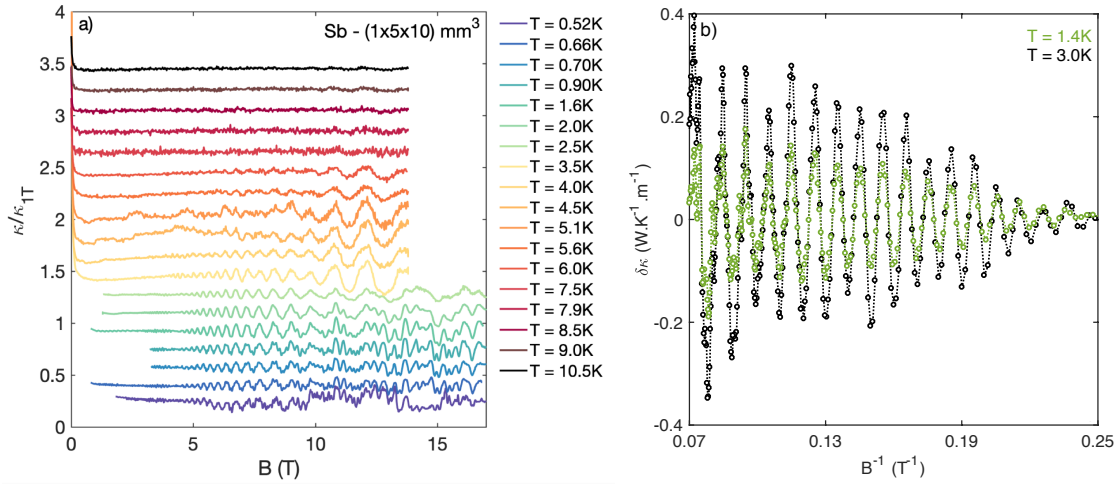


Fig. 6.9 **a)** Thermal conductivity  $\kappa$  plotted as  $\kappa/\kappa_{1T}$  a function of magnetic field for the large,  $\bar{s} = 2.2\text{mm}$  sample. All plots are shifted for clarity. The temperature was determined in the  $B$ -saturation regime. **b)** Oscillations of the thermal conductivity  $\delta\kappa$  ( $\delta\kappa = \kappa - \text{background}$ ) plotted as a function of  $B^{-1}$  for two temperatures  $T = 1.4\text{K}$  and  $T = 3.0\text{K}$ .

saturates typically around  $B = 1\text{T}$ , and further measurement of  $\kappa$  when the magnetic field is swept above  $B = 1\text{T}$  with a constant heat current is thus an isothermal measurement.

Figure 6.9 presents the temperature dependent magneto-thermal transport measurements performed on the  $\bar{s} = 2.2\text{mm}$  Sb sample.  $\kappa$  is presented in figure 6.9.a as a function of the magnetic field for different temperatures, which are evaluated in the  $B$ -saturated regime. Data up to  $B = 17\text{T}$  were measured in our dilution fridge whereas data limited at  $B = 14\text{T}$  were measured in the PPMS. The discrepancy between both sets of measurements is attributed to a small misalignment between the magnetic field and the trigonal direction of the sample from one setup to another.

As previously announced, the sudden drop of  $\kappa$  at very low magnetic field is followed by a constant thermal conductivity upon further increase of the magnetic field. However, as we can see in figure 6.9.a where  $\kappa/\kappa_{B=1T}$  is shown (graphs are shifted vertically for clarity), for  $B > 5\text{T}$  an oscillating pattern emerges in  $\kappa$ . The amplitude of the oscillations accounts for only a fraction of the signal value ( $\approx 5\%$  in this sample) and is temperature dependent; the amplitude of the oscillations increases from  $T = 0.5\text{K}$  to  $T = 5\text{K}$  before diminishing with further increase of temperature. At the highest temperature we studied in this sample,  $T = 10\text{K}$ , we hardly see any detectable oscillations.

We removed the background term (a polynomial fit) and plotted the oscillations as a function of  $B^{-1}$  in figure 6.9.b for two temperatures,  $T = 1.4\text{K}$  and  $T = 3.0\text{K}$ . We observe

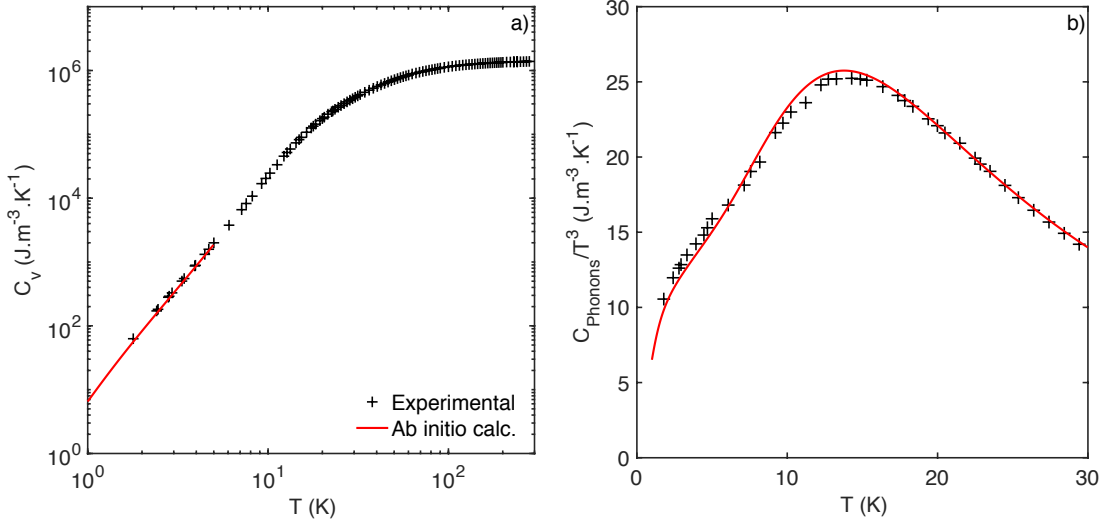


Fig. 6.10 **a)** Specific heat  $C_v$  as a function of temperature both from experimental results (black crosses) and ab initio calculation (red line). **b)** Specific heat plotted as  $C_v/T^3$  for both experimental and theoretical results.

$1/B$ -periodic oscillations. These oscillations are dominated by one frequency :  $f_1 = 96-101T$ . This frequency does not evolve with temperature. The data shown here are for the large sample only, but we observed similar  $1/B$ -periodic oscillations of  $\kappa$  in the other Sb samples with a major frequency  $f_1 \approx 100T$ . The amplitude of the oscillations evolve with sample size. The field sweep data regarding sample S1 are available in the appendix 2.

### 6.3.4 Study of the specific heat

To further shed light on the phonons contribution to the heat transport properties of Sb, we decided to take a closer look at the specific heat of this elemental system. Measurements have been realised by T. Lorenz and coworkers in Köln on a  $(2 \times 2 \times 1)$   $\text{mm}^3$  single crystal of Sb from the same batch as sample  $\bar{s} = 0.4\text{mm}$ .  $C_v$  was determined from  $T = 2\text{K}$  to  $T = 300\text{K}$ . We then separated the electronic and phononic contributions to the specific heat similarly to what we did in the case of  $\text{WP}_2$  (chapter 4).

We also report on a theoretical prediction of the phonon specific heat thanks to the computation of the phonon band structure of Sb by A. Subedi (details of the calculation are provided in the annex). The specific heat due to the phonons was then determined from this band structure.

Both the experimental and theoretical results are presented in Fig.6.10.a. There is a strong agreement between the experimental specific heat and the computed specific heat as

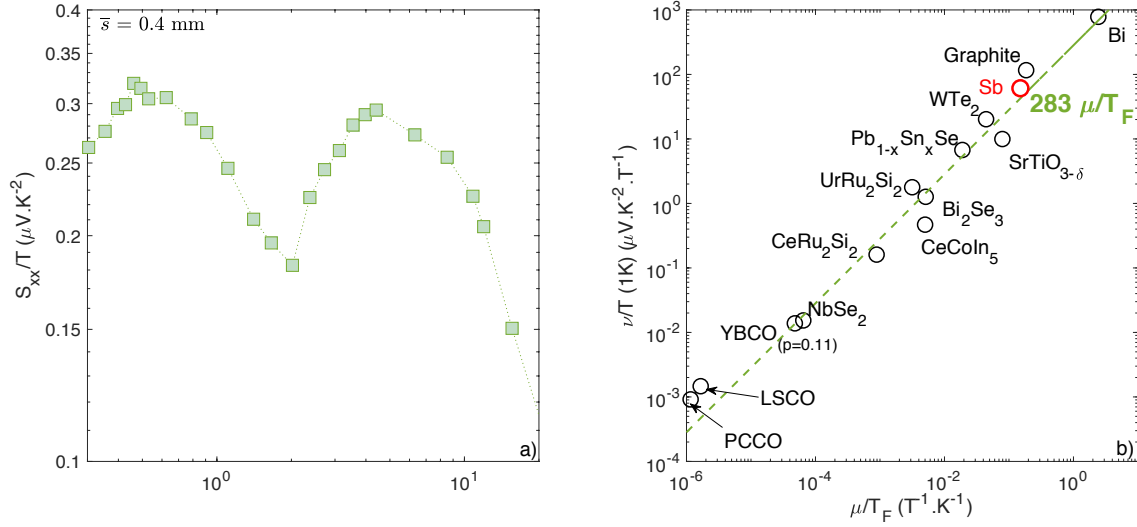


Fig. 6.11 **a)** Thermopower  $S_{XX}$  plotted as  $S_{XX}/T$  as a function of temperature without magnetic field in the small Sb sample. **b)** Nernst coefficient  $\nu$  plotted as  $\nu/T$  as a function of  $\mu/T_F$  for a variety of solids presented in [46]. The green line indicates the approximate behavior in the Fermi liquid limit.

functions of temperature. The specific heat of Sb decreases with decreasing temperature. To study the different components of  $C_v$ , we plot  $C_v/T^3$  as a function of temperature, both experimental and theoretical, in figure 6.10.b. Both plots show the same deviation from a  $T^3$  behavior at finite temperature, i.e. the same anharmonic behavior. Our results are also in agreement with previous experimental determinations of the specific heat of antimony [140, 141].

### 6.3.5 Study of the thermoelectric effects in Sb

In addition to the electrical and thermal conductivities, our experimental setup allows the measurement of the thermopower and Nernst coefficient. We will now report on the effect of temperature and magnetic field on these two coefficients of the thermoelectric tensor in Sb. The large and small samples were studied ( $\bar{s} = 2.2\text{mm}$  and  $\bar{s} = 0.4\text{mm}$ ).

The thermopower  $S_{xx}$  and the Nernst signal  $S_{xy}$  have been respectively defined in equations 2.14 and 2.17. We remind the reader that the Nernst coefficient is defined as  $\nu = S_{xy}/B$ .

**Temperature dependence** The thermopower of the small ( $\bar{s} = 0.4\text{mm}$ ) sample was first measured as a function of temperature in the absence of a magnetic field down to  $T = 0.3\text{K}$ . It is presented in figure 6.11.a as  $S_{xx}/T$ . We observe a small positive thermopower throughout

the entire range of temperature of this study.  $S_{xx}/T$  shows two maxima at  $T = 0.6\text{K}$  and  $T = 6\text{K}$  where it reaches a value close to  $0.3\mu\text{V.K}^{-2}$ . It then decreases at higher temperatures. The variation of  $S_{xx}/T$  between  $T = 0.3\text{K}$  and  $T = 10\text{K}$  do not exceed 50%. The peak at  $T = 6\text{K}$  is most likely due to the phonon drag effect.

Below  $T < 1\text{K}$ ,  $S_{xx}/T$  appears to saturate around  $0.3\mu\text{V.K}^{-2}$ . We remind the reader that, in the diffusive limit, the thermopower is only related to intrinsic properties of the system and not to the scattering of the carriers. It is approximated by equation 2.16. We can use this limit to evaluate a lower bound of the Fermi temperature  $T_F$  from the saturation value of  $S_{xx}/T$ . We find a lower bound for  $T_F = 1200\text{K}$ . If we now compute the Fermi temperature from the frequency of the QO in  $\rho_{22}$ , we reach an average value  $T_F \approx 1000\text{K}$ . The agreement between the Fermi temperature determined from QO and the lower limit evaluated from the thermopower measurement indicates that the thermoelectric response at low temperature is dominated by the diffusive response of charge carriers.

We now turn to the Nernst coefficient of Sb. Figure 6.12.a shows the Nernst coefficient  $v$  plotted as  $v/T$  as a function of temperature for different applied magnetic fields. At low temperatures,  $T < 6\text{K}$ , we observe a slowly varying Nernst coefficient. This Nernst coefficient seems to saturate at low temperature. Upon increasing temperature, an upward deviation is observed :  $v/T$  shows a peak at  $T = 6\text{K}$ . With further increase of the temperature  $-v/T$  decreases quickly and reaches  $10\mu\text{V.K}^{-2}.\text{T}^{-1}$  at  $T = 20\text{K}$ . Over the whole temperature range, the field dependence of  $-v/T$  remains small.

In the case of a Fermi liquid, the value of the Nernst coefficient is also determined by intrinsic properties of the system : the Fermi temperature of the system  $T_F$  and the mobility of the quasiparticles  $\mu$ .  $v$  is evaluated from equation 2.19. This law has been verified over several orders of magnitude in different systems. This expected quasiparticle contribution is shown as a dotted line in figure 6.12.a and gives a lower bound to  $v/T$ . We observe qualitatively in figure 6.12.a that  $-v/T \xrightarrow{T \rightarrow 0\text{K}} 283\mu/T_F$  in the large Sb sample. This result is further emphasized at lower temperature in figure 6.11.b where  $v/T$  ( $T = 1\text{K}$ ) is shown as a function of  $\mu/T_F$  for different systems. From this plot, we can confirm that Sb displays a Fermi liquid behavior at  $T = 1\text{K}$  and that its Nernst coefficient is high compared to systems which are not semi-metals. It is comparable to the  $v/T$  reported graphite and lower to the one of Bi [142].

At higher temperature, the peak observed in the Nernst coefficient implies the existence of a supplementary contribution to  $v$ , similarly what we report in  $S_{xx}/T$  which we associate with the phonon drag effect. We underline that this peak occurs at the same temperature in  $\kappa$ ,  $S_{xx}/T$  and  $v/T$ .

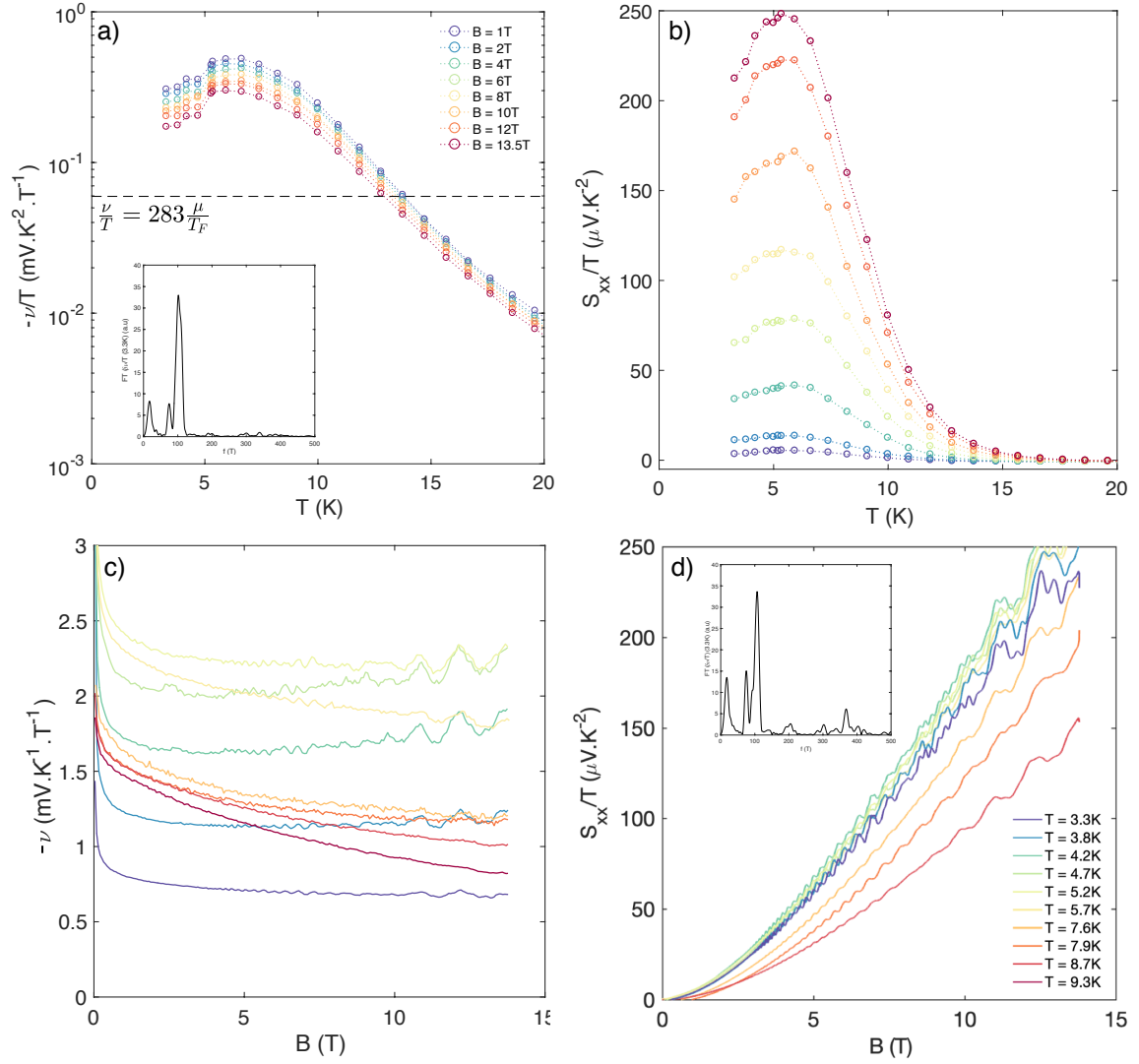


Fig. 6.12 **a)** Nernst coefficient  $\nu$  plotted as  $-\nu/T$  as a function of temperature at fixed magnetic fields. Inset shows the Fourier transform of  $\nu/T$  at  $T = 3.3\text{K}$ . **b)** Thermopower  $S_{XX}$  plotted as  $S_{XX}/T$  as a function of temperature at fixed magnetic fields. **c)** Nernst coefficient  $\nu$  plotted as  $-\nu$  as a function of magnetic field at fixed temperatures. **d)** Thermopower  $S_{XX}$  plotted as  $S_{XX}/T$  as a function of magnetic field at fixed temperatures. Inset shows the Fourier transform of  $S_{xx}/T$  at  $T = 3.3\text{K}$

The temperature dependence of the thermopower and the Nernst effect in static magnetic fields confirms the Fermi liquid behavior of Sb at low temperatures and points to the existence of a phonon drag effect at finite temperature.

**Field dependence** Upon application of a magnetic field we see a strong response in both the thermopower and the Nernst coefficient. The thermopower (Fig 6.12.b) shows a peak in temperature at  $T = 6\text{K}$  for all magnetic fields applied. It increases with increasing magnetic field as supported by its B-dependence in figure 6.12.d. For  $T > 6\text{K}$  the thermopower decreases with decreasing temperature and changes sign at high enough temperature. Finally, we observe QO in  $S_{xx}/T$  plotted as a function of  $B$ . The Fourier analysis of the signal shows two main frequencies, similarly to what we observed in the resistivity :  $f_1 = 100\text{T}$  and  $f_2 = 380\text{T}$ .

These QO were also observed in the field dependence of the Nernst coefficient plotted as  $-v$  in figure 6.12.c. Upon application of a magnetic field,  $-v$  decreases rapidly ( $B < 0.1\text{T}$ ) and plateaus with further increase of  $B$  for  $T < 6\text{K}$ . We notice that for  $T > 6\text{K}$ ,  $-v$  does not reach a plateau but rather decreases with increasing field. The QO are very well observed with symmetrical peaks (unlike what was reported in graphite [83]). The Fourier transform of  $v/T$  reveals only one major frequency  $f_1 = 100\text{T}$  which we showed to be associated with holes. The frequency associated with electrons pockets is not revealed by the Nernst coefficient oscillations.

Finally, we conclude that the thermoelectric tensor confirms the Fermi liquid behavior of Sb at low temperatures. Our observations in Sb are coherent with prior observation of strong thermoelectric effects in other semi-metals such as Bi and graphite. The thermoelectric tensor clearly shows QO which are consistent with the fermiology of Sb, previously determined from the electrical transport measurements. We add that our investigation confirms the existence of a 'phonon drag contribution' discussed in prior reports [7].

## 6.4 Discussion on the thermal transport properties of Sb

We have presented heat and charge transport measurements for slabs of antimony of different dimensions. We will now present a quantitative separation of the different contributions (namely phononic and electronic) to the thermal conductivity. From the electronic thermal conductivity, on one hand, we will show the recovery of the WFL at low temperature to be followed by a departure from this law upon warming. The study of this deviation reveals that a mismatch in the  $T^2$ -prefactor of electrical and thermal resistivities drives down the Lorenz ratio, similarly to what we reported in the case of  $\text{WP}_2$ . The phonon contribution, on the

other hand, displays  $1/B$ -periodic oscillations at high magnetic field. We will discuss the particular electron - phonon scattering phenomenon at the origin of this phenomenon.

### 6.4.1 Separation of the electronic and phononic thermal conductivities

The thermal conductivity of Sb is the sum of two components, the first is associated with charge carriers while the second results of a phononic contribution. We have introduced in chapter 2 how the two contributions can be separated in a system with a high MR. We will now use this method in Sb.

Our starting assumption is that  $\kappa$  is the sum of an electronic component and a phononic term. The existence of a third contribution, an ambipolar component is prevented by the same reasons as in the case of  $WP_2$  : the degeneracy of the electron and hole gases [110]. As a consequence,  $\kappa$  is written as the sum of two terms in equation 6.1.

$$\kappa = \kappa_e + \kappa_{ph} \quad (6.1)$$

Let's focus on the electronic term of  $\kappa$ . At finite temperature, we know that resistive (electron - electron) and (electron - phonon) scattering events induce a departure of the electronic Lorenz ratio from the Sommerfeld value in metals. This yields the following inequation for  $\kappa_e$  at finite temperature :

$$\kappa_e < \frac{L_0 T}{\rho} \quad (6.2)$$

In light of inequation 6.2, if a strong magnetic field is applied to Sb,  $\kappa_e$  will see its upper bound decrease proportionally to the increase observed in  $\rho$ . Figure 6.5.b shows that for  $T < 20K$ ,  $\rho$  increases by 4-5 orders of magnitude when  $B = 10T$  is applied to the system. We thus expect  $\kappa_e$  to drop by at least 4 orders of magnitude.

The gradual decrease of  $\kappa$  as a function of temperature and with increasing field was shown for sample S1 ( $\bar{s} = 0.4mm$ ) in figure 6.8. We will illustrate the separation of the contribution to  $\kappa$  on the example of the large S3 sample.

$\kappa/T$  as a function of  $T^2$  for this sample is shown in figure 6.13. For the different magnetic fields, in this low temperature regime ( $0 < T < 0.3K$ ),  $\kappa/T$  behaves as  $T^2$ . We can thus write  $\kappa$  under the following expression :  $\kappa = \alpha \times T + \beta \times T^3$ . We notice that the slope of  $\kappa/T$  as a function of  $T^2$ , does not depend on the magnetic field. Also, the intercept of  $\kappa/T$  with the y-axis decreases with increasing field. In each case though, it matches its respective  $L_0/\rho(B)$  (represented by the dotted line in figure 6.13). Above  $B = 5T$ , the intercept with the y-axis is too small to be resolved experimentally.

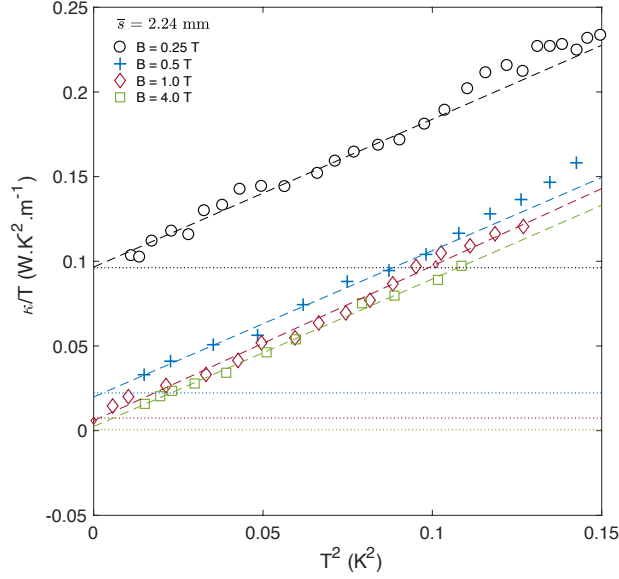


Fig. 6.13 Thermal conductivity plotted as  $\kappa/T$  as a function of  $T^2$  for different magnetic fields applied to S3. Data points are shown as markers while the dotted line correspond to  $L_0/\rho(B)$ . The Wiedemann-Franz law is satisfied if the intercept of  $\kappa/T$  matches the dotted line in the  $T = 0\text{K}$  limit. The broken line serves as a guide for the eyes.

First, the observation, at fixed  $B$ , of the match between the y-axis intercept of  $\kappa$  (i.e. T-linear component) and its corresponding  $L_0/\rho(B)$  value indicates that the Wiedemann-Franz law is experimentally recovered in the  $T \rightarrow 0\text{K}$  limit for the various applied magnetic fields.

Second, from the  $B$ -independent slope of  $\kappa/T$  as a function of  $T^2$ , we can conclude that the  $T^3$ -dependent part of the thermal conductivity saturates. This invariant component corresponds to the thermal conductivity which is associated with phonons and thus does not depend on the magnetic field for moderate fields. We thus associate  $\kappa_{B\text{-saturated}}$  shown in Fig.6.8.b with the phonons thermal conductivity.

We have determined quantitatively both the total thermal conductivity and the thermal conductivity due to phonons. We can now extract the electronic component of the thermal conductivity for the three samples :

$$\kappa_e = \kappa - \kappa_{B\text{-saturated}} \quad (6.3)$$

For sample  $\bar{s} = 2.2\text{mm}$  we plot  $\kappa$ ,  $\kappa_e$  and  $\kappa_{ph}$  simultaneously in figure 6.14.a. Both the electronic and the phononic contributions show a maximum in temperature, respectively at  $T = 4\text{K}$  and  $T = 7\text{K}$  in this sample. Also, we observe that for  $T < 3\text{K}$ ,  $\kappa_e$  becomes  $T$ -linear while  $\kappa_{ph} \ll \kappa_e$ . Below  $T = 2\text{K}$ , we can write  $\kappa = \kappa_e$  whereas above this temperature, the

phonons thermal conductivity increases faster than the electronic one. Both contributions account for roughly half of  $\kappa$  above  $T = 3\text{K}$ . This result is confirmed in the three samples by the comparison of  $\kappa_e$  shown on figure 6.14.b and their respective phonons contributions displayed in Fig.6.8.b.

Now that we have separated the two contributions which form  $\kappa$ , we will concentrate on the electronic fraction first. Let us define the electronic Lorenz ratio  $L_e/L_0 = \rho \kappa_e / L_0 T$  and plot it as a function of temperature in Fig.6.14.c. We observe that  $L_e/L_0 = 1$  below helium temperature. Upon increasing temperature, a size-dependent downward deviation is observed with a minimal  $L_e/L_0$  observed in the vicinity of  $T = 10\text{K}$ . The first observation confirms what we knew from the study of the total Lorenz ratio : the WFL is recovered at low enough temperature in the two Sb samples presented here. Second, and similarly to our study of  $\text{WP}_2$ , we can now determine the origin of this finite temperature departure from the WFL in Sb. To do so we extract and compare the different components of the electrical and thermal resistivities.

The thermal resistivity ( $WT$ ) is defined, as it was previously, by  $(WT) = L_0 T / \kappa_e$ . ( $WT$ ) increases with increasing temperature in figure 6.14.d. It is also plotted alongside as a function of  $T^2$  in figure 6.15.b while  $\rho_{22}$  is plotted as a function of  $T^2$  in figure 6.15.a . These plots reveal that both ( $WT$ ) and  $\rho_{22}$ , both in samples S1 and S3, scale as  $T^2$  up to  $T = 8\text{K}$ . These  $T^2$ -resistivities are both followed by upturns at higher temperature.

To determine the origin of this  $T^2$ -resistivity, we now separate the different contributions to  $\rho_{22}$  and ( $WT$ ). Assuming the validity of Matthiessen's rule in Sb, we can write the electrical and thermal resistivities under a sum of the residual, (electron - electron) and (electron - phonon) terms :

$$\rho = \rho_0 + A_2 T^2 + A_5 T^5 \quad (6.4)$$

$$WT = W_0 T + B_2 T^2 + B_3 T^3 \quad (6.5)$$

At low temperature, we have shown  $\rho_0 = (W_0 T)$  with the recovery of the WFL. After subtracting it to the resistivity, we can evaluate the prefactors of the  $T^2$ -dependent terms in both ( $WT$ ) and  $\rho$ . In the small sample S1, we find  $A_2 = 0.70\text{n}\Omega\cdot\text{cm}\cdot\text{K}^{-2}$  whereas  $B_2 = 0.81\text{n}\Omega\cdot\text{cm}\cdot\text{K}^{-2}$  is the thermal one. In the large Sb sample S3, the electrical resistivity  $T^2$ -prefactor is  $A_2 = 0.32\text{n}\Omega\cdot\text{cm}\cdot\text{K}^{-2}$  whereas the thermal one is  $B_2 = 0.63\text{n}\Omega\cdot\text{cm}\cdot\text{K}^{-2}$ . The size-dependence of  $A_2$  and  $B_2$  will be discussed in chapter 6.

We identify the upturn from the  $T^2$  behavior observed in both ( $WT$ ) and  $\rho_{22}$  to the emergence of an (electron - phonon) contribution to the resistivity. However, in Sb, the electron - phonon term does not appear to follow the expected Bloch-Gruneisen  $T^5$ -behavior.

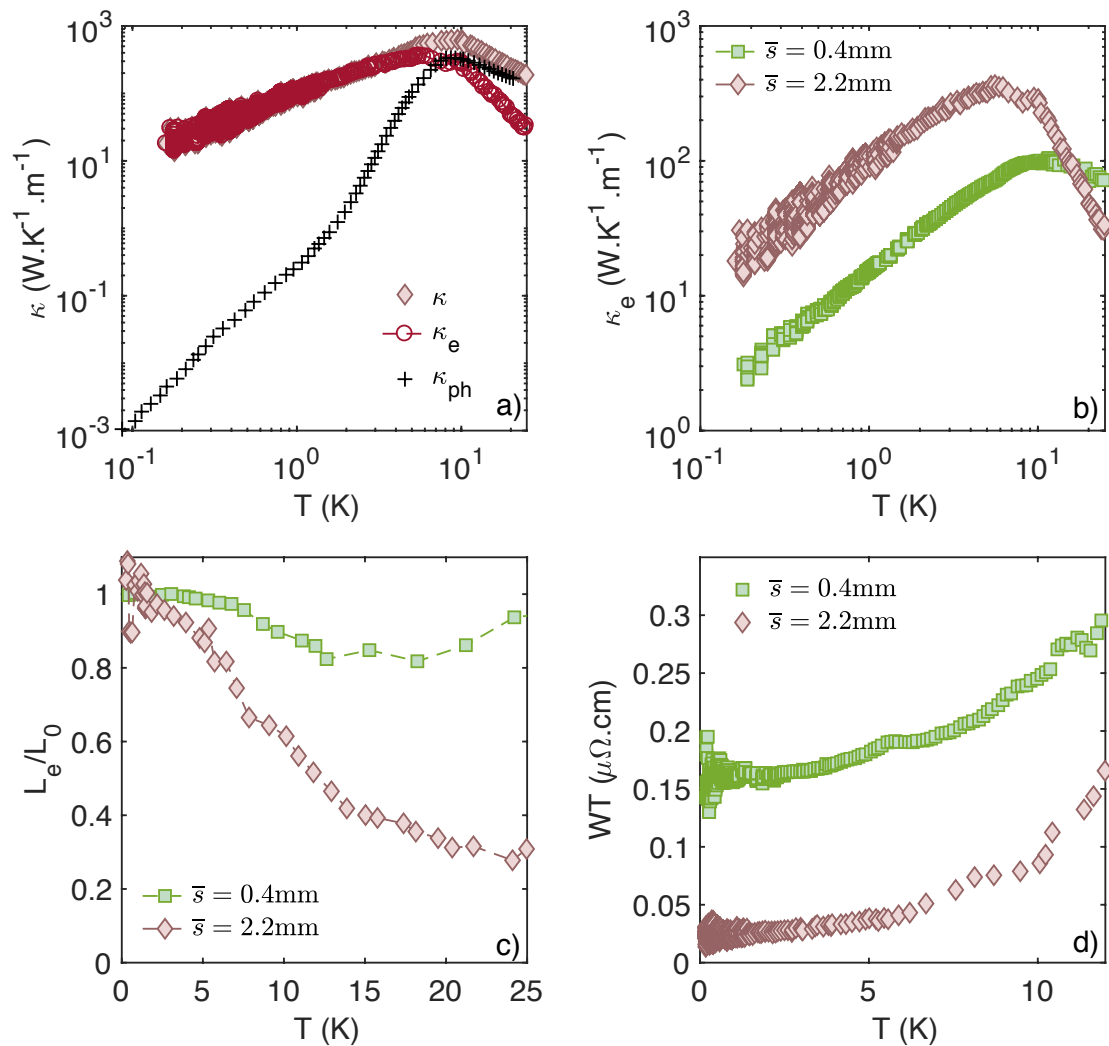


Fig. 6.14 **a)** Plot of the total thermal conductivity  $\kappa$ , the electronic part  $\kappa_e$  and the phonons' contribution  $\kappa_{ph}$  as a function of temperature for the large Sb sample. **b)**  $\kappa_e$  plotted as a function of temperature for the three Sb samples. **c)** Electronic Lorenz ratio plotted as a function of temperature for the three sample.  $L_e/L_0 = 1$  indicates the recovery of the WFL. **d)** Thermal resistivity ( $WT = L_0T/\kappa_e$ ) plotted as a function of temperature for the small and large samples.

We do not observe a  $T^3$  contribution, associated with (electron - phonon) scattering in ( $WT$ ) either. This is the case in all three samples. This observation of a small (electron - phonon) term in both resistivities is also confirmed by previous reports [12, 131, 132]. While we do not understand the evolution with temperature of the electron - phonon scattering term in Sb, we show that it is at least negligible up to  $T = 8\text{K}$  in this study.

We can thus associate the finite temperature deviation of the electronic Lorenz number  $L_e$  from the Sommerfeld value  $L_0$  to the mismatch in the  $T^2$ -prefactor of the electrical and thermal resistivity. Microscopically, it means that inter-electronic scattering events drive the Lorenz ratio down. In light of our study of  $\text{WP}_2$ , we can conclude that this phenomenon can be associated with the small-angle fraction of electronic collisions which contribute more to the thermal resistivity than they do to the electrical resistivity. The amplitude of the deviation observed in Sb ( $L = 0.46L_0$  at  $T \approx 10\text{K}$  in S3 is half what we observed in the case of  $\text{WP}_2$  ( $L = 0.23L_0$  at  $T \approx 10\text{K}$  in  $\text{WP}_2$  [110]. We will now discuss this difference considering the different topologies of the respective Fermi surfaces of the two materials.

We have previously shown that all hole/electron pockets of the FS of  $\text{WP}_2$  lay at the zone boundary and occupy a considerable fraction of the BZ 5.1. This favors small-q umklapp scattering events and thus a strong heat/charge transport dichotomy [118]. In contrast, the FS of Sb is composed of small electronic pockets buried in the Brillouin zone. This Fermi surface topology does not favor as much small-q electronic collisions as it does in  $\text{WP}_2$ . As a consequence, the observation of a smaller deviation to the WFL at finite temperature in Sb than in  $\text{WP}_2$  is coherent with the differences between the FS of these semimetals.

Finally, we can also compare the amplitude of the deviation to what was reported in two heavy fermions systems :  $\text{UPt}_3$  [32] and  $\text{CeRhIn}_5$  [31]. In both systems, the deviation of the Lorenz number from the Sommerfeld value was also associated to (electron - electron) scattering. The amplitude of the deviations are very similar to what we observe in Sb. The respective Fermi surfaces of these compounds are mostly located inside the Brillouin zone [143, 144]. This observation is coherent with our qualitative explanation of the amplitude of the electronic Lorenz number in various metals.

To summarize this section, we have presented a quantitative separation of the electronic and phononic parts of the thermal conductivity in Sb. We are then able to give a quantitative study of  $\kappa_e$  in presence of a non-negligible phonon contribution to the thermal transport. This study proves the experimental recovery of the Wiedemann-Franz law at low temperature in different sizes of Sb samples. We then report on a departure from the WFL at finite temperature. We associate this phenomenon, similarly to the case of  $\text{WP}_2$ , with abundant small-angle electronic collisions. The amplitude of the deviation is similar to what was observed in other metals yet smaller than what we reported on  $\text{WP}_2$ . We associate this

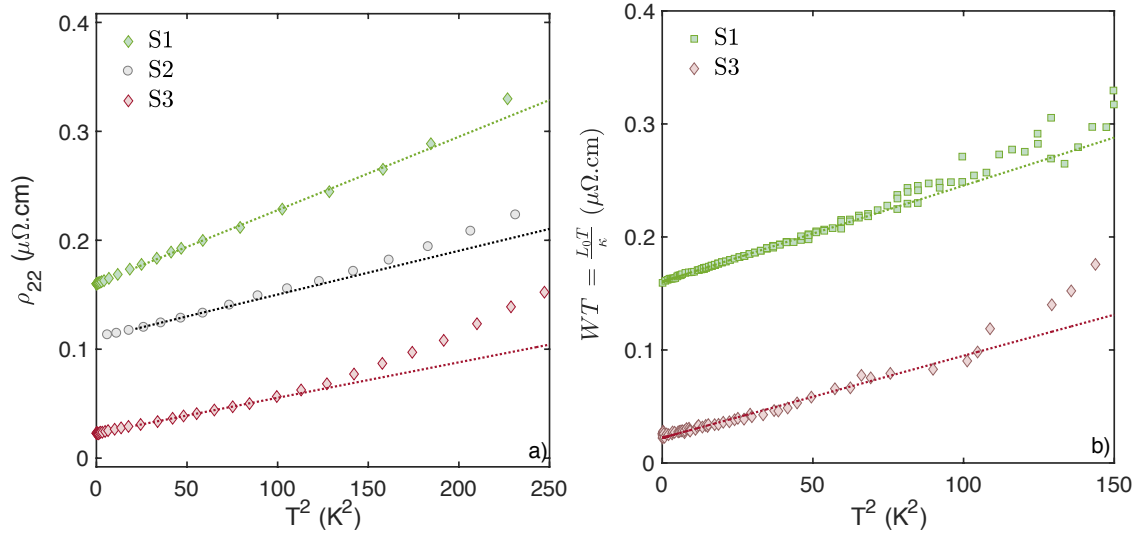


Fig. 6.15 **a)** Electrical resistivity  $\rho_{22}$  plotted as a function of  $T^2$  in the three Sb samples. **b)** Thermal resistivity ( $WT$ ) plotted as a function of  $T^2$  in the large and small Sb samples. The dotted lines correspond to fits to  $T^2$ -resistivities. Different x-axis ranges are used in the two plots.

difference with the dissimilarities of the Fermi surfaces of these compounds : large pockets located at zone boundary favor small-q electronic U-scattering in  $WP_2$  while Sb, with small FS pockets located inside the Brillouin zone, which, do not particularly favor vertical scattering.

## 6.4.2 Origin of the $1/B$ -periodic oscillations

While the previous section was devoted solely to the electronic transport properties of Sb, we will now shift our attention to the phononic fraction of the thermal conductivity. We have proven that  $\kappa_{ph}$  is independent of the magnetic field in the  $B < 5T$  region. However, when sweeping the magnetic field above this value we observe  $1/B$ -periodic oscillations of  $\kappa_{ph}$ , as seen in Fig.6.9. We now wish to determine the origin of these oscillations.

**Phononic origin of the oscillations** Figure 6.16.a compares the amplitude of the electrical resistivity  $\rho_{22}$  (green) and the thermal resistivity ( $WT$ ) (red) as a function of the magnetic field for  $T = 3K$  in sample S3. We notice that  $\rho_{22}$  is 6 orders of magnitude larger than ( $WT$ ) over the whole temperature range.

If the oscillations observed in  $\kappa = \kappa_{ph}$  were associated with a residual electronic fraction of the thermal conductivity,  $\delta\kappa_e$ , the amplitude of the oscillations would be bound to the am-

plitude of the resistivity oscillations by the Wiedemann-Franz law. The oscillations observed in  $(WT)$  and  $\rho_{22}$  would thus be of similar amplitudes. The large discrepancy between  $\rho_{22}$  and  $(WT)$  forbids this purely electronic scenario. We can conclude that these oscillations are not associated with straightforward SdH oscillations but rather with oscillations of  $\kappa_{ph}$ .

A second key feature which shines light on the origin of the oscillations of  $\kappa_{ph}$  is the comparison with the oscillations recorded in the resistivity and the Nernst coefficient. We plot in figure 6.16.b, along a common x-axis, the oscillations (background removed) observed in the aforementioned quantities :  $\delta\rho_{22}$ ,  $\delta\kappa$  and of the Nernst number  $\delta N = \delta v \times B$  as a function of  $B^{-1}$  for B from 6.25T to 12.5T. These measurements were all taken at  $T = 3\text{K}$  in sample S3 ( $\bar{s} = 2.24 \text{ mm}$ ). The electrical resistivity was previously shown in figure 6.5) while the raw Nernst coefficient can be found in figure 6.12.c.

We observe that all three quantities present  $1/B$ -periodic oscillations. The amplitude of the peaks observed in  $\rho_{22}$  decreases quickly with increasing  $1/B$  : only few oscillations are visible in the range of magnetic field studied here. The oscillations in the Nernst number and the thermal conductivity, on the other hand, can be resolved over a larger  $1/B$ -range.

The crucial feature we wish to emphasize in figure 6.16.b is the relative phase of  $\delta\rho_{22}$  and  $\delta\kappa$ . These two quantities oscillate in-phase according to one major frequency :  $f_1 = 100\text{T}$ . This observation confirms the non-SdH nature of the oscillations. Indeed, in the case of electronic thermal conductivity oscillations, the WFL would again impose that  $\kappa$  oscillates as  $1/\rho_{22}$ . As a consequence,  $\delta\rho_{22}$  and  $\delta\kappa$  would be in phase opposition. The synchronous oscillations of  $\kappa$  and  $\rho_{22}$  (and  $-N$ ), is another argument to support the non-electronic origin of the oscillations of  $\kappa_{ph}$ . We finally add that the observation of out-of-phase  $\delta\rho_{22}$  and  $\delta N$  is expected for a semimetal. The electrical resistivity reaches a minimal value when a Landau level is full which simultaneously corresponds to a maximum in the Nernst coefficient [46].

Similar observations have recently been reported in a variety of semimetals : in NbP (attributed to an ambipolar contribution) [136], TaAs (related to variations of the electron-phonon coupling) [137], TaAs<sub>2</sub> [145] and NbAs<sub>2</sub> [145]. They have also been reported half a century ago in Bi [134], Sb [132] and graphite [135]. Their origin remains poorly explored.

Our study is the first to track these oscillations down to low temperatures in a context of clear separation of the different contributions to the thermal conductivity. We are able to conclude that  $\delta\kappa$  is not associated with a violation of the Wiedemann-Franz but rather with oscillations of  $\kappa_{ph}$  with the population of the LL.

**Fourier transform analysis of  $\delta\kappa$**  We now turn to the spectral analysis of  $\delta\kappa$  to unveil more information on the nature of the (electron - phonon) scattering which leads to these oscillations. We present the Fourier transform of  $\delta\kappa$  in figure 6.17. We remind the reader that

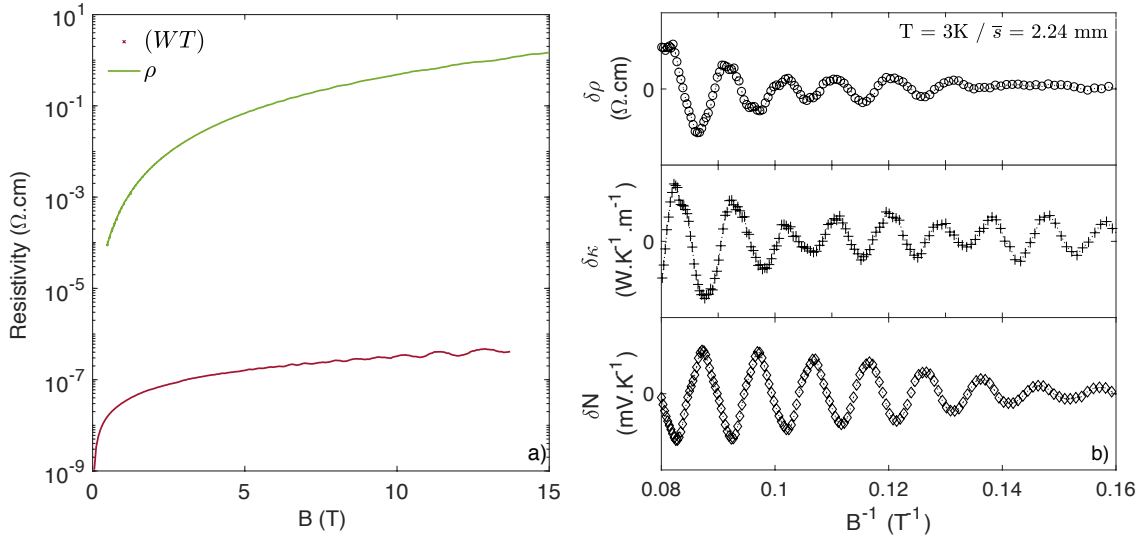


Fig. 6.16 **a)** Electrical  $\rho_{22}$  and thermal ( $WT$ ) resistivities plotted as a function of magnetic field for  $T = 3\text{K}$ . **b)** Quantum oscillations extracted, from top to bottom, from  $\rho_{22}$ ,  $\kappa$  and  $N$  (Nernst coefficient) in arbitrary units. All sweeps were realised at  $T = 3\text{K}$ . The vertical dotted lines serve as guides for the eye.

$\delta\kappa$  is defined by subtracting a polynomial fit to  $\kappa_{ph}$ . The Fourier transform is then computed over a window of magnetic field between 4T and 10T at a fixed temperature.

As an example, the resulting Fourier transform of  $\kappa_{ph}$  at  $T = 1\text{K}$  is shown in the inset of figure 6.17.b. In this case, and for all temperatures, we were able to track only one frequency in the FT signal : the peak at  $f_1 = 100\text{T}$ . The amplitude of this 100T-peak, labelled  $A_{FT}(\delta\kappa)$ , is plotted as a function of temperature in figure 6.17.a. The inset shows  $A_{FT}(\delta\kappa)/T^3$  as a function of temperature. For  $T < 4\text{K}$ ,  $A_{FT}(\delta\kappa)$  increases with increasing temperature. This increase follows a temperature dependence close to  $T^3$  as supported by the inset of 6.17.a. The amplitude  $A_{FT}(\delta\kappa)$  then reaches a maximum close to  $T = 4 - 5\text{K}$  before decreasing with any further increase of the temperature. We know that the frequency  $f_1$ , in this geometry of experiment, is associated with the hole pockets. In comparison, the spectral analysis of  $\rho_{22}$  contains the same peak at  $f_1 = 100\text{T}$  but also reveals a second peak at  $f_2 = 380\text{T}$  which is associated with the electron pockets. The inset of figure 6.17.b superposes the amplitude of the FT of  $\rho_{22}$  and  $\kappa$ . For  $\rho_{22}$ , the amplitude of the Fourier transform of the 380T-peak is smaller by a factor  $\approx 2$  in regard of the amplitude of the 100T-peak. While the peak at  $f_2 = 380\text{T}$  is visible in  $\rho_{22}$  it is not found in  $\kappa_{ph}$ . We can thus conclude that holes, through scattering events with the phonons, rather than electrons; drive the oscillations of  $\kappa_{ph}$ .

**Hole - phonon scattering** In the literature, the decrease of the phononic lifetime when a Landau level is depopulated has been previously discussed under the 'surf-riding' condition [49]. The Landau quantification acts as a frequency comb for the electron - phonon interaction. Upon depopulation of a Landau level by the increasing magnetic field, a phonon with an energy matching the energy difference between Landau levels is absorbed or emitted. This LL - phonon interplay is illustrated in the sketch of figure 6.17.b. A Multiple phonons process, such as  $\omega_{p,1} + \omega_{p,2} = \omega_c$ , could also be invoked. For the sake of simplicity we will only consider a single-phonon process in the following discussion.

Both the typical phonon wavelength and the LL smearing depend on temperature. These effects adding up, we expect  $\delta\kappa$  to have a strong temperature dependence. Figure 6.9.a gives a qualitative description of this effect : the amplitude of the oscillations, at a fixed magnetic field, presents a maximum between  $T = 2\text{K}$  and  $T = 8\text{K}$ . Both the amplitude and position of this maximum depend on the magnetic field. The existence of this peak in the amplitude of  $\delta\kappa$  as a function of temperature is further confirmed by the observation of a maximum in  $A_{FT}(\delta\kappa)$  (Fig.6.17.a).

We can understand the existence of this maximum and its field dependence 'by hand'. Hole - phonon scattering is strongly favored when the typical wavevector of acoustic phonons is small enough to match the small- $q$  of carriers (holes) in Sb, i.e. when  $q_{\text{phonons}} = 2k_F$ . We define  $T_{e\text{-phonon}}$  as the temperature at which this condition is satisfied.  $T_{e\text{-phonon}}$  can be understood as an effective Debye temperature; above  $T_{e\text{-phonon}}$  phonons have a typical  $q$ -vector too large in comparison to  $k_F$  to interact with the charge carriers.  $T_{e\text{-phonon}}$  is explicitly given by equation 6.6. After calculation, we find  $T_{e\text{-phonon}} \approx 30\text{K}$  in Sb. As a consequence, we do not expect oscillations of  $\kappa_{ph}$  above  $T = 30\text{K}$ .

$$T_{e\text{-phonon}} = \frac{2\hbar \times v_S \times k_F}{k_B}; \quad (6.6)$$

Since the oscillations are a signature of scattering events between acoustic phonons and charge carriers confined in LL, a third energy scale has to be considered : the energy difference between Landau levels. This difference is the cyclotron energy  $\hbar\omega_c$  with  $\omega_c = eB/m^*$ .

We can define a third characteristic temperature  $T_{\text{cyclo}}$  associated with this energy scale such as  $k_B * T_{\text{cyclo}} = \hbar\omega_c$ . At  $T_{\text{cyclo}}$ , the majority of phonons have sufficient energy to enable the transition of a hole from one LL to another. Scattering is thus favored. Below  $T_{\text{cyclo}}$  however, the emission rate of phonons is reduced as electrons become more degenerate. In the low temperature regime we expect a reduction of  $A_{FT}(\delta\kappa)$ . As an example at  $B = 1\text{T}$  :  $T_{\text{cyclo}} = 4\text{K}$ . This example can be transposed to other field. We thus expect the hole - phonon scattering rate to decrease at low temperature and, leading to a maximum in  $A_{FT}(\delta\kappa)$ .

Another argument which points towards the suppression of the oscillations at higher temperature too is the strong mismatch between the Dingle mobility and the Hall mobility :  $\mu_D \ll \mu_H$ . We know that the mobility of charge carriers decreases with increasing  $T$  [106] above  $T = 5\text{K}$ . As a matter of fact, the characteristic lifetime of quasiparticles decreases upon increasing electron - electron scattering. These features induce a decrease of  $A_{FT}(\delta\kappa)$  at higher temperature.

We can conclude that the observation of a maximum in the amplitude of the 100T-peak in the FT of  $\kappa_{ph}$  at finite temperature is coherent with the scattering of holes confined in Landau levels by acoustic phonons (sketch in Fig 6.17.b).

We will now give hints towards a quantitative approach of the evolution of the amplitude of the oscillations with temperature. Because of the nature of the scattering events,  $A_{FT}(\delta\kappa)$  has a temperature dependence due to both electrons and phonons. To isolate the thermal smearing of the LL we need to remove the temperature dependence due to the phonon population. We know that this quantity is proportional to  $\alpha \int D(q)n(q)dq$  where  $D(q)$  is the phonon dispersion,  $n(q)$  is the phonon population and  $\alpha$  a prefactor. This term is present in both  $\delta\kappa$  and  $\kappa_{ph}$ . Consequently, we propose to remove the temperature dependence due to phonons by normalizing  $\delta\kappa$  by the value of  $\kappa_{ph}$  at the said temperature.  $\kappa_{ph}$  can be found in figure 6.8 and the normalized result  $A_{FT}(\delta\kappa)/\kappa_{1T}$  is presented in figure 6.17.c. The temperature dependence of this normalized quantity is now independent of the phonon population; it is entirely ascribed to scattering with charge carriers. Electronic conductivity, whether it is electrical or thermal, depends linearly on the electronic density of state as a first approximation. We thus test the theory of Lifschitz-Kosevich as a first approach to understand the  $T$ -dependence of the normalized oscillations (as presented in Chapter 1 [49]).

A fit of  $A_{FT}/\kappa_{ph}$  to the  $R_T$  term is shown in red in figure 6.17.c. It yields an effective mass of the carrier of  $m = 0.3 \times m_0$ , to be compared with the mass of the hole pocket,  $m = 0.34 \times m_0$  at the origin of the 100T-oscillations [106]. However, the low temperature data cannot be explained in this framework; we observe a decrease of  $A_{FT}(\delta\kappa)/\kappa_{ph}$  with decreasing temperature below  $T = 1\text{K}$ .

However, the peak in  $A_{FT}(\delta\kappa)/\kappa_{ph}$  is reminiscent of the temperature dependence of amplitude of the QO reported in the thermopower  $S_{xx}$  of a dilute metal [46]. In this case, the evolution with temperature of the amplitude of the peak is set by the derivative of the electronic density of states. We propose a fit to the temperature derivative of the LK model (green) in figure 6.17. This fit yields an effective mass of the carrier  $m = 0.36 \times m_0$  which is in good agreement with the hole mass in Sb. A more detailed and explanatory analysis of the temperature evolution of  $A_{FT}(\delta\kappa)/\kappa_{ph}$  will be released after this manuscript. We remind the reader that only the  $R_T$  term in 2.30 depends on temperature.

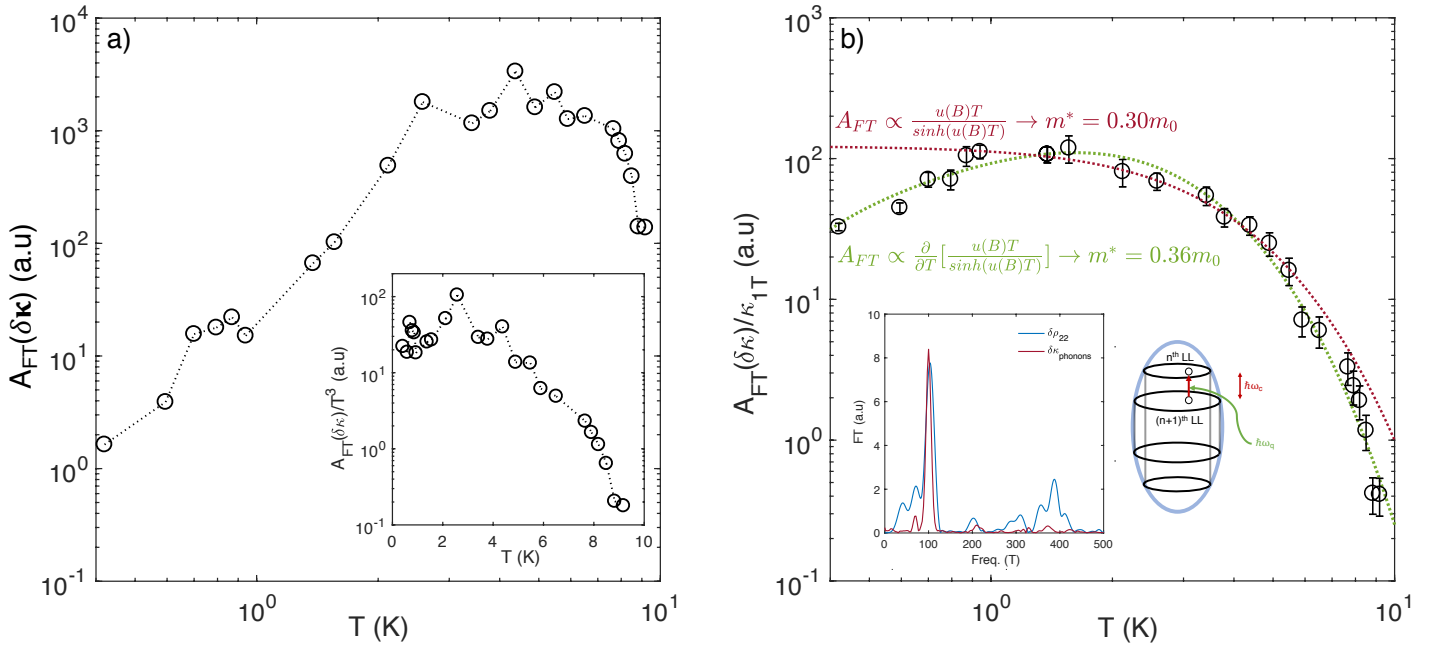


Fig. 6.17 **a)** Evolution with temperature of the amplitude the Fourier transform of the  $f_1 = 100T$  peak in  $\kappa_{ph}$  ( $A_{FT}(\delta\kappa)$ ) of Sb sample S3. Inset shows  $A_{FT}(\delta\kappa)/T^3$  as a function of temperature **c)** Amplitude of the 100T-peak normalized by the Phonons thermal conductivity  $A_{FT}(\delta\kappa)/\kappa_{ph}$  as a function of temperature. Black markers represent experimental data while the red and green dotted lines correspond respectively to fits to the LK model and its derivative. Error-bars are evaluated from both experimental noise and numerical analysis. The inset compares the Fourier transform (FT) of  $\kappa$  (red) and  $\rho_{22}$  at the same temperatures. Also featured as an inset is a sketch of an acoustic phonon absorbed by an electron in the  $N^{th}$  LL scattered to the  $(N + 1)^{th}$  LL.

## 6.5 Conclusion on the electronic and phononic transport properties of Sb

As a conclusion, we are able to clearly separate the contributions associated with phonons and electrons to the total thermal conductivity of Sb. The electronic part, on one hand, satisfies the WFL at low temperature, it deviates from it at  $T \approx 10\text{K}$ . We show that this deviation emerges from inter-electronic collisions. On the other hand, the phonon thermal conductivity does not evolve with the magnetic field except for the emergence of  $1/B$ -periodic oscillations at  $B > 5\text{T}$ . The amplitude of these oscillations and their relative phases in regard of the oscillations we report in  $\rho_{22}$  and  $\nu$  and finally the temperature dependence of the amplitude of the peaks, all discard a purely electronic origin for this signal. Instead, our observations point to the existence of a two quasiparticles scenario, lead by scattering events between acoustic phonons and holes confined in Landau level. This leads to the absorption/emission of phonons with a  $1/B$ -periodic frequency. Finally, we showed that a quantitative description of the oscillations is not an obvious problem : the LK theory is not able to account for the evolution of the amplitude of the oscillations with temperature.

# Chapter 7

## Hydrodynamic Flow of Quasiparticles

### Résumé du chapitre

Nous avons associé la forte déviation par rapport à la loi de Wiedemann-Franz qui est observée à température finie dans  $WP_2$  et Sb à une abondance particulière des processus de diffusion électronique à petits angles. À travers l'exemple d'hélium 3 liquide, dans son état normal, nous proposons un mécanisme alternatif à l'origine de la dichotomie entre les préfacteurs des résistivités  $T^2$  thermique et électrique : une abondance de collisions électroniques qui conservent le moment total (MC) par rapport aux collisions résistives et avec les bords. La composante quadratique de la résistivité thermique est alors associée à la fréquence des collisions MC tandis que la résistivité électrique est associée au processus de diffusion qui dégradent le moment total du gaz électronique. Dès lors, nous pouvons définir deux libres parcours moyens, un pour chacun des deux types de processus, ainsi qu'un troisième qui décrit les collisions avec les bords du système. Le régime de transport est alors dicté par la hiérarchie entre ces longueurs caractéristiques. R. N. Gurzhi avait prédit l'existence d'un régime de transport dominé par les collisions MC : le régime hydrodynamique des quasiparticules. Nous démontrons à travers l'analogie avec  $^3\text{He}$  que le critère d'émergence du régime hydrodynamique est satisfait dans  $WP_2$  et Sb à la transition entre les régimes diffusifs et ballistiques. Mais bien que ce régime soit a priori permis, cela ne constitue pas une preuve de son émergence. Ainsi, dans le cas de  $WP_2$  nous ne pouvons conclure définitivement sur l'existence ou non d'un régime hydrodynamique des électrons. En revanche, nous rapportons l'observation d'une dépendance en taille du ratio des préfacteurs des termes quadratiques en température des résistivités électriques et thermiques dans antimoine. Nous interprétons ce résultat comme une signature du régime hydrodynamique des électrons.

Parallèlement, notre étude d'antimoine révèle aussi l'existence d'une autre fenêtre de température liée à un écoulement visqueux de quasiparticules. Au sein de cet intervalle, le

libre parcours moyen des phonons augmente avec la température et dépend de la taille de l'échantillon. Cette observation est caractéristique d'un écoulement hydrodynamique des phonons. Cependant, cette conclusion est rendue paradoxale dans Sb par un régime basse température, jusqu'à  $T = 80$  mK, où une longueur intrinsèque limite le libre parcours moyen des phonons. Nous étudierons cette limitation à la lumière de la diffusion electrons - phonons mise en avant dans le chapitre précédent.

---

### Summary of the chapter

We have previously associated the strong heat/charge transport dichotomy observed at finite temperature in  $WP_2$  and Sb to a particular abundance of small-angle electronic scattering events. Yet, previous reports on the thermal conductivity of normal-state liquid  $^3\text{He}$  offer an alternative route to a  $T^2$ -prefactors dichotomy : the role of momentum-conserving yet energy-relaxing electronic collisions in regard to the momentum-relaxing collisions. We associate the momentum-conserving (MC) fermion-fermion collisions to the  $T^2$ -term of the thermal resistivity while the electrical  $T^2$ -resistivity is associated with momentum-relaxing (MR) scattering events affecting the charge carriers. Hence, we can define two mean-free-paths, one for each type of scattering process, as well as a third one which describes the collisions with the boundaries of the system. The regime of transport is determined by the hierarchy of these characteristic lengths. In particular, R. N. Gurzhi predicted the existence of a regime of transport dominated by MC collisions : the hydrodynamic regime. The analogy with  $^3\text{He}$  reveals that the hydrodynamic criterion is satisfied in both  $WP_2$  and Sb at the crossover between the ballistic and diffusive regimes. Even though this regime is permitted, its signature remain scarce. In the case of  $WP_2$ , the observation of hydrodynamic effects remains an open question. Nevertheless, in Sb, we interpret our observation of a size-dependent electrical to thermal  $T^2$ -prefactors ratio, i.e. a size-dependent electronic Lorenz number, as a signature of a hydrodynamic flow of electrons. Also, we show that the mean-free-path of phonons in Sb becomes size dependent over a finite temperature window. This result is reminiscent of previous observations of hydrodynamic flow of phonons in other materials. Yet, contrary to these reports, phonons in Sb do not reach the ballistic regime below this temperature window. We associate this discrepancy to the electron - phonon collisions which we have discussed in chapter 6.

---

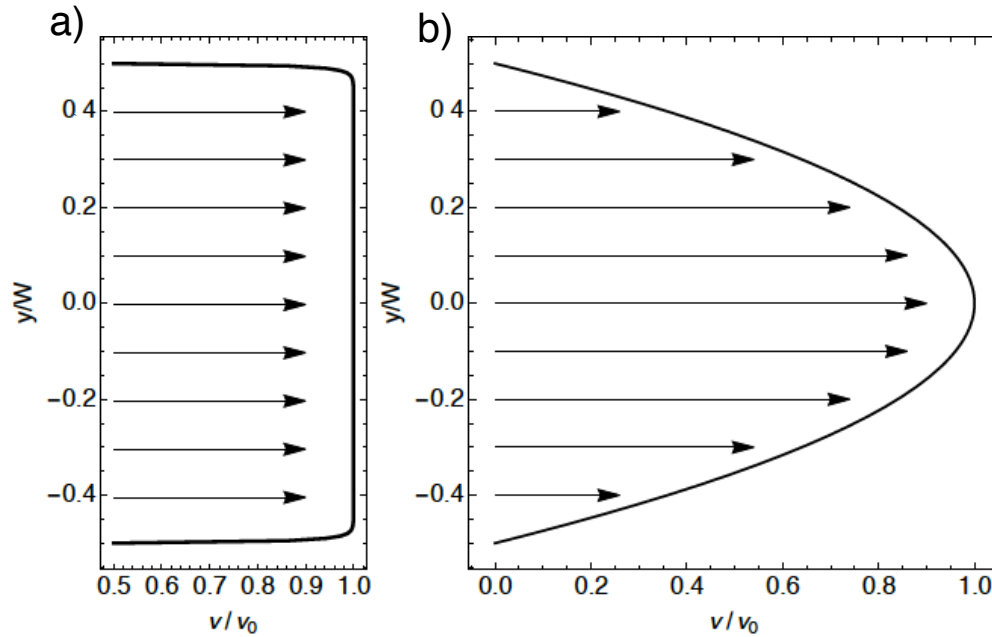


Fig. 7.1 **a)** Velocity profile of the quasiparticles in a 2D channel of width  $w$  in the diffusive regime of transport. Figure from A. Mackenzie [15]. **b)** Velocity profile of the quasiparticles in a 2D channel of width  $w$  in the hydrodynamic regime of transport [15]

## 7.1 Introduction to hydrodynamic transport

Let us first introduce the hydrodynamic description of quasiparticles flow and underline the experimental challenge that it constitutes. We will then present the thermal conductivity of normal state liquid  $^3\text{He}$  at low temperature to shine a different light on the charge and heat transport measurements reported in Chapter 5 and 6.

### 7.1.1 Gurzhi's hierarchy of scattering times

One of the main successes of the quantum theory of solids was to give a correct description of the basic features of the electrical conductivity of metals and the thermal conductivity of metals and dielectric compounds. At finite temperature, both quantities are set by the frequency of the collisions which degrade either the momentum or the energy of the quasiparticles. In the  $T \rightarrow 0\text{K}$  limit, the electrical conductivity is set by the scattering of charge carriers off the boundaries or impurities of the system while the thermal conductivity due to phonons vanishes. But in this low temperature limit, a large number of both metals and dielectrics display deviations from this expected behavior.

Amongst these deviations is the effect of momentum-conserving collisions. In the diffusive regime of transport, momentum-relaxing collisions are far more frequent than any

other type of scattering events. Only a negligible fraction of the quasiparticles reaches the boundaries of the system. This leads to a velocity profile similar to what is represented in figure 7.1.a : a flat profile independent of the width of the channel in which the quasiparticles flows.

Now if the rate of MC scattering events is higher than boundary scattering and resistive scattering, the MC collisions will redistribute momentum/energy of the quasiparticles over much shorter lengths than the resistive collisions. As a consequence, some discrepancies between QP located at different distances from the boundaries of the channel emerge. This is the hydrodynamic regime of transport which was first described by R.N. Gurzhi [13].

In a purely hydrodynamic regime, resistive scattering is entirely suppressed and dissipation occurs only at the boundaries. The further away the electron is from the boundaries, the hardest the MC collisions will make it for the QP to find a path to the boundaries of the system. Consequently, the further away from the boundary the QP is, the more unlikely it is to undergo a dissipative collision. The profile of velocity of the QP in the channel thus depends on the position of the QP in the channel : the velocity profile becomes parabolic (Fig.7.1.b). This regime is reminiscent of the flow of a viscous liquid in a pipe, i.e. a Poiseuille flow. Further developments of the implications of a hydrodynamic flow of QP from a theoretical standpoint were given recently [14, 15].

However, at finite temperature and whether it is for phonons or electrons, resistive scattering events are present. R. N. Gurzhi proposed that the hydrodynamic regime can survive under a particular hierarchy of scattering times which is detailed in inequation 7.1. This inequality is composed of 3 terms :  $\tau_N$  the scattering time between momentum-conserving collisions,  $\tau_R$  the one between resistive events and finally  $\tau_B$  the rate of boundary collisions. Following its definition, the hydrodynamic regime lays at the crossover between the diffusive and ballistic regimes.

$$\tau_N \ll \tau_B \ll \tau_R \quad (7.1)$$

Back in Chapter 2, we discussed the different regimes of phononic heat transport when we introduced the thermal conductivity of phonons in figure 2.3. Let us now focus on the hydrodynamic region. The thermal conductivity due to hydrodynamic phonons can grow up to a  $T^8$ -power law [37]. This high exponent power law is nonetheless never observed experimentally : U-scattering events are always present and only a fraction of the phonons fluid can enter the hydrodynamic regime. Yet, a viscous flow of phonons leads to  $\kappa_{phonons} \propto T^\gamma$ -dependent with  $\gamma > 3$ . For charge carriers, similar limits can be achieved. As an example, a change of sign of  $\frac{\partial \sigma}{\partial T}$  is predicted in the hydrodynamic regime. One of the signature of the viscous flow of electrons is an increase of the conductivity with increasing

temperature [146]. The possibility of measuring such a feature in an actual metallic system will be discussed later on. All in one, for all types of quasiparticle, the QP viscosity is associated with the rate of momentum-conserving collisions. If the viscosity is sufficiently high, the transport properties deviates from the 'simple' Boltzmann equation of transport which does not usually takes into account MC collisions. We will turn to experimental observations of electronic and phononic hydrodynamics.

### 7.1.2 An experimental challenge

The very first experimental observation of a hydrodynamic flow of quasiparticles in a solid came from thermal conductivity measurements in crystalline  $^4\text{He}$  by Mezhev-Deglin [147]. He revealed a size-dependent mean-free-path of phonons which increases with temperature in a temperature range squeezed between the ballistic and diffusive regimes of transport. Observations of phononic hydrodynamics, from similar signatures, have since been reported in a handful of systems :  $^3\text{He}$  [38], Bi [39], solid H [40],  $\text{SrTiO}_3$  [41] and Black P [42].

In the case of electron hydrodynamics, the first observation was reported in a 2D system by L. W. Molenkamp and M. J. M. de Jong [17]. More observations of hydrodynamic flow of electrons came only very recently and are still actively debated : graphene [19, 18],  $\text{PdCoO}_2$  [20] or  $\text{WP}_2$  [107]. All these studies report small hydrodynamic corrections to the electronic transport properties. Indeed, there are multiple difficulties preventing direct observation of electron hydrodynamics.

**$l_{MR} \ll \bar{s}$**  The emergence of a hydrodynamic regime of electrons is conditioned by a strong suppression of resistive collisions involving charge carriers. In all the aforementioned systems, the resistivity measurements revealed an electronic mean-free-path between resistive scattering events  $l_{MR}$  which is comparable to the size of the sample, i.e. ballistic electrons at low enough temperature.

**$l_{MC} \gg l_{MR}$**  The second length scale associated with the emergence of hydrodynamic effect in the flow of charge carriers is the mean-free-path between momentum-conserving collisions affecting electrons. Inequality 7.1 must be satisfied. Yet, there is no experimental determination of  $l_{MC}$  in the literature:  $l_{MC}$  was either ignored or evaluated from a theoretical model which provides an upper bound as defined in equation 7.2 [148].

$$l_{MC} = \frac{v_F}{\frac{k_b}{h} T_F \left(\frac{T}{T_F}\right)^2} \quad (7.2)$$

To set the state-of-the-art, we focus on this model first. According to this report,  $l_{MC}$  depends solely on  $T_F$  and the effective mass of the carriers. This is reminiscent of the thermal conductivity of  $^3\text{He}$ . We notice that the higher the Fermi temperature, the larger is the momentum-conserving mean-free-path of electrons. In this approximation, a viscous electronic flow is favored by a small Fermi temperature of the system. In summary, we should a priori expect to find hydrodynamic corrections in 'ultra-pure metals' with low Fermi temperature.

An example which illustrates this criterion is the absence of hydrodynamic corrections in the electrical resistivity of thin wires of potassium. Even though this system displays a very long resistive mean-free-path  $l_{MR} \gg \bar{v}$  [16], potassium has a high Fermi temperature  $T_F \approx 20000\text{K}$ . At low temperature,  $l_{MC} \approx l_{MR}$ . This result explains why there is no visible viscosity effects in thin wires of potassium. However, the most convincing evidence of hydrodynamic corrections to date was obtained in  $\text{PdCoO}_2$  which has a Fermi temperature  $T_F = 27000\text{K}$  [20]. We will now show how this study, through heat and charge transport measurements, gives quantitative details as to where one can expect to observe electronic hydrodynamic effects in a metal.

### 7.1.3 The case of $^3\text{He}$

The earliest reports on the experimental determination of the thermal conductivity of normal state liquid  $^3\text{He}$  were presented in the late 50s [149, 150]. They first showed that  $\kappa$  increases slowly with increasing temperature in the range  $T = 0.24\text{K}$  to  $T = 3.0\text{K}$ . A few years later, in an impressive experimental achievement, Anderson *et al* measured  $\kappa$  down to  $T = 20\text{mK}$  [151]. This experiment revealed the existence of a minimum in the thermal conductivity below which  $\kappa$  was found to increase with decreasing temperature down to the superfluid transition. This observation was confirmed by independent studies over a wide spectrum of pressure and temperature ranges [152–157].

We illustrate this result with one outstanding report by Greywall [158] in figure 7.2.a. It shows the thermal conductivity of normal liquid  $^3\text{He}$  along isochores for  $7\text{mK} < T < 1\text{K}$  and  $0 < P < 30\text{mbar}$ . The precision of this study is an order of magnitude higher than what was reported before.  $\kappa$ , as a function of temperature for different  $^3\text{He}$  densities, is shown in figure 7.2.a. Starting from  $T = 1\text{K}$ ,  $\kappa$  decreases as  $\sqrt{T}$  with decreasing temperature down to  $T \approx 100\text{mK}$ , where it reaches a minimum. The amplitude and temperature of this minimum both depend on the  $^3\text{He}$  density. With further cooling,  $\kappa$  evolves as  $1/T$  down to the superfluid transition. In terms of thermal resistivity, this  $\kappa \propto T^{-1}$  is equivalent to  $(WT) \propto T^2$ . We indicate that the viscosity of normal liquid  $^3\text{He}$  was also studied down to a few mK. An example, from Black *et al.* is shown in figure 7.2.b. Over the same range of

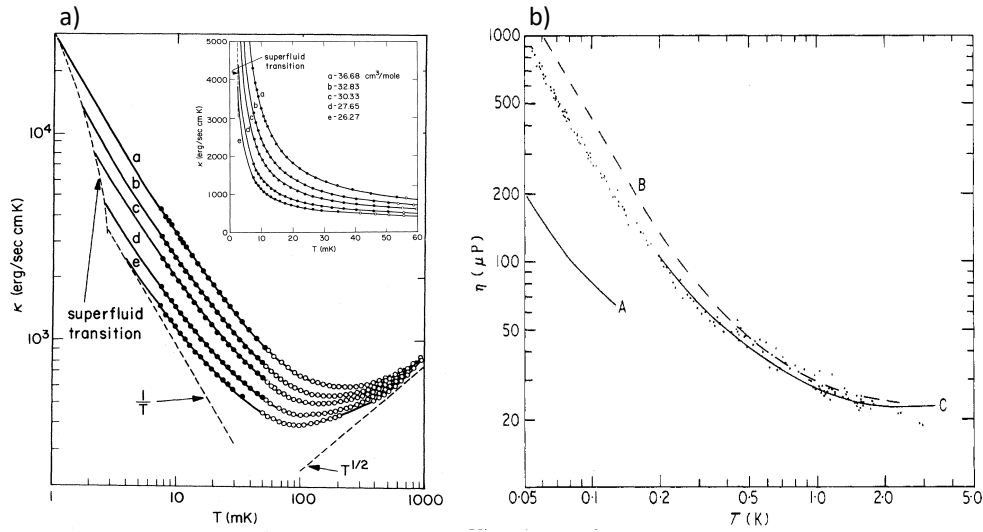


Fig. 7.2 **a)** Thermal conductivity of liquid normal  $^3\text{He}$  as a function of temperature. The different curves correspond to different  $^3\text{He}$  densities while the solid and open circles indicate two different experimental setups for the measurement. Inset show the  $T < 60\text{mK}$  region in a linear scale. Data from Greywall [158]. **b)** Viscosity as a function of temperature for liquid normal  $^3\text{He}$ . Experimental points by the  $45^\circ$  phase method for pure  $^3\text{He}$ . Curve A represents a saturated solution of  $^3\text{He}$  in  $^4\text{He}$ , curve B represents pure  $^3\text{He}$  by Betts *et al.* [159, 160]. Curve C represents a solution of around 5%  $^4\text{He}$  in  $^3\text{He}$ .

temperature as the thermal conductivity, the viscosity of liquid normal  $^3\text{He}$  is proportional to  $T^{-2}$ .

The temperature dependence of  $\kappa$  and  $\eta$  was already explained by the work of Abrikosov and Khatalinkov [161]. In 1959, they derived the transport equations for fermions in the framework of Landau's Fermi liquid theory. They showed the transport problem in the Fermi liquid to be formally identical to that of the Fermi gas. The transport coefficients were later computed exactly [162–164]. The thermodynamics and transport properties of  $^3\text{He}$  were consequently found to depend only on the amplitude of momentum-conserving two fermions scattering events, without any way to relax momentum. Let us illustrate the case of the thermal conductivity. According to the kinetic theory of gases, we can write equation 7.3 :

$$\kappa = \frac{1}{3} C_v \times v_F^2 \times \tau_Q \quad (7.3)$$

Here  $C_v$  is the volumetric specific heat,  $v_F$  is the Fermi velocity and  $\tau_Q$  is the characteristic time between quasiparticle collisions which contributes to the thermal resistivity. In the Fermi liquid theory, i.e. at very low temperature for a fermionic system,  $\tau_Q$  is proportional to  $T^{-2}$  because of the Pauli exclusion principle : only particles in a layer of thickness  $k_B T$

around the Fermi surface can scatter. The specific heat in the Fermi liquid theory is given by expression 7.4 where  $T_F$  is the Fermi temperature :

$$\frac{C_v}{R} = \frac{\pi^2 T}{2 T_F} \quad (7.4)$$

Being aware that the Fermi velocity is given by  $v_F^2 = 2k_B T_F / m^*$ , we wish to emphasize that, in this picture, the amplitude of the thermal resistivity due to fermion - fermion collisions depends only on the Fermi temperature and the effective mass of the quasiparticle.

As a conclusion, it has been known for half a century that in very low temperature  $^3\text{He}$ , the archetype of the Fermi liquid, normal inter-fermionic scattering events lead to a  $T^2$ -dependent thermal resistivity and a finite viscosity which scales as  $T^{-2}$ . We also indicate that in a Fermi liquid, the momentum-conserving electronic scattering rate is set by the temperature, the Fermi temperature of the system and the effective mass of the carriers.

## 7.2 Quantifying normal and resistive mean-free-paths of electrons

The problem of the experimental evaluation of the rate of boundary, momentum-conserving and momentum-relaxing scattering events affecting quasiparticles is crucial to the prediction of the hydrodynamic regime. In this section, we propose to evaluate the MC and MR mean-free-path respectively based on thermal conductivity and electrical resistivity measurements. We deduce from these results the temperature range which satisfies the hydrodynamic criterion in Sb and  $\text{WP}_2$ . The effect of impurities and sample-size on the hydrodynamic window will also be discussed.

### 7.2.1 Determination of a hydrodynamic temperature window

The possibility of a hydrodynamic flow of charge carriers was left aside in the previous chapters in the discussion on the origin of the discrepancy between heat and charge transport in Sb and  $\text{WP}_2$ . An abundance of small-q scattering events, associated with high energy dissipation and low momentum relaxation gives a satisfactory explanation for the observation of a particularly large deviation from the Wiedemann-Franz law at finite temperature in these systems. However, the observation of a 20-fold heat/charge transport dichotomy in a micro-ribbon of  $\text{WP}_2$  by Gooth *et al.* [107] had raised fundamental questions regarding the relevance of the scattering-based theory of charge and entropy transport by mobile electrons

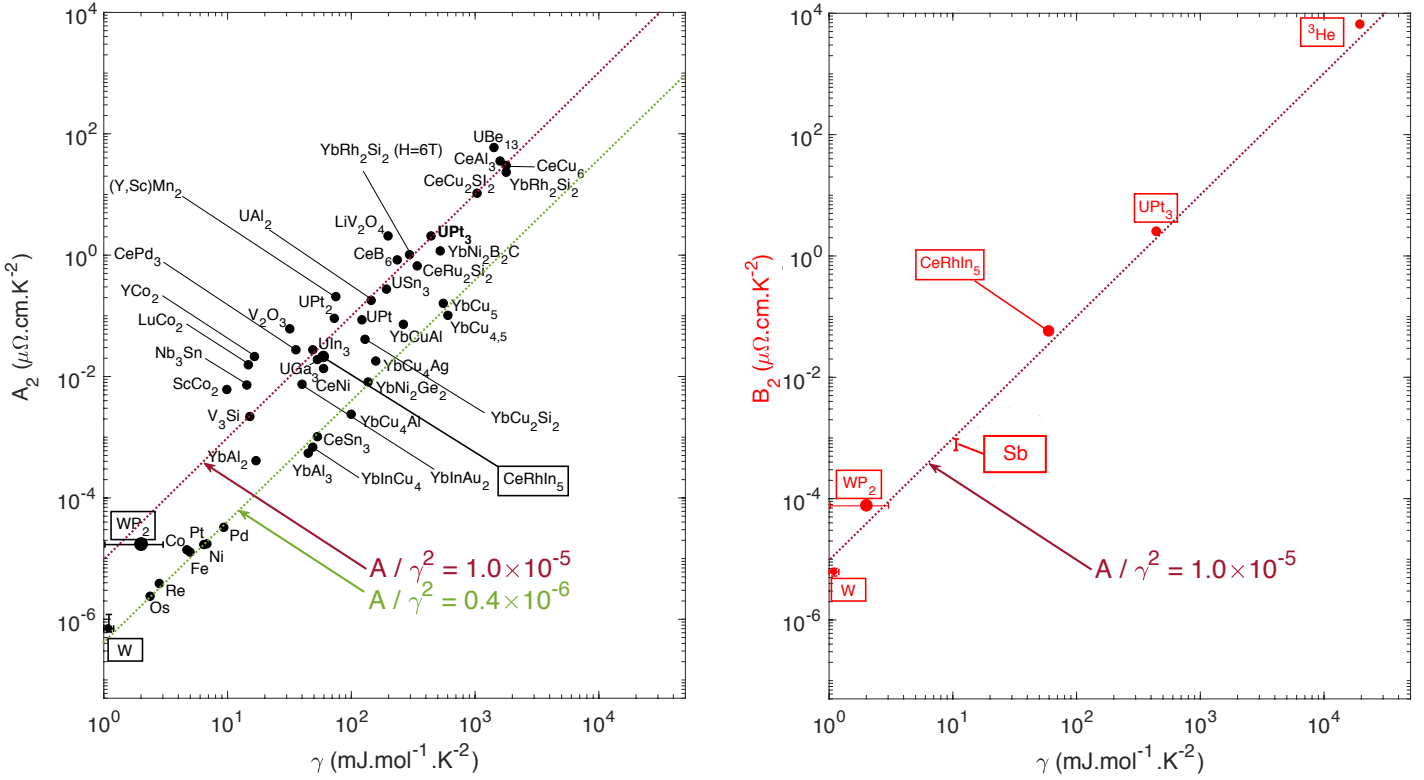


Fig. 7.3 **a**) The Kadowaki-Woods plot with  $A_2$  plotted as a function of fermionic specific heat  $\gamma$  (from  $C = \gamma T$ ) compiled by Tsujii *et al.* [166]. We have added the data for  $\text{WP}_2$  (This work),  $\text{W}$  [114] and  $\text{CeRhIn}_5$  [31, 167]. **b**) Plot of the  $B_2$  thermal  $T^2$ -prefactor as a function of fermionic specific heat  $\gamma$ . Data from  $^3\text{He}$  [158, 153, 168],  $\text{WP}_2$  (this work),  $\text{W}$  [114] and  $\text{CeRhIn}_5$  [31, 167] and  $\text{UPt}_3$  [32].

in this high mobility semi-metal. This result also came while the possible link between WFL breakdown and electron hydrodynamics was a subject of attention [21–24, 165].

We first turn to the case of normal state liquid  $^3\text{He}$ . In this liquid, fermionic collisions generate a thermal resistivity ( $WT$ ) =  $B_2 \times T^2$  in the absence of any momentum relaxation. Let us now present in Fig.7.3.b the magnitude of  $B_2$  (prefactor of the thermal  $T$ -square resistivity) for  $^3\text{He}$  alongside  $\text{CeRhIn}_5$ ,  $\text{WP}_2$  and  $\text{W}$  plotted as a function of  $\gamma$ , the fermionic specific heat. We notice that  $B_2$  scales with the universal Kadowaki-Woods plot (Figure ??a). This implies that, while  $A_2$  quantifies the size of momentum-relaxing collisions and  $B_2$  is a measure of energy-relaxing, yet momentum-conserving collisions, both scale roughly with the size of the phase space for fermion-fermion collisions, which (provided a constant fermion density) is set by  $\gamma^2$ . As a consequence, an alternate route can be used to explain the observation of  $B_2 > A_2$  both in  $\text{WP}_2$  and  $\text{Sb}$ : momentum-conserving collisions contribute to electronic transport.

### 7.3 Discussion on the emergence of a hydrodynamic electronic transport properties in WP<sub>2</sub> and Sb

We have shown in the previous section how an alternate route to the emergence of  $T^2$  thermal resistivity can be deduced from the physics of <sup>3</sup>He. We will use this analogy to discuss the implication of a strong mismatch in  $T^2$ -prefactors of thermal and electrical resistivities in WP<sub>2</sub> and Sb.

#### 7.3.1 Study of possible hydrodynamic signatures in WP<sub>2</sub>

**Hydrodynamic window** In respect to the chronology of this study, we first discuss the case of WP<sub>2</sub>. We turn to figure 7.4 to discuss the relative weight of momentum-conserving, momentum-relaxing and boundary scattering events in WP<sub>2</sub>. These data, previously shown in figure 5.4 and figure 5.5, reveal that at a finite temperature close to  $T = 9\text{K}$  :  $B_2 \times T^2 \approx \rho_0 = W_0 T \gg A_2 \times T^2$ . In other words, in this temperature region, momentum-conserving and boundary scattering events happen at a much higher rate than momentum-relaxing collisions : electrons are within the hydrodynamic hierarchy of scattering times. We can use the Drude model to approximate the characteristic frequencies associated with each type of scattering processes :  $f_{MC}$ ,  $f_{MR}$  and  $f_{boundaries}$ .

The resulting frequencies are plotted in figure 7.5.a. As temperature increases, the frequencies of MR and MC collisions increase. We define  $T_1$  as the temperature where  $f_{MC} = f_{boundaries}$  and  $f_2$  as the temperature where  $f_{MR} = f_{boundaries}$ . For WP<sub>2</sub>,  $T_1 = 10.3\text{K}$  and  $T_2 = 15.8\text{K}$ . For  $T < T_1$ , boundary scattering dominates transport. This is the ballistic regime of transport. For  $T > T_2$ , momentum-relaxing scattering events are the most frequent; this is the diffusive regime. However, for  $T_1 < T < T_2$ , momentum-conserving collisions are more frequent than boundary scattering which are more frequent than momentum-relaxing scattering events. For  $T_1 < T < T_2$ , the hydrodynamic requirement is satisfied in this WP<sub>2</sub> sample. Figure 7.5.a can be seen as a different illustration of the result yielded by figure 7.4 : the sample of WP<sub>2</sub> presented in Chapter 5 can enter the hydrodynamic regime. We note that, in the case of WP<sub>2</sub>, the hydrodynamic window coincides with the observed 20-fold decrease of  $L/L_0$  (at  $T = 13\text{K}$ ) [107] and our observation of a 4-fold decrease. This minimum is then associated with an excess of momentum flow in comparison to energy flow. In the hydrodynamic scenario, this coincidence is not an accident but rather a signature of the hydrodynamic flow of electrons. Figure 7.5 emphasizes that the position and the width of this hydrodynamic window are not solidly set. So far, we assumed that the residual resistivity of WP<sub>2</sub> was entirely due to boundary scattering. However, nothing is perfect in reality, so we

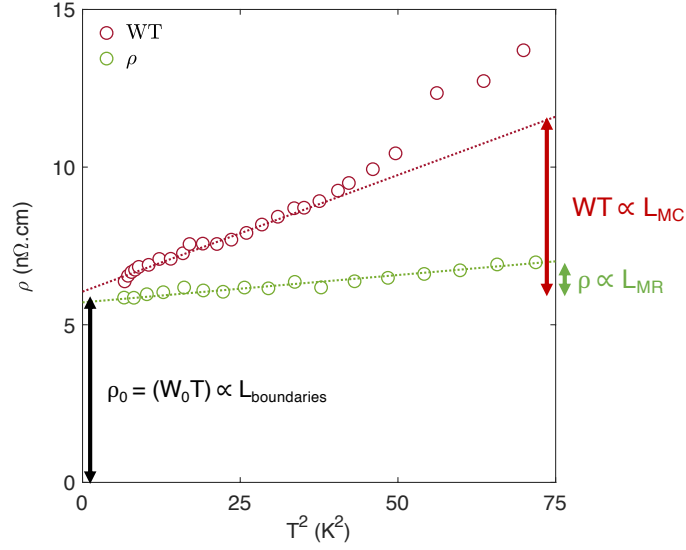


Fig. 7.4 Electrical resistivity  $\rho$  and thermal resistivity ( $WT$ ) plotted as a function of  $T^2$  for WP<sub>2</sub>. The arrows indicate the value of the residual resistivity  $\rho_0 = W_0T$ , the  $T^2$  electrical resistivity (associated with MR scattering)  $\rho$  at  $T^2 = 75\text{K}^2$  and the  $T^2$  thermal resistivity (associated with MC collisions) at  $T^2 = 75\text{K}^2$ . We observe that in the vicinity of  $T^2 = 75\text{K}^2$ , MC and boundary collisions dominates strongly over resistive scattering.

have to consider that the residual resistivity  $\rho_0$  contains a sizable component due to impurity scattering. In this case, one must write:

$$\rho_0 = \rho_{00} + \rho_{imp} \quad (7.5)$$

Here,  $\rho_{00}$  is due to boundary scattering whereas  $\rho_{imp}$  results of impurities and defects. We illustrate the effect of impurity scattering in the case of WP<sub>2</sub> in Figure 7.5. It represents the frequency of each scattering processes as a function of temperature. When  $\rho_{00}$  only represents 75% (Fig7.5.b)), one can still encounter a temperature range which satisfies Gurzhi's criterion. The hydrodynamic window is shifted to lower temperatures and gets narrower. However, if  $\rho_{00}$  becomes 50% (Fig7.5.c)) of the residual resistivity, then there is no range of temperature which allows the emergence of a hydrodynamic regime in WP<sub>2</sub>.

We reach here one of the main results of this study. In light of previous reports on the thermal conductivity of <sup>3</sup>He, the observation of a five-fold mismatch between thermal and electrical  $T^2$ -prefactors indicates the existence of a finite temperature window where momentum-conserving collisions outweigh the resistive ones and, as a consequence, where Gurzhi's hydrodynamic criterion is satisfied. We also emphasize that the hydrodynamic

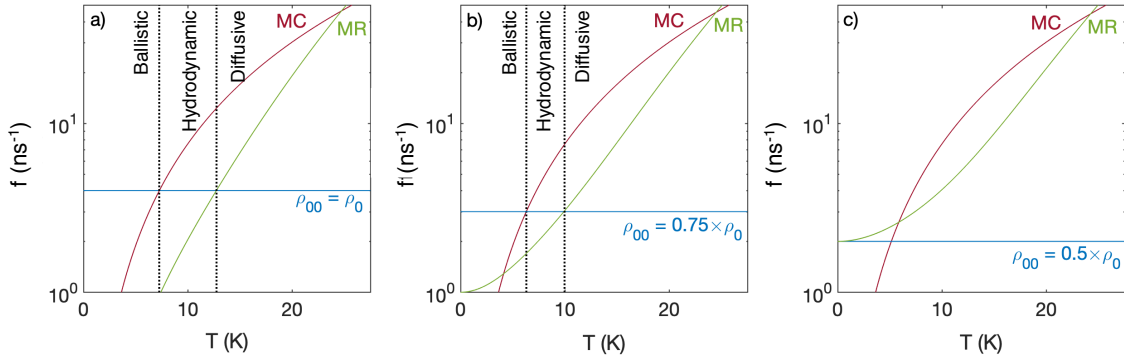


Fig. 7.5 The magnitude of  $B_2T^2$ , proportional to momentum-conserving (MC) electron-electron collisions is compared to  $A_2T^2 + A_5T^5$ , which is proportional to momentum-relaxing electron-phonon collisions and to boundary scattering described by  $\rho_{00}$ . A limited window where the hydrodynamic hierarchy is satisfied can be found for the three following cases. a)  $\rho_0$  is solely due to boundary scattering. b)  $\rho_{00}$ , due to boundary scattering, represents 75% of the total residual resistivity. c)  $\rho_{00}$ , represents 50% of the total residual resistivity.

regime of electrons is expected to occur in a finite temperature window squeezed between the ballistic and diffusive regimes and that the hydrodynamic window is fragile and not solidly set.

**Review of hydrodynamic signatures in  $WP_2$**  The hydrodynamic interpretation of the large heat/charge dichotomy in  $WP_2$  was initiated by Gooth *et al.*. We remind that they reported, from 2-points measurements, a 20-fold deviation from the WFL below  $T = 20K$  with no sign of recovery of the Wiedemann-Franz law down to  $T = 5K$  in a micro-ribbon (width =  $2.5\mu m$ ) of  $WP_2$ . Let us discuss this result and compare the two possible interpretations. To do so, we first assume  $f_{MC}$  and  $l_{MR}$  to be independent of the sample size in  $WP_2$ . With a sample about 50 time thinner than the one presented in this work,  $f_{boundaries}$  will be importantly increased ( $\rho_{0,2.5\mu m} \approx 100n\Omega.cm$ ). Adding this boundary mean-free-path on the figure 7.5, we observe that the hydrodynamic window closes for the micro-ribbon. From this first approach, we would not expect hydrodynamic effects in a micro-ribbon of  $WP_2$ . But as we will see through the example of Sb, the assumption of size-independent  $f_{MC}$  and  $f_{MR}$  may be wrong. Another observation which casts a shadow on the hydrodynamic interpretation is the absence of recovery of the WFL down to  $T = 5K$ . As we have underlined, the hydrodynamic regime emerges at the crossover between ballistic and diffusive regimes : a zero-temperature viscosity is not defined. In that sense, the absence of recovery of the Wiedemann-Franz law, which is a  $T \rightarrow 0K$  law, cannot be accounted for as an hydrodynamic signature. Lower temperature measurements would be required. We conclude that the emer-

gence of a hydrodynamic regime of electrons in WP<sub>2</sub> remains an open question. Both the semi-classical (Chapter 5) and hydrodynamic approaches are able to explain the experimental results obtained in WP<sub>2</sub>. On a final note, we wish to point out that the two solids in which an anomalously low  $L/L_0$  have been reported (W [114] and WP<sub>2</sub>) are those in which the  $T = 0$  ballistic limit is accessible and a hydrodynamic window can open up. Observation of hydrodynamic signatures in elemental tungsten is an unaddressed subject left for future research.

### 7.3.2 Size-dependence of the resistivity $T^2$ -prefactor in Sb

Benefiting from our experience on WP<sub>2</sub>, we turned to Sb to further probe the emergence of a hydrodynamic flow of electrons through electrical and thermal transport measurements. Contrary to the existing literature on electron hydrodynamics [20, 19, 18, 17, 107], we chose to study millimetric Sb samples. This decision was motivated by the possibility to reach millimetric electronic mean-free-paths in Sb at low temperature with a Fermi temperature one order of magnitude lower. As discussed in chapter 6, both the electrical and thermal resistivity behaves as  $T^2$  for  $T < 8\text{K}$ . We can thus compare the residual,  $A_2T^2$  and  $B_2T^2$  resistivities in the thin ( $\bar{s} = 0.35\text{mm}$ ) and thick ( $\bar{s} = 2.24\text{mm}$ ) Sb samples respectively shown in figure 7.6.a and b. In both slabs,  $B_2T^2 \approx \rho_0 > A_2T^2$  around  $T = 10\text{K}$ . This result is reminiscent of what we have just observed in WP<sub>2</sub> : in the hydrodynamic scenario, inspired by the case of <sup>3</sup>He, a large fraction of electron-electron scattering events conserves momentum and this is the reason for  $B_2 > A_2$ . We will see below that this hydrodynamic interpretation is favored by the size dependence of the  $B_2/A_2$  ratio. In this study of different sizes of Sb samples, we observe a size-dependence of the  $T^2$ -prefactors of the electrical and thermal resistivities. Along with data from the literature [130, 133, 131, 128], the results are plotted as a function of sample size  $\bar{s}$  in figure 7.6. We observe that both  $A_2$  (electrical  $T^2$ -prefactor) and  $B_2$  (thermal  $T^2$ -prefactor) decrease with increasing size. The comparison of  $A_2$  and  $B_2$  as a function of size reveals the first observation a size-dependent  $A_2/B_2$  ratio, which decreases sharply with  $\bar{s}$  : from the small S1 to the large S3 samples we observe  $A_{2,Small} = 2.0 \times A_{2,Large}$  to  $B_{2,Small} = 1.1 \times B_{2,Large}$ . We can safely exclude magnetoresistance effect, self heating and crystal misorientation to account for this phenomenon. We also underline that the fitting parameters were consistent during the whole study, on a constant temperature range ( $T = 2\text{K}$  to  $T = 8\text{K}$ ).

The observation of size-dependent  $A_2$  can be explained by the proximity to the electronic ballistic regime at low temperature. As an example, we point to studies on whiskers and thin films of metals, such as zinc [169] or cadmium [170]. They show evidence of dependence of the non-residual electrical resistivity with sample size. The smaller was the limiting

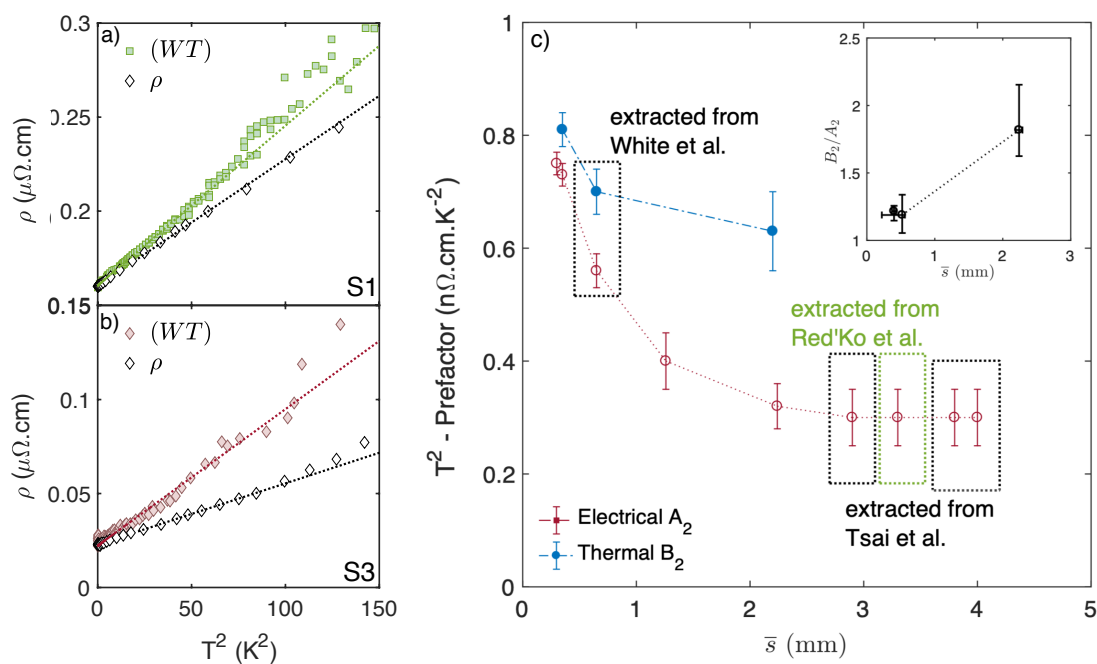


Fig. 7.6 **a)**  $\rho$  and  $(WT)$  plotted as functions of  $T^2$  in the thin Sb sample S1. **b)**  $\rho$  and  $(WT)$  plotted as functions of  $T^2$  in the large Sb S3. Both plots share a common x-axis. **c)**  $T^2$ -prefactors for the electrical ( $A_2$ ) and thermal ( $B_2$ ) resistivities as a function of the sample average cross section  $\bar{s}$ . Data from the literature [130, 131] are featured and indicated directly on the plot. Inset shows the evolution of the  $B_2/A_2$  ratio size.

dimension of the sample, the higher was the prefactor of the  $T$ -dependent part. The thickness dependence of  $B_2$  can be explained in a similar picture. It is true that in the diffusive regime, the  $T^2$ -prefactor of the resistivity is only dictated by the Fermi energy of the system and therefore is expected to be independent of the sample size. In the ballistic regime, however, a fraction of electrons do not suffer any collisions with other electrons during their trajectory from one end of the sample to the other. The thicker the sample, the larger is the fraction of such electrons. The decrease in the magnitude of  $B_2$  can be ascribed to the proximity of the ballistic regime. However, we notice that compared to  $A_2$ ,  $B_2$  displays much weaker thickness dependence (see inset figure 7.6.c). This is hard to explain in a scattering-based picture in which  $A_2$  and  $B_2$  would be affected in the same manner. In the hydrodynamic picture, on the other hand, if  $B_2$  is mainly set by the rate of momentum-conserving collisions, it would barely change with the thickness. Therefore the size-dependent  $B_2/A_2$  ratio strongly suggests a that a  $T^2$ -dependent thermal resistivity emerges in Sb due to MC electronic collisions.

In this hydrodynamic framework, we can evaluate the viscosity  $\eta$  of the electronic fluid in Sb. We present a first estimation of  $\eta$  from the kinetic theory of gases, detailed in equation 7.6, however we mention the existence of more through theoretical models describing the viscosity of the electron fluid at low temperatures [20, 15].

$$\eta = \frac{1}{3} l_e \hbar n^{4/3} (3\pi^2)^{1/3} \quad (7.6)$$

We find a dynamic viscosity  $\eta = 0.7$  cP in sample S3. This value is comparable to the dynamic viscosity of water at 30°C, similar to the viscosity of the electron fluid in PdCoO<sub>2</sub> [20] and an order of magnitude higher than what is reported in WP<sub>2</sub> [107]. We note that the electronic mean-free-path is an order of magnitude larger and the carrier density is orders of magnitude lower in Sb in comparison with PdCoO<sub>2</sub>. Remarkably, the order of magnitude of the dynamic viscosity is comparable. To conclude, the observation of a size-dependent  $A_2$  prefactor can be explained in a semi-classical context by the proximity with the ballistic regime. However, we report here the first observation of a size-dependent  $A_2/B_2$  ratio. We associate this feature with a deviation from the Boltzmann transport equation and point to the existence of an hydrodynamic regime of electrons in millimetric Sb samples.

### 7.3.3 Discussion on the thermal conductivity of phonons in Sb

Let us now discuss the flow of phonons in Sb. Just like the case of electrons, the emergence of a hydrodynamic regime of phonons is possible in-between ballistic and diffusive regimes [37]. In contrast to the case of electrons, for phonons, Umklapp scattering vanishes exponentially with temperature whereas normal scattering follows a power law [171]. This difference makes

phonon hydrodynamics more easily identifiable than its electronic counterpart. In this section, we report on the observation of a signature of phonon hydrodynamics in Sb : a strongly size-dependent and non-monotonous phonon mean-free-path over a finite temperature range. While the size-independent regime at higher temperature is easily understood in the diffusive picture, the absence of size-effect at lower temperature reveals that phonons remain far from the ballistic regime down to  $T = 0.08\text{K}$ .

### Size-dependent phonon mean-free-path

We first present the evolution with temperature of the mean-free-path associated with lattice vibrations in different size of Sb samples. This phonons mean-free-path,  $l_{\text{phonons}}$ , is defined through equation 7.7 where  $v_s$  is the speed of sound. The speed of sound along the bisectrix direction in Sb is quasi-constant over the temperature range of this study [172]). We will pursue with the following value :  $v_s = 3420\text{m.s}^{-1}$ . The mean-free-path of phonons is then determined by the ratio of  $\kappa_{\text{phonons}}$  and  $C_{\text{phonons}}$ .

$$l_{\text{phonons}} = \frac{3 \times \kappa_{\text{phonons}}}{C_{\text{phonons}} \times v_s} \quad (7.7)$$

We have previously demonstrated that  $\kappa_{B\text{-saturated}} = \kappa_{\text{phonons}}(B) \approx \kappa_{\text{phonons}}(B = 0\text{T})$ . The second quantity at play here is the specific heat of phonons. We also discussed its evolution with temperature and observed a deviation from the  $T^3$  behavior in chapter 5. Now, in order to compare the relative evolution of the phonons thermal conductivity and the phonons specific heat with temperature, we plot both of them on a common x-axis in figure 7.7 a and b. Both quantities deviate from  $T^3$  over different temperature ranges. As a consequence, the anharmonic behavior of  $C_v$  does not cancel out the variation of  $\kappa_{\text{phonons}}$  with temperature. This leads to the phononic mean-free-path represented as a function of temperature in figure 7.7.c. This plot contains results from this study alongside other extracted and analyzed from previous reports on millimetric samples by Blewer et al. [133] and White et al. [33] (red markers).

Starting from  $T = 80\text{mK}$ , we notice  $l_{\text{phonons}}$  to be smaller than the sample size in both S1 and S3. With increasing temperature,  $l_{\text{phonons}}$  decreases. All samples show the same size-independent phonon mfp up to  $T = 500\text{mK}$ . The data extracted from the literature, match remarkably well our data. Upon further heating,  $l_{\text{phonons}}$  reaches a minimum, then followed by a strong increase which leads to a local maximum. We illustrate these variations in the case of the large Sb sample S3. A local minimum of  $l_{\text{phonons}} = 15.8\mu\text{m}$  is reached at  $T = 1.55\text{K}$ . It is followed by a local maximum of  $l_{\text{phonons}} = 59.0\mu\text{m}$  at  $T = 5.46\text{K}$ . The temperatures of both extrema are shifted to lower values and the ratio maximum to minimum mfp gets

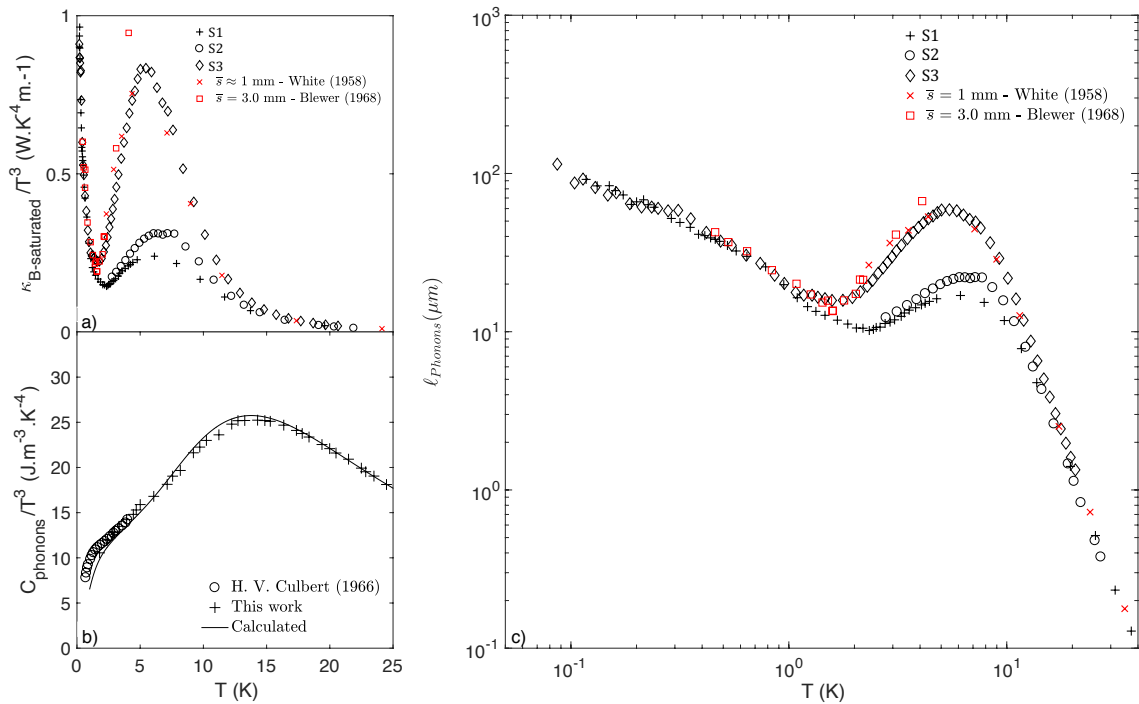


Fig. 7.7 **a)** Phonon thermal conductivity plotted as  $\kappa_{ph}/T^3$  for the three Sb samples (S1,S2,S3). Additional data extracted from the literature is also featured [33, 133]. **b)** Phononic part of the specific heat plotted as  $C_{phonons}/T^3$ . Data taken from [140] are also featured. **c)** Phonons mean-free-path  $l_{phonons}$  plotted as function of temperature for the same samples presented in a). The sound velocity was assumed to be  $v_s = 3420$  m.s<sup>-1</sup>.

larger as the size of the sample increases. In this temperature range, the mean-free-path of the phonons shows a strong size dependence. Upon further increase of the temperature, i.e. after the local maximum,  $l_{\text{phonons}}$  drops monotonically with no size dependence. We conclude on the existence of a temperature window where the mean-free-path of phonons is size dependent, squeezed between regions where it is not. The origin of the non-monotonous variation of  $l_{\text{phonons}}$  with temperature will be discussed in light of prior reports on phonons hydrodynamics in the next section.

### Hydrodynamic features of phonons heat transport in Sb

Let us first recall the thermal conductivity of InAs developed in chapter 3. We have shown that  $\kappa$  is due to phonons and varies with temperature as  $T^3$  up to  $T = 3\text{K}$ . At higher temperatures,  $\kappa/T^3$  decreases with further increasing temperature. This is understood by an increasing rate of Umklapp scattering of phonons with increasing temperature. For InAs,  $\kappa_{\text{phonons}}/T^3$  is a monotonous function of temperature.

In comparison, the example of InAs underlines the unusual evolution with temperature of  $l_{\text{phonons}}$  in Sb : over a finite temperature range, an increasing temperature leads to an increase of the phonon mean-free-path. This observation is reminiscent of what is predicted, and observed, in the case of a hydrodynamic flow of phonons. Just like in the case of electrons, if the hydrodynamic criterion is met, the normal collisions dominate phononic transport and reduce the fraction of quasiparticles which is able to reach the boundaries (where relaxation occurs). With further increase of the temperature, U-scattering of phonons sets in and marks the end of the hydrodynamic regime. As a consequence, one expects the phonon mean-free-path to have a local minimum at the onset of the hydrodynamic regime when the ballistic regime ends, i.e. a Knudsen minimum, followed by a local maximum when the diffusive regime sets-in : a Poiseuille peak. We turn to the previously reported signatures of phonon hydrodynamics for comparison. The variation of  $l_{\text{phonons}}$  with temperature for different sizes of Black P (a), Bi (b) and solid  $^4\text{He}$  systems is shown in figure 7.8. We observe that all systems display a Knudsen minimum and a Poiseuille peak. The hydrodynamic regime is set between these extrema and revealed by a clear signature : a size-dependent  $l_{\text{phonons}}$ . This is similar to what we observe in Sb. The effect is shifted to lower temperature with higher effect upon increasing size of the sample, similarly to what is observed in black P [42]. Moreover, in all but one of these compounds, the variation of  $l_{\text{phonons}}$  in the hydrodynamic regime does not exceed 50% while it reaches 400% in the large Sb sample. Only one study on solid  $^4\text{He}$  [147], featured in figure 7.8.c, shows a comparable size effect as the one we report here in Sb.

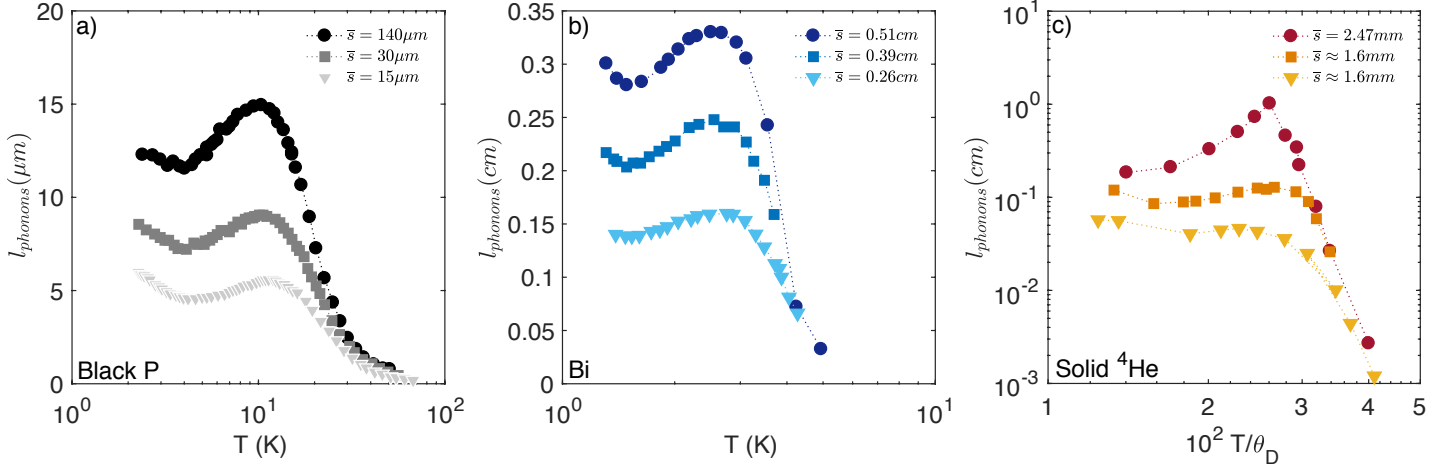


Fig. 7.8 **a)** Mean-free-path of phonons  $l_{phonons}$  plotted as a function of temperature for different size of Black P samples. Data from Machida *et al.* [42]. **b)**  $l_{phonons}$  plotted as a function of temperature for different size of Bi samples. Data from Kopylov *et al.* [39]. **c)**  $l_{phonons}$  plotted as a function of temperature for solid  $^4He$  grown in different sizes of ampoules. Data from L.P. Mehzov-Deglin [147].

We reach here the first conclusion of this section : the mean-free-path of phonons in Sb presents a signature of hydrodynamic phonons. Furthermore, the fourfold hydrodynamic correction found in Sb is one of the largest reported.

Nonetheless, the sub-Kelvin evolution of  $l_{phonon}$  mitigates this straightforward hydrodynamic interpretation. Below the hydrodynamic temperatures, the mean-free-path of the phonons in Sb presents no size dependence. This result implies that the ballistic regime of phonons is not reached yet, while we have seen that  $\kappa_{phonons} \propto T^3$  below  $T = 0.25K$ . The reports on Bi, Black P or He show clear evidence of ballistic phononic heat transport below the hydrodynamic temperature window (see Fig.7.8). This observation makes any conclusion on the emergence of a Poiseuille flow of phonons arguable : how can a crossover regime emerge if the crossover does not take place ? An answer to this question is revealed by another result we presented in chapter 5 : the emergence of  $1/B$ -periodic oscillations of  $\kappa_{ph}$  with the magnetic field. We showed that all acoustic phonons are able to scatter holes from one LL to another at  $T < T_{e-phonon} \approx 30K$  in Sb. These scattering events affect the flow of phonons and, a priori, affect  $l_{phonon}$ . Also, this phenomenon is set by  $k_F$ , so we expect it to be size-independent. Below the hydrodynamic window, we observe a regime of phononic transport which is limited not by the boundaries (ballistic) but by the scattering off the holes. Similar phenomenon is not observed in Black P, Bi or others due to lower carrier concentration : the regime  $q_{phonons} = 2k_F$  implies a larger length associated with

electron - phonon interaction than it does in Sb. Our observations can appear as paradoxical at first glance : on one side we observe a strong signature of a Poiseuille flow of phonons (comparable to what is observed in an insulator) which requires a strong suppression of MR scattering events to allow for MC scattering to dominate transport. On the other side we have shown a clear signature of resistive processes affecting the flow of quasiparticles. The apparent contradiction between these two results was addressed from a theoretical standpoint, by the possibility of the emergence of a second sound in a semiconductor [173] or an 'electron sound' in metals [146]. The former reveals that in a semiconductors, interaction with electrons can favor the emergence of a hydrodynamic flow of phonons. The latter proves that phonons can increase the rate of momentum-conserving inter-electrons collisions. Both conclusions require the system to be close to perfect compensation (which is the case for Sb). As a consequence, the observation of hydrodynamic features both for electrons and phonons are not antinomic. Even further, the onset of a strong hole-phonon interplay, with abundant N-collisions, can favor the hydrodynamic corrections and give hints to understand why the phonon hydrodynamic correction is larger in antimony than in other systems. As an example, the idea of a strongly interacting incoherent electron-phonon "soup" has been invoked to account for the unusual transport properties of YBCO [174].

### **Conclusion on the hydrodynamic regime in semimetals**

We previously associated the strong dichotomy between heat and charge transport to the angle-selectivity of electronic collisions. However, the thermal conductivity of normal-state liquid  $^3\text{He}$  reveals an alternate source of  $T^2$ -thermal resistivity : momentum-conserving collisions. The  $T^2$  thermal resistivity prefactor becomes a measure of energy-relaxing, yet momentum-conserving collisions and scales roughly with the size of the phase space for fermion-fermion collisions. This interpretation grants a direct access to the values of the scattering times involved in Gurzhi's hydrodynamic hierarchy. Looking back at our report on the heat and charge transport properties of  $\text{WP}_2$ , we show that the hydrodynamic regime is a priori favored by the abundance of momentum-conserving collisions in regard of boundary and momentum-relaxing collisions. Yet, no unequivocal signature of hydrodynamic effects has been reported to this day. Our study of millimetric Sb is more intriguing. In a context where the hydrodynamic criterion is satisfied, we report on a size-dependent  $T^2$ -prefactors ratio (electrical to thermal). To the best of our knowledge, this is the first instance of such observation which can only be explained in a hydrodynamic framework. It is however easier to satisfy the basic condition for a fully developed hydrodynamic regime for phonons than it is for electrons. Focusing on the thermal conductivity of phonons in Sb, we the existence of a temperature window where the mean-free-path of phonons becomes size-dependent

and increases with increasing temperature. We associate this phenomenon with a strong hydrodynamic correction, which only compares in amplitude with one report on solid  $^4\text{He}$ . Our claim of the observation of a hydrodynamic regime of phonons is however questioned by the absence of recovery of a ballistic regime of phonons down to  $T = 80\text{mK}$ . In light of prior reports on the lattice thermal conductivity of Sb and the observation of oscillations of the phonons thermal conductivity, we conclude that scattering between holes in Landau levels and phonons, favored at low temperature, induces an intrinsic length scale, smaller than all the samples of this study, which sets the low temperature phononic mean-free-path. As a conclusion, we report on the simultaneous hydrodynamic regimes of electrons and phonons in millimetric Sb samples.



# Chapter 8

## Conclusion

---

Throughout the three years of this study we addressed the broad subject of the charge and heat transport properties of low electronic density metals. Two main thematics stood out. The first deals with the existence of an ubiquitous ground state of 3D metals beyond the quantum limit; the second with the microscopic nature of the finite temperature violation of the Wiedemann-Franz law in semi-metals.

The first part was motivated by the observation of a succession of field-induced phase transitions in the deep quantum limit of graphite [61]. The quantum limit corresponds to the confinement of all electrons in the lowest Landau level under a sufficiently large magnetic field. In order to test the possibility of a universal phase diagram of 3D metals in the quantum limit, we turned to other low electronic density metals. The only systems which display a sufficiently low carrier concentration to allow an experimental study beyond the QL are found amongst the semi-metals and narrow gap semi-conductors. We refer to them as dilute metals. In particular, the III-V semi-conductor InAs appears as a great candidate to test our hypothesis : with a spherical single pocket Fermi surface located at the  $\Gamma$ -point of the BZ, InAs differs from graphite. Also, its transport properties had not been thoroughly investigated : previous studies only located the QL at  $B = 4\text{T}$  and reported on a sharp increase of the transverse magnetoresistivity in the deep quantum limit [8]. We measured the transverse, longitudinal and Hall resistivity of InAs down to  $T = 50\text{mK}$  and up to field as high as  $B = 56\text{T}$ . We show that an energy gap opens up in all three resistivities and increases monotonously up to  $B = 56\text{T}$ . This result is in contrast with the co-existence of a gapped out-of-plane resistivity and in-plane metallicity in graphite. In the case of InAs, we associated the opening of the gap with the 'magnetic freeze-out' of the electrons [78]. In graphite, the field-induced states have been attributed to a density wave driven by the electron - electron interaction

[25]. Both systems exhibit a field-induced state, but we conclude that the nature of the ground states differs from one system to another. This observation shows that the fate of a 3D electron gas deep in the quantum limit is not universal. Also, our discovery of a linear temperature-independent magnetoresistivity accompanied by vanishing thermoelectric coefficients at high-field in InAs points to the existence of a surface conduction channel in this system. This result echoes the explanation of the peculiar in-plane metallicity of graphite : the development of edge-state transport, which is expected to develop in the presence of a bulk gap [175, 61] and has been experimentally reported as a manifestation of the 3D quantum Hall effect in ZrTe<sub>5</sub> [98].

The second part of this thesis deals with the dichotomy between heat and charge transport observed in the vicinity of the ballistic regime in semi-metals. The starting point was a report by Gooth *et al.* [107] which pointed to an unprecedentedly large finite temperature violation of the Wiedemann-Franz law, with no sign of recovery down to  $T = 5\text{K}$ , in a micro-ribbon of WP<sub>2</sub>. This feature was associated with the emergence of a hydrodynamic regime of electrons. The premises of this regime were fixed by R.N. Gurzhi [13]; it requires a specific hierarchy of scattering times between momentum-conserving  $\tau_{MC}$ , momentum-relaxing  $\tau_{MR}$  and boundary scattering  $\tau_{Boundaries}$  affecting the quasiparticles :  $\tau_{MC} \ll \tau_{Boundaries} \ll \tau_{MR}$ . The first observation of a hydrodynamic flow of electrons was reported in a 2D system in the 90s [17] but it gained most of its attention more recently due to theoretical predictions [22, 23, 21] and its experimental observation in graphene [19] as well as a 3D system, PdCoO<sub>2</sub> [20]. Yet, the work of Gooth *et al.* was the first to establish a connection between a downward violation of the WFL and the possibility of a viscous flow of electrons.

Our four-terminal measurements of  $\kappa$  and  $\rho$  in three bulk needle-like single crystals (around 50 times thicker than the aforementioned work) confirms the observation of a quasi-unprecedentedly large downward deviation from the WFL in WP<sub>2</sub>. Around  $T = 2\text{K}$ , we observe the recovery of the WFL. We indicate that a downward deviation from the WFL at finite temperature in a metal is expected, whether it is because of inelastic electron - electron scattering like in heavy fermion systems [31, 32], or driven by electron - phonon collisions, as illustrated by our study of silver. Yet, the amplitude of the deviation in WP<sub>2</sub> only compares with one previous report in a high-purity W crystal [114]. To determine what was the microscopic origin of the deviation, we separated the different components of the electrical and thermal resistivities and showed that the  $T^2$ -prefactor of the thermal resistivity is 5 times larger than its electrical counterpart. We associate this mismatch with a particular abundance of small-angle electronic scattering, favored by the topology of the FS of WP<sub>2</sub>. We reach here a semi-classical explanation of the deviation from the WFL observed in WP<sub>2</sub>. Following our work, theoretical developments confirmed that clean compensated metals, do

not have, a priori, any lower boundary to their Lorentz ratio [120]. However, this conclusion was not the end of the story.

At sufficiently low temperature, the thermal conductivity of normal-state liquid  $^3\text{He}$  adopts a  $T^{-1}$  behavior, i.e. a  $T^2$ -dependent thermal resistivity emerges solely because of momentum-conserving fermion-fermion collisions. This observation becomes striking when added to the well-known Kadowaki-Woods plot (see figure 7.3) and yield one of the main result of this thesis : an alternate route to the  $B_2 \times T^2$  thermal resistivity we reported in  $\text{WP}_2$ . In addition to  $^3\text{He}$ , we observe that the prefactor of the  $T^2$ -thermal resistivity,  $B_2$ , reported in  $\text{CeRhIn}_5$  [31],  $\text{UPt}_3$  [32] or from our work on  $\text{WP}_2$  [110], all scale with the size of phase space for electron - electron collisions. In this framework, we can now associate this contribution to thermal resistivity with momentum-conserving yet energy-relaxing electronic collisions. Based on these observations, we can discuss the relative rate of MC, MR and boundary collisions. We establish that a temperature window which satisfies the hydrodynamic criterion opens up in  $\text{WP}_2$ , at the crossover between the ballistic and diffusive regimes. This interval of temperature is however narrow and highly sensitive to impurity scattering and we emphasize that a finite temperature downward deviation from the WFL in a compensated metal is not, by itself, a signature of hydrodynamic electronic transport. In light of our work on  $\text{WP}_2$ , we decided to further investigate the emergence of hydrodynamic effects in other semi-metals, with a lower Fermi temperature but equivalent purity. This choice was motivated by the predicted increase of the electronic viscosity of a Fermi liquid with decreasing  $T_F$ .

With a carrier density two orders of magnitude lower than  $\text{WP}_2$  and residual resistivities comparable to that of the  $\text{WP}_2$  needles, millimetric-Sb samples appeared as the adequate candidates. Contrary to the state-of-the-art work on electron hydrodynamics which has been reported in mesoscopic sized systems [107, 20, 19], we chose to work with large samples to suppress boundary scattering and explore phonon hydrodynamics as well. Unlike the case of  $\text{WP}_2$ , the phonon contribution to the thermal conductivity of Sb can not be neglected in regard of the electronic one. We were able to quantify both contributions.

Our study of the electronic fraction reveals the expected finite temperature violation of the WFL in Sb, reaching roughly half the amplitude of the one observed in  $\text{WP}_2$ . It is followed by a low temperature recovery of the WFL. Similarly to  $\text{WP}_2$ , a  $T^2$  thermal and electrical resistivity was determined at low temperature which, in the  $^3\text{He}$  scenario, reveals that the hydrodynamic criterion is satisfied in large Sb samples. We further measured different sizes of sample and observed one of the main result of this thesis : the evolution of the  $T^2$ -resistivities prefactors with sample size. While our report on a size-dependent  $A_2$  (electrical  $T^2$ -resistivity prefactor) can only account for a proximity to the ballistic regime

of electrons, our observation of a size-dependent  $B_2/A_2$  ratio (where  $B_2$  is the prefactor of the  $T^2$ -thermal resistivity) is a first and, to the best of our knowledge, not explained by the semi-classical theory. Rather, it fits the hydrodynamic narrative : as size increase, so does the rate of MC to MR electronic collisions. Yet, the amplitude of the hydrodynamic correction to electronic transport observed in Sb remain small. For future work, we pinpoint that high purity W samples present a ten-fold mismatch between  $T^2$  electrical and thermal prefactors as well as residual resistivity of the order of 100 p $\Omega$ .cm. In the hydrodynamic scenario, this makes W an even better playground than WP<sub>2</sub> or Sb for the study of electron hydrodynamics.

The phononic heat transport properties of Sb also shows the existence of strong hydrodynamic signatures, i.e. non-monotonous size-dependent evolution of the phonon mean-free-path over a finite temperature window. This observation was the initial illustration of the hydrodynamic flow of QP by Gurzhi [13], and previously reported in different solids [38–42]. The amplitude of the hydrodynamic correction observed in Sb exceeds almost all the others. The co-existence of hydrodynamic regimes of electrons and phonons can raise a few eyebrows : a Poiseuille flow of phonons requires a suppression of resistive events, yet we have shown evidences of resistive scattering of quasiparticles. This observation, supported by theoretical work [146], can be further probed by second sound measurements in Sb. In the context of perfectly compensated semi-metals, electron and phonon hydrodynamics can favor each other.

To conclude, this study of the charge and entropy transport of low electronic density metals relied on a variety of different energy scale. Through their comparison, we made some expected, yet previously unstated, connections between the physics of Helium 3, heavy fermions, hydrodynamic and field-induced metal-insulator transitions.

# References

- [1] N.W. Ashcroft and N.D. Mermin. *Solid State Physics*. Saunders College Publishing, Fort Worth, 1976.
- [2] TC Chi. Electrical resistivity of alkali elements. *Journal of Physical and Chemical Reference Data*, 8(2):339–438, 1979.
- [3] A Eiling and JS Schilling. Pressure and temperature dependence of electrical resistivity of pb and sn from 1-300k and 0-10 gpa-use as continuous resistive pressure monitor accurate over wide temperature range; superconductivity under pressure in pb, sn and in. *Journal of Physics F: Metal Physics*, 11(3):623, 1981.
- [4] AR Mackintosh. The fermi surface of metals. *Scientific American*, 209(1):110–121, 1963.
- [5] Martin JG Lee. The de haas—van alphen effect and the fermi surface of sodium. *Proceedings of the Royal Society of London. Series A. Mathematical and Physical Sciences*, 295(1443):440–457, 1966.
- [6] Andreas Hermann, Jürgen Furthmüller, Heinz W Gäggeler, and Peter Schwerdtfeger. Spin-orbit effects in structural and electronic properties for the solid state of the group-14 elements from carbon to superheavy element 114. *Physical Review B*, 82(15):155116, 2010.
- [7] JP Issi. Low temperature transport properties of the group v semimetals. *Australian Journal of Physics*, 32(6):585–628, 1979.
- [8] T. F. Rosenbaum, K. Andres, G. A. Thomas, and R. N. Bhatt. Sharp metal-insulator transition in a random solid. *Phys. Rev. Lett.*, 45:1723–1726, Nov 1980.
- [9] Nevill Mott. *Metal-insulator transitions*. CRC Press, 2004.
- [10] Nevill Francis Mott and Harry Jones. *The theory of the properties of metals and alloys*. Courier Corporation, 1958.
- [11] Xavier Blase, Etienne Bustarret, Claude Chapelier, Thierry Klein, and Christophe Marcenat. Superconducting group-iv semiconductors. *Nature materials*, 8(5):375, 2009.

- [12] B. N. Aleksandrov, V. V. Dukin, L. A. Maslova, and S. V. Tsivinskiĭ. Effect of Size and Temperature on the Electric Resistance of Antimony Single Crystals. *Soviet Journal of Experimental and Theoretical Physics*, 34:125, 1972.
- [13] R N Gurzhi. Hydrodynamic effects in solids at low temperature. *Soviet Physics Uspekhi*, 11(2):255, 1968.
- [14] Sean A Hartnoll. Theory of universal incoherent metallic transport. *Nature Physics*, 11(1):54, 2015.
- [15] Thomas Scaffidi, Nabhanila Nandi, Burkhard Schmidt, Andrew P. Mackenzie, and Joel E. Moore. Hydrodynamic electron flow and hall viscosity. *Phys. Rev. Lett.*, 118:226601, Jun 2017.
- [16] Z. Z. Yu, M. Haerle, J. W. Zwart, J. Bass, W. P. Pratt, and P. A. Schroeder. Negative temperature derivative of resistivity in thin potassium samples: The gurzhi effect? *Phys. Rev. Lett.*, 52:368–371, Jan 1984.
- [17] M. J. M. de Jong and L. W. Molenkamp. Hydrodynamic electron flow in high-mobility wires. *Phys. Rev. B*, 51:13389–13402, May 1995.
- [18] Jesse Crossno, Jing K Shi, Ke Wang, Xiaomeng Liu, Achim Harzheim, Andrew Lucas, Subir Sachdev, Philip Kim, Takashi Taniguchi, Kenji Watanabe, et al. Observation of the dirac fluid and the breakdown of the wiedemann-franz law in graphene. *Science*, 351(6277):1058–1061, 2016.
- [19] DA Bandurin, Iacopo Torre, R Krishna Kumar, M Ben Shalom, Andrea Tomadin, A Principi, GH Auton, E Khestanova, KS Novoselov, IV Grigorieva, et al. Negative local resistance caused by viscous electron backflow in graphene. *Science*, 351(6277):1055–1058, 2016.
- [20] Philip J. W. Moll, Pallavi Kushwaha, Nabhanila Nandi, Burkhard Schmidt, and Andrew P. Mackenzie. Evidence for hydrodynamic electron flow in pdcoo<sub>2</sub>. *Science*, 351(6277):1061–1064, 2016.
- [21] Victor Galitski, Mehdi Kargarian, and Sergey Syzranov. Dynamo effect and turbulence in hydrodynamic weyl metals. *Phys. Rev. Lett.*, 121:176603, Oct 2018.
- [22] Andrew Lucas, Jesse Crossno, Kin Chung Fong, Philip Kim, and Subir Sachdev. Transport in inhomogeneous quantum critical fluids and in the dirac fluid in graphene. *Phys. Rev. B*, 93:075426, Feb 2016.
- [23] Alessandro Principi and Giovanni Vignale. Violation of the wiedemann-franz law in hydrodynamic electron liquids. *Phys. Rev. Lett.*, 115:056603, Jul 2015.

- [24] Andrew Lucas and Sankar Das Sarma. Electronic hydrodynamics and the breakdown of the wiedemann-franz and mott laws in interacting metals. *Phys. Rev. B*, 97:245128, Jun 2018.
- [25] B Fauqué and K Behnia. Basic physics of functionalized graphite. *Springer International Publishing AG Switzerland*, pages 77–96, 2016.
- [26] Zengwei Zhu, Pan Nie, Benoît Fauqué, Baptiste Vignolle, Cyril Proust, Ross D. McDonald, Neil Harrison, and Kamran Behnia. Graphite in 90 t: Evidence for strong-coupling excitonic pairing. *Phys. Rev. X*, 9:011058, Mar 2019.
- [27] Sihang Liang, Satya Kushwaha, Tong Gao, Max Hirschberger, Jian Li, Zhijun Wang, Karoline Stolze, Brian Skinner, Bogdan Andrei Bernevig, Robert Joseph Cava, et al. A gap-protected zero-hall effect state in the quantum limit of the non-symmorphic metal khgsb. *Nature materials*, 18(5):443, 2019.
- [28] J.M. Ziman. *Principles of the Theory of Solids*. Cambridge University Press, 1972.
- [29] LD Landau. The theory of the fermi liquid. *Sov. Phys. JETP*, 3(6):920, 1957.
- [30] David Pines. *Theory of Quantum Liquids: Normal Fermi Liquids*. CRC Press, 2018.
- [31] Johnpierre Paglione, M. A. Tanatar, D. G. Hawthorn, R. W. Hill, F. Ronning, M. Sutherland, Louis Taillefer, C. Petrovic, and P. C. Canfield. Heat transport as a probe of electron scattering by spin fluctuations: The case of antiferromagnetic cerhin<sub>5</sub>. *Phys. Rev. Lett.*, 94:216602, Jun 2005.
- [32] Benoit Lussier, Brett Ellman, and Louis Taillefer. Anisotropy of heat conduction in the heavy fermion superconductor upt<sub>3</sub>. *Phys. Rev. Lett.*, 73:3294–3297, Dec 1994.
- [33] G. K. White and R. J. Tainsh. Lorenz number for high-purity copper. *Phys. Rev.*, 119:1869–1871, Sep 1960.
- [34] Mengliang Yao, Mona Zebarjadi, and Cyril P. Opeil. Experimental determination of phonon thermal conductivity and lorenz ratio of single crystal metals: Al, cu, and zn. *Journal of Applied Physics*, 122(13):135111, 2017.
- [35] Xiao Lin, Benoît Fauqué, and Kamran Behnia. Scalable t<sub>2</sub> resistivity in a small single-component fermi surface. *Science*, 349(6251):945–948, 2015.
- [36] AA Maznev and OB Wright. Demystifying umklapp vs normal scattering in lattice thermal conductivity. *American journal of physics*, 82(11):1062–1066, 2014.
- [37] H. Beck, P. F. Meier, and A. Thellung. Phonon hydrodynamics in solids. *Phys. stat. sol. (a)*, 24(1):11, 1974.

- [38] William C Thomlinson. Evidence for anomalous phonon excitations in solid He 3. *Physical Review Letters*, 23(23):1330, 1969.
- [39] VN Kopylov and LP Mezhov-Deglin. Study of kinetic coefficients of bismuth at helium temperatures. *Zhurnal Eksperimental'noj i Teoreticheskoy Fiziki*, 65(2):720–734, 1973.
- [40] N. N. Zholonko. Poiseuille flow of phonons in solid hydrogen. *Physics of the Solid State*, 48(9):1678–1680, Sep 2006.
- [41] Valentina Martelli, Julio Larrea Jiménez, Mucio Continentino, Elisa Baggio-Saitovitch, and Kamran Behnia. Thermal transport and phonon hydrodynamics in strontium titanate. *Phys. Rev. Lett.*, 120:125901, Mar 2018.
- [42] Y. Machida, A. Subedi, K. Akiba, A. Miyake, M. Tokunaga, Y. Akahama, K. Izawa, and K. Behnia. Observation of poiseuille flow of phonons in black phosphorus. *Science Advances*, 4(1):eaat3374, 2018.
- [43] Kamran Behnia. *Fundamentals of thermoelectricity*. OUP Oxford, 2015.
- [44] Kamran Behnia, Didier Jaccard, and Jacques Flouquet. On the thermoelectricity of correlated electrons in the zero-temperature limit. *Journal of Physics: Condensed Matter*, 16(28):5187, 2004.
- [45] Romain Bel, Kamran Behnia, and Helmuth Berger. Ambipolar nernst effect in NbSe<sub>2</sub>. *Physical review letters*, 91(6):066602, 2003.
- [46] Kamran Behnia and Hervé Aubin. Nernst effect in metals and superconductors: a review of concepts and experiments. *Reports on Progress in Physics*, 79(4):046502, 2016.
- [47] Zengwei Zhu, Benoît Fauqué, Kamran Behnia, and Yuki Fuseya. Magnetoresistance and valley degree of freedom in bulk bismuth. *Journal of Physics: Condensed Matter*, 30(31):313001, 2018.
- [48] EM Lifshitz. Zh. é ksp. teor. fiz. 29, 894 1955 sov. phys. *JETP*, 2:73, 1956.
- [49] D. Shoenberg. *Magnetic Oscillations in Metals*. Cambridge University Press, September 2009.
- [50] Clément Collignon. *De la densité des fluides électroniques dans deux oxydes supraconducteurs*. PhD thesis, ESPCI, 2017.
- [51] Jérôme Béard, Julien Billette, Nelson Ferreira, Paul Frings, Jean-Marc Lagarrigue, Florence Lecouturier, and Jean-Pierre Nicolin. Design and tests of the 100-t triple coil at Incmi. *IEEE Transactions on Applied Superconductivity*, 28(3):1–5, 2017.

- [52] RW Powell, Cho Yen Ho, and Peter Edward Liley. *Thermal conductivity of selected materials*, volume 8. US Department of Commerce, National Bureau of Standards Washington, DC, 1966.
- [53] V Celli and N David Mermin. Ground state of an electron gas in a magnetic field. *Physical Review*, 140(3A):A839, 1965.
- [54] S. B. Hubbard, T. J. Kershaw, A. Usher, A. K. Savchenko, and A. Shytov. Millikelvin de haas–van alphen and magnetotransport studies of graphite. *Phys. Rev. B*, 83:035122, Jan 2011.
- [55] John Desmond Bernal. The structure of graphite. *Proceedings of the Royal Society of London. Series A, Containing Papers of a Mathematical and Physical Character*, 106(740):749–773, 1924.
- [56] Philip Richard Wallace. The band theory of graphite. *Physical Review*, 71(9):622, 1947.
- [57] JC Slonczewski and PR Weiss. Band structure of graphite. *Physical review*, 109(2):272, 1958.
- [58] JW McClure. Band structure of graphite and de haas-van alphen effect. *Physical Review*, 108(3):612, 1957.
- [59] S Tanuma, R Inada, A Furukawa, O Takahashi, Y Iye, and Y Onuki. Physics in high magnetic fields. *Springer Series in Solid State Sciences*, 1981.
- [60] Hiroshi Yaguchi and John Singleton. A high-magnetic-field-induced density-wave state in graphite. *Journal of Physics: Condensed Matter*, 21(34):344207, 2009.
- [61] Benoît Fauqué, David LeBoeuf, Baptiste Vignolle, Marc Nardone, Cyril Proust, and Kamran Behnia. Two phase transitions induced by a magnetic field in graphite. *Physical review letters*, 110(26):266601, 2013.
- [62] David LeBoeuf, CW Rischau, Gabriel Seyfarth, R Küchler, Martin Berben, Steffen Wiedmann, Wojciech Tabis, Medhi Frachet, Kamran Behnia, and Benoit Fauque. Thermodynamic signatures of the field-induced states of graphite. *Nature communications*, 8(1):1337, 2017.
- [63] Hiroshi Yaguchi and John Singleton. Destruction of the field-induced density-wave state in graphite by large magnetic fields. *Physical review letters*, 81(23):5193, 1998.
- [64] Daijiro Yoshioka and Hidetoshi Fukuyama. Electronic phase transition of graphite in a strong magnetic field. *Journal of the Physical Society of Japan*, 50(3):725–726, 1981.

- [65] Kohzoh Takahashi and Yasutami Takada. Charge-and spin-density-wave instabilities in high magnetic fields in graphite. *Physica B: Condensed Matter*, 201:384–386, 1994.
- [66] Kazuto Akiba, Atsushi Miyake, Hiroshi Yaguchi, Akira Matsuo, Koichi Kindo, and Masashi Tokunaga. Possible excitonic phase of graphite in the quantum limit state. *Journal of the Physical Society of Japan*, 84(5):054709, 2015.
- [67] Zengwei Zhu, RD McDonald, A Shekhter, BJ Ramshaw, KA Modic, FF Balakirev, and N Harrison. Magnetic field tuning of an excitonic insulator between the weak and strong coupling regimes in quantum limit graphite. *Scientific reports*, 7(1):1733, 2017.
- [68] KH.I. Amirkhanov, R.I. Bashirov, and M.M. Gadzhialiev. Quantum Oscillations of the Nernst-Ettingshausen Effect in Indium Arsenide. *Phys. Stat. sol.*, 20(13):322–324, 1967.
- [69] G. Bauer and H. Kahlert. Low-temperature non-ohmic galvanomagnetic effects in degenerate *n*-type inas. *Phys. Rev. B*, 5:566–579, Jan 1972.
- [70] VV Karataev, MG Milvidskii, NS Rytova, and VI Fistul. Compensation in *n*-type inas. *Soviet Physics-Semiconductors*, 11(9):1009–1011, 1977.
- [71] Arūnas Krotkus and Zigmās Dobrovolskis. *Electrical conductivity of narrow-gap semiconductors*. Mokslas, 1988.
- [72] L. A. Kaufman and L. J. Neuringer. Magnetic Freezeout and And Tailing in *n*-InAs. *Physical Review B*, 2:1840–1846, 1970.
- [73] Craig E Pryor and Michael E Flatté. Landé *g* factors and orbital momentum quenching in semiconductor quantum dots. *Physical review letters*, 96(2):026804, 2006.
- [74] A Kadri, RL Aulombard, K Zitouni, M Baj, and L Konczewicz. High-magnetic-field and high-hydrostatic-pressure investigation of hydrogenic-and resonant-impurity states in *n*-type indium arsenide. *Physical Review B*, 31(12):8013, 1985.
- [75] MI Dyakonov, AL Efros, and DL Mitchell. Magnetic freeze-out of electrons in extrinsic semiconductors. *Physical Review*, 180(3):813, 1969.
- [76] SD Jog and PR Wallace. A theory of magnetic freezeout for semiconductors in the ultra-quantum limit. *Journal of Physics C: Solid State Physics*, 11(13):2763, 1978.
- [77] R Mansfield and L Kuztalan. Magnetoresistance and hall effect in *n*-type indium antimonide in the magnetic freeze-out region. *Journal of Physics C: Solid State Physics*, 11(20):4157, 1978.

- [78] M. Shayegan, V. J. Goldman, and H. D. Drew. Magnetic-field-induced localization in narrow-gap semiconductors  $\text{Hg}_{1-x}\text{Cd}_x\text{Te}$  and  $\text{InSb}$ . *Physical Review B*, 38(8):5585–5602, 1988.
- [79] Shuichi Ishida. Magnetic-field induced metal–nonmetal transition in  $n\text{-insb}$ . *Journal of the Physical Society of Japan*, 72(Suppl. A):151–152, 2003.
- [80] Ramesh G Mani. Possibility of a metal-insulator transition at the mott critical field in  $\text{insb}$  and  $\text{hg } 1- x \text{ cd } x \text{ te}$ . *Physical Review B*, 40(11):8091, 1989.
- [81] R Mansfield and G Azhdarov. Negative magnetoresistance in indium arsenide in the extreme quantum limit. *physica status solidi (b)*, 87(1):163–167, 1978.
- [82] Anindya Das, Yuval Ronen, Yonatan Most, Yuval Oreg, Moty Heiblum, and Hadas Shtrikman. Zero-bias peaks and splitting in an  $\text{al-inas}$  nanowire topological superconductor as a signature of majorana fermions. *Nature Physics*, 8(12):887, 2012.
- [83] Benoît Fauqué, Zengwei Zhu, Tim Murphy, and Kamran Behnia. Nernst response of the landau tubes in graphite across the quantum limit. *Phys. Rev. Lett.*, 106:246405, Jun 2011.
- [84] CM Jaworski, RC Myers, E Johnston-Halperin, and JP Heremans. Giant spin seebeck effect in a non-magnetic material. *Nature*, 487(7406):210, 2012.
- [85] G. Le Guillou and H. J. Albany. Phonon conductivity of  $\text{inas}$ . *Phys. Rev. B*, 5:2301–2308, Mar 1972.
- [86] Benoît Fauqué, Nicholas P. Butch, Paul Syers, Johnpierre Paglione, Steffen Wiedmann, Aurélie Collaudin, Benjamin Grena, Uli Zeitler, and Kamran Behnia. Magnetothermoelectric properties of  $\text{bi}_2\text{se}_3$ . *Phys. Rev. B*, 87:035133, Jan 2013.
- [87] Tian Liang, Quinn Gibson, Jun Xiong, Max Hirschberger, Sunanda P Koduvayur, Robert Joseph Cava, and Nai Phuan Ong. Evidence for massive bulk dirac fermions in  $\text{pb } 1- x \text{ sn } x \text{ se}$  from nernst and thermopower experiments. *Nature communications*, 4:2696, 2013.
- [88] Y Iye, PM Tedrow, G Timp, Mansour Shayegan, MS Dresselhaus, G Dresselhaus, A Furukawa, and S Tanuma. High-magnetic-field electronic phase transition in graphite observed by magnetoresistance anomaly. *Physical Review B*, 25(8):5478, 1982.
- [89] H. Ochimizu, T. Takamasu, S. Takeyama, S. Sasaki, and N. Miura. High-field phase in the magnetic-field-induced electronic phase transition of graphite. *Phys. Rev. B*, 46:1986–1991, Jul 1992.

- [90] H Yaguchi, Y Iye, T Takamasu, and N Miura. Magnetic-field-induced electronic phase transition in graphite: Pulse field experiment at 3He temperatures. *Physica B: Condensed Matter*, 184(1-4):332–336, 1993.
- [91] Yo Machida, Xiao Lin, Woun Kang, Koichi Izawa, and Kamran Behnia. Colossal seebeck coefficient of hopping electrons in (tmtsf) 2 pf 6. *Physical review letters*, 116(8):087003, 2016.
- [92] L. Ö. Olsson, C. B. M. Andersson, M. C. Håkansson, J. Kanski, L. Ilver, and U. O. Karlsson. Charge accumulation at inas surfaces. *Phys. Rev. Lett.*, 76:3626–3629, May 1996.
- [93] Johanna Lieb, Valeria Demontis, Domenic Prete, Daniele Ercolani, Valentina Zanier, Lucia Sorba, Shimpei Ono, Fabio Beltram, Benjamin Sacépé, and Francesco Rossella. Ionic-liquid gating of inas nanowire-based field-effect transistors. *Advanced Functional Materials*, 29(3):1804378, 2019.
- [94] Paul Syers, Dohun Kim, Michael S Fuhrer, and Johnpierre Paglione. Tuning bulk and surface conduction in the proposed topological kondo insulator smb 6. *Physical review letters*, 114(9):096601, 2015.
- [95] YS Eo, K Sun, Ç Kurdak, D-J Kim, and Z Fisk. A new method for characterizing bulk and surface conductivities of three-dimensional topological insulators: inverted resistance measurements. *arXiv preprint arXiv:1708.05762*, 2017.
- [96] B Andrei Bernevig, Taylor L Hughes, Srinivas Raghu, and Daniel P Arovas. Theory of the three-dimensional quantum hall effect in graphite. *Physical review letters*, 99(14):146804, 2007.
- [97] FJ Burnell, B Andrei Bernevig, and DP Arovas. Scenario for fractional quantum hall effect in bulk isotropic materials. *Physical Review B*, 79(15):155310, 2009.
- [98] Fangdong Tang, Yafei Ren, Peipei Wang, Ruidan Zhong, John Schneeloch, Shengyuan A Yang, Kun Yang, Patrick A Lee, Genda Gu, Zhenhua Qiao, et al. Three-dimensional quantum hall effect and metal–insulator transition in zrte 5. *Nature*, 569(7757):537, 2019.
- [99] BJ Ramshaw, KA Modic, Arkady Shekhter, Yi Zhang, Eun-Ah Kim, Philip JW Moll, Maja D Bachmann, MK Chan, JB Betts, F Balakirev, et al. Quantum limit transport and destruction of the weyl nodes in taas. *Nature communications*, 9(1):2217, 2018.
- [100] G. Autès, D. Gresch, M. Troyer, A. A. Soluyanov, and O. V. Yazyev. Robust type-ii weyl semimetal phase in transition metal diphosphides  $xp_2$  ( $x = \text{Mo}, \text{w}$ ). *Phys. Rev. Lett.*, 117:066402, Aug 2016.

- [101] M-Y Yao, Nan Xu, QS Wu, Gabriel Autès, Nitesh Kumar, Vladimir N Strocov, Nicholas C Plumb, M Radovic, Oleg V Yazyev, Claudia Felser, et al. Observation of weyl nodes in robust type-ii weyl semimetal  $wp_2$ . *Physical review letters*, 122(17):176402, 2019.
- [102] Nitesh Kumar, Yan Sun, Kaustuv Manna, Vicky Suess, Inge Leermakers, Olga Young, Tobias Forster, Marcus Schmidt, Binghai Yan, U Zeitler, Claudia Felser, and Chandra Shekhar. Extremely high magnetoresistance and conductivity in the type-ii weyl semimetal  $wp_2$ . *Nature Communications*, 8, 11 2017.
- [103] R. Schönemann, N. Aryal, Q. Zhou, Y.-C. Chiu, K.-W. Chen, T. J. Martin, G. T. McCandless, J. Y. Chan, E. Manousakis, and L. Balicas. Fermi surface of the weyl type-ii metallic candidate  $wp_2$ . *Phys. Rev. B*, 96:121108, Sep 2017.
- [104] Aifeng Wang, D. Graf, Yu Liu, Qianheng Du, Jiabao Zheng, Hechang Lei, and C. Petrovic. Large magnetoresistance in the type-ii weyl semimetal  $wp_2$ . *Phys. Rev. B*, 96:121107, Sep 2017.
- [105] Mazhar N Ali, Jun Xiong, Steven Flynn, Jing Tao, Quinn D Gibson, Leslie M Schoop, Tian Liang, Neel Haldolaarachchige, Max Hirschberger, Nai Phuan Ong, et al. Large, non-saturating magnetoresistance in  $wte_2$ . *Nature*, 514(7521):205, 2014.
- [106] Benoît Fauqué, Xiaojun Yang, Wojciech Tabis, Mingsong Shen, Zengwei Zhu, Cyril Proust, Yuki Fuseya, and Kamran Behnia. Magnetoresistance of semimetals: The case of antimony. *Phys. Rev. Materials*, 2:114201, Nov 2018.
- [107] J Gooth, F Menges, N Kumar, V Süß, C Shekhar, Y Sun, U Drechsler, R Zierold, C Felser, and B Gotsmann. Thermal and electrical signatures of a hydrodynamic electron fluid in tungsten diphosphide. *Nature Communications*, 9(1):4093, 2018.
- [108] C. Uher and H. J. Goldsmid. Separation of the Electronic and Lattice Thermal Conductivities in Bismuth Crystals. *Physica Status Solidi B Basic Research*, 65:765–772, October 1974.
- [109] I. Y. Korenblit, M. E. Kuznetsov, V. M. Muzhdaba, and S. S. Shalyt. Electron Heat Conductivity and the Wiedemann-Franz Law for Bi. *Soviet Journal of Experimental and Theoretical Physics*, 30:1009, 1969.
- [110] Alexandre Jaoui, Benoît Fauqué, Carl Willem Rischau, Alaska Subedi, Chenguang Fu, Johannes Gooth, Nitesh Kumar, Vicky Süß, Dmitrii L. Maslov, Claudia Felser, and Kamran Behnia. Departure from the wiedemann–franz law in  $wp_2$  driven by mismatch in t-square resistivity prefactors. *npj Quantum Materials*, 3(1):64, 2018.
- [111] G. Seyfarth, J. P. Brison, G. Knebel, D. Aoki, G. Lapertot, and J. Flouquet. Multigap superconductivity in the heavy-fermion system  $cecoi_n_5$ . *Phys. Rev. Lett.*, 101:046401, Jul 2008.

- [112] G. K. White and R. J. Tainsh. Electron scattering in nickel at low temperatures. *Phys. Rev. Lett.*, 19:165–166, Jul 1967.
- [113] Y. Shiomi, Y. Onose, and Y. Tokura. Effect of scattering on intrinsic anomalous hall effect investigated by lorentz ratio. *Phys. Rev. B*, 81:054414, Feb 2010.
- [114] D. K. Wagner, J. C. Garland, and R. Bowers. Low-temperature electrical and thermal resistivities of tungsten. *Phys. Rev. B*, 3:3141–3149, May 1971.
- [115] V I. Pal, H K. Yudson and D L. Maslov. Resistivity of non-galilean-invariant fermi- and non-fermi liquids. *Lith. J. Phys.*, 52:142–164, Sep 2012.
- [116] Alan J. Bennett and M. J. Rice. Exact solutions of boltzmann’s equation for combined electron-electron electron-impurity scattering. *Phys. Rev.*, 185:968–970, Sep 1969.
- [117] Gábor Zala, B. N. Narozhny, and I. L. Aleiner. Interaction corrections at intermediate temperatures: Longitudinal conductivity and kinetic equation. *Phys. Rev. B*, 64:214204, Nov 2001.
- [118] Dmitrii L. Maslov, Vladimir I. Yudson, and Andrey V. Chubukov. Resistivity of a non-galilean-invariant fermi liquid near pomeranchuk quantum criticality. *Phys. Rev. Lett.*, 106:106403, Mar 2011.
- [119] Conyers Herring. Simple property of electron-electron collisions in transition metals. *Phys. Rev. Lett.*, 19:167–168, Jul 1967.
- [120] Songci Li and Dmitrii L Maslov. Lorentz ratio of a compensated metal. *Physical Review B*, 98(24):245134, 2018.
- [121] Yi Liu and Roland E. Allen. Electronic structure of the semimetals bi and sb. *Phys. Rev. B*, 52:1566–1577, Jul 1995.
- [122] Shuzo Takano, Masao Koga, and Yasukuni Matsumoto. Quantum oscillations of the velocity of sound in antimony. *Journal of the Physical Society of Japan*, 44(2):453–459, 1978.
- [123] D. Shoenberg and William Lawrence Bragg. The de haas-van alphen effect. *Philosophical Transactions of the Royal Society of London. Series A, Mathematical and Physical Sciences*, 245(891):1–57, 1952.
- [124] Lee R. Windmiller. de haas-van alphen effect and fermi surface in antimony. *Phys. Rev.*, 149:472–484, Sep 1966.
- [125] N. B. Brandt, N. Y. Minina, and C. Chen-Kang. De Haas-Van Alphen Effect in Antimony at Very Low Temperatures. *Soviet Journal of Experimental and Theoretical Physics*, 24:73, January 1967.

- [126] W. R. Datars and J. Vanderkooy. Cyclotron resonance and the fermi surface of antimony. *IBM Journal of Research and Development*, 8(3):247–252, July 1964.
- [127] Y. A. Bogod, B. I. Verkin, and V. B. Krasovitskii. Some Features of the Electric Conductivity and Magnetoresistance of Antimony at Low Temperatures. *Soviet Journal of Experimental and Theoretical Physics*, 34:142, 1972.
- [128] M. S. Bresler and N. A. Red'ko. Galvanomagnetic phenomena in antimony at low temperatures. *Soviet Physics JETP*, 34(1), 1972.
- [129] N B. Brandt, E A. Svistova, and T V. Gorskaya. Electrical resistance of antimony in a magnetic field up to 420 koe at liquid helium temperature. *Journal of Experimental and Theoretical Physics - J EXP THEOR PHYS*, 26, 01 1968.
- [130] G. K. White and S. B. Woods. The thermal and electrical resistivity of bismuth and antimony at low temperatures. *The Philosophical Magazine: A Journal of Theoretical Experimental and Applied Physics*, 3(28):342–359, 1958.
- [131] C. L. Tsai, D. Waldorf, K. Tanaka, and C. G. Grenier. Mutual drag effect in the magnetoresistivity of antimony. *Phys. Rev. B*, 17:618–625, Jan 1978.
- [132] J. R. Long, C. G. Grenier, and J. M. Reynolds. Electron and lattice transport phenomena in an antimony crystal at liquid-he<sup>4</sup> temperatures. *Phys. Rev.*, 140:A187–A201, Oct 1965.
- [133] R. S. Blewer, N. H. Zebouni, and C. G. Grenier. Lattice thermal conductivity, nernst-ettinghausen effect, and specific heat in antimony at low temperature. *Phys. Rev.*, 174:700–710, Oct 1968.
- [134] M. C. Steele and J. Babiskin. Oscillatory thermomagnetic properties of a bismuth single crystal at liquid helium temperatures. *Phys. Rev.*, 98:359–367, Apr 1955.
- [135] C. Ayache and M. Locatelli. *Phonon Scattering in Condensed Matter*. Plenum Pres, 1980.
- [136] U Stockert, RD Dos Reis, MO Ajeesh, SJ Watzman, M Schmidt, C Shekhar, JP Heremans, C Felser, M Baenitz, and M Nicklas. Thermopower and thermal conductivity in the weyl semimetal nbp. *Journal of physics. Condensed matter: an Institute of Physics journal*, 29(32):325701, 2017.
- [137] Junsen Xiang, Sile Hu, Meng Lv, Jiahao Zhang, Lingxiao Zhao, Wei Li, Ziyu Chen, Shuai Zhang, Yi-feng Yang, Jiantao Wang, et al. Giant magnetic quantum oscillations and chiral anomaly in the thermal conductivity of a weyl semimetal. *arXiv preprint arXiv:1801.08457*, 2018.

- [138] Aurélie Collaudin, Benoît Fauqué, Yuki Fuseya, Woun Kang, and Kamran Behnia. Angle dependence of the orbital magnetoresistance in bismuth. *Phys. Rev. X*, 5:021022, Jun 2015.
- [139] Mazhar N. Ali, Leslie Schoop, Jun Xiong, Steven Flynn, Quinn Gibson, Max Hirschberger, N. P. Ong, and R. J. Cava. Correlation of crystal quality and extreme magnetoresistance of WTe<sub>2</sub>. *EPL (Europhysics Letters)*, 110(6):67002, jun 2015.
- [140] Harvey V. Culbert. Low-temperature specific heat of arsenic and antimony. *Phys. Rev.*, 157:560–563, May 1967.
- [141] Warren DeSorbo. Low temperature specific heat of bismuth and tungsten. *The Journal of Physical Chemistry*, 62(8):965–967, 1958.
- [142] Kamran Behnia, Marie-Aude Méasson, and Yakov Kopelevich. Nernst effect in semimetals: The effective mass and the figure of merit. *Phys. Rev. Lett.*, 98:076603, Feb 2007.
- [143] GJ McMullan, MR Norman, AD Huxley, N Doiron-Leyraud, J Flouquet, GG Lonzarich, A McCollam, and SR Julian. The fermi surface and f-valence electron count of upT<sub>3</sub>. *New Journal of Physics*, 10(5):053029, 2008.
- [144] Donovan Hall, E. C. Palm, T. P. Murphy, S. W. Tozer, C. Petrovic, Eliza Miller-Ricci, Lydia Peabody, Charis Quay Huei Li, U. Alver, R. G. Goodrich, J. L. Sarrao, P. G. Pagliuso, J. M. Wills, and Z. Fisk. Electronic structure of cerIn<sub>5</sub>: de Haas–van Alphen and energy band calculations. *Phys. Rev. B*, 64:064506, Jul 2001.
- [145] X Rao, X Zhao, X-Y Wang, HL Che, LG Chu, G Hussain, T-L Xia, and XF Sun. Quantum oscillation of thermal conductivity and violation of weidemann-franz law in TaS<sub>2</sub> and NbS<sub>2</sub>. *arXiv preprint arXiv:1906.03961*, 2019.
- [146] RN Gurzhi and VM Kontorovich. Electron sound in metals. *SOV PHYS JETP*, 28(3):577–582, 1969.
- [147] LP Mezhov-Deglin. Measurement of the thermal conductivity of crystalline He<sup>4</sup>. *SOVIET PHYSICS JETP*, 22(1), 1966.
- [148] Gabriele F. Giuliani and John J. Quinn. Lifetime of a quasiparticle in a two-dimensional electron gas. *Phys. Rev. B*, 26:4421–4428, Oct 1982.
- [149] LJ Challis and J Wilks. The thermal conductivity of liquid He<sup>3</sup>. In *Proceedings*, page 38. Ohio State University Research Foundation, 1957.
- [150] DM Lee and Henry A Fairbank. Heat transport in liquid He<sup>3</sup>. *Physical Review*, 116(6):1359, 1959.

- [151] A. C. Anderson, J. I. Connolly, O. E. Vilches, and J. C. Wheatley. Experimental thermal conductivity of helium-3. *Phys. Rev.*, 147:86–93, Jul 1966.
- [152] John Irving Connolly. *Thermal conductivity of liquid helium three*. PhD thesis, University of Illinois at Urbana-Champaign, 1965.
- [153] W. R. Abel, R. T. Johnson, J. C. Wheatley, and W. Zimmermann. Thermal conductivity of pure  $\text{he}^3$  and of dilute solutions of  $\text{he}^3$  in  $\text{he}^4$  at low temperatures. *Phys. Rev. Lett.*, 18:737–740, May 1967.
- [154] Jerry F Kerrisk and William E Keller. Thermal conductivity of fluid  $\text{he}^3$  and  $\text{he}^4$  at temperatures between 1.5 and 4.0 k and for pressures up to 34 atm. *Physical Review*, 177(1):341, 1969.
- [155] David S Betts and Richard Marshall. Transport in fluid helium-3 under pressure. *Journal of Low Temperature Physics*, 1(6):595–607, 1969.
- [156] John C Wheatley. Experimental properties of superfluid  $\text{he}^3$ . *Reviews of Modern Physics*, 47(2):415, 1975.
- [157] R Mitchell, AD Eastop, E Faraj, and JR Hook. The specific heat capacity and thermal conductivity of normal liquid  $^3\text{he}$ . *Journal of low temperature physics*, 64(1-2):43–63, 1986.
- [158] Dennis S. Greywall. Thermal conductivity of normal liquid  $^3\text{He}$ . *Phys. Rev. B*, 29:4933–4945, May 1984.
- [159] DS Betts, DW Osborne, B Welber, and J Wilks. The viscosity of liquid helium 3. *Philosophical Magazine*, 8(90):977–987, 1963.
- [160] DS Betts, Bernard Augustus Keen, and J Wilks. The viscosity and acoustic impedance of liquid helium-3. *Proceedings of the Royal Society of London. Series A. Mathematical and Physical Sciences*, 289(1416):34–45, 1965.
- [161] AA Abrikosov and IM Khalatnikov. The theory of a fermi liquid (the properties of liquid  $^3\text{he}$  at low temperatures). *Reports on Progress in Physics*, 22(1):329, 1959.
- [162] G. A. Brooker and J. Sykes. Transport properties of a fermi liquid. *Phys. Rev. Lett.*, 21:279–282, Jul 1968.
- [163] H Højgaard Jensen, Henrik Smith, and John W Wilkins. Exact transport coefficients for a fermi liquid. *Physics Letters A*, 27(8):532–533, 1968.
- [164] H. Højgaard Jensen, Henrik Smith, and John W. Wilkins. Upper and lower bounds on transport coefficients arising from a linearized boltzmann equation. *Phys. Rev.*, 185:323–337, Sep 1969.

- [165] Jennifer Coulter, Ravishankar Sundararaman, and Prineha Narang. Microscopic origins of hydrodynamic transport in the type-ii weyl semimetal  $\text{Wp}_2$ . *Phys. Rev. B*, 98:115130, Sep 2018.
- [166] N Tsujii, K Yoshimura, and K Kosuge. Deviation from the kadowaki-woods relation in yb-based intermediate-valence systems. *Journal of Physics: Condensed Matter*, 15(12):1993, 2003.
- [167] R. A. Fisher, F. Bouquet, N. E. Phillips, M. F. Hundley, P. G. Pagliuso, J. L. Sarrao, Z. Fisk, and J. D. Thompson. Specific heat of  $\text{CeRhIn}_5$ : pressure-driven evolution of the ground state from antiferromagnetism to superconductivity. *Phys. Rev. B*, 65:224509, May 2002.
- [168] John Wheatley. LIQUID  $\text{He}_3$ , LIQUID MIXTURES OF  $\text{He}_3$  AND  $\text{He}_4$ , AND DILUTION REFRIGERATION. *Journal de Physique Colloques*, 31(C3):C3–109–C3–118, 1970.
- [169] Yu P Gaidukov and Ya Kadletsova. Temperature dependence of the resistance of filamentary zinc crystals. *Sov. Phys. JETP*, 30(4):637–640, 1970.
- [170] Yu P Gaidukov and J Kadlecova. Effect of dimensions on temperature dependence of resistance in cadmium whiskers. *physica status solidi (a)*, 2(2):407–413, 1970.
- [171] C.C Ackerman and R.A Guyer. Temperature pulses in dielectric solids. *Annals of Physics*, 50(1):128 – 185, 1968.
- [172] AP Korolyuk. Dispersion of sound velocity and the electron relaxation time in bismuth and anti mony. *Zh. Eksp. Teor. Fiz*, 65:1963–1969, 1973.
- [173] B.I. Shklovskii and L.E. Gurevich. Theory of the second sound in semiconductors. *Soviet Physics Solid State*, 8(10), 1967.
- [174] Jiecheng Zhang, Eli M Levenson-Falk, BJ Ramshaw, DA Bonn, Ruixing Liang, WN Hardy, Sean A Hartnoll, and Aharon Kapitulnik. Anomalous thermal diffusivity in underdoped  $\text{YBa}_2\text{Cu}_3\text{O}_{6+x}$ . *Proceedings of the National Academy of Sciences*, 114(21):5378–5383, 2017.
- [175] F Arnold, A Isidori, E Kampert, B Yager, M Eschrig, and J Saunders. Charge density waves in graphite: towards the magnetic ultraquantum limit. *Physical review letters*, 119(13):136601, 2017.

# List of figures

1.1	<b>a)</b> Fermi surface of Sodium in the first Brillouin zone of the body centered cubic lattice from Lee [5]. <b>b)</b> Fermi surface of lead in the first Brillouin zone of a cubic face centered Bravais lattice. Figure from Hermann <i>et al.</i> [6]. <b>c)</b> Schematic representation of the typical band structure of metals, semi-conductors, semi-metals, zero-gap systems and insulators. Examples of materials corresponding to each class are indicated. Figure from J.P. Issi [7]	2
1.2	Evolution of the electronic density of states and band structure with increasing doping in a semi-conductor. Doping increases from a to e. Coloured area represents filled states. Sketch from Blase <i>et al.</i> [11]	3
2.1	<b>a)</b> Sketch of the evolution of the maximum phonon wave-vector with temperature. <b>b)</b> A schematic representation highlighting the difference between horizontal and vertical inelastic scattering. Both kinds of processes degrade heat transport. Their effect on momentum transport is however very different. Arrows indicate scattering from one state to another.	13
2.2	Illustration of an Umklapp inter-electronic collisions on a top view of the Fermi surface of $WP_2$ . The arrows illustrate wave-vectors during an inter-band Umklapp and small-angle scattering event. $k_{i,n}^{\vec{}}$ and $k_{f,n}^{\vec{}}$ are carrier momenta, $k_{f,2}^{\vec{}} - k_{i,2}^{\vec{}} = \vec{q}$ and $k_{f,1}^{\vec{}} - k_{i,1}^{\vec{}} = \vec{G} + \vec{q}$ .	16
2.3	Predicted phononic thermal conductivity as a function of temperature. Regions A,B,C and D correspond respectively to the ballistic, hydrodynamic, Ziman and diffusive regimes phonons. Figure from Beck <i>et al.</i> [37]	18
2.4	<b>a)</b> Quantized energy levels of a 3D electron gas in a magnetic field. The electrons are confined in Landau cylinders for $B \neq 0$ . Only states within the Fermi sphere, $ \mathbf{k}  < k_F$ are occupied. <b>b)</b> First observation of QO in magnetization measurement (dHvA effect) of Bismuth at $T = 14.2K$ .	23

- 3.1 **a)** The cryostat is equipped with a superconducting magnet (reaching up to  $B = 17\text{T}$ ) at ESPCI Paris. One may notice the metallic stool left by an unnamed student during a field sweep up to  $B = 17\text{T}$ . **b)** Schematic representation of a dilution fridge. The cooling power emerges from the dilution of the light phase ( $^3\text{He}$ ) to the mixed, and heavier, phase (deep blue). The sample holder is in thermal contact with the mixing chamber. Figure from C. Collignon [50]. 27
- 3.2 **a)** Transverse magnetoresistivity measurement geometry **b)** Longitudinal magnetoresistivity measurement geometry **c)** Hall resistivity measurement geometry . . . . . 29
- 3.3 **a)** Photography of the sample holder used to measure, amongst other, the thermal conductivity, thermopower and Nernst coefficient in the  $(1 \times 5 \times 10) \text{mm}^3$  Sb sample fixed on the cold finger. **b)** Zoom on the sample. The cold finger, hot and cold thermometer and sample heater are indicated by arrows. **c)** Schematic representation of the sample holder [43]. . . . . 31
- 3.4 **a)**  $\kappa/T$  and  $L_0/\rho$  plotted for the Ag sample at  $B = 0\text{T}$  (red) and  $B = 10\text{T}$  (green). The WFL is recovered when the two graphs, at equal field, meet. **b)** Lorenz number of the Ag sample as a function of temperature plotted for  $B = 0\text{T}$  and  $B = 10\text{T}$ . . . . . 34
- 4.1 Schematic representation of the Fermi surface of graphite in the Brillouin zone by S.B. Hubbard *et al.* [54]. The electron and hole pockets are located along the H-K-H and H-K'-H direction of the BZ. . . . . 37
- 4.2 **a)** In-plane magnetoresistance ( $R_a$ ) of Kish graphite up to  $B = 70\text{T}$  for temperatures between  $T = 1.5\text{K}$  and  $T = 10\text{K}$ . The magnetic field is applied along the  $c$ -axis. The curves are shifted for clarity. **b)**  $R_c$  (shown in d) as a function of  $T^{-1}$  for  $B = 47\text{T}$  (circles) and  $B = 64\text{T}$  (squares) in a log scale. Dashed lines are Arrhenius fits to  $R_c$ . **c)**  $R_a$  as a function of temperature for  $B = 64\text{T}$ . **d)** Out-of-plane magnetoresistance  $R_c$  in semi-logarithmic scale of Kish graphite up to  $B = 80\text{T}$  and down to  $T = 0.44\text{K}$ . **e)** Field dependence of the gap deduced from the activating behavior of  $R_c$ . Inset is a sketch of the occupied Landau sub-levels with increasing magnetic field. **f)**  $(B^{-1}, \log(T))$  phase diagram of graphite. Graph from Le Boeuf *et al.* [62]. . . . . 39

- 4.3 **a)** Field dependence of the in-plane resistivity  $\rho_{xx}$  and the out-of-plane resistivity  $\rho_{zz}$  of a kish graphite sample up to  $B = 90.5\text{T}$  at  $T = 1.4\text{K}$  from Zhu *et al.* [26]. Sketches show the measurement geometries. **b)** Field dependence of  $\rho_{zz}/\rho_{xx}$ . The QL as well as the three phases are indicated by dotted lines. The zero-field anisotropy reaches 500. **c)**  $(B^{-1}, T)$  phase diagram of graphite with inputs from Zhu *et al.* (black) and this work (red). 41
- 4.4 **a)** In-plane resistivity  $R_a$  plotted as a function of temperature for a sample of natural graphite (labelled NG-1) of high quality. **b)** In-plane magnetoresistivity  $R_{xx}$  plotted as a function of  $B$  up to  $B = 86\text{T}$  at various temperature for sample NG-1. . . . . 41
- 4.5 Resistivity of undoped n-type InAs as a function of temperature. Sample is a slab of dimension  $(0.75 \times 0.5 \times 6)\text{ mm}^3$ . The dotted vertical line indicates the value of u-InAs Fermi temperature  $T_F = 130\text{K}$ . . . . . 44
- 4.6 **a)** Transverse magnetoresistance ( $j_Q \perp B$ )  $\rho_{xx}$  as a function of magnetic field up to  $B = 14\text{T}$  for different temperatures. **b)** Longitudinal ( $j_Q \parallel B$ ) magnetoresistance  $\rho_{zz}$  as a function of magnetic field up to  $B = 14\text{T}$  for the same array of temperatures. Both datasets were acquired during the same experimental run. **c)** Magnetoresistance  $\rho$  as a function of the magnetic field for various angle  $\theta = (\vec{j}_Q, \vec{B})$  from transverse ( $\theta = 0^\circ$ ) to longitudinal ( $\theta = 90^\circ$ ) geometries. Temperature was set to at  $T = 2.15\text{K}$ . **d)** Magnetoresistance  $\rho_\theta$  plotted as  $\rho_\theta/\rho_{\theta=0}$  as a function of the angle  $\theta = (\vec{j}_Q, \vec{B})$  for static magnetic fields at  $T = 2.15\text{K}$ . All sets of data were acquired during the same experimental run. . . . . 45
- 4.7 **a)** Left-axis : computed Fermi energy  $E_F$  plotted as a function of magnetic field for u-InAs. Right axis :  $\rho_{xx}$  plotted as a function of magnetic field at  $T = 2.0\text{K}$  **b)** Logarithm of the amplitude of the QO ( $\delta\rho_{xx}$  determined by removing a polynomial background to the magnetoresistance) plotted as  $\log \delta\rho_{xx}/T$  as a function of temperature. The straight line fit corresponds to an effective mass  $m^* = 0.023 \times m_0$  determined at  $B = 3.85\text{T}$ . The inset shows the evolution of  $m^*$  with field. **c)** Evolution of the QO plotted as a function of  $B^{-1}$  for different angles  $\theta$ . The inset shows the extracted frequency of QO as a function of the angle. . . . . 47

- 4.8 **a)** Schematic representation of the emergence of the magnetic freeze-out regime in regard of the relative spatial extension of the electronic wave-function  $a_b$  and the average distance between impurities  $n^{1/3}$ . **b)** Evolution of  $\rho_{xx}$ ,  $\rho_{zz}$  and  $\rho_{xy}$  in undoped n-InSb in the magnetic freeze-out regime in the quantum limit. The carrier concentration is 10 times lower than u-InAs. . . . . 49
- 4.9 **a)** Transverse magnetoresistance  $R_{xx}$  as a function of the magnetic field up to  $B = 56\text{T}$  at various temperatures from  $T = 1.5\text{K}$  to  $T = 40\text{K}$ . Measurement in pulsed field realised in LNCMI Toulouse on u-InAs sample #1. Signal is not symmetrized which explains the low field difference with c.. **b)** Longitudinal magnetoresistance  $R_{zz}$  as a function of the magnetic field up to  $B = 56\text{T}$  at various temperatures from  $T = 1.5\text{K}$  to  $T = 40\text{K}$ . Measurement in pulsed field realised in LNCMI Toulouse on u-InAs sample #2. **c)** Transverse magnetoresistivity  $\rho_{xx}$  as a function of the magnetic field up to  $B = 34\text{T}$  at various temperatures from  $T = 0.33\text{K}$  to  $T = 25\text{K}$ . Measurement in static field realised in LNCMI Grenoble on u-InAs sample #3. **d)** Hall resistivity  $\rho_{xy}$  as a function of the magnetic field up to  $B = 34\text{T}$  at various temperatures from  $T = 0.33\text{K}$  to  $T = 25\text{K}$ . Measurement in static field realised in LNCMI Grenoble on u-InAs sample #3. Inset shows the low field Hall resistivity. . . . . 51
- 4.10 **a)** Electronic concentration  $n_H$  as a function of magnetic field for various temperatures in u-InAs. **b)** Mobility of the charge carriers  $\mu_H$  determined from the Hall resistivity plotted as a function of magnetic field for various temperatures in u-InAs. . . . . 53
- 4.11 **a)** Thermal conductivity  $\kappa$  plotted as a function of temperature in u-InAs. The green dotted line indicate a  $T^3$  dependence. **b)** Thermopower plotted as  $S_{xx}/T$  for applied magnetic fields  $B = 0\text{T}$  and  $B = 23\text{T}$ . . . . . 54
- 4.12 **a)**  $S_{xx}/T$  plotted as a function of magnetic field for various temperatures. Temperatures are separated in two plots for clarity. **b)** Nernst coefficient, plotted as  $v/T$  as a function of magnetic field for various temperatures. The inset focuses the  $T = 650\text{mK}$  Nernst coefficient  $v/T$ . Both graphs share the same legend. . . . . 55

- 4.13 **a) u-InAs**  $\rho_{zz}$  plotted as a function of  $T^{-1}$  in a semi-log scale for different magnetic fields. **b) u-InAs**  $\rho_{zz}$  plotted as a function of  $T^{-1}$  in a semi-log scale for different magnetic fields. In panels a and b the dotted lines correspond to a fit to an Arrhenius law. **c) u-InAs** Energy gap deduced from an Arrhenius law corresponding to the  $\rho_{xx}$  (a) and  $\rho_{zz}$  (b) data. **d) Graphite** In-plane resistance  $R_a$  of a natural graphite sample plotted as a function of  $T$  for different magnetic fields. Data plotted as function of magnetic field in the appendix. **e) Graphite** Out-of-plane resistance of natural graphite sample NG-3  $R_c$  plotted as a function of  $T^{-1}$  in a semi-log scale for different magnetic fields. **f) Energy gap** deduced from an Arrhenius law fit of the  $R_c$  data presented in panel (b) (sample NG-3) and data by Fauqué *et al.* [61] . . . . . 58
- 5.1 **a)** DFT computed band structure of  $WP_2$  along high symmetry direction of the Brillouin zone [100]. **b)** DFT-computed 3D Fermi Surface of  $WP_2$  in the rectangular BZ. . . . . 65
- 5.2 **a)** Resistivity along the a-axis as a function of temperature for different applied magnetic fields. Sample is a needle-like single crystal of  $WP_2$ . **b)** Magnetoresistance of  $WP_2$  as a function of  $B$  in the high field region for different temperatures. Both datasets are from Kumar *et al.* [102] . . . . . 66
- 5.3 **a)** Thermal conductivity (blue) and electrical resistivity (red) of a micro-ribbon of  $WP_2$  measured by Gooth *et al.* [107]. **b)** Lorenz ratio  $L(T) = \kappa/T\sigma$  plotted as  $L(T)/L_0$  as a function of temperature.  $L_0$  is the Sommerfeld value of the Lorenz ratio. Inset shows a focus on the low temperature region. 67
- 5.4 **a)** Resistivity  $\rho_a$ , measured along the  $a$ -axis of a single crystal of  $WP_2$  as a function of temperature for  $B = 0T$  and  $B = 10T$ . **b)** Resistivity  $\rho_a$  (n $\Omega$ .cm) plotted as a function of  $T^2$ . Inset shows  $\delta\rho_a$  plotted as a function of  $T^5$  up to  $T = 20K$ . . . . . 70
- 5.5 **a)** Thermal conductivity  $\kappa$ , measured along the  $a$ -axis of a single crystal of  $WP_2$  as a function of temperature for  $B = 0T$  and  $B = 10T$ . **b)** Thermal resistivity,  $WT = \frac{L_0 T}{\kappa}$ , as a function of  $T^2$ . The dotted line is a linear fit to the  $T < 8K$  data. The inset shows  $\delta WT = WT - W_0 T - B_2 T^2$  as a function of  $T^3$  expressed in n $\Omega$ .cm. . . . . 70
- 5.6 **a)** Specific Heat plotted as  $C_p/T$  as a function of  $T^2$  for  $WP_2$ . The inset shows the specific heat plotted as  $C_p$  as a function of  $T$  up to  $T = 100K$ . **b)** Thermal conductivity,  $\kappa$ , as a function of temperature in  $WP_2$  for  $B = 0T$  (black dots) and  $B = 10T$  (green dots). The dotted line corresponds to the ballistic thermal conductivity of phonons in  $WP_2$ . . . . . 73

- 5.7 **a)** Ratio of Lorenz,  $L(T) = \frac{\kappa}{T\sigma}$  to Sommerfeld  $L_0 = 2.44 \times 10^{-8} \text{ W}\cdot\Omega\cdot\text{K}^{-2}$ , numbers as a function of temperature (red). The data reported for a micro-ribbon of  $\text{WP}_2$  [107] are shown in green. **b)**  $L(T)/L_0$  as a function of temperature in  $\text{CeRhIn}_5$  [31]. **c)**  $L(T)/L_0$  as a function of temperature for an Ag wire with a  $50\mu\text{m}$  diameter and 99.99% purity.  $\text{WP}_2$  and Ag were measured with the same experimental setup. . . . . 74
- 5.8 **a)** Inelastic electrical resistivity  $\delta\rho$  caused by phonon scattering in  $\text{WP}_2$  (Black) and Ag (Red) as a function of  $T^5$ . **b)** Inelastic thermal resistivity,  $\delta WT$ , in  $\text{WP}_2$  (Black) and Ag (Red) as a function of  $T^3$ . The ratio of the two slopes is similar for heat and charge transport. . . . . 76
- 6.1 **a)** Band structure of Sb along various symmetry lines from [121]. **b)** Brillouin zone for the rhombohedral structure. **c)** Representation of the Fermi surface of Sb from [122]. **d)** Fermi surface of the electron pockets (at the L-point) and hole pockets (at the T-point) according to the Liu and Allen [121] tight-binding model. Close to the T-point the 6 ellipsoids merge to form a unique object. Experimentally no evidence allows to conclude whether or not the ellipsoids merge. . . . . 81
- 6.2 **a)** Magnetoresistance of selected semimetals ( $(\rho(B) - \rho_0)/\rho_0$ ) : Sb (red), Bi (blue) and  $\text{WTe}_2$  (green) as a function of magnetic field at  $T = 2\text{K}$  from [106]. The black line indicates a  $B^2$  behavior. **b)**  $\rho_{22}$  plotted here as a function of  $B$  in a linear scale [106]. Quantum oscillations appear for  $B > 3\text{T}$ . **c)** Oscillating part of the resistivity  $\delta\rho$  as a function of  $B^{-1}$  at  $T = 2\text{K}$ . The inset shows a sketch of the Fermi surface of Sb and the direction along which the field is applied. **d)** Fourier transform of the oscillations reported in (c). 83
- 6.3 **a)** Thermal conductivity as a function of temperature for a millimetric Sb sample. The full line corresponds to  $\kappa$ , the line with markers (circles) refers to  $\kappa_{ph}$  and the broken line is  $\kappa_e$ . The graph is from [130]. **b)** The high-field thermomagneto-resistivity  $\gamma_{11} = L_0 T / \kappa$  as a function of magnetic field. Graph taken from [132]. . . . . 85
- 6.4 **a)** Electrical resistivity along the bisectrix direction  $\rho_{22}$  as a function of temperature for three different geometries of Sb samples denoted by the  $\bar{s}$  parameter. The inset explicitly defines  $\bar{s}$  and the orientation of the crystals. Note that the  $\bar{s}=1.26\text{mm}$  sample displays irregular dimensions and poor orientation. **b)** The same  $\rho_{22}$  plotted here as a function  $T^2$ . The red markers refer to data from Fauqué et al. [106] with a sample geometry defined by  $\bar{s}=0.3\text{mm}$ . . . . . 86

- 6.5 **a)** Transverse magnetoresistance  $MR = (\rho(B) - \rho_0)/\rho_0$  as a function of magnetic field for two samples at  $T = 100\text{mK}$ . The red dotted line shows a  $T^2$  behavior. **b)**  $\rho_{22}$  plotted here as a function  $T$  for the small and large samples both at  $B = 0\text{T}$  and  $B = 10\text{T}$ . . . . . 88
- 6.6 **a)**  $\rho_{22}$  as a function of  $B$  for various temperatures in sample  $\bar{s} = 2.2\text{mm}$ . The magnetic field is applied along the trigonal direction. **b)** Fourier transform of  $\rho_{22}$  presented in a. **c)**  $\rho_{21}$  as a function of  $B$  for various temperatures in sample  $\bar{s} = 2.2\text{mm}$ . The magnetic field is applied along the trigonal direction. **d)** Fourier transform of  $\rho_{21}$  in c. . . . . 89
- 6.7 **a)** Thermal conductivity  $\kappa$  plotted as a function of temperature for three different bulk Sb geometries. The measurements were done along the bisectrix direction of the samples. **b)** Lorenz ratio  $L(T) = \kappa\rho/(T.L_0)$  plotted as a function of temperature for the three samples. The same colormap is used in a and b. . . . . 90
- 6.8 **a)** Thermal conductivity  $\kappa$  plotted as a function of temperature for the small,  $\bar{s} = 0.4\text{mm}$  sample. Black circles represent  $B = 0\text{T}$  data whereas black crosses refer to  $B = 5\text{T}$  data. The color-map represents an increase of the magnetic field from  $B = 0\text{T}$  to  $B = 2\text{T}$  with a step of  $B = 0.05\text{T}$ . Above  $B = 1.4\text{T}$  there is no visible difference in the temperature dependence of  $\kappa$ . Inset shows  $\kappa$  as a function of  $B$  for the same sample at  $T \approx 2\text{K}$ . The temperature of the sample changes when sweeping the field upon a constant heat current. **b)** Non magnetic field dependent thermal conductivity  $\kappa_{B\text{-saturated}}$  as a function of temperature for the three Sb samples. The broken black line represents a  $T^3$  behavior. . . . . 92
- 6.9 **a)** Thermal conductivity  $\kappa$  plotted as  $\kappa/\kappa_{1T}$  a function of magnetic field for the large,  $\bar{s} = 2.2\text{mm}$  sample. All plots are shifted for clarity. The temperature was determined in the B-saturation regime. **b)** Oscillations of the thermal conductivity  $\delta\kappa$  ( $\delta\kappa = \kappa - \text{background}$ ) plotted as a function of  $B^{-1}$  for two temperatures  $T = 1.4\text{K}$  and  $T = 3.0\text{K}$ . . . . . 93
- 6.10 **a)** Specific heat  $C_v$  as a function of temperature both from experimental results (black crosses) and ab initio calculation (red line). **b)** Specific heat plotted as  $C_v/T^3$  for both experimental and theoretical results. . . . . 94
- 6.11 **a)** Thermopower  $S_{XX}$  plotted as  $S_{XX}/T$  as a function of temperature without magnetic field in the small Sb sample. **b)** Nernst coefficient  $\nu$  plotted as  $\nu/T$  as a function of  $\mu/T_F$  for a variety of solids presented in [46]. The green line indicates the approximate behavior in the Fermi liquid limit. . . . . 95

- 6.12 **a)** Nernst coefficient  $\nu$  plotted as  $-\nu/T$  as a function of temperature at fixed magnetic fields. Inset shows the Fourier transform of  $\nu/T$  at  $T = 3.3\text{K}$ . **b)** Thermopower  $S_{XX}$  plotted as  $S_{XX}/T$  as a function of temperature at fixed magnetic fields. **b)** Nernst coefficient  $\nu$  plotted as  $-\nu$  as a function of magnetic field at fixed temperatures. **d)** Thermopower  $S_{XX}$  plotted as  $S_{XX}/T$  as a function of magnetic field at fixed temperatures. Inset shows the Fourier transform of  $S_{xx}/T$  at  $T = 3.3\text{K}$  . . . . . 97
- 6.13 Thermal conductivity plotted as  $\kappa/T$  as a function of  $T^2$  for different magnetic fields applied to S3. Data points are shown as markers while the dotted line correspond to  $L_0/\rho(B)$ . The Wiedemann-Franz law is satisfied if the intercept of  $\kappa/T$  matches the dotted line in the  $T = 0\text{K}$  limit. The broken line serves as a guide for the eyes. . . . . 100
- 6.14 **a)** Plot of the total thermal conductivity  $\kappa$ , the electronic part  $\kappa_e$  and the phonons' contribution  $\kappa_{ph}$  as a function of temperature for the large Sb sample. **b)**  $\kappa_e$  plotted as a function of temperature for the three Sb samples. **c)** Electronic Lorenz ratio plotted as a function of temperature for the three sample.  $L_e/L_0 = 1$  indicates the recovery of the WFL. **d)** Thermal resistivity  $(WT) = L_0T/\kappa_e$  plotted as a function of temperature for the small and large samples. . . . . 102
- 6.15 **a)** Electrical resistivity  $\rho_{22}$  plotted as a function of  $T^2$  in the three Sb samples. **b)** Thermal resistivity  $(WT)$  plotted as a function of  $T^2$  in the large and small Sb samples. The dotted lines correspond to fits to  $T^2$ -resistivities. Different x-axis ranges are used in the two plots. . . . . 104
- 6.16 **a)** Electrical  $\rho_{22}$  and thermal  $(WT)$  resistivities plotted as a function of magnetic field for  $T = 3\text{K}$ . **b)** Quantum oscillations extracted, from top to bottom, from  $\rho_{22}$ ,  $\kappa$  and  $N$  (Nernst coefficient) in arbitrary units. All sweeps were realised at  $T = 3\text{K}$ . The vertical dotted lines serve as guides for the eye. 106

- 6.17 **a)** Evolution with temperature of the amplitude the Fourier transform of the  $f_1 = 100\text{T}$  peak in  $\kappa_{ph}$  ( $A_{FT}(\delta\kappa)$ ) of Sb sample S3. Inset shows  $A_{FT}(\delta\kappa)/T^3$  as a function of temperature **c)** Amplitude of the 100T-peak normalized by the Phonons thermal conductivity  $A_{FT}(\delta\kappa)/\kappa_{ph}$  as a function of temperature. Black markers represent experimental data while the red and green dotted lines correspond respectively to fits to the LK model and its derivative. Error-bars are evaluated from both experimental noise and numerical analysis. The inset compares the Fourier transform (FT) of  $\kappa$  (red) and  $\rho_{22}$  at the same temperatures. Also featured as an inset is a sketch of an acoustic phonon absorbed by an electron in the  $N^{th}$  LL scattered to the  $(N + 1)^{th}$  LL. . . . . 109
- 7.1 **a)** Velocity profile of the quasiparticles in a 2D channel of width  $w$  in the diffusive regime of transport. Figure from A. Mackenzie [15]. **b)** Velocity profile of the quasiparticles in a 2D channel of width  $w$  in the hydrodynamic regime of transport [15] . . . . . 113
- 7.2 **a)** Thermal conductivity of liquid normal  $^3\text{He}$  as a function of temperature. The different curves correspond to different  $^3\text{He}$  densities while the solid and open circles indicate two different experimental setups for the measurement. Inset show the  $T < 60\text{mK}$  region in a linear scale. Data from Greywall [158]. **b)** Viscosity as a function of temperature for liquid normal  $^3\text{He}$ . Experimental points by the  $45^\circ$  phase method for pure  $^3\text{He}$ . Curve A represents a saturated solution of  $^3\text{He}$  in  $^4\text{He}$ , curve B represents pure  $^3\text{He}$  by Betts *et al.* [159, 160]. Curve C represents a solution of around 5%  $^4\text{He}$  in  $^3\text{He}$ . . . . . 117
- 7.3 **a)** The Kadowaki-Woods plot with  $A_2$  plotted as a function of fermionic specific heat  $\gamma$  (from  $C = \gamma T$ ) compiled by Tsujii *et al.* [166]. We have added the data for ,  $\text{WP}_2$  (This work), W [114] and  $\text{CeRhIn}_5$  [31, 167]. These compounds are indicated by boxes. **b)** Plot of the  $B_2$  thermal  $T^2$ -prefactor as a function of fermionic specific heat  $\gamma$ . Data from  $^3\text{He}$  [158, 153, 168],  $\text{WP}_2$  (this work), W [114] and  $\text{CeRhIn}_5$  [31, 167] and  $\text{UPt}_3$  [32]. . . . . 119
- 7.4 Electrical resistivity  $\rho$  and thermal resistivity ( $WT$ ) plotted as a function of  $T^2$  for  $\text{WP}_2$ . The arrows indicate the value of the residual resistivity  $\rho_0 = W_0 T$ , the  $T^2$  electrical resistivity (associated with MR scattering)  $\rho$  at  $T^2 = 75\text{K}^2$  and the  $T^2$  thermal resistivity (associated with MC collisions) at  $T^2 = 75\text{K}^2$ . We observe that in the vicinity of  $T^2 = 75\text{K}^2$ , MC and boundary collisions dominates strongly over resistive scattering. . . . . 121

- 7.5 The magnitude of  $B_2T^2$ , proportional to momentum-conserving (MC) electron-electron collisions is compared to  $A_2T^2 + A_5T^5$ , which is proportional to momentum-relaxing electron-phonon collisions and to boundary scattering described by  $\rho_0$ . A limited window where the hydrodynamic hierarchy is satisfied can be found for the three following cases. a)  $\rho_0$  is solely due to boundary scattering. b)  $\rho_0$ , due to boundary scattering, represents 75% of the total residual resistivity. c)  $\rho_0$ , represents 50% of the total residual resistivity. . . . . 122
- 7.6 a)  $\rho$  and  $(WT)$  plotted as functions of  $T^2$  in the thin Sb sample S1. b)  $\rho$  and  $(WT)$  plotted as functions of  $T^2$  in the large Sb S3. Both plots share a common x-axis. c)  $T^2$ -prefactors for the electrical ( $A_2$ ) and thermal ( $B_2$ ) resistivities as a function of the sample average cross section  $\bar{s}$ . Data from the literature [130, 131] are featured and indicated directly on the plot. Inset shows the evolution of the  $B_2/A_2$  ratio size. . . . . 124
- 7.7 a) Phonon thermal conductivity plotted as  $\kappa_{ph}/T^3$  for the three Sb samples (S1,S2,S3). Additional data extracted from the literature is also featured [33, 133]. b) Phononic part of the specific heat plotted as  $C_{phonons}/T^3$ . Data taken from [140] are also featured. c) Phonons mean-free-path  $l_{phonons}$  plotted as function of temperature for the same samples presented in a). The sound velocity was assumed to be  $v_s = 3420 \text{ m.s}^{-1}$ . . . . . 127
- 7.8 a) Mean-free-path of phonons  $l_{phonons}$  plotted as a function of temperature for different size of Black P samples. Data from Machida *et al.* [42]. b)  $l_{phonons}$  plotted as a function of temperature for different size of Bi samples. Data from Kopylov *et al.* [39]. c)  $l_{phonons}$  plotted as a function of temperature for solid  $^4\text{He}$  grown in different sizes of ampoules. Data from L.P. Mezhov-Deglin [147]. . . . . 129
- 1 a)  $R_a$  plotted as a function of temperature in sample NG-2 b)  $R_a$  plotted as a function of field for various temperatures in sample NG-2. . . . . 163
- 2 a) Resistivity  $\rho$ , measured along the  $a$ -axis, of  $\text{WP}_2$  as a function of  $T^2$  for the three samples S1, S2 and S3. b) Phonons contribution to the electrical resistivity  $\delta\rho = \rho - \rho_0 - AT^2$  as a function of  $T^5$  for the same three samples. Inset shows a fit of  $\delta\rho$  to a  $T^5$  law with  $A_5 = 3.9 \times 10^{-15} \text{ } \Omega\cdot\text{cm}\cdot\text{K}^{-5}$ . We observe a downward deviation for  $T > 20\text{K}$ . . . . . 164

- 
- 3 a) Thermal resistivity,  $WT = \frac{L_0 T}{\kappa}$ , as a function of  $T$  for the three WP<sub>2</sub> samples. b) Ratio of Lorenz,  $L(T) = \frac{\kappa}{T\sigma}$ , to Sommerfeld,  $L_0 = 2.44 \times 10^{-8} W.\Omega.K^{-2}$ , numbers as a function of temperature for the same three samples. c) Here we show  $WT - W_0 T$  as a function of  $T^2$  for the three samples. d) Plot of the phonon component of the thermal resistivity  $\delta WT = WT - W_0 T - BT^2$  as a function of  $T$ . The black line corresponds to a  $T^3$  fit. . . . 165
- 4 Thermal conductivity of samples  $\bar{s} = 0.52$  mm Sb samples as a function of magnetic field for different temperatures. Inset shows the background removed oscillations plotted as a function of  $B^{-1}$ . . . . . 166



# Supplementary Data

## .1 Supplementary Data : Graphite

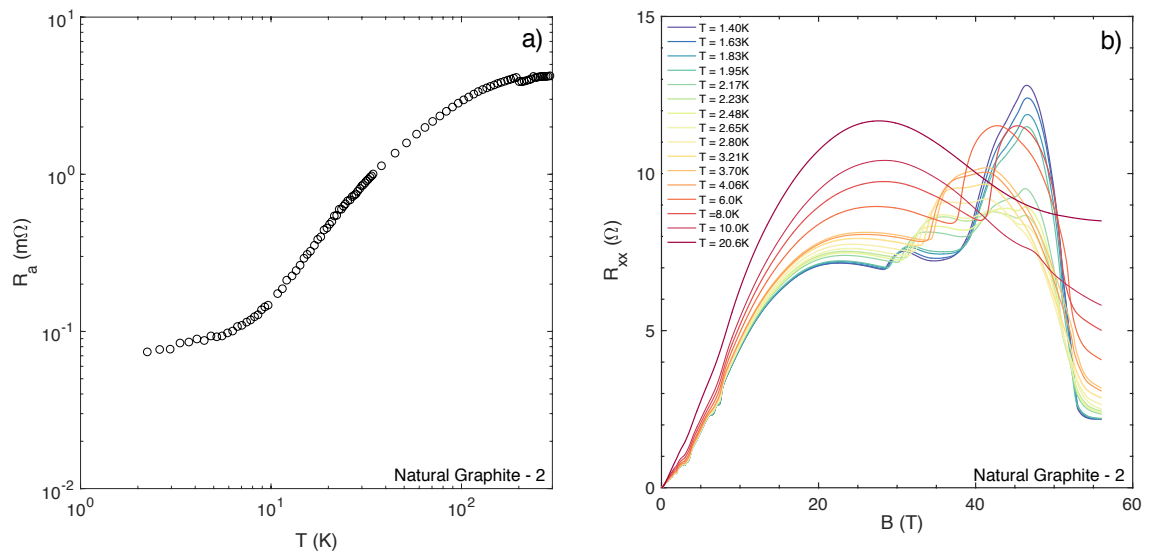


Fig. 1 **a)**  $R_a$  plotted as a function of temperature in sample NG-2 **b)**  $R_a$  plotted as a function of field for various temperatures in sample NG-2.

We report here on the in-plane resistivity of a natural graphite sample labelled NG-2.  $R_a$ , which display a RRR = 60, is plotted as a function of temperature in figure 1.a. The in-plane field dependence is plotted up to  $B = 56$ T (measured in pulsed field, LNCMI Toulouse, France) in figure 1.b. This data are used in chapter 4 to study the in-plane metallicity of graphite in the field-induced states.

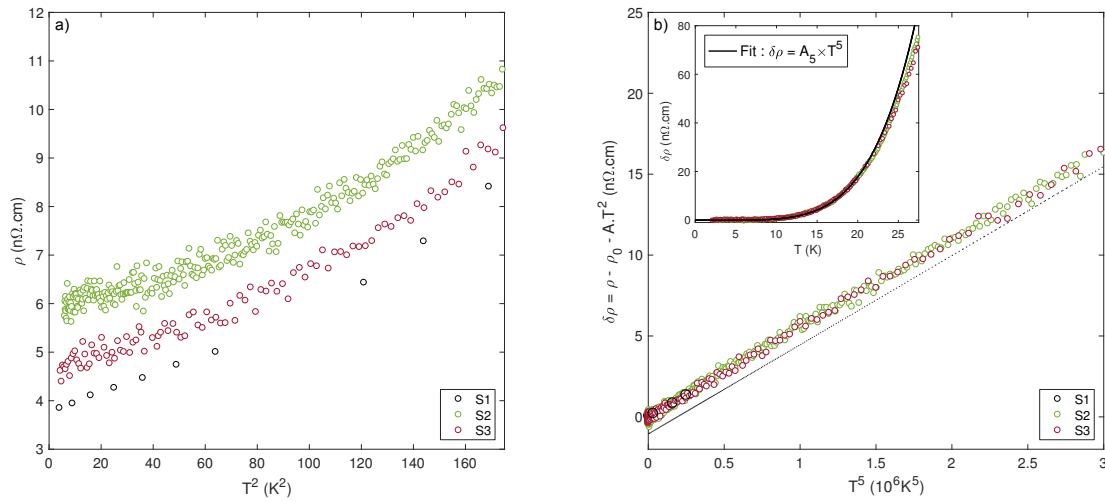


Fig. 2 a) Resistivity  $\rho$ , measured along the  $a$ -axis, of  $WP_2$  as a function of  $T^2$  for the three samples S1, S2 and S3. b) Phonons contribution to the electrical resistivity  $\delta\rho = \rho - \rho_0 - AT^2$  as a function of  $T^5$  for the same three samples. Inset shows a fit of  $\delta\rho$  to a  $T^5$  law with  $A_5 = 3.9 \times 10^{-15} \text{ } \Omega\cdot\text{cm}\cdot\text{K}^{-5}$ . We observe a downward deviation for  $T > 20\text{K}$ .

## .2 Supplementary Data : $WP_2$

We measured 3 different single crystals of  $WP_2$ , all grown in the same batch. The sample presented in the corpus is S3. In table 1 we present their geometries and basic electrical characteristics.

All the samples were measured along the same direction, with  $j \parallel (a\text{-axis})$  for both heat and electrical currents. The result for the electrical conductivity in all three samples are shown in Fig.2. Besides the residual resistivity  $\rho_0$ , we see that both the  $T^2$ -dependent and  $T^5$ -dependent terms are equal from one sample to another.

From Fig.3 we can deduce that the  $T^2$ -dependent and  $T^3$ -dependent terms of the thermal resistivity,  $WT$ , are also equivalent in the three different samples. We thus confirm that besides the residual terms, the electrical and thermal resistivities are reproducible from one sample to another with comparable size.

Sample	Length (mm)	Width ( $\mu\text{m}$ )	Thickness ( $\mu\text{m}$ )	$\rho_0$ (nΩ.cm)	RRR = $\rho(300\text{K})/\rho(2\text{K})$
S1	1.5	80-100	110	3.94	11200
S2	1.9	90-100	110	5.85	7600
S3	0.9	80-110	120	4.69	9600

Table 1 Presentation of the different  $WP_2$  samples

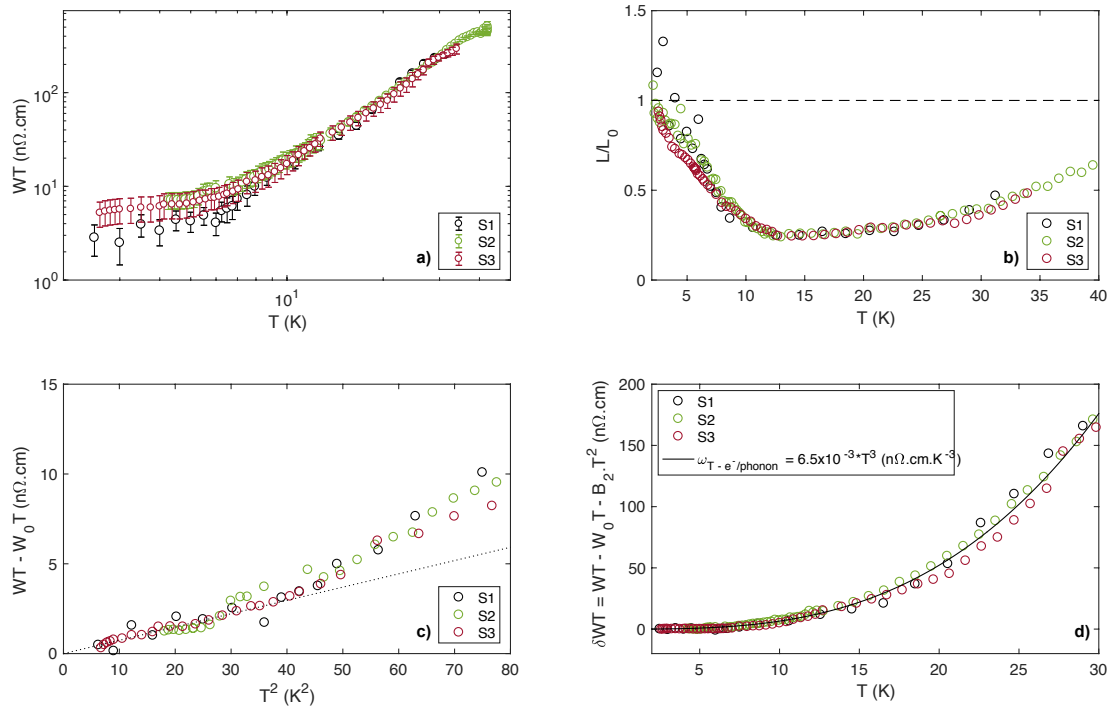


Fig. 3 a) Thermal resistivity,  $WT = \frac{L_0T}{\kappa}$ , as a function of  $T$  for the three WP<sub>2</sub> samples. b) Ratio of Lorenz,  $L(T) = \frac{\kappa}{T\sigma}$ , to Sommerfeld,  $L_0 = 2.44 \times 10^{-8} \text{ W}\cdot\Omega\cdot\text{K}^{-2}$ , numbers as a function of temperature for the same three samples. c) Here we show  $WT - W_0T$  as a function of  $T^2$  for the three samples. d) Plot of the phonon component of the thermal resistivity  $\delta WT = WT - W_0T - BT^2$  as a function of  $T$ . The black line corresponds to a  $T^3$  fit.

### .3 Supplementary Data : Sb

We report here on oscillations of the phonon thermal conductivity in the small Sb sample, similar to our report on the large Sb samples. The amplitude of the oscillations, featured in figure 4, in this sample is smaller and the oscillations remain  $1/B$ -periodic with a frequency close to  $f \approx 100T$ .

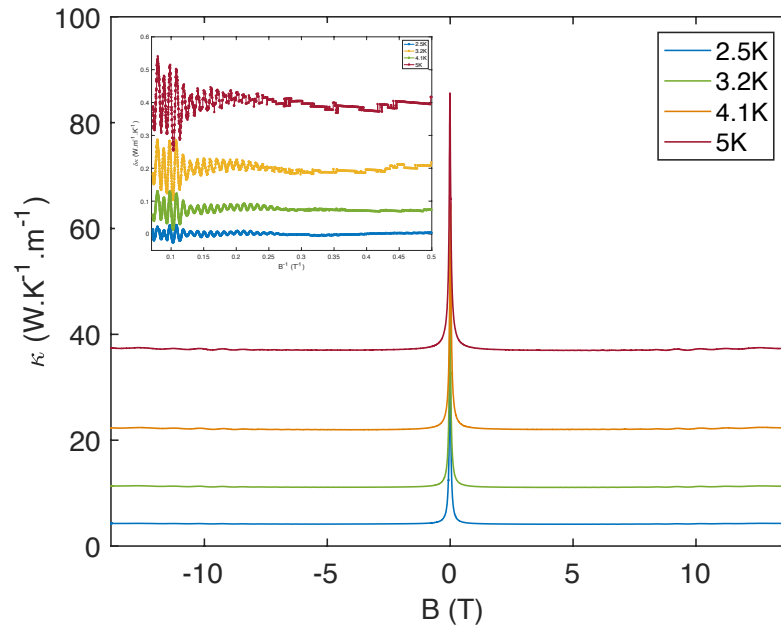


Fig. 4 Thermal conductivity of samples  $\bar{s} = 0.52$  mm Sb samples as a function of magnetic field for different temperatures. Inset shows the background removed oscillations plotted as a function of  $B^{-1}$ .